

Electronic Thesis and Dissertation Repository

1-22-2020 2:30 PM

Rational Interface Design for High-Performance All-Solid-State Lithium Batteries


Changhong Wang, *The University of Western Ontario*

Supervisor: Sun Xueliang, *The University of Western Ontario*

A thesis submitted in partial fulfillment of the requirements for the Doctor of Philosophy degree in Mechanical and Materials Engineering

© Changhong Wang 2020

Follow this and additional works at: <https://ir.lib.uwo.ca/etd>

 Part of the [Ceramic Materials Commons](#), [Other Materials Science and Engineering Commons](#), [Polymer and Organic Materials Commons](#), [Thermodynamics Commons](#), and the [Transport Phenomena Commons](#)

Recommended Citation

Wang, Changhong, "Rational Interface Design for High-Performance All-Solid-State Lithium Batteries" (2020). *Electronic Thesis and Dissertation Repository*. 6798.
<https://ir.lib.uwo.ca/etd/6798>

This Dissertation/Thesis is brought to you for free and open access by Scholarship@Western. It has been accepted for inclusion in Electronic Thesis and Dissertation Repository by an authorized administrator of Scholarship@Western. For more information, please contact wlsadmin@uwo.ca.

Abstract

All-solid-state lithium batteries (ASSLBs) have gained substantial attention owing to their excellent safety and high energy density. However, the development of ASSLBs has been hindered by large interfacial resistance originating from the detrimental interfacial reactions, poor solid-solid contact, and lithium dendrite growth. The research in this thesis aims at achieving high-performance ASSLBs via rational interface design and understanding the interfacial reaction mechanisms.

At the cathode interface, an ideal dual core-shell nanostructure was first designed. Moreover, single-crystal $\text{LiNi}_{0.5}\text{Mn}_{0.3}\text{Co}_{0.2}\text{O}_2$ (SC-NMC532) cathode was compared with polycrystalline NMC532, the former exhibits much enhanced Li^+ diffusion kinetics in ASSLIBs. Besides, it is found that the interfacial structural degradation significantly impedes interfacial Li^+ transport in ASSLIBs. Fortunately, the interfacial coating is demonstrated to be effective in suppressing interfacial degradation.

Furthermore, the ionic conductivity of interfacial layer LNTO was purposely tuned to investigate the effect of interfacial ionic conductivity on ASSLIBs, it is revealed that enhancing the interfacial ionic conductivity is very crucial for high-performance ASSLBs. The conclusion was confirmed by the in-situ growth of Li_3InCl_6 . The high Li^+ -conductive Li_3InCl_6 coated LCO demonstrates an ultra-small interfacial resistance of $0.13 \Omega\cdot\text{cm}^{-2}$ and excellent electrochemical performance.

At the anode interface, an inorganic-organic hybrid interlayer and a solid-state plastic crystal electrolyte were successfully engineered to prevent the interfacial reactions and lithium dendrite formation. Last but not least, a solid-liquid hybrid electrolyte was developed as interfacial solid-liquid electrolyte interphase (SLEI) to achieve high-performance ASSLBs.

In summary, the discoveries in this thesis provide important guidance to achieve high-performance ASSLBs via rational interface design.

Keywords

All-solid-state lithium batteries, cathode interface, anode interface, Li metal anode, interfacial nanostructure, interfacial Li⁺ transport kinetics, molecular layer deposition, atomic layer deposition, interfacial reactions, solid-solid contact.

Lay Summary

Because of the high energy density and a great safety feature, all-solid-state lithium batteries (ASSLBs) have aroused substantial attention in recent years. However, large interfacial resistance originating from the detrimental interfacial reactions, poor solid-solid contact, and lithium dendrite growth hinders the realization of ASSLBs. This thesis described various interfacial strategies to overcome the large interface resistance. In addition, advanced characterizations including synchrotron radiation and high-resolution transmission electron microscopy (HRTEM) were adopted to understand interfacial Li^+ transport kinetics and interfacial reaction mechanism.

Specifically, an ideal dual core-shell nanostructure was first designed at the cathode interface, which demonstrates high-performance ASSLBs. Furthermore, single-crystal cathodes were found much better than polycrystalline cathodes in ASSLBs. Besides, via HRTEM and synchrotron radiation characterization, it is found that the oxygen loss from the cathode materials can deteriorate the interfacial structure change of oxide cathodes. Fortunately, the interfacial coating is demonstrated to be effective in suppressing interfacial structure change. Moreover, it is also found that the interfacial ionic conductivity of the coating layer is very crucial for achieving high-performance ASSLBs. Following this conclusion, a high Li^+ -conductive Li_3InCl_6 coating layer was in-situ grown on the LCO surface, demonstrating an ultra-small interfacial resistance.

An inorganic-organic hybrid interlayer and a solid-state plastic crystal electrolyte were successfully engineered to prevent the interfacial reactions and lithium dendrite formation at the anode interface. Last but not least, a solid-liquid hybrid electrolyte was developed as an interfacial solid-liquid electrolyte interphase (SLEI) for high-performance solid-state batteries.

In summary, the discoveries in this thesis provide important guidance to achieve

high-performance ASSLBs via rational interface design.

Co-authorship Statement

1.

Title: Sulfide Electrolytes and Their Solid-State Lithium Batteries: From Fundamental Research to Practical Manufacture

Authors: Changhong Wang, Yang Zhao, Jianwen Liang, Xiaona Li, Xueliang Sun

The final version of this manuscript will be submitted to a high-impact journal. All the authors contributed to designing, writing, and modifying the manuscript.

2.

Title: Manipulating Interfacial Nanostructure to Achieve High-Performance All-Solid-State Lithium-Ion Batteries

Authors: Changhong Wang, Xia Li, Yang Zhao, Mohammad N. Banis, Jianwen Liang, Xiaona Li, Yipeng Sun, Keegan R. Adair, Qian Sun, Yulong Liu, Feipeng Zhao, Sixu Deng, Xiaoting Lin, Ruying Li, Yongfeng Hu, Tsun-Kong Sham, Huan Huang, Li, Zhang, Rong Yang, Shigang Lu, and Xueliang Sun

The final version of this manuscript has been published in *Small Methods*, 2019, 1900261. DOI: 10.1002/smtd.201900261. X.S. supervised the project. C.W. conceived this idea, synthesized the electrodes, characterized the samples, tested the electrochemical performances, and wrote this manuscript. X.L. and M.B. performed the in situ XAS and TEM characterization in CLS and McMaster University, respectively. X.L. and J.L. helped with experimental optimization. Y.Z. and Y.S. helped with the ALD process. K.A. polished the language. R.L. helped with SEM and purchasing all the chemicals. All the

authors discussed the results and commented on the manuscript.

3.

Title: Single Crystal Cathodes for High-Energy and High-Power All-Solid-State Lithium-Ion Batteries

Authors: Changhong Wang, Sooyeon Hwang, Jianwen Liang, Xiaona Li, Changtai Zhao, Yipeng Sun, Jiwei Wang, Nathaniel Holmes, Ruying Li, Huan Huang, Shangqian Zhao, Li Zhang, Shigang Lu, Dong Su, and Xueliang Sun

The final version of this manuscript has been submitted to *Nano Letters*. C. W. and X. Sun conceived the idea. C. W. designed all the experiments and electrochemical characterizations. S. H. and D. S. helped with TEM characterization and analysis. J. L. and X. L. interpreted the experimental results. C. Z., Y. S., and J. W. discussed all the experimental results. N. H. polished the language. R. L helped with purchasing all the chemicals. C. W. wrote the manuscript. All the authors discussed the results and commented on the manuscript. The whole project was supervised by X. S.

4.

Title: Deciphering Oxygen Release of Layered Oxide Cathodes and Its Effect on Sulfide-based All-Solid-State Batteries

Authors: Changhong Wang, Sooyeon Hwang, Ming Jiang, Jianwen Liang, Xiaona Li, Sankha Mukherjee, Yipeng Sun, Mohammad Norouzi Banis, Changtai Zhao, Ruying Li, Huan Huang, Shangqian Zhao, Li, Zhang, Shigang Lu, Chandra Veer Singh, Dong Su and Xueliang Sun

The final version of this manuscript will be submitted, X. Sun supervised the whole

project. C. Wang conceived the idea and designed all the experiments and electrochemical characterizations. M. Jiang, Sankha Mukherjee, and C. Singh conducted the first-principles calculations. S. H. and D. S. helped with TEM characterization and analysis. J. L. and X. L. interpreted the experimental results. M. Banis. Y. Sun helped with synchrotron characterization. C. Z., Y. S., and J. W. discussed all the experimental results. N. H. polished the language. R. L helped with purchasing all the chemicals. C. W. wrote the manuscript. All the authors discussed the results and commented on the manuscript.

5.

Title: Unravelling Interfacial Ion Transport in All-Solid-State Lithium-Ion Batteries

Authors: Changhong Wang, Jianwen Liang, Yang Zhao, Xiaona Li, Sooyeon Hwang, Keegan Adair, Yulong Liu, Xia Li, Sixu Deng, Xiaofei Yang, Ruying Li, Huan Huang, Li, Zhang, Shigang Lu, Dong Su, and Xueliang Sun.

The final version of this manuscript has been submitted to **Nano Energy**.

X. Sun supervised the project. C. Wang conceived this idea, synthesized the electrodes, tested the electrochemical performances, performed characterization and wrote this manuscript. S. Hwang and D. Su helped in the TEM characterization. R. Li helped with SEM and purchased all the chemicals. All authors discussed the results and commented on the manuscript.

6.

Title: Eliminating Interfacial Resistance in All-Inorganic Batteries by In-situ Interfacial

Growth of Li_3InCl_6

Authors: Changhong Wang, Jianwen Liang, Ming Jiang, Xiaona Li, Sankha Mukherjee, Keegan Adair, Matthew Zheng, Yang Zhao, Feipeng Zhao, Shuming Zhang, Ruying Li, Huan Huang, Shangqian Zhao, Li Zhang, Shigang Lu, Chandra Veer Singh, Xueliang Sun

The final version of this manuscript has been submitted to *Advanced Functional Materials*; C. W. and J. L. equally contributed to this work and designed all the experiments and characterizations. M. J. and S. M. performed theoretical calculations. X. L. help with halide electrolyte synthesis. K. A. and M. B. helped with synchrotron characterizations. R. L. helped with purchasing all the chemicals. C. W. wrote the manuscript. All the authors discussed the results and commented on the manuscript. C. S. supervised the theoretical calculations. The whole project was supervised by X. S.

7.

Title: Stabilizing Interface between $\text{Li}_{10}\text{SnP}_2\text{S}_{12}$ and Li Metal by Molecular Layer Deposition

Authors: Changhong Wang, Yang Zhao, Qian Sun, Xia Li, Yulong Liu, Jianwen Liang, Xiaona Li, Xiaoting Lin, Ruying Li, Keegan R. Adair, Li, Zhang, Rong Yang, Shigang Lu, and Xueliang Sun

The final version of this manuscript has been published in *Nano Energy*, 2018,53, 168-174; C. W., Y. Z., and Q. S. conceived the idea and designed the experiments. X. S. directed the project. R. L. helps with purchasing chemicals and characterizations. Y. L., J. L., X. L., and X. L. help in data analysis. C.W. wrote the manuscript. All authors

discussed the results and commented on the manuscript.

8.

Title: Solid-State Plastic Crystal Electrolytes: Effective Protection Interlayers for Sulfide-Based All-Solid-State Lithium Metal Batteries

Authors: Changhong Wang, Keegan R Adair, Jianwen Liang, Xiaona Li, Yipeng Sun, Xia Li, Jiwei Wang, Qian Sun, Feipeng Zhao, Xiaoting Lin, Ruying Li, Huan Huang, Li Zhang, Rong Yang, Shigang Lu, Xueliang Sun

The final version of this manuscript has been published in *Advanced Functional Materials*, 2019, 29, **1900392**. DOI: 10.1002/adfm.201900392. Xueliang Sun supervised the overall project; Changhong Wang conceived the idea and conducted all the experiments and wrote the manuscript. Keegan Adair polished the language. Jianwen Liang and Xiaona Li discussed the idea. Yipeng Sun, Xia Li performed the synchrotron characterizations. Jiwei Wang helped with 3D schematic. Qian Sun, Feipeng Zhao, Xiaoting Lin discussed the results. Ruying Li ordered all the chemicals. All authors contributed editorial comments on the manuscript.

9.

Title: Boosting the performance of lithium batteries with solid-liquid hybrid electrolytes: Interfacial properties and effects of liquid electrolytes

Authors: Changhong Wang, Qian Sun, Yulong Liu, Yang Zhao, Xia Li, Xiaoting Lin, Mohammad Norouzi Banis, Minsi Li, Weihan Li, Keegan R Adair, Dawei Wang, Jianneng Liang, Ruying Li, Li Zhang, Rong Yang, Shigang Lu, Xueliang Sun

The final version of this manuscript has been published in *Nano Energy*, 2018, 48, 35-43. Xueliang Sun supervised the overall project; Changhong Wang performed all the

experiments and wrote the manuscript. Qian Sun and Yulong Liu helped with the synthesis of oxide electrolytes. Mohammad Norouzi Banis, Minsi Li, Weihan Li helped synchrotron characterizations. All authors contributed editorial comments on the manuscript.

Dedication

The thesis is dedicated to my wife, my parents, my sisters, and my grandparents.

The present is theirs; the future, for which I really worked, is mine.

-Nikola Tesla

Acknowledgments

This Ph.D. work was accomplished in Professor Xueliang (Andy) Sun's Nanomaterials and Energy Group at the University of Western Ontario (UWO). I would like to thank everyone that has helped me throughout the past four years.

First of all, I would like to express my sincerest gratitude to my supervisor, Prof. Xueliang (Andy) Sun, a Professor in Department of Mechanical and Materials Engineering (MME) at UWO, Canada Research Chair, Fellow of the Canadian Academy of Engineering and Fellow of the Royal Society of Canada. In 2016, I contacted Prof. Sun by email to see if I can pursue my Ph.D. degree under his group. He quickly replied to my email and expressed his strong interests to recruit me. After a Skype meeting online, his knowledge and elegance as the scientist had left a deep impression on me. I am very grateful that he provided the opportunity and an incredible platform for me to work and study here and gave me strong support for my research in the past four years. As my supervisor, Prof. Sun always encourages me to think about the fundamental question, to gain insights into basic scientific issues, and to balance the challenges between engineering and science. Moreover, what I learned from him is not only how to engage in scientific research, but also how to plan a career and life and how to get along with people in a sagacious manner. Dr. Sun's dedication to the lab, his diligence, brilliance, patience, and kindness have greatly inspired me. I believe that all the experience, knowledge, and technical skills I gained here would make a profound impact on my future career and life.

I would also like to thank Mrs. Ruying (Kathy) Li, Dr. Sun's wife, and our lab manager. I cannot forget her maternal care and patient help to my life and my research, and even my family here in London. In the past years, she provided countless help to me and my family. No words can express my gratitude to her in my mind.

I am also grateful to my advisory committee members, Dr. Robert Klassen and Dr. Liying Jiang, professors in the Department of Mechanical and Materials Engineering at UWO, for their valuable advice and discussions toward the completion of this Ph.D. thesis.

I am also indebted to my colleagues at the University of Western Ontario throughout the past four years. I would like to thank Dr. Jianwen Liang and Dr. Qian Sun for his highly constructive comments and guidance on my research. Each discussion with them is like brainstorming, which inspired me a lot in my research and generating innovative ideas and proposed constructive strategies to address challenges. In addition, I also would like to thank Dr. Xia Li for her training on SEM, batteries and other instruments when I joined the group. I am also grateful to Dr. Biqiong Wang, Dr. Zhongxin Song, and Dr. Yulong Liu for their training on all kinds of experimental machine and nanomaterial growth, such as ALD, CNT and graphene growth, and solid electrolyte synthesis. I would also like to extend my appreciation to other colleagues Mr. Keegan Adair, Mr. Nathaneil, Dr. Xiaofei Yang, Dr. Wei Xiao and the "study group" of Mrs. Minsi Li, Mrs. Xiaoting Lin, Mr. Jiwei Wang. Last but not least, Thanks to every other colleagues from the groups: Dr. Weihan Li, Dr. Mohammad Norouzi Banis, Dr. Hossein Yadegari, Dr. Dawei Wang, Dr. Lei Zhang, Dr. Muhammad Iqbal, Dr. Changtai Zhao, Dr. Sixu Deng, Dr. Li Hou, Mr. Jianneng Liang, Mr. Junjie Li, Miss Xuejie Gao, Miss Jing Luo, Mr. Yipeng Sun, Miss Alicia Koo, Mr. Sizhe Wang, Mr. Fanpeng Kong, Mr. Matthew Zheng; and all the former members who studied and worked in the group.

I am grateful to Dr. Mark Biesinger at Surface science Western for his XPS measurement and discussion on the data. I also thank Prof. Chandra Singh, Mr. Ming Jiang, and Dr. Sankha Mukherjee from the University of Toronto for them doing DFT calculations.

Sincerely thank the funding supports from Nature Sciences and Engineering Research Council of Canada (NSERC), Canada Research Chair (CRC) program, Canada Foundation of Innovation (CFI), MITACS accelerate fellowships and the University of

Western Ontario. Without financial support, the work would not have been possible to be finished.

Last but not least, I would like to express my appreciation from my heart to my family. Without their support, financially and emotionally, I cannot complete my Ph.D. thesis. Their unconditional love, encouragement, motivation, and support over the past few years are incalculable. I feel deeply guilty that I cannot accompany them in the past years.

Changhong Wang

October 30th, 2019

CMLP 1325 office of Western Engineering

Table of Contents

Abstract.....	I
Lay Summary.....	III
Co-authorship Statement.....	V
Acknowledgments.....	XII
Table of Contents.....	XV
List of Tables.....	XXII
List of Figures.....	XXIII
List of Appendices.....	XXXVII
List of Abbreviations.....	XXXVIII
Chapter 1	1
1. Introduction.....	1
1.1 Background and Motivation.....	1
1.2 State-of-the-Art of Solid-State Sulfide Electrolytes.....	3
1.2.1 Fundamental of Sulfide Electrolytes.....	3
1.2.2 Typical Sulfide Electrolytes.....	4
1.2.3 <i>Thio</i> -LISICON ($\text{Li}_{10\pm 1}\text{MP}_2\text{X}_{12}$) Family.....	6
1.2.4 Lithium Argyrodites ($\text{Li}_6\text{PS}_5\text{X}$, X= Cl, Br, I).....	11
1.2.5 Glassy and Glass-Ceramic Li_2S - P_2S_5 System.....	12
1.3 Stability of Sulfide Electrolytes.....	14
1.3.1 Chemical Stability of Sulfide Electrolytes.....	14
1.3.2 Electrochemical Stability of Sulfide Electrolytes.....	16
1.4. Interface Challenges of SE-based ASSLIBs.....	18

1.4.1 Cathode Interface of SE-based All-Solid-State Lithium Batteries	18
1.4.2 Anode Interface of SE-based All-Solid-State Lithium Batteries	27
1.5 Demonstrations of SE-based ASSLIBs.....	31
1.5.1 Solid-State SE-based ASSLIBs.....	31
1.5.2 SE-based All-Solid-State Lithium-Sulfur Batteries	35
1.5.3. Manufacturing Protocol of Solid-State Lithium Batteries	38
1.6 Thesis Objectives	40
1.7 Thesis Organization.....	42
1.8 References	46
Chapter 2	64
2. Experimental Apparatus and Characterization Techniques.....	64
2.1 Experimental Apparatus.....	64
2.2 Characterizations Techniques	65
2.2.1 Physical Characterizations	65
2.3 Electrochemical Characterizations.....	70
2.4 References	71
Chapter 3	72
3 Manipulating Interfacial Nanostructure to Achieve High-Performance All-Solid-State Lithium-Ion Batteries.....	72
3.1 Introduction	73
3.2 Experimental Procedures.....	74
3.2.1 Synthesis of One-Shell LNO@LCO and Dual Shell Structured LGPS@LNO@LCO.	74
3.2.2 Characterizations.....	75

3.2.3 Electrochemical Performance	76
3.3 Results and Discussion	77
3.4 Conclusions	88
3.5 Acknowledgments	89
3.6 References	89
3.7 Supporting Information	93
Chapter 4	102
4. Single Crystal Cathodes Increasing Power and Energy Density of All-Solid-State Batteries	102
4.1 Introduction	103
4.2 Experiments and Characterizations	104
4.2.1 Surface Modification of SC-NMC532 and PC-NMC532	104
4.2.2 Characterizations	104
4.2.3 Assembly of ASSLIBs	105
4.3. Results and Discussion	106
4.4. Conclusions	113
4.5 Acknowledgements	113
4.6 References	114
4.7 Supporting Information	118
Chapter 5	124
5. Deciphering Oxygen Release of Single-Crystal NMC532 and Its Effect on Sulfide-based ASSLIBs	124
5.1 Introduction	125
5.2 Experimental Sections	126

5.2.1 Surface Modification of SC-NMC532	126
5.2.2 Characterizations	127
5.2.3 Assembly of ASSLIBs	128
5.2.4 DFT Calculation	128
5.3 Results and Discussion	129
5.4. Conclusions	137
5.5 Acknowledgements	138
5.6 Author Contribution	138
5.7 References	139
5.8 Supporting Information	143
Chapter 6	149
6. Unraveling Interfacial Ion Transport in All-Solid-State Lithium-Ion Batteries	149
6.1. Introduction	150
6.2 Experimental Section	151
6.2.1 Synthesis of $\text{LiNb}_{0.5}\text{Ta}_{0.5}\text{O}_3$ (LNTO)	151
6.2.2 Synthesis of LNTO@NMC532	152
6.2.3 Characterizations	152
6.2.4 Assembly of All-Solid-State Lithium-Ion Batteries	152
6.3. Results and Discussion	153
6.3.1 Synthesis of Interfacial $\text{LiNb}_{0.5}\text{Ta}_{0.5}\text{O}_3$ (LNTO) with Different Ionic Conductivities.	153
6.3.2 Electrochemical Performance of LNTO@NMC532-based ASSLIBs	158
6.3.3 Quantifying Li^+ Diffusivity of LNTO@NMC532	160
6.4. Conclusions	163

6.5 Acknowledgments	163
6.6 Author Contributions.....	164
6.7 References	164
6.8 Supporting Information	170
Chapter 7	178
7. Eliminating Interfacial Resistance in All-Inorganic Batteries by In-situ Interfacial Growth of Li_3InCl_6	178
7.1 Introduction	179
7.2 Experimental Section	180
7.2.1 In-situ Synthesis of Li_3InCl_6 @ LiCoO_2 Electrodes	180
7.2.2 Characterizations.....	181
7.2.3 Electrochemical Performances.....	181
7.2.4 DFT Calculation.....	182
7.3 Results and Discussion.....	184
7.3.1 Synthesis and Characterization of LIC and LIC@LCO.....	184
7.3.2 Interfacial Interaction between LIC and LCO	187
7.3.3 Electrochemical Performance of LIC@LCO	189
7.4 Conclusions	195
7.5 Acknowledgements	196
7.6 Author contributions	196
7.7 References	198
7.8 Supplementary Information.....	202
Chapter 8	214
8. Stabilizing Interface between $\text{Li}_{10}\text{SnP}_2\text{S}_{12}$ and Li Metal by Molecular Layer Deposition	

.....	214
8.1 Introduction	215
8.2 Experimental Section	216
8.2.1 Li Preparation.....	216
8.2.2 Electrochemical Measurements	217
8.2.3 Characterizations.....	217
8.3 Results and Discussion.....	218
8.4 Conclusions	226
8.5 Acknowledgments	226
8.6 Author Contribution	227
8.7 References	227
8.8 Supporting Information	231
Chapter 9	239
9. Solid-State Plastic Crystal Electrolytes: Effective Protection Interlayers for Sulfide-based All-Solid-State Lithium Metal Batteries	239
9.1 Introduction	240
9.2 Experimental Section	242
9.2.1 Preparation of Plastic Crystal Electrolytes.....	242
9.2.2 Electrochemical Measurements	242
9.2.3 Characterizations.....	243
9.3 Results and Discussion.....	244
9.4 Conclusion.....	252
9.5 Acknowledgments.....	253
9.6 References	254

9.7 Supporting Information	258
Chapter 10	270
10. Boosting the Performance of Lithium Batteries with Solid-Liquid Hybrid Electrolytes: Interfacial Properties and Effects of Liquid Electrolytes.....	270
10.1 Introduction	271
10.2. Experimental Section	272
10.2.1 Synthesis of LATP and Glass-ceramic LATP	272
10.2.2 Materials Characterizations.....	273
10.2.3 Electrochemical Measurements	273
10.3 Results and Discussion.....	275
10.4 Conclusion.....	287
10.5 Acknowledgements	288
10.6 References	288
10.7 Supporting Information	292
Chapter 11	301
11. Conclusions and Perspectives	301
11.1 Conclusions	302
11.2 Perspectives	306
11.3 Main Contribution of This Thesis	309
Appendices.....	311
Curriculum Vitae	315

List of Tables

Table 1-1 State-of-the-art of solid-state SEs in the aspect of ionic conductivity, activation energy, and crystalline structure.	5
Table 1-2 Surface coating that has been developed so far for suppressing interfacial resistance.....	23

List of Figures

Figure 1-1 Overview of challenges and corresponding strategies of SEs and their ASSLIBs.	2
Figure 1-2 (a) Impedance plots of the conductivity data from low to high temperatures and Arrhenius conductivity plots of $\text{Li}_{10}\text{GeP}_2\text{S}_{12}$. (b) Current-voltage curve of a $\text{Li}/\text{Li}_{10}\text{GeP}_2\text{S}_{12}/\text{Au}$ cell 1 mV s^{-1} between -0.5 and 5.0 V at 25 °C. (c) The framework structure and lithium ions that participate in ionic conduction. (d) Framework structure of $\text{Li}_{10}\text{GeP}_2\text{S}_{12}$. (e) Conduction pathways of lithium ions in $\text{Li}_{10}\text{GeP}_2\text{S}_{12}$	8
Figure 1-3 (a) Li-ion migration path (left panels) and calculated energy path (right panels) in bcc. (b) Illustration of energy profiles for single-ion migration (pink) versus multiple-ion concerted migration (blue). (c) Energy landscape of single Li^+ migration (upper) and the energy barrier of concerted migration (lower) in LATP, as calculated using the NEB method.	9
Figure 1-4 (a) The first-principles calculation results of the voltage profile and phase equilibrium of LGPS solid electrolyte upon lithiation and delithiation. Cyclic voltammetry of $\text{Li}/\text{LGPS}-\text{Pt}/\text{Pt}$ semi-blocking electrode at a scan rate of $0.1 \text{ mV}\cdot\text{s}^{-1}$ in the voltage range of 0-2.0 V (b) and 1.0-3.5 V (c).	17
Figure 1-5 (a) The two-phase boundary of oxides and sulfides, and the defect chemistry situation after the formation of SCL; (b) Introduction of ionic-conducting intermediate layer (IL) between the two phases; ⁹⁴ (c) Interface structure between FePO_4 and Li_3PS_4 before and after the FP-MD. Schematic illustrations of the interfacial Li concentration. (d-f) The equilibrium concentrations expected by the conventional model and indicated by the present calculations for the LCO/LPS interface (a and c) as well as the LCO/LNO/LPS (b and d). The Li concentrations in (e) and (f) describe the expected	

changes at the initial stage of charging for both interfaces, respectively.21

Figure 1-6 (a) Cross-sectional HAADF-STEM image of $\text{LiCoO}_2/\text{Li}_2\text{S-P}_2\text{S}_5$ interface after initial charging and cross-sectional EDX line profiles for Co, P, and S elements. The arrow presents the positions at which EDX measurements were taken.⁹⁷ (b) S 2p and P 2p XPS spectra of the composite LCO electrode of LCO/ $\text{Li}_6\text{PS}_5\text{Cl}$ /Li-In half-cells: before cycling (pristine), after 25 cycles, and after 25 cycles with increasing etching depths of the electrode from 5 to 20 μm . (c) Electrochemical window of the proposed and previously demonstrated coating layer materials applied between SEs and cathode materials. The dashed line marks the equilibrium voltage to fully de-lithiate the materials.¹²⁰ (d) The ALD deposition of Li-Ti-O, Li-Nb-O, Li-Ta-O, Li-Si-O, and Li-P-O interfacial coating materials for SE-based ASSLIBs.24

Figure 1-7 (a) Schematic diagram representing the microstructure of the composite electrodes without and with ionic liquids (LiG3), showing that LiG3 improves the imperfect solid-solid contacts. Carbon additives included in the composite electrode are not shown in the scheme. (b) Schematic diagram of ASSLMBs versus ASSLMBs with the PCE interlayer. (c) Schematic diagram illustrating fabrication of sheet-type electrodes and ASLBs applying solution process of SEs; coating and infiltration with SEs.⁶⁶ and (d). Schematic illustration of the mixture electrode and the $0.4\text{LiI}-0.6\text{Li}_4\text{SnS}_4$ -coated LiCoO_2 electrode. The dark blue and yellow regions indicate LiCoO_2 and SE, respectively. FESEM surface images of $0.4\text{LiI}-0.6\text{Li}_4\text{SnS}_4 / \text{LiCoO}_2$ mixture electrode and d) $0.4\text{LiI}-0.6\text{Li}_4\text{SnS}_4$ -coated LiCoO_2 electrode. The arrows indicate void spaces.¹³⁹26

Figure 1-8 (a) Illustration of Different Types of Li Metal-SE Interfaces. Type 1: Stable interface. Type 2: MIEC, Type 3: SEI. (b) . X-ray photoelectron spectra recorded during the deposition of 31 nm Li metal on $\text{Li}_{10}\text{GeP}_2\text{S}_{12}$. S 2p, Ge 3d, and P 2p/Ge 3p detail spectra are shown for different deposition states. With increasing Li deposition time LGPS decomposes. The identified species are marked and labeled in the spectra.¹⁴⁷

Reproduction with permission from ref.55. (c) Schematic of the experimental set-up for operando NDP.¹⁴⁸ (d) An inorganic-organic hybrid interphase enabled by molecular layer deposition suppress the interfacial reactions and lithium dendrite formation between $\text{Li}_{10}\text{SnP}_2\text{S}_{12}$ and Li metal interface. (e) Schematic diagrams of the Li/ $\text{Li}_7\text{P}_3\text{S}_{11}$ interface with a uniform thin LiF (or LiI) interphase layer and HFE (or I solution) infiltrated sulfide electrolyte.¹⁴⁹ (f) Galvanostatic cycling of the Li/LPS/Li and Li/LPS30I/Li cells at constant current densities at a,b) 25 °C, c,d) 60 °C, e,f) and 100 °C. The time for each charge and discharge is 1 h.....28

Figure 1-9 (a) Charge-discharge curves of LiCoO_2 in all-solid-state batteries at 14 $\text{mA}\cdot\text{g}^{-1}$. (b) Charge and discharge curve of $\text{LiNi}_{1.5}\text{Mn}_{0.5}\text{O}_2/\text{Li}_{10}\text{GeP}_2\text{S}_{12}/\text{Li}$ solid-state batteries (c) Long-term cycling stability of the $\text{Li}_4\text{Ti}_5\text{O}_{12}$ anode in ASSLIBs (d) The discharge curves of $\text{LiNi}_{1/3}\text{Mn}_{1/3}\text{Co}_{1/3}\text{O}_2$ electrodes prepared by conventional dry mixing and solution process.¹⁶⁸ (e) Schematic diagram of the nonwoven scaffold reinforced free-standing ASSLIBs. (f) The charge-discharge curves of mono-cells and bipolar cells.....34

Figure 1-10 (a). Long-term cycle performance of the cell with $80\text{Li}_2\text{S}\cdot 20\text{LiI}$ electrode materials for 2000 cycles at 2C and (b) its charge-discharge curves. (c) Long term cycling stability of $\text{Co}_8\text{S}_9/\text{Li}_7\text{P}_3\text{S}_{11}$ composites at $1.27 \text{ mA}\cdot\text{cm}^{-2}$.⁸⁴ (d) Schematic diagram of an all-solid-state Li–Se battery. (e) Typical discharge/charge profiles of Se and S cathodes in all-solid-state batteries at 50 mA g^{-1} at room temperature. (f) Cycling performance at 50 mA g^{-1} and corresponding Coulombic efficiencies of all-solid-state Li-Se batteries.37

Figure 1-11 (a) Cathode fabrication process. (b) Anode fabrication process. (c) Fabrication process of solid-state electrolyte layer. (d) Assembly process of solid-state batteries. (e) One prototype of SE-based ASSLIBs based NMC622 and Graphite with a dimension of $8 \text{ cm} \times 6 \text{ cm}$. (f) The cross-sectional SEM image of the SE-based ASSLIBs. (g) First-cycle charge-discharge voltage profiles of the pouch-type full-cells at 0.025C. 40

Figure 1-12 The structure of this thesis.	46
Figure 2- 1 (a) Chemical reaction process of ALD and MLD deposition process. (b) Savannah 200 ALD system (Veeco/carbon nanotube (CNT) division of the Veeco Instruments Inc.).	64
Figure 2- 2 (a) Principle of FE-SEM operations. ^[3] (b) An Hitachi S-4800 scanning electron microscopy.	65
Figure 2- 3 (a) The principle of X-ray diffraction. (b) The Bruker D8 advance diffractometer XRD system.	66
Figure 2- 4 (a) The main principle of Raman spectroscopy. (b) HORIBA Scientific LabRAM HR Raman spectrometer system.	67
Figure 2- 5 (a) The principles of X-ray photoelectron spectroscopy. (b) Schematic drawing of a typical XPS setup with photon source (X-rays, UV-light, laser or Synchrotron radiation).	68
Figure 2- 6 (a) The principle of generating synchrotron radiation. (b) The principle of X-ray absorption spectroscopy (XAS).	69
Figure 2- 7 The configurations of a coin cell and a mould cell with their physical pictures.	70
Figure 3-1 Schematic diagram of ASSLIBs with various interfacial nanostructure. (A) LiCoO ₂ directly mixed with Li ₁₀ GeP ₂ S ₁₂ without interfacial design for ASSLIBs. (B) A one-shell LiNbO ₃ @LiCoO ₂ cathode for ASSLIBs. (C) A dual shell	

LGPS@LNO@LCO for ASSLIBs.77

Figure 3-3 Structural and elemental analysis of one-shell LNO@LCO and dual shell LGPS@LNO@LCO. (A) A TEM image of one-shell LNO@LCO particles. (B) a high-resolution TEM image of one-shell LNO@LCO particles. (C) Energy-dispersive X-ray spectroscopic (EDS) mapping of Co, Nb, and O by HAADF-STEM. (D). SEM image of the one-shell LNO@LCO/LGPS electrode. (E) SEM image of the mixture of the dual shell structured LGPS@LNO@LCO electrode. (F) FIB cross-section image of LGPS@LNO@LCO. (G) Co mapping. (H) P mapping. (I) S mapping.79

Figure 3-4 Electrochemical performance of ASSLIBs with pristine LCO, one-shell LNO@LCO, and dual-shell structured LGPS@LNO@LCO. (A) Charge-discharge curves. (B) Cycling stability and Coulombic efficiency. (C) CV curves of dual shell structured LGPS@LNO@LCO. (D) CV curves of one-shell LNO@LCO/LGPS electrodes. (E) Galvanostatic Intermittent Titration Technique (GITT). (F) Rate performance. (G) Discharge curves at various current densities. (H) Ragone plot.81

Figure 3-5 In-situ XANES of ASSLIBs during the initial charge-discharge process. (A) S K-edge of the bare LCO/LGPS cathode. (B) The first deviation of the bare LCO/LGPS electrode. (C) S K-edge of the one-shell LNO@LCO/LGPS electrode. (D) The first deviation of the one-shell LNO@LCO/LGPS electrode.84

Figure 3-6 Ex-situ XPS characterizations on the pristine LGPS (top), bare LCO/LGPS electrodes after 100 cycles (middle), and one-shell LNO@LCO/LGPS electrodes after 100 cycles (bottom). (A) S 2p spectra, (B) P 2p spectra, (C) Ge 3d spectra.86

Figure 3-7 (A-C) one-shell LNO@LCO/LGPS electrodes. (D-F) dual shell structured LGPS@LNO@LCO electrodes.87

Figure 4-1 (a) Illustration of SC-NMC532 in SE-based ASSBs. (b) Illustration of PC-NMC532 in SE-based ASSBs. (c) A cross-sectional image of LGPS@LNT0@SC-NMC532, in which Li⁺ has a continuous conducting pathway. (d) A cross-sectional image of LGPS@LNT0@PC-NMC532, in which Li⁺ is transported across many grain boundaries..... 106

Figure 4-2 Structural Characterization of LNT0@SC-NMC532 and LNT0@PC-NMC532. (a) An SEM image of LNT0@SC-NMC532. (b) An SEM image of LNT0@PC-NMC532. (c) HRTEM image of LNT0@SC-NMC532. (d) HAADF image of LNT0@SC-NMC532 and (e) Co, Mn, Nb, and Ta mapping. (f) A combination of Ni and Ta elemental maps of LNT0@SC-NMC532 acquired with STEM-EDX. 107

Figure 4-3 Electrochemical Performance of LNT0@SC-NMC532 and LNT0@PC-NMC532. (a) Initial charge/discharge curves of SC-NMC532, PC-NMC532, and pristine SC-NMC532 in the conventional liquid electrolyte (LE). (b) Cycling stability of SC-NMC532 and PC-NMC532. (c) Discharge curves of SC-NMC532 and PC-NMC532 under various current densities. (d) Rate performance of SC-NMC532 and PC-NMC532. (e) The Ragone plots of SC-NMC632-based ASSLIBs and previously reported ASSLIBs. (f) Charging-discharging GITT curves of SC-NMC532. (g) Charging-discharging GITT curves of PC-NMC532..... 109

Figure 4-4 Quantification of Li⁺ diffusion coefficients of SC-NMC532 and PC-NMC532 during the initial charge/discharge process. (a) Comparison of the GITT behavior and polarization curves during the initial charge process. (b) Li⁺ diffusion coefficients of LNT0@SC-NMC532 and LNT0@PC-NMC532 at different charge states. (c) Comparison of GITT behavior and polarization curves during the initial discharge process. (d) Li⁺ diffusion coefficients of LNT0@SC-NMC532 and LNT0@PC-NMC532 at different discharge states..... 111

Figure 5-1 HR-TEM images of pristine SC-NMC532 and LNTO@SC-NMC532. (a) HAADF image of single-crystal NMC532. (b) Ni, (c) Mn, (d) Co, (e) O elemental maps of SC-NMC532 acquired with STEM-EDX. (f) Bright-field TEM image of $\text{LiNb}_{0.5}\text{Ta}_{0.5}\text{O}_3$ coating on SC-NMC532. (g) HAADF image of LNTO@SC-NMC532. (h) Ni, (i) Mn, (j) Ta, (k) Nb, (l) a combination of Ni and Ta mapping results obtained from LNTO@SC-NMC532 with STEM-EDX..... 130

Figure 5-2 Electrochemical Performance of pristine SC-NMC532 and LNTO@SC-NMC532. (a) Comparison of the charge/discharge curves of pristine SC-NMC532 and LNTO@SC-NMC532. (b) EIS of bare SC-NMC532 and LNTO@SC-NMC532 after initially charging to 3.8V. (c) Cycling stability of pristine SC-NMC532 and LNTO@-SC-NMC532. (d) Rate performance of LNTO@SC-NMC532. (e) Charging/Discharging curves under different current densities..... 131

Figure 5-3 XPS Spectra of LGPS, SC-NMC532/LGPS electrode after 100 cycles, and LNTO@SC-NMC532 electrode after 100 cycles. (a) full survey. (b) S 2p spectra. (c) P 2p spectra. (d) Mn 2p spectra..... 133

Figure 5-4 Interfacial structure change and chemical evolution of SC-NMC532. (a) HAADF-STEM image of pristine SC-NMC532. (b) HAADF-STEM image of SC-NMC532-after 100 cycles. (c) HAADF- STEM image of LNTO@SC-NMC532 after 100 cycles. (d) Illustration of a layered R-3m structure. (e) Illustration of a spinel Fd-3m structure. (f) Illustration of a rock-salt structure. 135

Figure 5-5 First-principles calculation to determine the formation energy of oxygen vacancies in SC-NMC532. (a) The formation energy of oxygen vacancies as a function of Li vacancy numbers. (b) The comparison of Ni d states after removing Li atoms from the supercell. (c) The comparison of Mn d states after removing Li atoms from the

supercell. The Fermi level is set to be 0 eV. (d) Illustration of oxygen vacancies in $\text{LiNi}_{0.5}\text{Mn}_{0.3}\text{Co}_{0.2}\text{O}_2$ supercells under different Li vacancy contents..... 136

Figure 6-1 Characterizations on $\text{LiNb}_{0.5}\text{Ta}_{0.5}\text{O}_3$ (LNTO) and LNTO@NMC532. (a) XRD patterns of $\text{LiNb}_{0.5}\text{Ta}_{0.5}\text{O}_3$ (LNTO) annealed at various temperatures. (b) EIS profile of LNTO after annealing at different temperatures. (c) The ionic conductivity of LNTO annealing at different temperatures. (d) TEM image of LNTO@NMC532 annealed at 350°C. (e) TEM image of LNTO@NMC532 annealed at 450°C. (f) TEM image of LNTO@NMC532 annealed at 550°C. (g) STEM-EDX mapping of Nb, Ta and Ni-Ta combination..... 154

Figure 6-2 EIS profiles of ASSLIBs being charged at different cut-off voltages. (a) LNTO@NMC532-350, (b) LNTO@NMC532-450, (c) LNTO@NMC532-550..... 156

Figure 6-3 Electrochemical performance of LNTO@SC-NMC532-based ASSLIBs. (a) the comparison of the charge-discharge curves of LNTO@NMC532-350, LNTO@NMC532-450, and LNTO@NMC532-550. (b) The cycling stability and Coulombic efficiency of LNTO@NMC532-350, LNTO@NMC532-450, and LNTO@NMC532-550. (c) CV profiles of LNTO@NMC532-350. (d) CV profiles of LNTO@NMC532-450. (e) CV profiles of LNTO@NMC532-550. (f) Rate performance of LNTO@NMC532-350, LNTO@NMC532-450, and LNTO@NMC532-550. (g) Discharge curves with different current densities of LNTO@NMC532-350, LNTO@NMC532-450, and LNTO@NMC532-550. (h) The comparison of electrochemical performance with previous results related to SE-based ASSLIBs..... 157

Figure 6-4 Analysis of Li^+ transport kinetics. (a) Initial discharging GITT profiles of LNTO@NMC532-350, LNTO@NMC532-450, and LNTO@NMC532-550. (b) Typical

GITT curves marked with IR drop. (c) Li^+ diffusion coefficient of LNT@NMC532-350, LNT@NMC532-450, and LNT@NMC532-550 as a function of depth of discharge (DOD). (d) Schematics of Li^+ transport across the electrode-electrolyte interface with different energy barriers..... 160

Figure 7-1 (a) Illustration of the in-situ synthesis of Li_3InCl_6 on LiCoO_2 (LIC@LCO). (b) SEM image of LIC@LCO-15wt%. (c) Elemental O mapping. (d) Elemental Cl mapping. (e) Cross-sectional SEM image of LIC@LCO-15wt%. (f) Elemental Cl and O combined mapping. (g) Elemental In and Co combined mapping. 185

Figure 7-2 Chemical Interaction between LIC and LCO. XPS spectra of LIC@LCO-15wt%. (a) In 3d spectra. (b) O 1s spectra. (c) Cl 2p spectra. (d) The binding energy between the LCO (110) and different LIC surfaces. (e) PDOS of s, p, d orbitals of O, Cl, In, and Co. (f) Differential charge density of the LCO(110)/LIC(100) interface..... 186

Figure 7-3 Electrochemical performance of LIC@LCO electrodes. (a) initial charge/discharge curves of LIC@LCO electrodes with various ratios. (b) Cycling stability. (c) CV curves. (d) Rate Performance of LIC@LCO. (e) Discharge curves of LIC@LCO-15wt% and LIC@LCO-10wt% under various current densities. (g) Charge/discharge curves of high-loading LIC@LCO electrodes. (g) Ragone plot..... 189

Figure 7-4 In situ/operando Raman and ex-situ XAS spectra of LIC@LCO-15wt% in AIBSs. (a) Charging curves of LIC@LCO electrodes at the current density of $0.13 \text{ mA}\cdot\text{cm}^{-2}$. (b) Raman spectra of the LIC@LCO electrode during the charging process. (c) Contour plot of LIC@LCO during the charging process. (d) Discharging curves of LIC@LCO electrodes at the current density of $0.13 \text{ mA}\cdot\text{cm}^{-2}$. (e) Raman spectra of LIC@LCO electrodes during the discharging process. (f) Contour plot of LIC@LCO

during the discharging process. (g) XAS of Cl K-edge. (h) XAS of In L3-edge. (i) XAS of Co K-edge.....192

Figure 7-5 (a) Illustration of schematic view of LCO(110)/LIC(100) interface under the electrical field of $-0.3\text{V}/\text{\AA}$, $-0.2\text{V}/\text{\AA}$, $-0.1\text{V}/\text{\AA}$, $0\text{V}/\text{\AA}$, $0.1\text{V}/\text{\AA}$, $0.2\text{V}/\text{\AA}$, and $0.3\text{V}/\text{\AA}$. (b) The variation of binding energy of LCO(110)/LIC(100) interface as a function of electric field strength.194

Figure 8-1 Schematic illustration of SE-based ASSLMBs. (a) SE-based ASSLMBs. (b) The resistive layer at the interface between Li and SEs. (c) Alucone layer on the Li surface. (d) The chemical structure of alucone deposited by MLD.....218

Figure 8-2 Characterizations of $\text{Li}_{10}\text{SnP}_2\text{S}_{12}$ (LSPS). (a) Crystal structure of LSPS. (b) XRD pattern of as-prepared LSPS. (c) EIS profiles of LSPS at various temperatures. (d) Arrhenius plot of LSPS conductivity.220

Figure 8-3 Electrochemical impedance spectra of Li symmetric cells. (a) Time-dependent EIS spectra of bare Li-LSPS-Li. (b) Time-dependent EIS spectra of 10alucone Li-LSPS-Li. (c) Time-dependent EIS spectra of 30alucone Li-LSPS-Li. (d) Time-dependent EIS spectra of 50alucone Li-LSPS-Li.221

Figure 8-4 Comparison of Li^+ plating/stripping behavior of Li symmetric cells at a current density of 0.1 mA cm^{-2} with an areal capacity of 0.1 mAh cm^{-2} . (a) 10 cycles alucone (10alucone Li) versus bare Li. (b,c) Voltage profiles of the 10alucone Li and the bare Li foil in the 1st cycle and the 25th cycle, respectively. (d) 30 cycles alucone (30alucone Li) versus bare Li. (e, f) Voltage profiles of the 30alucone Li and the bare Li foil in the 1st cycles and the 25th cycle, respectively. (g) 50 cycles alucone (50alucone Li) versus

the bare Li. (h,i) Voltage profiles of the 50 μ m-thick Li and the bare Li foil in the 1st cycle and the 25th cycle, respectively.....222

Figure 8-5 Electrochemical performance of all-solid-state lithium metal batteries. (a) Initial charge-discharge curves of LiCoO₂-based ASSLMBs at 0.01C at room temperature. (b) Initial charge-discharge curves of LiCoO₂-based ASSLMBs at 0.1C at 55 °C. (c) Charge-discharge curves of LiCoO₂-based ASSLMBs at the 2nd and 60th cycles. (d) Cycle performance of LiCoO₂-based ASSLMBs at 55 °C.....225

Figure 9-1 (a) Schematic diagram of ASSLMBs. (b) Schematic diagram of ASSLMBs with the PCE interlayer.....244

Figure 9-2 (a) Photographs of PCE (5 mol% LiTFSI in SN) at 60 °C (left) and room temperature (right), (b) XRD patterns of SN, LiTFSI, and PCE. (c) EIS spectra of PCE. (d) Arrhenius plot of PCE. The insert is the photo of the laminated PCE. (e) EIS spectra of PCE-LGPS-PCE composite electrolytes. (f) Arrhenius plot of PCE-LGPS-PCE composite electrolytes.....245

Figure 9-3 Overpotential of the Li⁺ plating/stripping of Li symmetric cells. (a) Li/LGPS/Li and Li/PCE-LGPS-PCE/Li at 0.13 mA.cm⁻². (b) Voltage profile comparison from 100 to 105 hours. (c) rate-performance of Li/PCE-LGPS-PCE/Li at various current densities from 0.13 to 0.64 mA.cm⁻². (d) Typical voltage profiles at different current density.....247

Figure 9-4 Electrochemical performances of ASSLMBs. (a) Charge-discharge curves of LiFePO₄/LGPS/Li at 0.1C. (b) Charge-discharge curves of LiFePO₄/PCE-LGPS-PCE/Li at 0.1C and 0.5C. (c) Cycle stabilities of LiFePO₄/LGPS/Li at 0.1C and LiFePO₄/PCE-LGPS-PCE/Li at 0.5C. (d)

Charge-discharge curves of PAN-S/LGPS/Li at 0.13 mA.cm⁻². (e) Charge-discharge curves of PAN-S/PCE-LGPS-PCE/Li at 0.13 mA.cm⁻². (f) Cycle stabilities of PAN-S/LGPS/Li and PAN-S/PCE-LGPS-PCE/Li at 0.13 mA.cm⁻².248

Figure 9-5 X-ray absorption spectra of LGPS, LGPS on the Li surface after cycling, and LGPS with the PCE interlayer after cycling, respectively. (a) P K-edge spectra. (b) S K-edge spectra.251

Figure 9-6 X-ray photoelectron spectroscopy of the LGPS on the Li surface after cycling (a, c, e) and the LGPS with the PCE interface after cycling (b, d, f), respectively. (a, b) S 2p spectra. (c,d) P 2p spectra. (e,f) Ge 3d spectra.252

Figure 10-1 Schematic diagram of 3D continuous Li⁺ ion flux. (a) Illustration of lithium-ion and electron fluxes inside the conventional cathode. (b) A trace amount of LE was added to both sides of the SE, filling the pores within the cathode as well as wetting the Li metal surface.....275

Figure 10-2 Comparison between LATP and GC-LATP. (a) the SEM image of the LATP precursor after annealing (700 °C, 2 hours). (b) the SEM image of the GC-LATP precursor after mechanical milling for 80 hours. (c) the SEM image of the LATP pellet after post-annealing (960 °C, 6 hours). (d) the SEM image of the GC-LATP pellet after post-annealing (960 °C, 6 hours). (e) XRD spectra of LATP precursors with different ball-milling time. (f) XRD spectra of LATP and GC-LATP pellets after post-annealing (960 °C, 6 hours).276

Figure 10-3 Chemical compatibility of GC-LATP in carbonate liquid electrolytes. (a) Comparison of XRD patterns of GC-LATP pellets before and after being soaking in LE for one week. (b) Comparison of Raman spectra of GC-LATP pellets before and after

being soaking in LE for one week. (c) Al K-edge and (d) Ti L-edge XANES spectra recorded in the FLY mode and (e) Al K-edge & (f) Ti L-edge XANES spectra recorded in the TEY mode of GC-LATP pellets before and after being soaking in LE for one week.
279

Figure 10-4 Electrochemical performances of LiFePO₄-based quasi-solid-state lithium-ion batteries employing GC-LATP\LE hybrid electrolytes. (a) Charge-discharge curves of LiFePO₄ at 0.1 C, (1 C = 170 mA.g⁻¹). (b) Rate performance of LiFePO₄ at various current densities ranging from 0.1 C to 4 C. (c) Long-term cycling performance of LiFePO₄ with quantified volume of LE at a current density of 1C. (d) The cycling performance of high areal loading LiFePO₄ cathodes in conventional LE and GC-LATP\LE hybrid electrolytes.....281

Figure 10-5 Evaluation of the GC-LATP and Li metal interface stability. (a) Electrochemical impedance spectra of the symmetric cell with a structure of Li\GC-LATP\Li. (b) Electrochemical impedance spectra of the symmetric cell with a structure of Li\LE\GC-LATP\LE\Li. The volume of LE is 2 μL. (c) Comparison of the plating/stripping profiles between Li\GC-LATP\Li and Li\LE\GC-LATP\LE\Li symmetric cells. (d) The voltage profile of Li\LE\GC-LATP\LE\Li symmetric cells. (e) The voltage profile of Li\GC-LATP\Li symmetric cells284

Figure 10-6 X-ray photoelectron spectra of GC-LATP pellets before and after electrochemical cycling. (a) Ti 2p. (b) P 2p. (c) C 1s. (d) F 1s. Top: before cycling, Bottom: after cycling.....286

Figure 11-1 Summary of challenges and proposed strategies of SEs and their ASSLIBs.
302

List of Appendices

Appendix A: Permission John Wiley and Sons for Published Article on Small Methods	311
Appendix B: Permission from Elsevier for Published Article on <i>Nano Energy</i>	312
Appendix C: Permission John Wiley and Sons for Published Article on Advanced Functional Materials.	313
Appendix D: Permission from Elsevier for Published Article on <i>Nano Energy</i>	314

List of Abbreviations

A

ALD: atomic layer deposition

AISSB: all-Inorganic Solid-State Batteries

ASSLB: all-solid-state lithium battery

ASSLIB: all-solid-state lithium-ion battery

ASSLMB: all-solid-state lithium metal battery

C

CE: Coulombic efficiency

CV: cyclic voltammetry

D

DEC: diethyl carbonate

DME: 1, 3-dimethoxyethane

E

EC: ethylene carbonate

EDS: energy dispersive spectroscopy

EELS: electron energy loss spectroscopy

EIS: electrochemical impedance spectroscopy

EXAFS: extended X-ray absorption spectroscopy

F

FIB: focused ion beam

FTIR: Fourier-transformed infrared spectroscopy

H

HRTEM: high-resolution transmission electron microscopy

L

LCO: lithium cobalt oxide

LGPS: $\text{Li}_{10}\text{GeP}_2\text{S}_{12}$

LNO: LiNbO_3

LNTO: $\text{LiNb}_{0.5}\text{Ta}_{0.5}\text{O}_3$

LATP: lithium aluminum titanium phosphate ($\text{Li}_{1.4}\text{Al}_{0.4}\text{Ti}_{1.6}(\text{PO}_4)_3$)

LPS: lithium phosphorus sulfide

LIB: lithium-ion batteries

Li-S: lithium-sulfur

M

MLD: molecular layer deposition

N

NEXAFS: Near edge X-ray absorption fine structure

P

PC-NMC532: polycrystalline $\text{LiNi}_{0.5}\text{Mn}_{0.3}\text{Co}_{0.2}\text{O}_2$

PAN-S: polyacrylonitrile-sulfur

S

SE: sulfide electrolyte

SEI: Solid electrolyte interphase

SEM: secondary electron microscopy

SLEI: solid-liquid electrolyte interphase

SC-NMC532: single-crystal $\text{LiNi}_{0.5}\text{Mn}_{0.3}\text{Co}_{0.2}\text{O}_2$

T

TEM: transmission electron microscopy

X

XAS: X-ray absorption spectroscopy

XRD: X-ray diffraction

XPS: X-ray photoelectron spectrometer

Chapter 1

1. Introduction

1.1 Background and Motivation

Lithium-ion batteries (LIBs) have been successfully applied to smart grids and consumer electronics since its commercialization in 1991 because of their high volumetric and gravimetric energy density, high power density, long lifespan, and no memory effect.¹ Due to the widespread use of LIBs, the Nobel Prize in chemistry in 2019 has been awarded to Stanley Whittingham, John Goodenough, and Akira Yoshino for their great contribution to the development of LIBs. In recent years, a lot of fire/explosion incidents of mobile phones and electric vehicles caused public concerns on the safety of LIBs. Besides, the high price and short driving mileage of electric vehicles per charge highly request for high-energy-density LIBs.^{2, 3} Therefore, the ever-increasing requirement on LIBs impels people to develop high-energy-density and high safety LIBs.

All-solid-state lithium-ion batteries (ASSLIBs) are gaining worldwide attention due to potentially high energy density and improved safety.⁴⁻⁸ To achieve ASSLIBs, a solid-state electrolyte is an indispensable component. Over the past decades, tremendous efforts have been devoted to developing highly Li⁺-conductive solid-state, such as oxide electrolytes, sulfide electrolytes (SEs), polymer electrolytes.^{8, 9} Among these solid-state electrolytes, SEs generally exhibits the highest ionic conductivity ($10^{-3} \sim 10^{-2}$ S/cm) and favorable mechanical property. However, large interfacial resistance, bad air stability, and narrow electrochemical window of SEs significantly impede the development of SE-based ASSLIBs. In recent years, a lot of exciting results and benchmark achievements on SEs and SE-based ASSLIBs have been demonstrated.

In this chapter, we first reviewed the state-of-the-art of the typical sulfide electrolytes, including *thio*-LISICON family ($\text{Li}_{10\pm 1}\text{MP}_2\text{X}_{12}$, M = Ge, Si, Sn, Al or P, and X = O, S or Se), Li argyrodites ($\text{Li}_6\text{PS}_5\text{X}$, X=Cl, Br, I), and gassy and glass-ceramic $\text{Li}_2\text{S-P}_2\text{S}_5$ system, aiming at unraveling the relationship between the crystal structure and ionic conduction mechanism side the crystal structure (**Figure 1-1**). Then, the recent progress on electrochemical and chemical stabilities of SEs were also examined and discussed, which is very critical for the large-scale application of SE-based ASSLIBs. Next, the cathodic and anodic interfacial challenges between the cathode/anode and SEs together with the promising and emerging strategies are discussed, respectively. Furthermore, the encouraging achievement of SE-based ASSLIBs and ASS Li-S batteries are summarized. To reveal the promise of SE-based ASSLIBs, manufacturing protocols for ASSLIBs were examined. Last not but least, the thesis objectives and structure are listed at the end of this chapter.

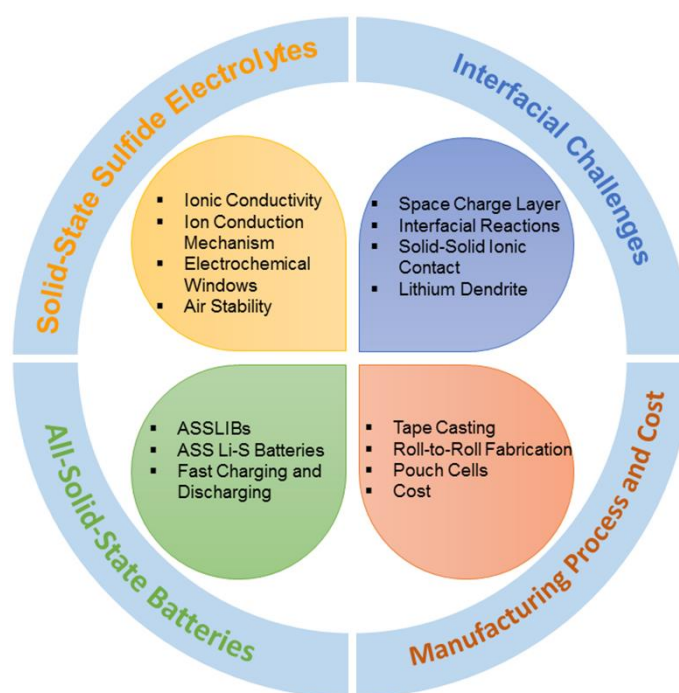


Figure 1-1 Overview of challenges and corresponding strategies of SEs and their ASSLIBs.

1.2 State-of-the-Art of Solid-State Sulfide Electrolytes

1.2.1 Fundamental of Sulfide Electrolytes

High ionic conductivity of solid-state SEs is one of the prerequisites for achieving high-performance ASSLIBs. Understanding the behavior of lithium-ion (Li^+) transport inside the solid-state electrolytes is fundamental and critical. Up to now, the Nernst-Einstein relationship together with Fick Diffusion law is widely adopted to describe the Li^+ conduction in the solid-state electrolytes.

The ionic conductivity of solid-state electrolytes can be described by the Nernst-Einstein equation.^{11, 12}

$$\sigma = \frac{\rho z^2 F^2}{K_B T} D(T) \quad (1)$$

where ρ is the molar density of diffusing ions in the unit cell. F , K_B , and z are the Faraday constant, the Boltzmann constant, and the charge of lithium ions is +1, respectively.

According to the Fick diffusion law, ions mobility in solid-state electrolytes can be described as below.

$$D = D_0 e^{-E_a/K_B T} \quad (2)$$

Where D_0 is, E_a is activation energy for lithium-ion hopping through the solid-state electrolytes. K_B is Boltzmann constant, T is the temperature in a Kelvin unit.

Therefore, the ionic conductivity can be simply derived as:

$$\sigma = \frac{A_0}{T} e^{-E_a/K_B T} \quad (3)$$

Where A_0 is the pre-exponential factor, which combines molar density and other factors

and constants mentioned above.

Based on this mathematical analysis, theoretically, there are two general ways to increase the ionic conductivity of SEs. The first is to increase the concentration of diffusive Li^+ in solid electrolytes, corresponding to molar density ρ in the equation (1). For example, Masahiro Tatsumisago *et al.* found that increasing the percentage of Li_2S in $\text{Li}_2\text{S-P}_2\text{S}_5$ composites increases the overall ionic conductivity of solid-state electrolytes.¹³ This conclusion was also verified by density functional theory calculation.¹² The second approach is to increase the diffusion coefficient of lithium ions in solid-state electrolytes, which is to minimize the activation energy (E_a) for Li^+ hopping between neighboring sites in solid-state electrolytes. Gerbrand Ceder *et al.* conducted a theoretical simulation, finding that activation barriers for Li^+ migration in solid electrolytes significantly affect the ion conduction.¹⁴

Besides to the high ionic conductivity, other requirements of SEs should be met before the successful commercialization of SEs in ASSLIBs,^{15, 16} such as, (1) low electrical conductivity to avoid the self-discharge behavior on shelf, (2) low cost, (3) wide electrochemical window to adopt the high-voltage cathodes and high capacity anodes (e.g. Li metal), and (4) excellent air-stability, which enable the process of SEs in dry room with a dewpoint ($-50^\circ\text{C}\sim-70^\circ\text{C}$).

1.2.2 Typical Sulfide Electrolytes

With theoretical guidance, a lot of effort has been made to develop solid-state SEs. Hitherto, a lot of SEs have been synthesized with high ionic conductivity (**Table 1**). It should be highlighted that some representative SEs already exhibit the high ionic conductivity over that of conventional liquid organic electrolytes ($10.2 \text{ mS}\cdot\text{cm}^{-1}$ for 1 M LiPF_6 , EC/DMC),³ such as $\text{Li}_{9.54}\text{Si}_{11.74}\text{P}_{1.44}\text{S}_{11.7}\text{Cl}_{0.3}$ ($25 \text{ mS}\cdot\text{cm}^{-1}$),⁸ $\text{Li}_{10}\text{GeP}_2\text{S}_{12}$ ($12 \text{ mS}\cdot\text{cm}^{-1}$),⁹ $\text{Li}_7\text{P}_3\text{S}_{11}$ ($17 \text{ S}\cdot\text{cm}^{-1}$), $\text{Li}_{3.45}[\text{Sn}_{0.09}\text{Si}_{0.36}]\text{P}_{0.55}\text{S}_4$ ($11 \text{ mS}\cdot\text{cm}^{-1}$).¹⁷ Here, to be

succinct, the typical solid-state SEs, thio-LISICON ($\text{Li}_{10\pm 1}\text{MP}_2\text{S}_{12}$, $\text{M} = \text{Ge, Si, Sn, Al}$ or P , and $\text{X} = \text{O, S}$ or Se), argyrodites ($\text{Li}_6\text{PS}_5\text{X}$, $\text{X} = \text{Cl, Br, I}$), and glass-ceramic $\text{Li}_2\text{S-P}_2\text{S}_5$ system are selected for the discussion, giving the insight into the relationship between the crystal structure and ionic conduction mechanism side the crystal structure.

Table 1-1 State-of-the-art of solid-state SEs in the aspect of ionic conductivity, activation energy, and crystalline structure.

Chemical Composition	Ionic Conductivity at RT (S/cm)	Activation Energy	Crystal Structure	Ref.
$\text{Li}_{10}\text{GeP}_2\text{S}_{12}$	1.2×10^{-2}	24 kJ/mol	thio-LISICON	9
$\text{Li}_{10}\text{SnP}_2\text{S}_{12}$	4×10^{-3}	0.60 eV	thio-LISICON	18
$\text{Li}_{11}\text{AlP}_2\text{S}_{12}$	8.02×10^{-4}	25.4 kJ/mol	thio-LISICON	19
$\text{Li}_{9.54}\text{Si}_{1.74}\text{P}_{1.44}\text{S}_{11.7}\text{Cl}_{0.3}$	2.5×10^{-2}	23 kJ/mol	thio-LISICON	20
$\text{Li}_{9.6}\text{P}_3\text{S}_{12}$	1.2×10^{-3}	25 kJ/mol	thio-LISICON	8
$\text{Li}_{10+x}\text{Ge}_{1+x}\text{P}_{2-x}\text{S}_{12}$ ($x=0.35$)	1.42×10^{-2}	24 kJ/mol	thio-LISICON	21
$\text{Li}_{3.25}\text{Ge}_{0.25}\text{P}_{0.75}\text{S}_4$	2.2×10^{-3}	20 kJ/mol	thio-LISICON	22
$\text{Li}_{10.35}[\text{Sn}_{0.27}\text{Si}_{1.08}]\text{P}_{1.65}\text{S}_{12}$	1.1×10^{-2}	19kJ/mol	thio-LISICON	23
$\text{Li}_{6+x}\text{P}_{1-x}\text{Ge}_x\text{S}_5\text{I}$	1.8×10^{-2}	n/a	thio-LISICON	24
$\text{Li}_6\text{PS}_5\text{Cl}$	1.9×10^{-3} 1.33×10^{-3}	0.38 eV	Argyrodite	25, 26
$\text{Li}_6\text{PS}_5\text{Br}$	6.8×10^{-3}	0.32 eV	Argyrodite	25
$\text{Li}_6\text{PS}_5\text{I}$	4.6×10^{-7}	0.26 eV	Argyrodite	25
$\text{Li}_7\text{Ge}_3\text{PS}_{12}$	1.1×10^{-4}	25 kJ/mol	Argyrodite	27
$\text{Li}_{3.833}\text{Sn}_{0.833}\text{As}_{0.166}\text{S}_4$	1.39×10^{-3}	0.21 eV	n/a	28
$\text{Li}_7\text{P}_3\text{S}_{11}$	17×10^{-2}	17 kJ/mol	Glass ceramic	29
$70\text{Li}_2\text{S}.30\text{P}_2\text{S}_5$	3.2×10^{-3}	18 kJ/mol	Glass ceramic	13

$70\text{Li}_2\text{S} \cdot (30-x)\text{P}_2\text{S}_5 \cdot x\text{P}_2\text{O}_5$	3×10^{-3}	17 kJ/mol	Glass ceramic	30
$75\text{Li}_2\text{S} \cdot 25\text{P}_2\text{S}_5$	2×10^{-4}	34 kJ/mol	amorphous	31

1.2.3 *Thio*-LISICON ($\text{Li}_{10\pm 1}\text{MP}_2\text{X}_{12}$) Family

The *thio*-LISICON family with a chemical formula of ($\text{Li}_{10\pm 1}\text{MP}_2\text{X}_{12}$, (M = Ge, Si, Sn, Al or P, and X = O, S or Se) possess a high ionic conductivity, thus arousing great interests of material scientists.³ Historically, the earliest study on the *thio*-LISICON system can date back to 2001 by Ryoji Kanno.²² They obtained an ionic conductivity of 2.2×10^{-3} S/cm at 25 °C by simply sintering the starting materials (Li_2S , GeS_2 , and P_2S_5) at 700 °C for 8 hours. Late on, a series of *thio*-LISICON-typed lithium sulfide electrolytes were developed, such as ternary Li_2S – SiS_2 – Al_2S_3 and Li_2S – SiS_2 – P_2S_5 systems.³²⁻³⁶ With the continuous efforts, Kamaya *et al.* reported the lithium superionic conductor in 2011, $\text{Li}_{10}\text{GeP}_2\text{S}_{12}$ (LGPS), which exhibited an unprecedented conductivity of 1.2×10^{-2} S cm^{-1} at room temperature as shown in **Figure 1-2a**.⁹ This result literally sparks a new wave of enthusiasm in developing LGPS-typed sulfide electrolytes.³⁷⁻⁴² $\text{Li}_{10}\text{GeP}_2\text{S}_{12}$ also shows good electrochemical stability (5 V vs Li^+/Li) against metallic lithium anodes (**Figure 1-2b**). By synchrotron XRD and neutron diffraction measurements, the crystal structure of $\text{Li}_{10}\text{GeP}_2\text{S}_{12}$ was clearly analyzed. This superionic conductor has a 3D framework structure (**Figure 1-2c**) and one-dimensional (1D) Li conduction path along the c-axis (**Figure 1-2d**).⁴³⁻⁴⁵ The 1D conduction pathway is formed by LiS_4 tetrahedra in the 16h and 8f sites, which share a common edge and form a 1D tetrahedron chain. These chains are connected by common corners of the LiS_4 tetrahedra (Fig. 3e). Interestingly, Y. Mo *et al.* reported that the Li^+ transport of $\text{Li}_{10}\text{GeP}_2\text{S}_{12}$ is not only along the c-axis, maybe also along two other pathways in the ab plane by ab initio molecular dynamics simulations.⁴⁶ In 2016, R. Kanno *et al.* reported that a fast lithium superionic conductor $\text{Li}_{9.54}\text{Si}_{11.74}\text{P}_{1.44}\text{S}_{11.7}\text{Cl}_{0.3}$, shows the three-dimensional (3D) conduction

pathways (1D along the *c* axis + 2D in the *ab* plane). The highest conductivity (25 mS.cm⁻¹) of Li_{9.54}Si_{1.74}P_{1.44}S_{11.7}Cl_{0.3} is the highest among all reported solid electrolytes so far.²⁰ In addition, the high ionic conductivity of LGPS is also confirmed by solid-state NMR technique, which shows that Li⁺ hopping in LGPS is nearly an isotropic process with a low activation energy of 0.22 eV.⁴⁷ By the neutron diffraction and maximum entropy method, the one-dimensional Li⁺ conduction pathway of LGPS changes to a three-dimensional conduction pathway at elevated temperatures.⁴⁵ Based on well-built knowledge of LGPS, the sodium analogs were also developed for all-solid-state sodium-ion batteries, such as Na₁₀SnP₂S₁₂,⁴⁸ and Na₁₁Sn₂PSe₁₂.⁴⁹

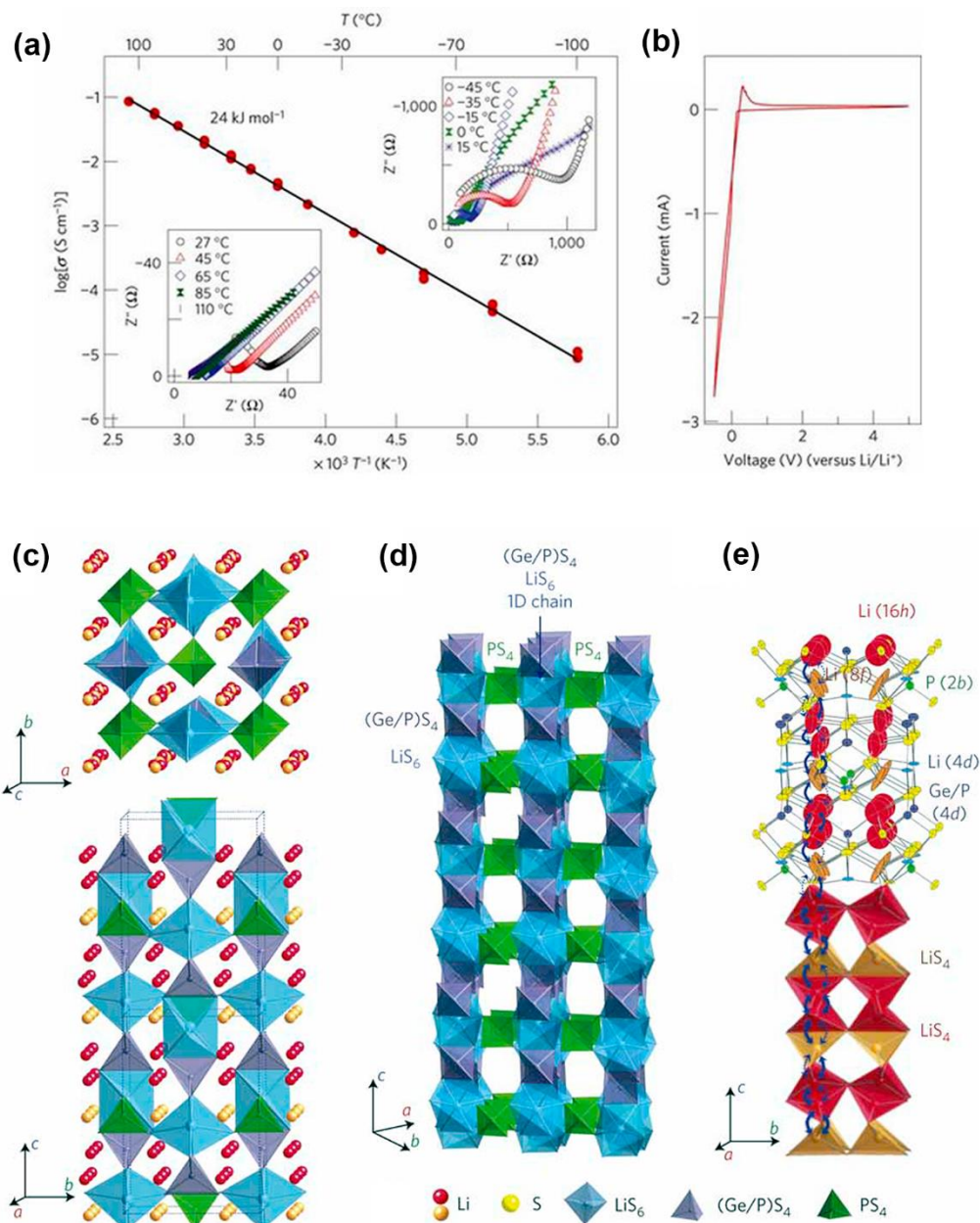


Figure 1-2 (a) Impedance plots of the conductivity data from low to high temperatures and Arrhenius conductivity plots of $\text{Li}_{10}\text{GeP}_2\text{S}_{12}$. (b) Current-voltage curve of a $\text{Li}/\text{Li}_{10}\text{GeP}_2\text{S}_{12}/\text{Au}$ cell 1 mV s^{-1} between -0.5 and 5.0 V at $25 \text{ }^\circ\text{C}$. (c) The framework structure and lithium ions that participate in ionic conduction. (d) Framework structure of $\text{Li}_{10}\text{GeP}_2\text{S}_{12}$. (e) Conduction pathways of lithium ions in $\text{Li}_{10}\text{GeP}_2\text{S}_{12}$.

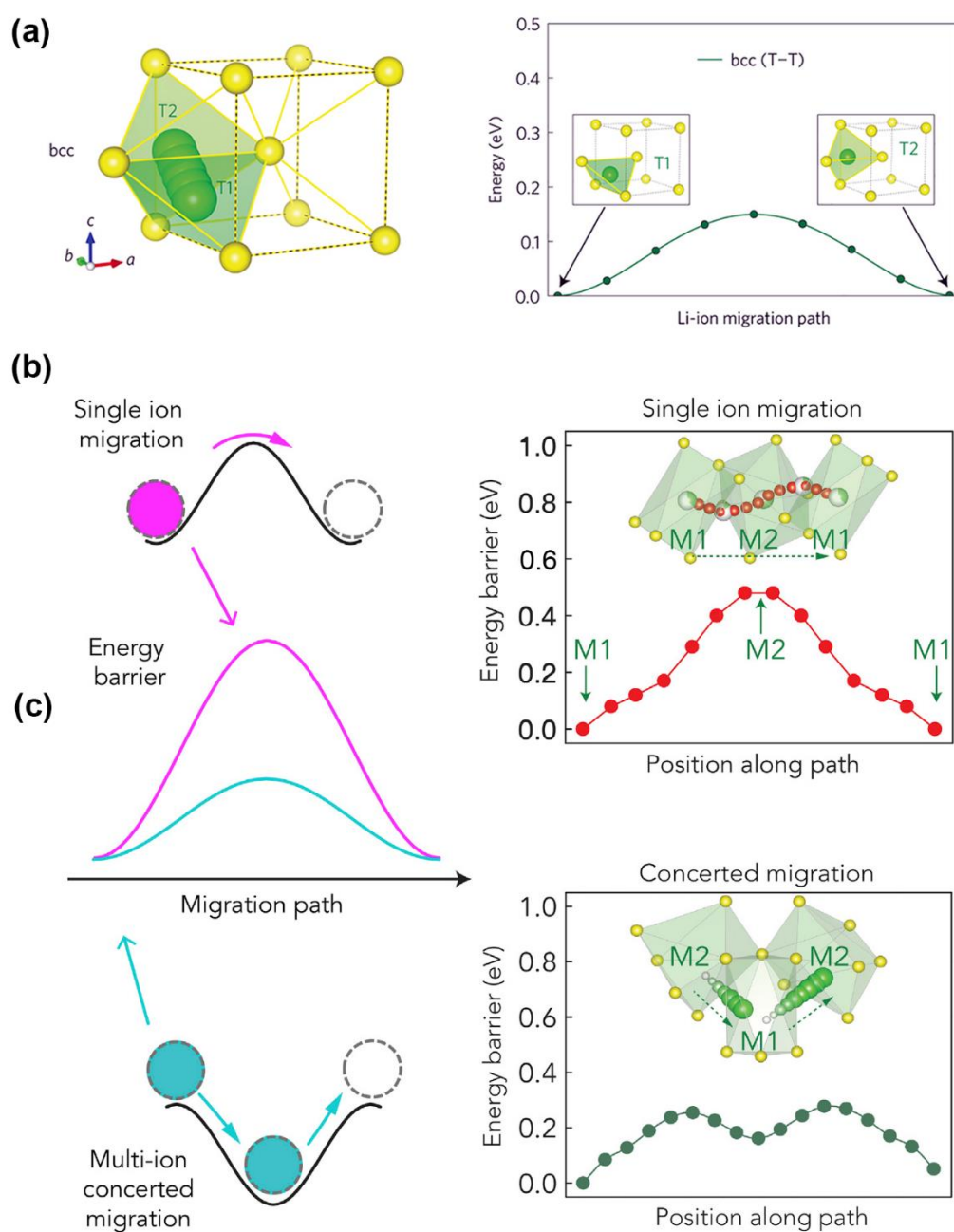


Figure 1-3 (a) Li-ion migration path (left panels) and calculated energy path (right panels) in bcc. (b) Illustration of energy profiles for single-ion migration (pink) versus multiple-ion concerted migration (blue). (c) Energy landscape of single Li⁺ migration (upper) and the energy barrier of concerted migration (lower) in LATP, as calculated using the NEB method.

For a long time, the discovery of solid-state electrolytes is totally based on the intuition and trial and error experiments, which is tedious and ineffective. Nowadays, the theoretical calculation has been widely conducted to rationally design sulfide electrolytes toward high ionic conductivity.⁵⁰ Remarkably, Gerbrand Ceder *et al.* investigated the relationship between anion packing and ionic transport by comparing transport energy barriers of three crystal lattices: body-centered cubic (bcc), face-centered cubic (fcc), and hexagonal close-packed (hcp) lattices. It turns out that a bcc anion framework that allowed direct hopping of Li between adjacent tetrahedral sites possessing the lowest activation barrier (**Figure 3a**).¹⁴ More interestingly, Y. Mo *et al.* revealed that lithium-ion hopping in superionic conductors is not a single ion migration process but a multi-ion concerted migration process.⁵⁰ As displayed in **Figure 3b** and **3c**, the energy barrier for single ion hopping in solid-state electrolytes is much higher than that of multi-ion concerted migration. In addition, the phase stability, electrochemical stability, and ionic conductivity of $\text{Li}_{10\pm 1}\text{MP}_2\text{X}_{12}$ (M=Ge, Si, Sn, Al or P, and X=O, S or Se) were systematically compared by *ab initio* molecular dynamics (MD) simulations.⁵¹ The results show that isovalent cation substitutions have a small effect on the similar phase stability, electrochemical stability, and Li^+ conductivity, while aliovalent cation substitutions (M= Al or P) with corresponding changes in the Li^+ concentration also seem to have a small effect on the Li^+ conductivity. In addition, the oxygen-substituted $\text{Li}_{10}\text{MP}_2\text{O}_{12}$ compounds are predicted not to be stable and have much lower Li^+ conductivities than their sulfide counterparts, while the selenium-substituted $\text{Li}_{10}\text{MP}_2\text{Se}_{12}$ compounds show a marginal improvement in conductivity, but at the expense of reduced electrochemical stability.⁵¹

Another concern of LGPS-typed solid electrolytes is costly because Germanium is highly expensive. Therefore, the replacement of Ge with Sn, Al, Si to form $\text{Li}_{10}\text{SnP}_2\text{S}_{12}$,^{52, 53} $\text{Li}_{11}\text{AlP}_2\text{S}_{12}$,¹⁹ $\text{Li}_{3.45}\text{Si}_{0.45}\text{P}_{0.55}\text{S}_4$,⁴⁴ could substantially lower the raw material cost without sacrificing ionic conductivity too much.¹⁸ A lot of fast ion conductors with a

thio-LISICON structure show an ionic conductivity around $10^{-2} \sim 10^{-3}$ S/cm, as tabulated in Table 1. Besides, a lot of sodium sulfide analogous with a *thio*-LISICON structure were also developed for all-solid-state sodium batteries. For instance, $\text{Na}_{10}\text{SnP}_2\text{S}_{12}$ was reported with the highest room-temperature ionic conductivity of $0.4 \text{ mS}\cdot\text{cm}^{-1}$,⁴⁸ which is rivaling the conductivity of the best sodium sulfide electrolytes to date.

1.2.4 Lithium Argyrodites ($\text{Li}_6\text{PS}_5\text{X}$, X= Cl, Br, I)

The argyrodite family of compounds with the general formula $\text{A}_{12-m-x}^+(\text{M}^{m+}\text{Y}_4^{2-})\text{Y}_{2-x}^{2-}\text{X}^x-$, where $\text{A}^+ = \text{Li}^+, \text{Cu}^+, \text{Ag}^+$; $\text{M}^{m+} = \text{Si}^{4+}, \text{Ge}^{4+}, \text{Sn}^{4+}, \text{P}^{5+}, \text{As}^{5+}$; $\text{Y}^{2-} = \text{O}^{2-}, \text{S}^{2-}, \text{Se}^{2-}, \text{Te}^{2-}$; $\text{X}^- = \text{Cl}^-, \text{Br}^-, \text{I}^-$; $0 \leq x \leq 2$ are named after the mineral Ag_8GeS_6 .⁵⁴⁻⁵⁷ Hans-Jorg Deiseroth *et al.* firstly identified that $\text{Li}_6\text{PS}_5\text{X}$ is a class of lithium-ion conductors with an unusually high Li^+ mobility.⁵⁶ Following that, they conducted a series of research on the structure, phase transition, and lithium-ion conduction of lithium argyrodites by molecular dynamics simulation, solid-state NMR, and impedance spectroscopy,⁵⁸⁻⁶⁰ showing that lithium argyrodites with a cubic phase possess three-dimensional lithium-ion conduction pathways.^{55, 61} Virginie Viallet *et al.* reported that the room-temperature ionic conductivities of $\text{Li}_6\text{PS}_5\text{Cl}$, $\text{Li}_6\text{PS}_5\text{Br}$, and $\text{Li}_6\text{PS}_5\text{I}$ are 6.2×10^{-4} S/cm, 4.6×10^{-4} S/cm, and 1.9×10^{-4} S/cm, respectively.²⁶ Besides to the excellent ionic conductivity, the halogen argyrodites also show excellent electrochemical stability from 0 to 7 V versus Li^+/Li and a low electronic conductivity on the order of 10^{-10} S/cm.^{26, 62} By virtue of density functional theory molecular dynamics simulations, Marnix Wagemaker *et al.* investigated the origin of the lithium-ion conductivity in argyrodite solid electrolytes,⁶³ elucidating that not only lithium-ion vacancies but the influence of halogen atoms on their local surroundings also play an important role in the Li-ion diffusion of $\text{Li}_6\text{PS}_5\text{Cl}$ and $\text{Li}_6\text{PS}_5\text{Br}$. In addition, the distribution of the halogen ions in the crystal structure results in the big difference in the lithium-ion conductivity between $\text{Li}_6\text{PS}_5\text{Cl}$ and $\text{Li}_6\text{PS}_5\text{I}$, which is several orders of magnitude, suggesting that tuning the distribution of halogen ions in

lithium argyrodites during synthesis can increase the Li-ion conductivity of these materials. Furthermore, simulations were also performed on $\text{Li}_5\text{PS}_4\text{X}_2$ ($\text{X} = \text{Cl}, \text{Br}, \text{or I}$), which show Li-ion conductivities similar to those of $\text{Li}_6\text{PS}_5\text{Cl}$ and $\text{Li}_6\text{PS}_5\text{Br}$, suggesting that the $\text{Li}_5\text{PS}_4\text{X}_2$ compounds are interesting new compositions for solid-state electrolytes.⁶³ In addition, lithium halides can enhance the electrochemical stability of solid-state sulfide electrolytes against metallic lithium anodes.⁶⁴ As demonstrated by Ezhiylmurugan Rangasamy *et al.*, iodine-based $\text{Li}_7\text{P}_2\text{S}_8\text{I}$ have a superior electrochemical window up to 10 V vs. Li^+/Li .⁴⁰ Comparing to LGPS-type sulfide electrolytes, lithium argyrodites can be easily synthesized by liquid methods, which is good for size and morphology control.⁶⁵⁻⁶⁷ However, the ionic conductivity of sulfide electrolytes synthesized by liquid methods is generally lower than conventional solid-state sintering.⁶⁶

1.2.5 Glassy and Glass-Ceramic $\text{Li}_2\text{S-P}_2\text{S}_5$ System

Compared with crystalline solid-state sulfide electrolytes, glassy superionic conductors have several advantages such as isotropic properties for ion migration, wide selection of chemical composition, easy control of properties with changing chemical composition.⁶⁸⁻⁷⁰ Generally, the ionic conductivity in a glass is higher than that in the corresponding crystal as a glass usually has large free volume.⁶⁸ In addition, a metastable phase, which is thermodynamically unstable at a given temperature, can be easily formed when heating a glass over the glass transition temperature (T_g).⁷¹ In the case of crystallization from $\text{AgI-Ag}_2\text{O-M}_x\text{O}_y$ ($\text{M}=\text{B}, \text{Ge}, \text{P}, \text{Mo}$) glasses with extremely high concentrations of AgI, the high-temperature superionic phase of $\alpha\text{-AgI}$ was successfully precipitated and stabilized in a glass matrix to obtain an extremely high ion conductivity of 10^{-1} S/cm at room temperature.^{72, 73} Hitherto, a variety of sulfide and oxysulfide glassy electrolyte system have been developed.^{68, 69, 74-76}

In accordance with the Nernst-Einstein relationship we discussed above, there are two

universal approaches to enhance the ionic conductivity of a glassy electrolyte. One strategy is to enhance charge carrier concentration; another one is to improve the mobility of carrier ions.⁶⁸ To increase the carrier ion concentration is to vary the ratio of starting materials by different synthesis techniques, such as high-energy ball milling. However, it is worthwhile to note that there is an optimum concentration of lithium-ion in $\text{Li}_2\text{S-P}_2\text{S}_5$ because increasing the concentration of lithium ions would also affect other factors, such as density, porosity, and crystal structure.¹² To enhance the ion mobility of carrier ions, so far there are two strategies, one strategy is the utilization of “mixed-anion effect” by combining sulfide and oxide anions (in oxysulfide systems) and the other is the precipitation of superionic metastable crystals by careful heat-treatment of glasses.^{68, 70} For example, $\text{Li}_2\text{S-P}_2\text{S}_5$ glass-ceramics shows extremely high ionic conductivity (3.2×10^{-3} S/cm) at ambient temperature with an extremely low activation energy of 12 kJ/mol,¹³ which is much higher than that of glassy $\text{Li}_2\text{S-P}_2\text{S}_5$. In this glass-ceramic, the new superionic metastable crystalline phase $\text{Li}_7\text{P}_3\text{S}_{11}$,^{77, 78} which could not be obtained by the usual solid-state reaction, was precipitated by the heating of the glass. These results suggest that the formation of a superionic metastable phase is the most remarkable advantage of glass-based solid electrolytes. The enhancement is also attributable to the decrease of grain boundary resistance by the softening of glass powders at an elevated temperature.⁷⁴ Up to now, the highest ionic conductivity of 1.7×10^{-2} S/cm with a low activation energy of 17 kJ/mol of the $\text{Li}_2\text{S-P}_2\text{S}_5$ system has been reported via a hot pressing process to reduce the grain boundary resistance.²⁹

In addition, the increased surface energy of Li_3PS_4 could also enhance the surface conduction mechanism because the surface defects enhance the lithium vacancy.^{79, 80} Bulk Li_3PS_4 is a γ phase that has a low ionic conductivity of 3×10^{-7} S cm^{-1} at room temperature.^{81, 82} When heated to 195 °C, γ - Li_3PS_4 is converted to the high-conduction β - Li_3PS_4 phase, which shows an abrupt increase of ionic conductivity in the Arrhenius plot as shown in Fig. 5a. However, β - Li_3PS_4 is meta-stable at elevated temperature and

easily reverts to stable phase γ -Li₃PS₄ at the temperature under 195 °C. So how to stabilize the high-conduction β -Li₃PS₄ at room temperature is a big challenge. Fortunately, C. Liang and coworkers discovered that by increasing the surface energy of Li₃PS₄, β -Li₃PS₄ could stable at room temperature owing to the chemical lattice distortion.⁷⁹ Actually, this phenomenon is akin to the stabilization of *a*-AgI by reducing its particle size to the nanometer range.^{80, 83} Similar to the lithium argyrodites, glassy and glass-ceramic Li₂S-P₂S₅ system also can be synthesized by the liquid method, such as β -Li₃PS₄⁷⁹ and Li₇P₃S₁₁.^{71, 84, 85}

1.3 Stability of Sulfide Electrolytes

1.3.1 Chemical Stability of Sulfide Electrolytes

Solid-state sulfide electrolyte is highly hygroscopic, causing the hydrolysis of solid-state sulfide electrolyte in moisture, thus generating harmful H₂S gases. To address this challenge, C. Liang *et al.* demonstrated that substituting tin with arsenic in Li₄SnS₄ provides both a high ionic conductivity of 1.39×10^{-3} S cm⁻¹ at room temperature and outstanding chemical stability to water. The pristine Li₄SnS₄ has an ionic conductivity of 7.1×10^{-5} S cm⁻¹ at 25 °C. Low concentration doping of As is causing a decrease in ionic conductivity. The highest conductivity of 1.39×10^{-3} S cm⁻¹ is achieved with a composition of Li_{3.833}Sn_{0.833}As_{0.166}S₄. Impressively, after exposure to humid air, the ionic conductivity of Li_{3.833}Sn_{0.833}As_{0.166}S₄ were negligible comparing with that of β -Li₃PS₄.²⁸ The excellent chemical stability of Li_{4-x}Sn_{4-x}As_xS₄ can be explained by the theory that soft acids, such as tin and arsenic, preferentially react with soft bases, like sulfur, rather than with hard acids, such as oxygen.²⁸ Similarly, according to hard and soft acid and base (HSAB) theory, they also demonstrated the air-stable Na₃SbS₄ synthesized by both solid-state sintering and solution-based process,^{86, 87} In terms of the Li₂S-P₂S₅ system, those having PS₄³⁻ anions were reported to exhibit the highest chemical

stability, because the PS_4^{3-} anion is more difficult to hydrolyze from the water in the air comparing to other ions ($\text{P}_2\text{S}_7^{2-}$).³⁸

Another general approach is to introduce new compounds into the $\text{Li}_2\text{S}\text{-P}_2\text{S}_5$ system. As demonstrated by Takamasa Ohtomo *et al.*, the addition of x FeS to $(1-x)$ ($0.75\text{Li}_2\text{S}\cdot 0.25\text{P}_2\text{S}_5$) can suppress the generation of H_2S gas.⁸⁸ 30 mol% FeS dramatically suppresses the generation of harmful H_2S gas from the solid-state sulfide electrolytes. The increase in the amount of FeS in $x\text{FeS}$ ($1-x$) ($0.75\text{Li}_2\text{S}\cdot 0.25\text{P}_2\text{S}_5$) linearly decreases the generation of H_2S from the solid-state sulfide electrolytes, the optimal mole content of FeS in $0.75\text{Li}_2\text{S}\cdot 0.25\text{P}_2\text{S}_5$ is 40%.

Instead of introducing compounds, elemental substitution also can ameliorate the air-stability of sulfide electrolytes.⁸⁹ X. Xu et al demonstrated that Zn, O co-doping the Li_3PS_4 glass-ceramic ($\text{Li}_{3.06}\text{P}_{0.98}\text{Zn}_{0.02}\text{S}_{3.98}\text{O}_{0.02}$) exhibits excellent stability against humid air, lithium metal, and chlorobenzene solvent.⁸⁹ L. Zhang *et al* report O-doped $\text{Li}_6\text{PS}_5\text{Br}$ exhibits excellent dendrite suppression capability, superior electrochemical and chemical stability against Li metal as well as high voltage oxide cathodes, and good air stability.⁹⁰

So far, the air stability of sulfide electrolytes is a big hurdle, which dramatically limits the widespread application of sulfide electrolytes. The current widely-used approach can improve air stability but sacrifice the ionic conductivity. New strategies to enhance the air-stability of sulfide electrolytes without deteriorating their ionic conductivity should be developed in the future, such as nanostructured sulfide electrolytes with an air-stable outer layer. As long as the outer layer does not block the Li^+ diffusion between SE particles, both the high ionic conductivity and good air-stability can be achieved.

1.3.2 Electrochemical Stability of Sulfide Electrolytes

To realize the high energy density of rechargeable lithium batteries, solid-state sulfide electrolytes are desired to couple with metallic lithium anodes and high-voltage cathodes. Thus, a large electrochemical window is required. In the past, the electrochemical window of reported solid-state electrolytes, such as LGPS family, $\text{Li}_2\text{S}-\text{P}_2\text{S}_5$, is boasted to be 5 V vs Li^+/Li , which was evaluated by testing the cell with a structure of $\text{Li}/\text{electrolyte}/\text{inert metal}$ at the scanning rate of $1 \text{ mV}\cdot\text{s}^{-1}$. Recently, C. Wang *et al.* claimed that the electrochemical window of $\text{Li}_{10}\text{GeP}_2\text{S}_{12}$ is overestimated.⁹¹ Based on theoretical calculation, the stable electrochemical window of $\text{Li}_{10}\text{GeP}_2\text{S}_{12}$ is only from 1.71 ~ 2.14 V vs. Li^+/Li , as displayed in **Figure 4a**. The CV curves also show the reduction peak of 1.7 V and the oxidation peak of 2.1 V as shown in **Figures 4b** and **4c**. The oxygen substitution is probably a solution.⁹² A. Hayashi *et al.* reported that by substituting 3 mol% of P_2O_5 for P_2S_5 in the $70\text{Li}_2\text{S}\cdot(30-x)\text{P}_2\text{S}_5\cdot x\text{P}_2\text{O}_5$ glass-ceramics, an wide electrochemical window of the glass-ceramic was shown up to 10 V (vs. Li^+/Li) while the ionic conductivity is still maintained at $3.0\times 10^{-3} \text{ S cm}^{-1}$ at room temperature with the lowest activation energy of 16 kJ mol^{-1} for ionic conduction. In addition, the introduction of halides may be another solution. C. Liang *et al* found that induction of LiI to Li_3PS_4 can dramatically improve the electrochemical stability up to 10V Li^+/Li .⁴⁰ Most interestingly, a core-shell structured Li-Si-P-S was designed.⁹³ The more Si content was synthesized on the shell, which results in the stable window of 0.7 ~ 3.1 V. It should be mentioned that the stable window is much larger than theoretical prediction (1.7 ~ 2.1 V). In the future, electrochemically stable solid electrolytes should be developed, which also bring in the benefit at the interfacial stability against both cathode and anode materials.

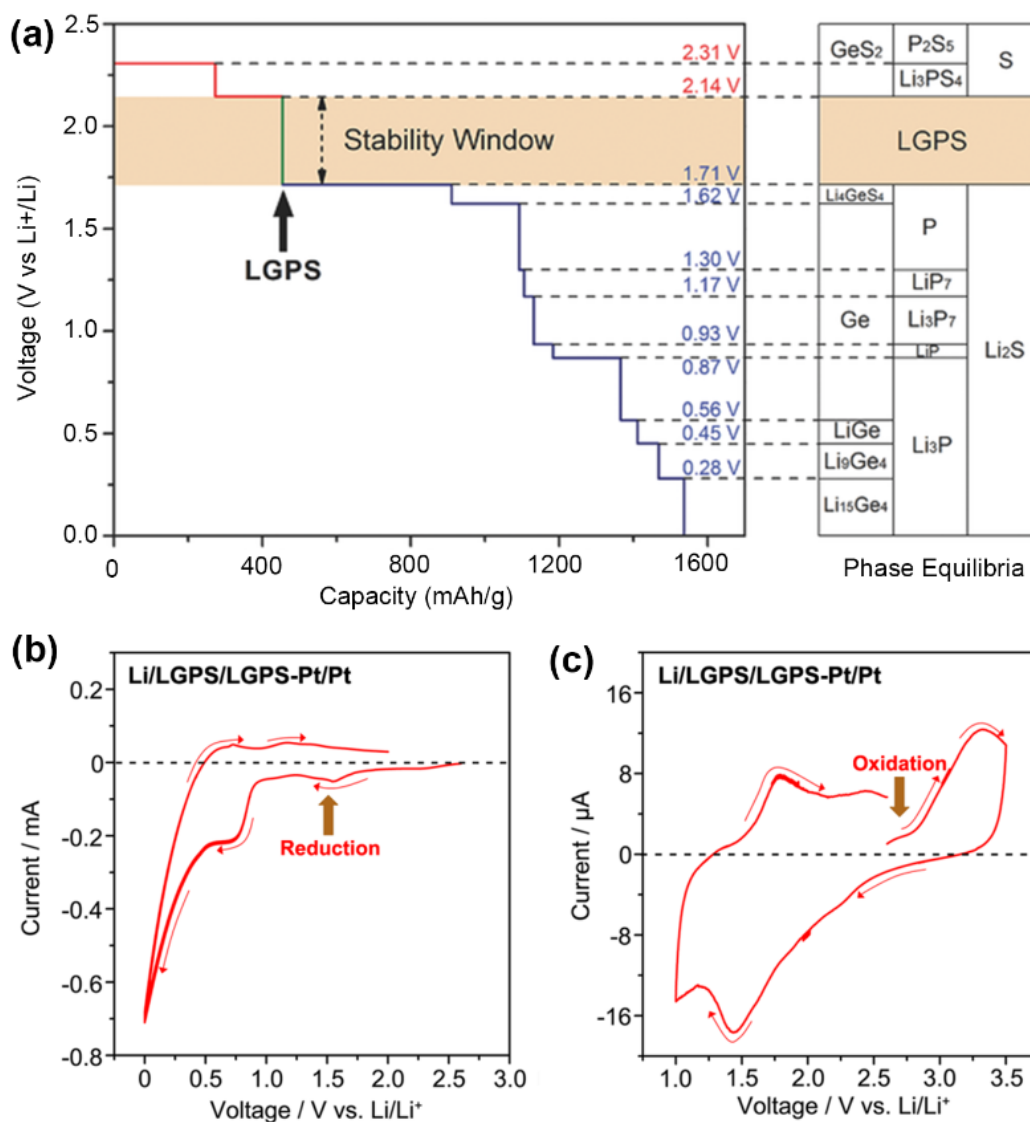


Figure 1-4 (a) The first-principles calculation results of the voltage profile and phase equilibria of LGPS solid electrolyte upon lithiation and delithiation. Cyclic voltammetry of Li/LGPS-Pt/Pt semi-blocking electrode at a scan rate of $0.1 \text{ mV}\cdot\text{s}^{-1}$ in the voltage range of 0-2.0 V (b) and 1.0-3.5 V (c).

As a short summary, the ionic conductivity (around 10^{-2} S/cm) of sulfide electrolytes so far is comparable to that of conventional liquid electrolytes. However, the synthesis of sulfide electrolytes is mainly based on time-consuming ball milling and energy consumption high-temperature solid-state sintering method. In recent years, liquid-phase synthesis was developed to synthesize the sulfide electrolytes, but the ionic

conductivity is generally lower than that synthesized by solid-state methods. Therefore, the effective and economical methods to obtain sulfide electrolytes with high ionic conductivity are highly demanded. In addition, the air-stability of sulfide electrolytes should be significantly improved by either elemental substitution or nanostructure design. Moreover, to guarantee the superiority of ASSLIBs in terms of energy density and safety, the electrochemical window of sulfide electrolytes should be expanded to enable the use of lithium metal and high-voltage cathodes.

1.4. Interface Challenges of SE-based ASSLIBs

As summarized in Table 1, the ionic conductivities of some solid-state sulfide electrolytes almost rival that of conventional organic liquid electrolytes ($\sim 10^{-2}$ S/cm). However, the state-of-the-art electrochemical performances of ASSLIBs are still behind those of liquid electrolyte-based lithium batteries. The reason is the huge interfacial resistance, which is originated from the inferior solid-solid contact and significant interface reactions, impeding Li^+ transport across the electrode/electrolyte interface. In addition, the space charge layer at the cathode interface also impedes the lithium-ion transfer, as revealed in previous studies.^{94,95} In the following section, cathodic and anodic interfacial behaviors in SE-based ASSLIBs will be discussed together with the promising strategies, respectively.

1.4.1 Cathode Interface of SE-based All-Solid-State Lithium Batteries

Space charge layer formation, interfacial reactions, and interfacial ionic contact between the cathode materials and SEs are three main challenges in SE-based ASSLIBs.^{96, 97,96, 98-100} Specifically, the Li^+ will transport from SEs to cathode material to reach a chemical equilibrium, especially in the first charging process, leading to a lithium-deficient layer at

the interface, which generally exhibits large interface resistance.⁹⁶ The second one is the interfacial reactions^{96,97} For instance, mutual diffusions of Co, P, and S at the interface between LiCoO₂ and Li₂S-P₂S₅ were clearly observed by scanning transmission electron microscopy with energy dispersive X-ray spectroscopy.⁹⁷ Thirdly, improving the interfacial ionic contact can dramatically improve the rate-performance of ASSLIBs.¹⁰¹

(i) Space Charge Layer

The concept of a “space charge layer” was first put forward by Carl Wagner in 1972 to explain the interfacial electric conductivity between two semiconductors.¹⁰² Afterwards, J. Maier made great efforts on understanding the effects of the space charge layer on various solid-solid interfaces.¹⁰³ In recent years, the space charge layer was extended to explain the cathodic interfacial phenomenon of all-solid-state lithium batteries.¹⁰⁴ In view of this, understanding the origin of the space charge layer is necessary and critical for developing solid-state electrolytes towards ASSLIBs. Typically, two models were put forward to explain the interfacial carrier redistribution: Gouy-Chapman model and Mott-Schottky model,⁹⁴ which are addressing general solid-solid interface. Below we take the sulfide electrolyte/oxide cathode interface as an example, which would be more constructive for developing solid-state sulfide electrolytes.

As schematically shown in **Figure 1-5a**, due to the difference in chemical potentials between the solid-state sulfide electrolyte and oxide cathode, a space charge layer forms at the boundary in accordance with thermodynamic equilibrium. Generally, oxides have a higher chemical potential than sulfides, thus lithium ions thermodynamically transfer from solid-state electrolytes to oxide cathodes to reach thermal dynamic equilibrium, forming a lithium-depletion layer at the cathodic surface.¹⁰⁵ Meanwhile, electrons of oxide cathodes, which are generally a mixing conductor, will eliminate the concentration of lithium interstitials at the interface, extending the thickness of the space charge layer. Since the transferring capability of lithium ions at the interface is subjected to the

movement of lithium interstitials, the lithium-depletion layer will definitely enlarge the interfacial resistance, increasing the polarization and worsening the rate capability. The DFT calculation clearly showed the preferential removal of lithium ions from the Li_3PS_4 side upon charging. As shown in **Figure 1-5c**, when the oxide cathode (FePO_4) contacted with sulfide electrolytes, part of lithium ions in the electrolyte move to cathode structure.¹⁰⁶ This result reveals that the space-charge layer appears as a lithium-depleted layer at the $\text{LiFePO}_4/\text{Li}_3\text{PS}_4$ interface, which should make the interface highly resistive owing to the absence of charge-carrying lithium ions.⁹⁸

When an intermediate layer interposed between the oxide and sulfide, the space charge layer can be ameliorated (**Figure 1-5b**). To clarify the effect of the buffer layer at the interface, Y. Tateyama *et al.* also performed the theoretical calculation on the $\text{LiCoO}_2/\beta\text{-Li}_3\text{PS}_4$ interface and discussed the Li^+ behavior at the interface with and without interfacial layer.⁹⁶ As shown in **Figure 1-5d**, due to their chemical potential difference, lithium-ion redistribution occurs when the LCO contacts with LPS. Comparatively, the LiNbO_3 (LNO) buffer layer can alleviate the ion redistribution due to its low electronic conductivity. More interestingly, the calculation results found that the surface adsorption of Li^+ is the main contribution to the equilibrium space charge layer (**Figure 1-5e**). The LCO/LPS interface has more attractive Li adsorption sites while the interposition of the LNO buffer layer forms a smooth interface without Li^+ adsorption sites. Thus, the interposition of LNO can eliminate the Li^+ surface adsorption, mitigating the space charge layer. In the initial stage of charging (**Figure 1-5f**), lithium ions at the LCO/LPS interface are expected to transfer into the bulk LPS by releasing the electron to the cathode. This is the underlying reason for the observed voltage profile slope at the beginning of charging in many experimental results.¹⁰⁶⁻¹⁰⁸ Recently, it was demonstrated that removing carbon additives from cathode composites also can eliminate the slope at the beginning of charging.^{107, 108} Actually, the introduction of carbon additives also aggravates the space charge effect at the interface between the cathode and

sulfide electrolytes. Moreover, some researchers also revealed that the space charge effect in the cathode/oxide electrolyte interface has a negligible effect on the lithium-ion transfer across the interface.^{109, 110} In the future, the quantitative studies on the space charge effect are recommended.

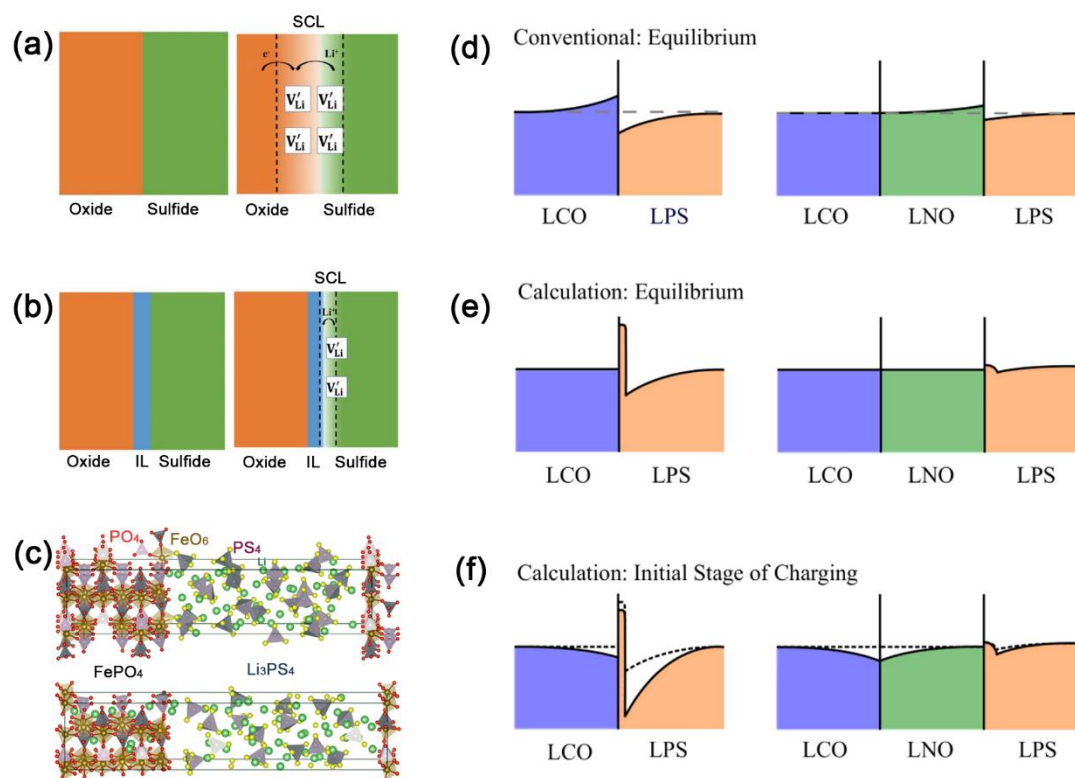


Figure 1-5 (a) The two-phase boundary of oxides and sulfides, and the defect chemistry situation after the formation of SCL; (b) Introduction of ionic-conducting intermediate layer (IL) between the two phases;⁹⁴ (c) Interface structure between $FePO_4$ and Li_3PS_4 before and after the FP-MD. Schematic illustrations of the interfacial Li concentration. (d-f) The equilibrium concentrations expected by the conventional model and indicated by the present calculations for the LCO/LPS interface (a and c) as well as the LCO/LNO/LPS (b and d). The Li concentrations in (e) and (f) describe the expected changes at the initial stage of charging for both interfaces, respectively.

(II) Interfacial Reactions at the Cathode Interface

Besides the space charge effect, the interfacial reaction is another contributor to the huge interfacial resistance. Numerous studies based on either first-principles calculations or experimental investigation have revealed that undesirable chemical reactions or elemental diffusions at the electrode/sulfide interface during the charge-discharge process.^{111, 112} A. Sakuda *et al.* first conducted the transmission electron microscopy study on the interface between LiCoO₂ and Li₂S-P₂S₅, clearly observing a 10 nm interfacial layer at the interface, which is resulted from the elemental diffusion of Co, P, and S.(**Figure 1-6a**)⁹⁷ By first-principles calculations, Y. Tateyama *et al.* revealed that the mixing of Co and P is energetically preferable to the unmixed states at the LiCoO₂/β-Li₃PS₄ interface.¹¹¹ Moreover, the surface-sensitive X-ray photoelectron spectroscopy (XPS) has been widely adopted to characterize the interfacial reactions between the electrode materials and sulfide electrolytes.¹¹³⁻¹¹⁵ As shown in **Figure 1-6b**, sulfides electrolytes are oxidized to elemental S, sulfites, phosphates, and high-oxidization-state P₂S_x compounds after 25 charge-discharge cycles.¹¹³ These highly insulative interphases dramatically hinder the Li⁺ transfer across the electrode/electrolyte interface.

To mitigate the interfacial reactions, a buffer layer is generally interposed between electrodes and sulfide electrolytes.^{114, 116} So far, both lithium-ion conducting coating layers, such as LiNbO₃,¹¹⁷ Li₄Ti₅O₁₂,¹¹⁸ and Li₂SiO₃,^{97, 119} or oxides, for instance, Al₂O₃, TiO₂, and even ternary BaTiO₃, are reported to dramatically reduce the cathodic interfacial resistance. By the first-principles calculation, Y. Mo *et al* revealed that Li-Ta-O, Li-Nb-O, Li-Si-O, Li-Ti-O, and Li-P-O possess a wide electrochemical window (**Figure 1-6c**), suggesting that these coating materials are stable at the electrode/electrolyte interface during the cycling.¹²⁰ Up till now, these coating materials have been verified in experimental studies. **Table 1-2** lists out the coating materials and coating techniques for suppressing interface resistance of all-solid-state batteries. It is

obvious that the coating materials are generally developed by sol-gel methods or spraying coating, which are very difficult to control the thickness and uniformity of the critical coating layer. As a remedy, X. Sun et al synthesized Li-Nb-O,¹²¹ Li-Si-O,¹²² Li-Ta-O,¹²³ Li-P-O,¹²⁴ Li-Ti-O¹²⁵ by atomic layer deposition, which shows a great advantage on the thickness controllability and conformality (**Figure 1-6d**). Most interestingly, G. Ceder et al predicted that LiPO₃ possesses a wide electrochemical window, which can be a good coating material for high-voltage cathodes, such as LiNi_{0.5}Mn_{1.5}O₃, LiCoPO₄.¹²⁶

Table 1-2. Surface coating that has been developed so far for suppressing interfacial resistance.

Cathode	Coating materials	Coating technique	Reference
LiCoO ₂	Li ₂ SiO ₃	Sol-gel method	Akitoshi Hayashi (2009) ¹²⁷
LiCoO ₂	Li ₄ Ti ₅ O ₁₂	Spray coating	Kazunori Takada (2006) ¹¹⁸
LiCoO ₂	LiNbO ₃	Spray coating	Kazunori Takada (2007) ¹¹⁷
LiMn ₂ O ₄	LiNbO ₃	Spray coating	Kazunori Takada (2012) ⁹⁹
LiCoO ₂	LiTaO ₃ LiNbO ₃ Li ₄ Ti ₅ O ₁₂	Spray coating	Kazunori Takada (2008) ¹²⁸
LiCoO ₂	Al ₂ O ₃	Atomic layer deposition	Se-Hee Lee (2012) ¹²⁹
LiNi _{0.5} Mn _{1.5} O ₄	LiNbO ₃	Sol-gel method	Masaaki Hirayama (2016) ¹³⁰
LiNi _{0.8} Co _{0.15} Al _{0.05} O ₂	Li ₂ O-ZrO ₂	Sol-gel method	Yuichi Aihara (2014) ¹³¹
NiS	Li ₂ S-P ₂ S ₅	Pulsed laser deposition	Masahiro Tatsumisago (2013) ¹³²

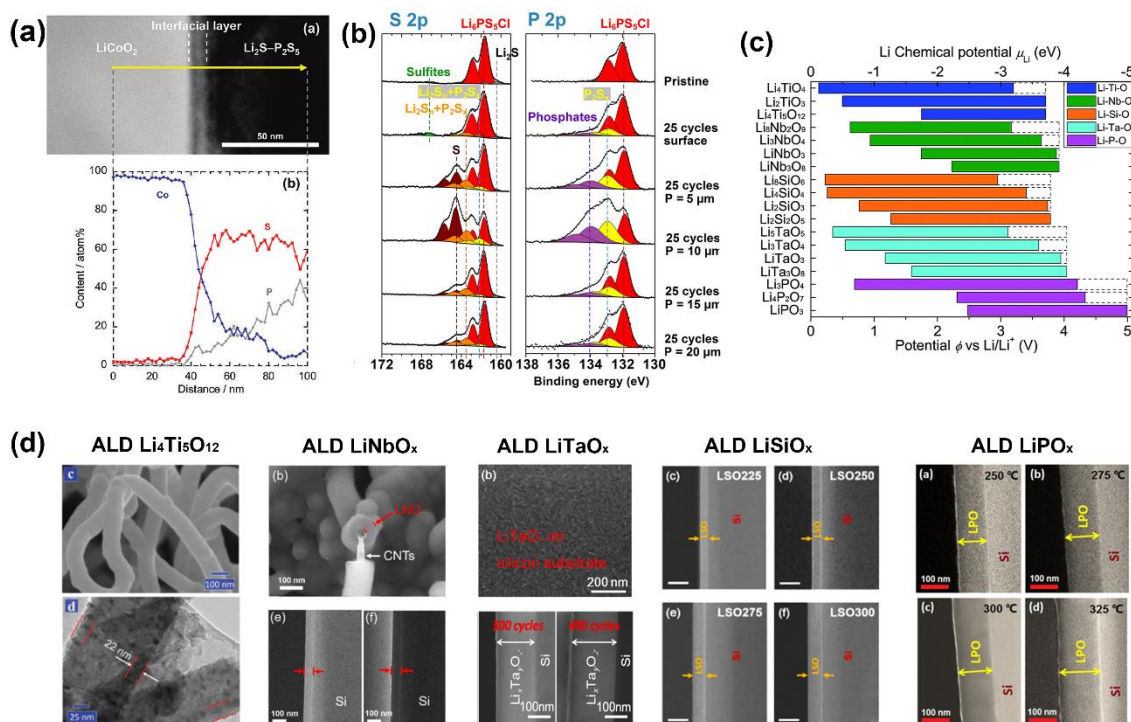


Figure 1-6 (a) Cross-sectional HAADF-STEM image of LiCoO₂/Li₂S-P₂S₅ interface after initial charging and cross-sectional EDX line profiles for Co, P, and S elements. The arrow presents the positions at which EDX measurements were taken.⁹⁷ (b) S 2p and P 2p XPS spectra of the composite LCO electrode of LCO/Li₆PS₅Cl/Li-In half-cells: before cycling (pristine), after 25 cycles, and after 25 cycles with increasing etching depths of the electrode from 5 to 20 μm. (c) Electrochemical window of the proposed and previously demonstrated coating layer materials applied between SEs and cathode materials. The dashed line marks the equilibrium voltage to fully de-lithiate the materials.¹²⁰ (d) The ALD deposition of Li-Ti-O, Li-Nb-O, Li-Ta-O, Li-Si-O, and Li-P-O interfacial coating materials for SE-based ASSLIBs.

(III) Improvement of Solid-Solid contact in the Cathode of ASSLIBs

Apart from the space charge layer and interfacial reactions, solid-solid contact between electrode materials and sulfide electrolytes also dramatically limit the current drain.

Improving the solid-solid contact in solid-state lithium batteries can dramatically improve the electrochemical performance of solid-state lithium batteries.¹³³⁻¹³⁵ A very general approach to improve the solid-solid contacts is to use a soft or liquid-state lithium-ion conductive material.¹³⁵ However, due to the highly reactive nature of sulfide electrolytes, it is very challenging to find the suitable soft and liquid-state lithium-ion materials for sulfide-based ASSLIBs. Y. Jung *et al.* reported an ionic liquid (trimethylene glycol dimethyl ether and LiTFSI with a high Li salt concentration) exhibits excellent compatibility with SEs.^{101, 136} Using a small amount of the ionic liquid, the ionic contact in the cathode composites is dramatically improved (**Figure 1-7a**). In addition, a plastic crystal electrolyte (succinonitrile-based LiTFSI) was found compatible with sulfide electrolytes, which can also improve the ionic contact in the cathode composites and suppress lithium dendrite formation at the anode interface (**Figure 1-7b**).¹³⁷

Another approach to improve the solid-solid contact is to employ soluble sulfide electrolyte, which is a homogeneous sulfide solution, to coat the cathode materials or even infiltrate into the conventional electrodes (**Figure 1-7c**). After evaporating all the solvents and post-annealing, the intimate ionic contact between electrode materials and sulfide electrolytes can be guaranteed, as shown in **Figure 1-7d**. Using this approach, the large-scale roll-to-roll process can be adopted for fabricating the bulk-type all-solid-state lithium batteries.^{66, 138} Impressively, some air-stable soluble sulfide electrolytes and soluble sodium analogs are also developed.^{86, 139} However, the soluble sulfide electrolytes generally show relatively low ionic conductivity ($< 10^{-3} \text{ S.cm}^{-1}$) even after post-annealing.^{133, 134, 140} In addition, the solvent selection is also very critical for the soluble sulfide electrolytes.⁶⁷ In the future, it is highly desired to develop a green, effective and economic synthesis route to obtain the soluble sulfide electrolyte with high ionic conductivity and good air stability.

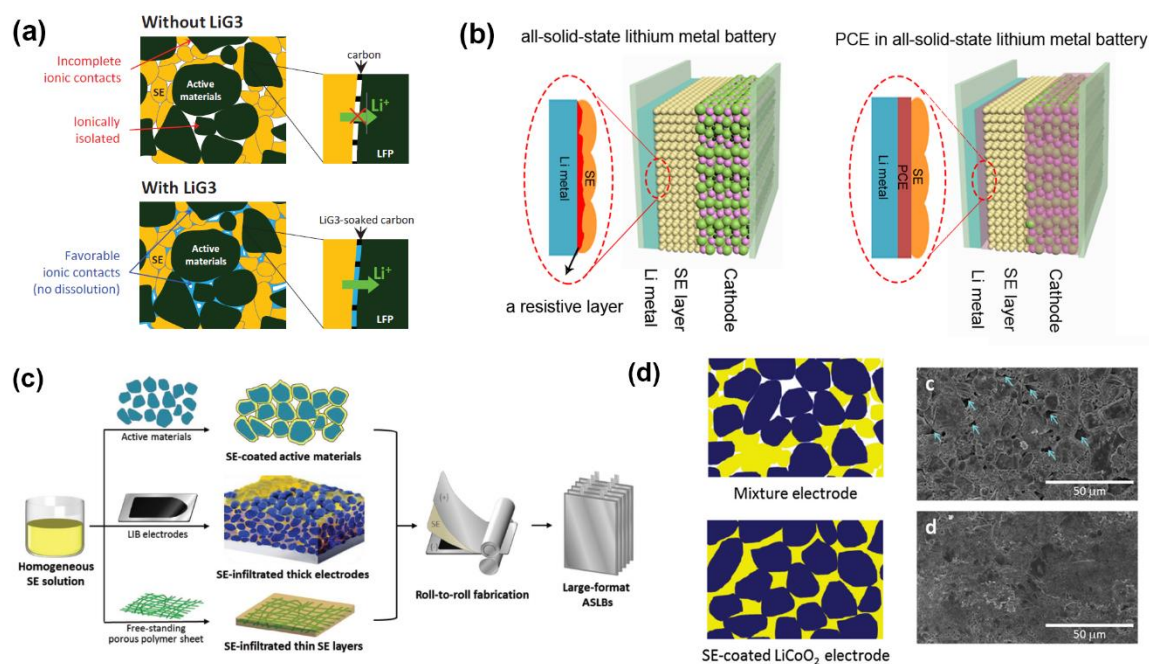


Figure 1-7 (a) Schematic diagram representing the microstructure of the composite electrodes without and with ionic liquids (LiG3), showing that LiG3 improves the imperfect solid-solid contacts. Carbon additives included in the composite electrode are not shown in the scheme. **(b)** Schematic diagram of ASSLMs versus ASSLMs with the PCE interlayer. **(c)** Schematic diagram illustrating fabrication of sheet-type electrodes and ASLBs applying solution process of SEs; coating and infiltration with SEs.⁶⁶ and **(d)**. Schematic illustration of the mixture electrode and the $0.4\text{LiI}-0.6\text{Li}_4\text{SnS}_4$ -coated LiCoO_2 electrode. The dark blue and yellow regions indicate LiCoO_2 and SE, respectively. FESEM surface images of $0.4\text{LiI}-0.6\text{Li}_4\text{SnS}_4$ / LiCoO_2 mixture electrode and **d)** $0.4\text{LiI}-0.6\text{Li}_4\text{SnS}_4$ -coated LiCoO_2 electrode. The arrows indicate void spaces.¹³⁹

At the cathode interface, it is well-acknowledged that the space charge layer, interfacial reactions, and solid-solid contacts between cathode materials and sulfide electrolytes are three barriers limiting the advancement of SE-based ASSLIBs. In the future, advanced characterization techniques, such as high-resolution TEM and synchrotron-based analysis,

are suggested to reveal the detailed and systematic interfacial information. In addition, in-situ characterization should be developed to deepen the understanding of interfacial lithium-ion transfer behaviors in SE-based ASSLIBs. Moreover, the durability and ionic conductivity of the interfacial coating layer should be examined. The soluble sulfide electrolytes are very promising to improve the solid-solid contact and also compatible with roll-to-roll fabrication process. Nevertheless, it is worthy to note that there is still a big room for the improvement of the ionic conductivity of soluble sulfide electrolytes.

1.4.2 Anode Interface of SE-based All-Solid-State Lithium Batteries

Among all the known anode materials, the lithium metal anode, which has high theoretical capacity (3862 mAh g^{-1}), the lowest operating potential (-3.040 V vs standard hydrogen electrodes (SHE)), is supposed to be an ideal anode for all types of high-energy-density lithium batteries, including lithium-sulfur batteries and Li-air batteries.^{4, 141-144} However, severe safety concerns, associated with eventual internal short circuits caused by the lithium dendrite growth during the repeated lithiation and delithiation process, impede the commercialization of lithium metal anodes in lithium ions batteries.¹⁴⁵ Solid-state electrolytes maybe give a new opportunity to the use of lithium metal as the anode, maximizing the energy density of current lithium-ion batteries and pushing forward the development of the next-generation lithium-sulfur batteries and lithium-oxygen batteries.^{4, 145} However, when contacting a lithium metal anode, SEs are thermodynamically reduced to form new phases, such as Li_2S , Li_3P ,^{95, 146} leading to the large interfacial resistance. In addition, lithium dendrites still grow through the grain boundary, resulting in the short circuits in solid-state batteries. Therefore, the interfacial reactions and lithium dendrite formation are two big challenges facing the Li/SE anode interface.

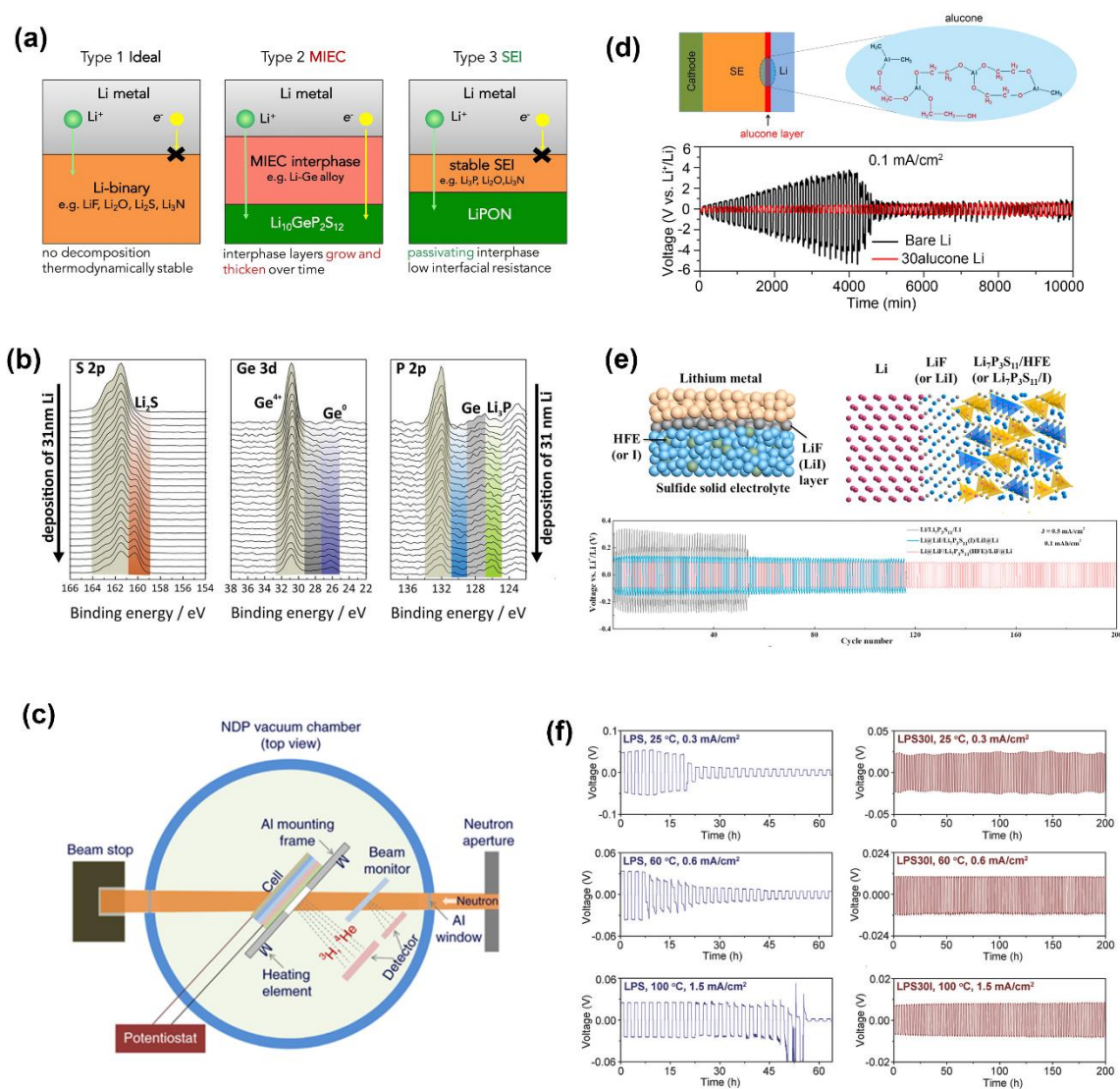


Figure 1-8 (a) Illustration of Different Types of Li Metal-SE Interfaces. Type 1: Stable interface. Type 2: MIEC, Type 3: SEI. (b) . X-ray photoelectron spectra recorded during the deposition of 31 nm Li metal on Li₁₀GeP₂S₁₂. S 2p, Ge 3d, and P 2p/Ge 3p detail spectra are shown for different deposition states. With increasing Li deposition time LGPS decomposes. The identified species are marked and labeled in the spectra.¹⁴⁷ Reproduction with permission from ref.55. (c) Schematic of the experimental set-up for operando NDP.¹⁴⁸ (d) An inorganic-organic hybrid interphase enabled by molecular layer deposition suppress the interfacial reactions and lithium dendrite formation between Li₁₀SnP₂S₁₂ and Li metal interface. (e) Schematic

diagrams of the Li/Li₇P₃S₁₁ interface with a uniform thin LiF (or LiI) interphase layer and HFE (or I solution) infiltrated sulfide electrolyte.¹⁴⁹ (f) Galvanostatic cycling of the Li/LPS/Li and Li/LPS30I/Li cells at constant current densities at a,b) 25 °C, c,d) 60 °C, e,f) and 100 °C. The time for each charge and discharge is 1 h.

Over the past years, a lot of investigations based on either in-situ characterizations or theoretical calculations have shown that SEs are not stable against Li metal.¹⁵⁰⁻¹⁵⁷ To clarify the anode interface, three types of the Li-SE interface are proposed^{151, 158} (I) Type I: the stable interface, in which the solid electrolytes are thermodynamically stable against Li metal (**Figure 8a**). Naturally, the interfaces with Li binary compounds, such as Li/LiF, Li/Li₃N, Li/Li₂S, and Li/Li₂O, belong to this type. (II) Type II: the mixed ionic-electronic conducting interphase (MIEC), in which the sulfide electrolytes are thermodynamically unstable against reaction with Li metal, and both the electron and lithium-ion can penetrate through, leading to the continuous decomposition of sulfide electrolytes and consequently the short circuits of all-solid-state batteries. (III) Type III: solid electrolyte interphase (SEI), which shows sufficient ionic conductivity but negligible electronic conductivity, thus the SEI is non-growing and can suppress the interfacial reactions and lithium dendrite formation.^{147, 152} Ideally, the stable and non-growing SEI is favorable as long as the resulting resistance and IR drop across the SEI layer is not too large.

J. Janek *et al.* developed *in-situ* X-ray photoelectron spectroscopy (XPS) to probe the interfacial instability of Li₁₀GeP₂S₁₂ at the lithium metal anode. In combination with time-resolved electrochemical measurements, *in-situ* XPS offers detailed information on the chemical reactions at the Li/LGPS interface. The decomposition of Li₁₀GeP₂S₁₂ leads to the formation of an MIEC interphase composed of Li₃P, Li₂S, and Li-Ge alloy (**Figure 1-8b**).¹⁴⁷ These decomposed compounds are also predicted by DFT calculations.¹¹²

Another challenge to develop SE-based ASSLMBs is the lithium dendrite formation.¹⁵⁹ M. Tatsumisago *et al.* firstly use in-situ SEM to investigate the lithium deposition and dissolution mechanism in bulk-type solid-state lithium batteries with Li₂S-P₂S₅ glass-ceramics.¹⁶⁰ At a high current density, uniform lithium deposition triggers large cracks, leading to irreversible lithium deposition and dissolution. But the unfavorable cracks could be avoided using a small current density.¹⁶¹ Remarkably, by virtue of the operando neutron diffraction profile (NDP) study (**Figure 1-8c**), it was revealed by C. Wang *et al* that the lithium dendrite formation in solid-state electrolytes is due to their high electronic conductivity. Therefore, minimizing the electronic conductivity of solid-state electrolytes instead of increasing their ionic conductivity is very critical for eliminating the lithium dendrite formation in ASSLIBs.¹⁴⁸

To suppress the interfacial reactions and lithium dendrite formation at the SE/Li anode interface. Various strategies have been proposed over the past years. The widely adopted approach is surface modification.^{28, 162, 163} As an example, an inorganic and organic hybrid interlayer as an artificial SEI, which was deposited by molecular layer deposition, was engineered at the Li₁₀SnP₂S₁₂/Li metal interface (**Figure 1-8d**). The results confirm that artificial SEI can spontaneously suppress the interfacial reactions and lithium dendrite formation. In addition, the LiF or LiI interphase layers, which are stable against Li metal,⁹⁵ were also proven very effective to suppress the interfacial reactions and lithium dendrite formation (**Figure 1-8e**). Apart from the external coating and/or interfacial modification, it is very attractive to solve above-mentioned interfacial issues by tuning the composition of SEs.^{64, 90, 149} For example, C. Wang *et al* demonstrated that the critical current density is improved significantly after incorporating LiI into Li₂S-P₂S₅ glass, reaching 3.90 mA cm⁻² at 100 °C after adding 30 mol% LiI. In addition, stable cycling of the Li-Li cells for 200 h is also achieved at 1.50 mA cm⁻² at 100 °C (**Figure 1-8f**).⁶⁴

Although the interfacial reactions and lithium dendrite formation at the SE/Li interface can be suppressed by either external interface modification or tuning the internal composition of SEs. The area capacity for Li plating/stripping is around 0.1 ~ 0.5 mAh.cm⁻², which is definitely far from the requirement of the real application of Li metal. Furthermore, the Coulombic efficiency of Li metal in solid-state batteries has never been examined so far. To ensure the long cycling life (>2000 cycles) of Li metal, the Coulombic efficiency of Li metal must be higher than 99.99%, provided that 20% Li are consumed during the electrochemical cycling.

1.5 Demonstrations of SE-based ASSLIBs

1.5.1 Solid-State SE-based ASSLIBs

Due to the high ionic conductivity of SEs, high-performance ASSLIBs have been widely demonstrated. In 2011, R. Kanno *et al* demonstrated the excellent reversibility of LiCoO₂ with highly ion-conductive Li₁₀GeP₂S₁₂ at the current density of 14 mA.g⁻¹ (0.1C) (**Figure 1-9a**). With continuous efforts. In 2016, Li_{9.54}Si_{1.74}P_{1.44}S_{11.7}Cl_{0.3} was reported to show the highest conductivity of 2.5×10^{-2} S cm⁻¹. The Li_{9.54}Si_{1.74}P_{1.44}S_{11.7}Cl_{0.3}-based ASSLIBs exhibited not only the excellent cycling performance with 75% of the first discharge capacity remaining after over 500 cycles and Coulombic efficiency of 100% but also the excellent rate capabilities with discharge current densities of 150 C at 25 °C and 1500 C at 100 °C.⁸ The high power density is comparable to that of supercapacitors.⁸ Moreover, the high-capacity and high-voltage electrodes have also been investigated in SE-based ASSLIBs, such as LiNi_{0.8}Co_{0.15}Al_{0.05}O₂,¹⁶⁴ LiNi_{1/3}Mn_{1/3}Co_{1/3}O₂,¹⁶⁵ LiNi_{0.6}Co_{0.2}Mn_{0.2}O₂,¹⁶⁶ LiNi_{0.8}Co_{0.1}Mn_{0.1}O₂,¹¹⁵ LiNi_{0.5}Mn_{1.5}O₄,¹³⁰ As demonstrated by Masaaki Hirayama *et al.*, the high-voltage cathode, LiNi_{0.5}Mn_{1.5}O₄, delivers a specific capacity of 80 mAh.g⁻¹ with an average voltage of 4.3 V, using Li₁₀GeP₂S₁₂ solid-electrolytes and Li metal

anodes.(**Figure 1-9b**)¹³⁰

When comparing the electrochemical performance of these electrode materials in solid-state batteries with those in liquid electrolytes, the capacity and cycling stability of ASSLIBs are generally lower. Generally, these high-voltage electrodes exhibit a high electrochemical potential than sulfide electrolytes, thus the interfacial reactions between electrodes and SEs cannot completely be suppressed even by interfacial coating. As a consequence, the cycling stability of these electrodes are not as stable as those of liquid electrolytes. In addition, the volume change of electrode materials during the charge-discharge process results in the “contact loss” between electrodes and SEs.^{115, 167} Using zero-strain materials as the electrode, such as $\text{Li}_4\text{Ti}_5\text{O}_{12}$, solid-state batteries exhibit remarkable cycling performance within 700 cycles (**Figure 1-9c**). Moreover, the electrode-electrolyte contact plays an important role in the capacity of ASSLIBs.¹³² The conventional dry mixing leads to the point-to-point contact between electrodes and SEs, while solution-based methods can increase the electrode-electrolyte contact by coating the electrode particles with SEs, which can dramatically improve the capacity of ASSLIBs (**Figure 1-9d**).¹⁶⁸

Although a lot of encouraging achievements in ASSLIBs have been made, cell-based (not electrode-material-based) energy density is in a stage of infancy. To enable both volumetric and gravimetric energy density of ASSLIBs comparable with those of commercial lithium-ion batteries, the desired thickness of the SE layer should be less than 50 μm , according to the numerical analysis.^{169, 170} Therefore, achieving a thin film of solid-state electrolyte is of vital importance, although it is technically very challenging.¹⁷¹ Meaningfully, Y- Jung et al. on the first-ever reported a bendable and thin sulfide solid electrolyte film reinforced with a mechanically compliant poly(paraphenylene terephthalamide) nonwoven (NW) scaffold, which enables the fabrication of free-standing and stackable ASLBs with high energy density and high rate capabilities (**Figure 1-9e**).

The ASLB, using a thin ($\sim 70 \mu\text{m}$) NW-reinforced SE film, exhibits a 3-fold increase of the cell-energy-density compared to that of a conventional cell without the NW scaffold.¹³⁸ In the future, developing advanced techniques for the fabrication of SE thin film with a low cost is very critical for the practical application of all-solid-state lithium batteries.

As a short summary, to enable ASSLIBs, there are several parameters to be considered. (1) The interfacial reactions between the electrode and SEs should be totally suppressed to enable long-term cycling stability. (2) The electrode-electrolyte contact area should be maximized either by physical deposition or solution method coating. (3) The volume change of electrode materials can result in the “loss contact” between the electrodes and SEs. Therefore, the strategies to accommodate the volume change of ASSLIBs need to be developed in the future. (4) Last but not least, the advanced techniques, such as 3D printing, to fabricate the thin SE layer to increase the cell-level energy density of ASSLIBs should be developed.

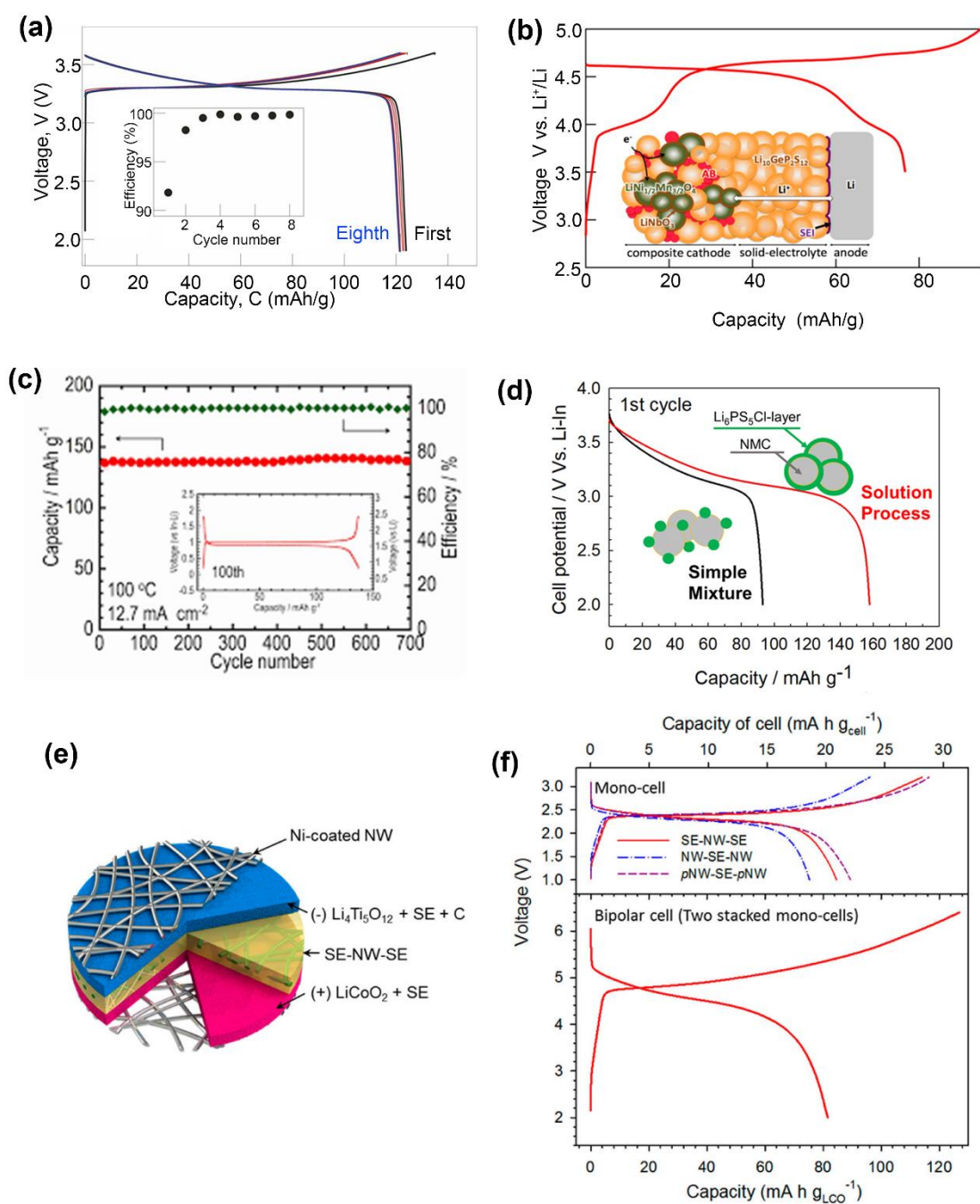


Figure 1-9 (a) Charge-discharge curves of LiCoO_2 in all-solid-state batteries at 14 mA.g^{-1} . (b) Charge and discharge curve of $\text{LiNi}_{1.5}\text{Mn}_{0.5}\text{O}_2/\text{Li}_{10}\text{GeP}_2\text{S}_{12}/\text{Li}$ solid-state batteries (c) Long-term cycling stability of the $\text{Li}_4\text{Ti}_5\text{O}_{12}$ anode in ASSLIBs (d) The discharge curves of $\text{LiNi}_{1/3}\text{Mn}_{1/3}\text{Co}_{1/3}\text{O}_2$ electrodes prepared by conventional dry mixing and solution process.¹⁶⁸ (e) Schematic diagram of the nonwoven scaffold

reinforced free-standing ASSLIBs. (f) The charge-discharge curves of mono-cells and bipolar cells.

1.5.2 SE-based All-Solid-State Lithium-Sulfur Batteries

Lithium-sulfur (Li-S) batteries have been considered as one of the most promising next-generation battery technologies with the potential of possessing energy densities at least twice those of state-of-the-art Li-ion batteries.^{172, 173} However, the intermediate polysulfides, especially the long-chain polysulfides, easily dissolve in the liquid electrolyte causing the “shuttle effect”.¹⁷⁴ The notorious phenomenon leads to fast capacity degradation, low Coulombic efficiency, severe self-discharge.^{175, 176} To solve this headache problem, the replacement of liquid organic electrolytes with solid-state SEs may be the ultimate approach.¹⁷⁷ Therefore, SE-based all-solid-state Li-S batteries have been demonstrated.¹⁷⁸⁻¹⁸⁰ A glass-type $75\text{Li}_2\text{S}-25\text{P}_2\text{S}_5$ (stoichiometric Li_3PS_4) electrolyte has been applied to develop high-performance solid Li-S batteries. An initial capacity as high as 1600 mAh g^{-1} with a high Coulombic efficiency of 99% was demonstrated.¹⁸¹ Besides, no obvious capacity degradation within 100 cycles was observed. However, all-solid-state Li/S batteries exhibit a very low utilization of active materials.¹⁸² Now it is widely acknowledged that the three-phase interface between active materials, carbon additives, and SEs is very critical to achieve high reversible capacity in ASSLSBs. Therefore, a lot of nanocomposites have been rationally designed to achieve both high capacity and long cycling stability. For example, C. Wang *et al* synthesized a nanocomposite consisting of nanosized Li_2S , carbon matrix, and $\text{Li}_6\text{PS}_5\text{Cl}$. The homogeneous nanocomposite electrode achieved a large reversible capacity of 830 mAh/g (71% utilization of Li_2S) at 50 mA/g for 60 cycles.¹⁸³ Chengdu Liang’s group fabricated core-shell structured Li_2S nanoparticles with Li_2S as the core and Li_3PS_4 as the shell, functioning as the lithium superionic sulfide (LSS) cathode for lithium-sulfur batteries.¹⁸⁴ which shows an initial discharge capacity of 1216 mAh g^{-1} (based on the

sulfur content) at 60 C, which accounts for a 73% utilization of Li_2S , and still maintains a 70% capacity after 100 cycles.

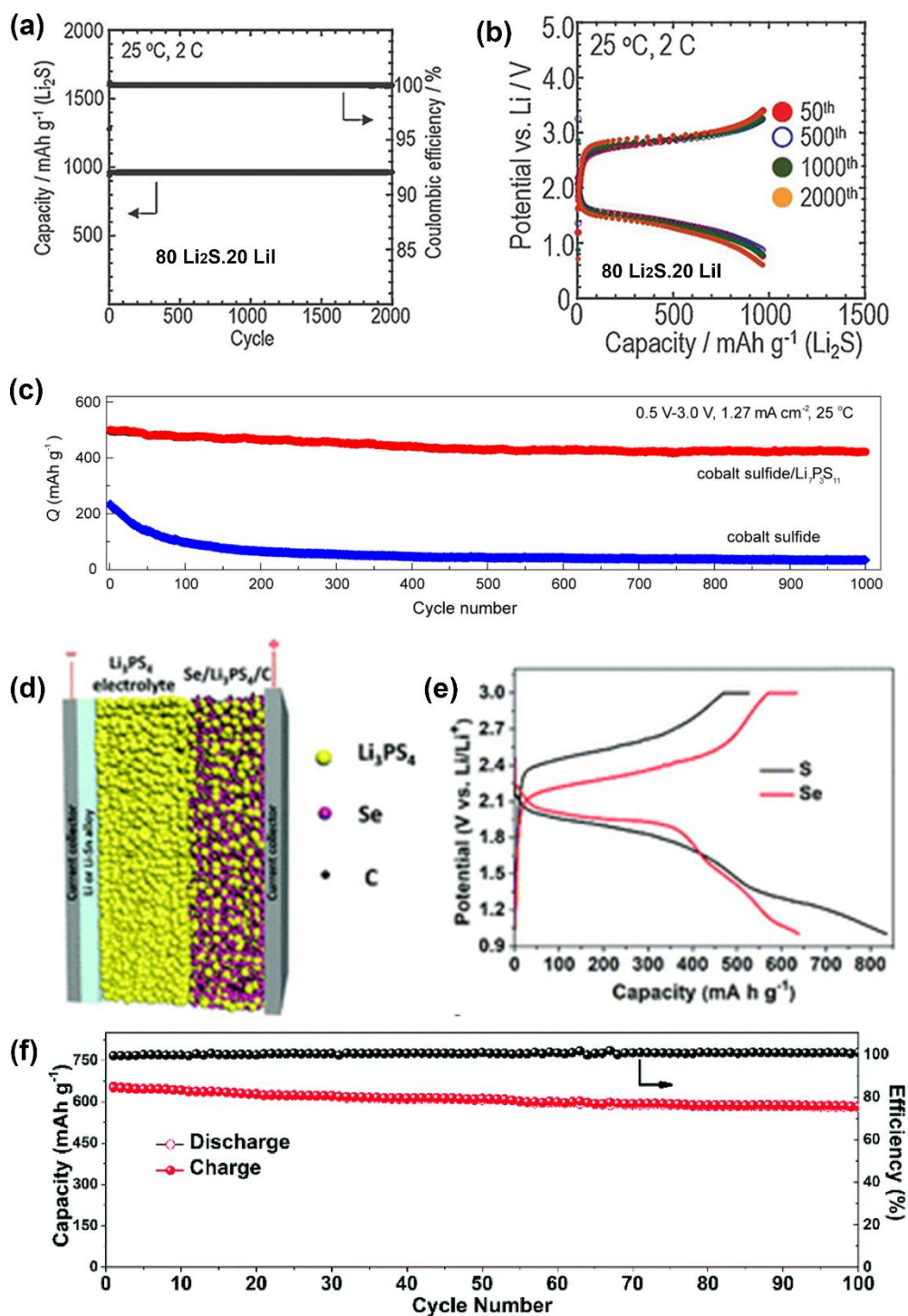


Figure 1- 10 (a). Long-term cycle performance of the cell with 80Li₂S·20LiI electrode materials for 2000 cycles at 2C and (b) its charge-discharge curves. (c) Long term cycling stability of Co₈S₉/Li₇P₃S₁₁ composites at 1.27 mA.cm⁻².⁸⁴ (d) Schematic diagram of an all-solid-state Li–Se battery. (e) Typical discharge/charge profiles of Se and S cathodes in all-solid-state batteries at 50 mA g⁻¹ at room temperature. (f) Cycling performance at 50 mA g⁻¹ and corresponding Coulombic efficiencies of all-solid-state Li-Se batteries.

M. Tatsumisago *et al* demonstrated that using lithium halides (LiCl, LiBr, and LiI) can dramatically improve the utilization of Li₂S in ASSLS batteries. Specifically, 80Li₂S.20LiI can achieve 1100 mAh.g⁻¹ at 0.5C (corresponding to 95% of theoretical capacity) and 980 mAh.g⁻¹ at 2C (**Figure 1-10a and 1-10b**). More impressively, the ASSLS batteries remain 980 mAh.g⁻¹ for 2000 cycles without capacity decay. The cycling performance of the Li-S batteries is the best so far among all the Li-S batteries with not only solid electrolytes but also organic liquid electrolytes.

Beside to elemental sulfur (S₈) and Li₂S, a lot of metal sulfides, such as TiS₂ and CuS, has also been demonstrated in ASSLS batteries, because metals sulfides have a high electronic conductivity than S₈ and Li₂S. Recently, Co₈S₉/Li₇S₃S₁₁ nanocomposites have been rationally designed for ASSLS batteries, which display 1000 cycles at 1.24 mA.cm⁻² at room temperature. (**Figure 1-10c**)

All-solid-state Li-Se batteries have also been demonstrated by our group.¹⁸⁵ Compared to elemental S₈, selenium (Se) possesses a higher electronic conductivity, thus showing great promise in all-solid-state batteries. Se–Li₃PS₄–C is synthesized by ball milling, which is used as the cathode composites for ASS Li-Se batteries (**Figure 1-10d**). Because of the higher electronic conductivity (1×10⁻³ S.cm⁻¹) of Se than that of S₈ (0.5 ×10⁻²⁷ S.cm⁻¹), Se–Li₃PS₄–C cathodes exhibit a smaller polarization than that of S₈ (Figure 9e). Due to the high electronic and ionic conductivity of Se–Li₃PS₄–C cathode

composites, the all-solid-state Li-Se batteries exhibit an initial capacity of 652 mAh.g⁻¹ (corresponding to 96% theoretical capacity), which remains at 585 mAh.g⁻¹ after 100 cycles (**Figure 1-10e**).

As a short summary, to enable high-performance all-solid-state Li-S batteries, first, the insulative nature of S₈ and Li₂S dramatically limits the utilization of active materials. Therefore, improving the electronic conductivity of sulfur cathodes is of great importance to obtain a high reversible capacity of solid-state Li-S batteries. Second, the intimate contact between active materials, carbon additives, and SEs determines the long-term cycling stability of ASSLSBs. In addition, the volume change of sulfur cathode (78%) in ASSLSBs has not been investigated yet. Lithium dendrite formation is also a big challenge facing ASSLSBs, which requires more effort in the near future.

1.5.3. Manufacturing Protocol of Solid-State Lithium Batteries

To transfer the laboratory research to industrial mass production, some scientists and engineers have already examined the viability of ASSLIBs and some promising and practical processes have been demonstrated.^{66, 134, 186} Noticeably, J. Schnell et al thoroughly evaluated the challenges and requirements for the industrial production of ASSLIBs and ASSLMBs via the joint discussion from research institutes, material suppliers, and automotive manufacturers in a workshop.¹⁸⁷ In general, the cathode, the anode, and the SE separator can be made by three steps, including component mixing, lamination, and layer compaction (**Figure 1-11a-c**). Specifically, the cathode composite fabrication process can similar with the conventional electrode fabrication process, in which active materials, solid-state sulfide electrolytes, binders, carbon additives are mixed to make a slurry, which can be tape-casted or extruded on the current collector, following by calendaring and/or sintering process (**Figure 1-11a**). It should be mentioned that core-shell cathode particles should be suggested to avoid the interfacial

reactions between cathode particles and SEs.^{188, 189} For graphite or $\text{Li}_4\text{Ti}_5\text{O}_{12}$ anodes, the fabrication process can be same as the cathode composite process. However, if using Li metal as the anode, the fabrication process should be re-engineered. Potential fabrication protocols for Li metal anodes include extrusion, dip coating, vapor deposition, and electrochemical plating (**Figure 1-11b**), but the cost of these process have not been examined yet. Besides to the cathodes and anode composites, an ultrathin SE separator ($< 50 \mu\text{m}$) is highly required for realizing high-energy-density ASSLIBs comparable to conventional LIBs.¹⁶⁹ **Figure -11c** depicts the fabrication process of thin SE separators, including tape casting, extrusion, and vapor deposition, which is similar to the cathode composition fabrication process, while the substrate may be different. For example, the cathode and anode composition layer can be the substrate for making SE layers.¹⁸⁷ **Figure 1-11d** displays the assembly process of solid-state cells, which includes layer cutting, cell stacking, isostatic pressing, welding, and packaging. Due to the air sensitivity of SEs, the cathode composite and SE separators should be processed in an Ar atmosphere unless air-stable SEs are used, while Li metal should be processed in a dry room because of the chemical sensitivity of Li metal.

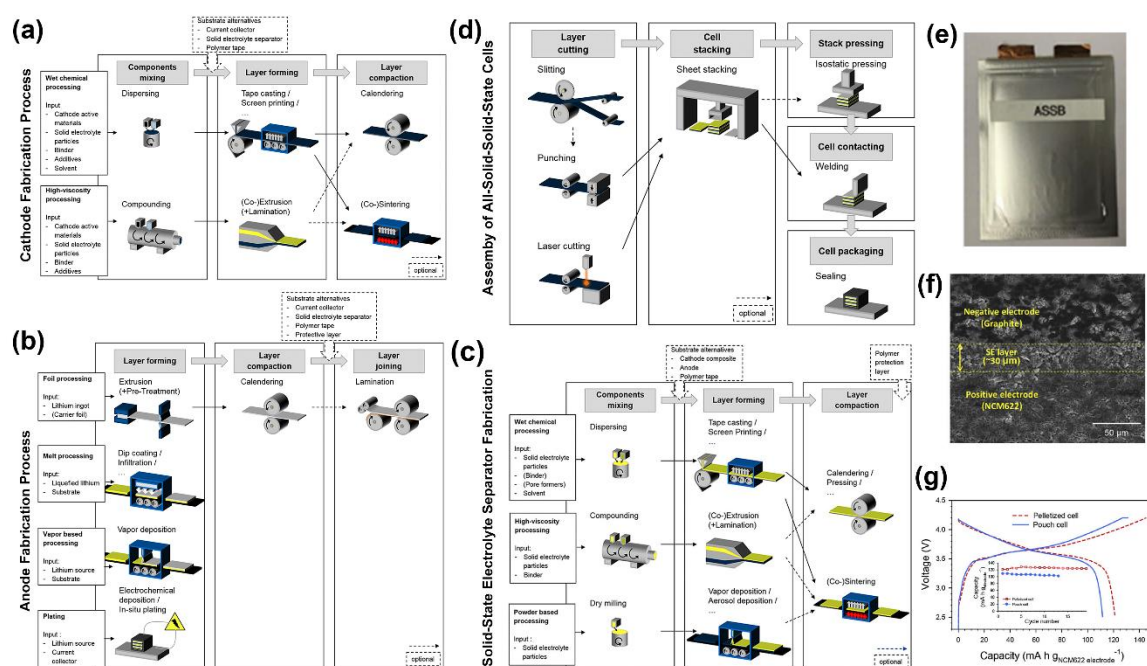


Figure 1-11 (a) Cathode fabrication process. (b) Anode fabrication process. (c) Fabrication process of solid-state electrolyte layer. (d) Assembly process of solid-state batteries. (e) One prototype of SE-based ASSLIBs based NMC622 and Graphite with a dimension of 8 cm × 6 cm. (f) The cross-sectional SEM image of the SE-based ASSLIBs. (g) First-cycle charge-discharge voltage profiles of the pouch-type full-cells at 0.025C.

More importantly, the prototype of pouch cells based on $\text{LiNi}_{0.6}\text{Mn}_{0.2}\text{Co}_{0.2}\text{O}_2$ (NMC622) and graphite has been successfully demonstrated by Y-S Jung's group (Figure 11e).¹⁹⁰ Its cross-sectional SEM image clearly shows that the 30 μm SE layer is sandwiched between NMC622 positive layer and graphite anode layer (Figure 11f). Figure 11g shows the initial charge-discharge curves of pelletized and pouch-type NCM622/graphite full-cells at 0.025C at 25 °C and 30 °C, respectively. The discharge capacities for the pelletized and pouch-type NCM622/graphite full-cells are 121 mAh g^{-1} and 112 mAh g^{-1} , respectively, which is corresponding to 190 Wh kg^{-1} and 184 Wh kg^{-1} based on total weight of the electrodes (active materials, SEs, carbon additives, polymeric binders, and current collectors). The volumetric energy density of the pouch-type full cell is calculated to be 432 Wh L^{-1} . Although the pioneering success in fabrication pouch-cell SE-based ASSLIBs, there are still a lot of engineering challenges remained, such as the selection of solvents, binders, slurry viscosity, quality control, process stability. We believe that with the joint effort from academia and industry SE-based ASSLIB and ASSLMBs can be successfully commercialized with a reasonable cost and high energy density in the near future.

1.6 Thesis Objectives

As thoroughly reviewed above, there are three main challenges impeding the development of ASSLIBs, including (1) insufficient ionic conductivity of solid-state

electrolytes, (2) large interfacial resistance between electrodes and solid electrolytes originating from the insufficient solid-solid contact and detrimental interfacial reactions between electrodes and solid electrolytes, and (3) lithium dendrite growth in ASSLIBs. In order to achieve high-performance all-solid-state batteries, I have devoted significant time to eliminate interfacial resistance as well as suppressing the Li dendrite growth by various strategies at the nanoscale or the molecular level. All the research results can be generally separated into two parts:

Part 1: Developing different strategies to stabilize the cathode interface

- (1) To regulate the interfacial nanostructure, aiming for improving the solid-solid contact as well as minimizing the interfacial reaction. In addition, the relationship between interfacial nanostructure and electrochemical performance will be derived. Furthermore, the functionality of the interfacial layers will be discussed.
- (2) To improve the power density and energy density of ASSLIBs, single-crystal cathodes will be investigated in comparison with polycrystalline counterparts. Moreover, the Li^+ diffusion coefficient between single-crystal cathodes and polycrystalline cathodes will be quantified and compared.
- (3) Furthermore, advanced high-resolution transmission electron microscopy and x-ray photoelectron spectroscopy are employed to understand the interfacial reactions between single-crystal NMC532 and sulfide electrolytes. The underlying mechanism of interfacial reactions and structure change of layered oxide cathodes will be discussed.
- (4) To understand the interfacial Li^+ transport kinetics across the coating layer itself, the interfacial coating with various ionic conductivities will be engineered. Then the relationship between the interfacial Li^+ conductivity and electrochemical performance of ASSLIBs can be discussed.

- (5) To enhance the interfacial Li^+ transport kinetics, a halide electrolyte (Li_3InCl_6) will be used as the coating layer for ASSLIBs, aiming at improving the solid-solid contact and minimizing interfacial reactions.

Part 2: Developing different strategies to stabilize the anode interface

- (6) A molecular layer deposition is able to deposit an organic and inorganic hybrid thin film on Li metal surface, thus a buffer layer can be successfully built between the Li metal and solid electrolyte. Based on this, ASSLMBs can be fabricated with improved cycling life and capacity.
- (7) A plastic crystal electrolyte is investigated to suppress interfacial reactions and lithium dendrite growth between sulfide electrolytes and lithium metal anodes. In addition, solid-solid contact between electrodes and solid electrolytes can be improved by the solid-liquid transformability of the plastic crystal electrolyte.
- (8) To improve the ionic contact between oxide electrolytes and lithium metal, a solid-liquid interface can be developed, which can prevent the reduction of oxide solid electrolytes by lithium metal. In addition, the properties of solid-liquid electrolyte interphase are discussed in detail.

1.7 Thesis Organization

This thesis consists of 11 chapters (one introductory chapter, one experimental and characterization details, eight articles plus one conclusive chapter) and satisfies the requirements on Integrated-Article form as outlined in the *Thesis Regulation Guide* by the School of Graduate and Postdoctoral Studies (SGPS) of the University of Western Ontario. Specifically, it organizes according to the following sequence:

Chapter 1 gives an introduction to the motivation to develop ASSLIBs, the current status of solid-state electrolytes and their chemical/electrochemical stability. In addition,

cathode/anode interfacial challenges and proposed strategies, as well as the demonstration of ASSLIBs and all-solid-state Li-S batteries, are presented. Finally, the research objectives and organization of the thesis are illustrated.

Chapter 2 outlines the experimental details of ASSLIBs, including methods to modify the cathode and anode interface and the synthesis of solid-state electrolytes. The characterization tools for physical-chemical and electrochemical properties are listed as well.

Chapter 3 illustrates the effect of the interfacial nanostructure of the cathode composite on the electrochemical of ASSLIBs, in which dual-core-shell interfacial nanostructure was realized by combining atomic layer deposition and wet-chemistry dispersion process. Due to the dual-core-shell nanostructure design, in which the inner layer preventing the interfacial reaction while the outer layer improving the solid-solid contact between cathode materials and sulfide electrolytes, ASSLIBs demonstrated the excellent electrochemical performance. This work highlights the importance of interfacial nanostructure in all-solid-state batteries.

Chapter 4 shows the different electrochemical performance of single-crystal cathode and polycrystalline cathodes. By quantifying the Li^+ diffusion coefficient, it is found that the single-crystal $\text{LiNi}_{0.5}\text{Mn}_{0.3}\text{Co}_{0.2}\text{O}_2$ exhibits a 6~14 times higher Li^+ diffusion coefficient. As a result, the single-crystal $\text{LiNi}_{0.5}\text{Mn}_{0.3}\text{Co}_{0.2}\text{O}_2$ -based ASSLIBs demonstrated both high-power density and high energy density.

Chapter 5 investigates the mechanism of interfacial reactions between $\text{LiNi}_{0.5}\text{Mn}_{0.3}\text{Co}_{0.2}\text{O}_2$ and sulfide electrolytes. It is found that oxygen loss from the layered oxide cathodes is a trigger for the interfacial reactions, which in turn induces the interfacial structural change from a layered structure to rocksalt structure. Fortunately, the interfacial coating was demonstrated to be effective in mitigating the interfacial

reactions.

Chapter 6 deciphers the effect of interfacial ionic conductivity of a coating layer on the electrochemical performance. The detailed interracial Li^+ transport kinetics are discussed in this part, which highlights the importance of improving interfacial Li^+ conductivity toward the high-performance ASSLIBs.

Chapter 7 reports an in-situ growth of Li_3InCl_6 on the LiCoO_2 surface. Due to excellent wide electrochemical windows and high-ionic conductivity, Li_3InCl_6 -coated LiCoO_2 exhibits both long cycle life and high rate performance. In addition, the interfacial interaction between Li_3InCl_6 and LiCoO_2 is also investigated in this part.

Chapter 8 employs molecular layer deposition (MLD) to develop an inorganic-organic hybrid interlayer (alucone) at the interface between the Li metal and SEs. It is found that the alucone layer can serve as an artificial solid electrolyte interphase (SEI). As a result, interfacial reactions between Li and SEs are significantly suppressed by intrinsically blocking electron transfer at the interface. In addition, lithium dendrites are suppressed. Coupled with a LiCoO_2 cathode, ASSLMBs with 30 MLD cycles of alucone on Li metal exhibit a high initial capacity of 120 mAh g^{-1} and can retain a capacity of 60 mAh g^{-1} after 150 cycles. This work exemplifies the use of MLD to stabilize the interface between SEs and Li metal for ASSLMBs.

Chapter 9 describes a solid-state plastic crystal electrolyte (PCE) as an interlayer in SE-based ASSLMBs. It is demonstrated that the PCE interlayer can prevent interfacial reactions and lithium dendrite formation between SEs and Li metal. As a result, ASSLMBs with LiFePO_4 exhibit a high initial capacity of 148 mAh.g^{-1} at 0.1 C and 131 mAh.g^{-1} at 0.5 C ($1\text{C}=170 \text{ mA.g}^{-1}$), which remains at 122 mAh.g^{-1} after 120 cycles at 0.5C. All-solid-state Li-S batteries based on the polyacrylonitrile-sulfur composite are also demonstrated, showing an initial capacity of 1682 mAh.g^{-1} . The second discharge

capacity of 890 mAh.g⁻¹ keeps at 775 mAh.g⁻¹ after 100 cycles. This work provides a new avenue to address the interfacial challenges between Li metal and SEs, enabling the successful adoption of Li metal in sulfide-based all-solid-state lithium metal batteries with high energy density.

Chapter 10 quantifies the amount of LE at the interface, which is used to eliminate the large interfacial resistance. It is found that as little as 2 μ l of LE at the interface can successfully enable a hybrid LiFePO₄/LATP/Li battery with a specific capacity of 125 mAh g⁻¹ at 1C and 98 mAh g⁻¹ at 4C. Excess LE has no further contribution to the electrochemical performance. Furthermore, the rigid SSE could suppress the formation of lithium dendrites, especially in the case with a high cathode loading (9.1 mg.cm⁻²), suggesting the feasibility of high energy density SSLBs using Li metal anodes. The interfacial analysis reveals that an interfacial solid-liquid electrolyte interphase (SLEI) was formed at the interface, preventing the reduction of LATP by Li metal, thus ensuring the long-term durability of LATP in LE.

Chapter 11 summarizes the results and contributions of the thesis work and provides an outlook on all-solid-state lithium batteries.

The structure of the research work in this thesis is illustrated in the following figure.

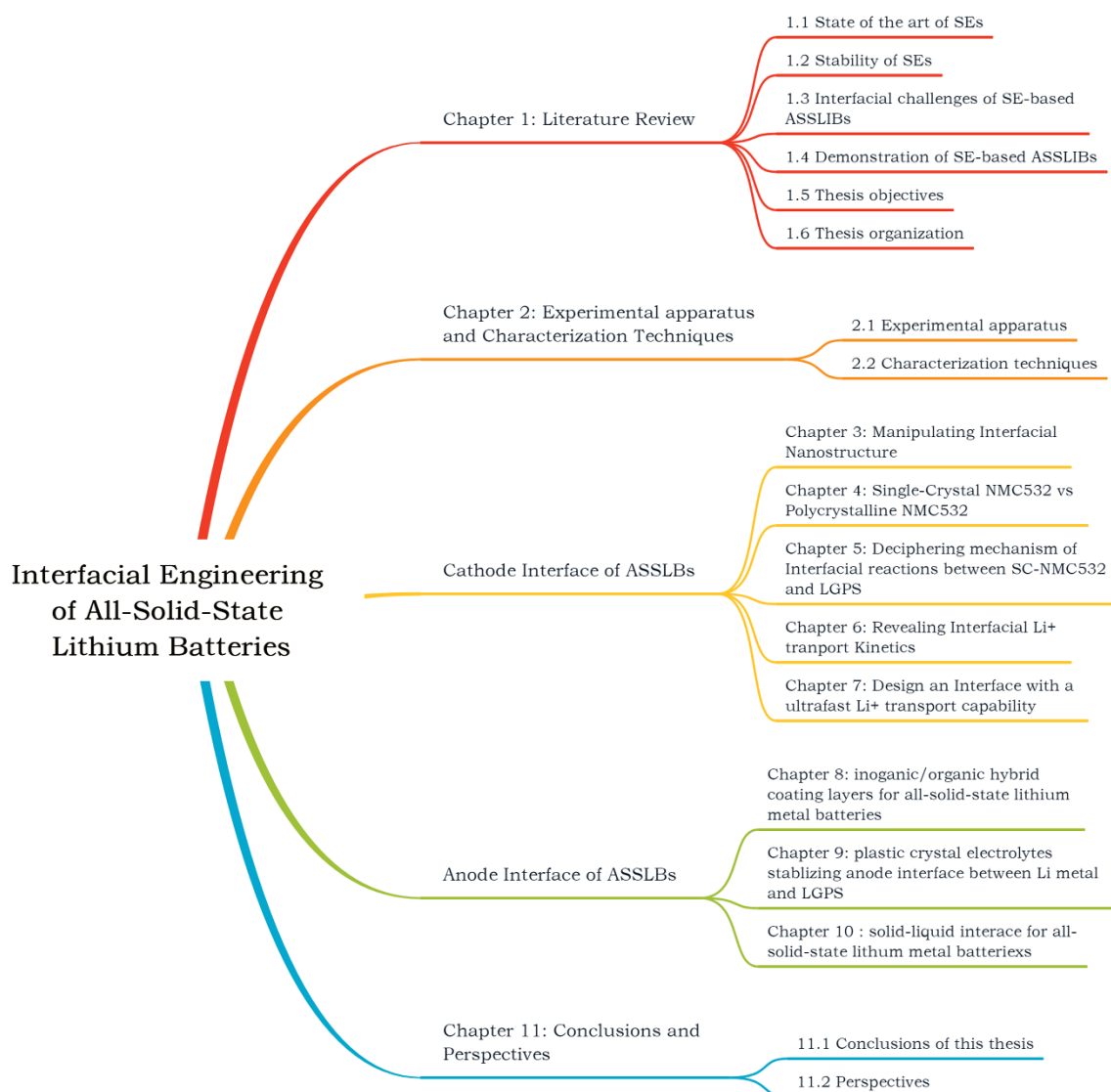


Figure 1-12 The structure of this thesis.

1.8 References

1. J. M. Tarascon and M. Armand, *Nature*, 2001, **414**, 359-367.
2. T. Yim, C. Y. Choi, J. Mun, S. M. Oh and Y. G. Kim, *Molecules*, 2009, **14**, 1840-1851.

3. K. Xu, *Chem. Rev.*, 2004, **104**, 4303-4418.
4. J. W. Choi and D. Aurbach, *Nat. Rev. Mater.*, 2016, **1**, 16013.
5. Y. Zhao, K. Zheng and X. Sun, *Joule*, 2018, 1-22.
6. A. Manthiram, X. Yu and S. Wang, *Nat. Rev. Mater.*, 2017, **2**, 16103.
7. P. K. Ho, B. Qiang, K. D. Hyeon, O. D. Yang, Z. Yizhou, M. Yifei and J. Y. Seok, *Adv. Energy Mater.*, 2018, **0**, 1800035.
8. Y. Kato, S. Hori, T. Saito, K. Suzuki, M. Hirayama, A. Mitsui, M. Yonemura, H. Iba and R. Kanno, *Nat. Energy*, 2016, **1**, 16030.
9. N. Kamaya, K. Homma, Y. Yamakawa, M. Hirayama, R. Kanno, M. Yonemura, T. Kamiyama, Y. Kato, S. Hama, K. Kawamoto and A. Mitsui, *Nat. Mater.*, 2011, **10**, 682-686.
10. A. Hayashi, A. Sakuda and M. Tatsumisago, *Frontiers in Energy Research*, 2016, **4**.
11. J. C. Bachman, S. Muy, A. Grimaud, H.-H. Chang, N. Pour, S. F. Lux, O. Paschos, F. Maglia, S. Lupart, P. Lamp, L. Giordano and Y. Shao-Horn, *Chem. Rev.*, 2016, **116**, 140-162.
12. T. Baba and Y. Kawamura, *Frontiers in Energy Research*, 2016, **4**.
13. F. Mizuno, A. Hayashi, K. Tadanaga and M. Tatsumisago, *Adv. Mater.*, 2005, **17**, 918-921.
14. Y. Wang, W. D. Richards, S. P. Ong, L. J. Miara, J. C. Kim, Y. Mo and G. Ceder, *Nat Mater*, 2015, **14**, 1026-1031.

15. V. Thangadurai, S. Narayanan and D. Pinzaru, *Chem. Soc. Rev.*, 2014, **43**, 4714-4727.
16. R. J. Chen, W. J. Qu, X. Guo, L. Li and F. Wu, *Mater. Horizons*, 2016, **3**, 487-516.
17. Y. Sun, K. Suzuki, S. Hori, M. Hirayama and R. Kanno, *Chem. Mater.*, 2017, **29**, 5858-5864.
18. P. Bron, S. Johansson, K. Zick, J. Schmedt auf der Günne, S. Dehnen and B. Roling, *J. Amer. Chem. Soc.*, 2013, **135**, 15694-15697.
19. P. Zhou, J. Wang, F. Cheng, F. Li and J. Chen, *Chem. Commun.*, 2016, **52**, 6091-6094.
20. Y. Kato, S. Hori, T. Saito, K. Suzuki, M. Hirayama, A. Mitsui, M. Yonemura, H. Iba and R. Kanno, *Nature Energy*, 2016, **1**, 16030.
21. O. Kwon, M. Hirayama, K. Suzuki, Y. Kato, T. Saito, M. Yonemura, T. Kamiyama and R. Kanno, *Journal of Materials Chemistry A*, 2015, **3**, 438-446.
22. R. Kanno and M. Murayama *J. Electrochem. Soc.*, 2001, **148**, A742-A746.
23. Y. Sun, K. Suzuki, S. Hori, M. Hirayama and R. Kanno, *Chem. Mat.*, 2017, **29**, 5858-5864.
24. M. A. Kraft, S. Ohno, T. Zinkevich, R. Koerver, S. P. Culver, T. Fuchs, A. Senyshyn, S. Indris, B. J. Morgan and W. G. Zeier, *J. Am. Chem. Soc.*, 2018, **140**, 16330-16339.
25. R. P. Rao and S. Adams, *physica status solidi (a)*, 2011, **208**, 1804-1807.
26. S. Boulineau, M. Courty, J.-M. Tarascon and V. Viallet, *Solid State Ion.*, 2012, **221**, 1-5.

27. Y. Inoue, K. Suzuki, N. Matsui, M. Hirayama and R. Kanno, *Journal of Solid State Chemistry*, 2017, **246**, 334-340.
28. G. Sahu, Z. Lin, J. Li, Z. Liu, N. Dudney and C. Liang, *Energy Environ. Sci.*, 2014, **7**, 1053-1058.
29. Y. Seino, T. Ota, K. Takada, A. Hayashi and M. Tatsumisago, *Energy Environ. Sci.*, 2014, **7**, 627-631.
30. K. Minami, A. Hayashi and M. Tatsumisago, *Solid State Ion.*, 2008, **179**, 1282-1285.
31. A. Hayashi, S. Hama, H. Morimoto, M. Tatsumisago and T. Minami, *Journal of the American Ceramic Society*, 2001, **84**, 477-479.
32. M. Murayama, R. Kanno, M. Irie, S. Ito, T. Hata, N. Sonoyama and Y. Kawamoto, *Journal of Solid State Chemistry*, 2002, **168**, 140-148.
33. M. Murayama, R. Kanno, Y. Kawamoto and T. Kamiyama, *Solid State Ion.*, 2002, **154-155**, 789-794.
34. R. Kanno, M. Murayama and K. Sakamoto, in *Solid State Ion.*, 2002, DOI: doi:10.1142/9789812776259_0003, pp. 13-22.
35. M. Murayama, N. Sonoyama, A. Yamada and R. Kanno, *Solid State Ion.*, 2004, **170**, 173-180.
36. T. Inada, T. Kobayashi, N. Sonoyama, A. Yamada, S. Kondo, M. Nagao and R. Kanno, *J. Power Sources*, 2009, **194**, 1085-1088.
37. K. Minami, A. Hayashi, S. Ujiie and M. Tatsumisago, *Solid State Ion.*, 2011, **192**, 122-125.

38. H. Muramatsu, A. Hayashi, T. Ohtomo, S. Hama and M. Tatsumisago, *Solid State Ion.*, 2011, **182**, 116-119.
39. I.-H. Chu, H. Nguyen, S. Hy, Y.-C. Lin, Z. Wang, Z. Xu, Z. Deng, Y. S. Meng and S. P. Ong, *ACS Applied Materials & Interfaces*, 2016, **8**, 7843-7853.
40. E. Rangasamy, Z. Liu, M. Gobet, K. Pilar, G. Sahu, W. Zhou, H. Wu, S. Greenbaum and C. Liang, *J. Amer. Chem. Soc.*, 2015, **137**, 1384-1387.
41. Y. Zhu, X. He and Y. Mo, *Journal of Materials Chemistry A*, 2016, **4**, 3253-3266.
42. B. R. Shin, Y. J. Nam, D. Y. Oh, D. H. Kim, J. W. Kim and Y. S. Jung, *Electrochim. Acta*, 2014, **146**, 395.
43. Y. Kato, R. Saito, M. Sakano, A. Mitsui, M. Hirayama and R. Kanno, *J. Power Sources*, 2014, **271**, 60.
44. S. Hori, K. Suzuki, M. Hirayama, Y. Kato, T. Saito, M. Yonemura and R. Kanno, *Faraday Discuss.*, 2014, **176**, 83-94.
45. O. Kwon, M. Hirayama, K. Suzuki, Y. Kato, T. Saito, M. Yonemura, T. Kamiyama and R. Kanno, *J. Mater. Chem. A*, 2015, **3**, 438.
46. Y. Mo, S. P. Ong and G. Ceder, *Chem. Mat.*, 2012, **24**, 15-17.
47. A. Kuhn, V. Duppel and B. V. Lotsch, *Energy Environ. Sci.*, 2013, **6**, 3548.
48. W. D. Richards, T. Tsujimura, L. J. Miara, Y. Wang, J. C. Kim, S. P. Ong, I. Uechi, N. Suzuki and G. Ceder, *Nature Communications*, 2016, **7**, 11009.
49. Z. Yu, S.-L. Shang, D. Wang, Y. C. Li, H. P. Yennawar, G. Li, H.-T. Huang, Y. Gao, T. E. Mallouk, Z.-K. Liu and D. Wang, *Energy Storage Materials*, 2019, **17**, 70-77.

50. X. He, Y. Zhu and Y. Mo, *Nature Communications*, 2017, **8**, 15893.
51. S. P. Ong, Y. Mo, W. D. Richards, L. Miara, H. S. Lee and G. Ceder, *Energy Environ. Sci.*, 2013, **6**, 148-156.
52. I. Tarhouchi, V. Viallet, P. Vinatier and M. Ménétrier, *Solid State Ion.*, 2016, **296**, 18-25.
53. P. Bron, S. Johansson, K. Zick, J. Schmedt auf der Günne, S. Dehnen and B. Roling, *Journal of the American Chemical Society*, 2013, **135**, 15694-15697.
54. R. B. Beeken, J. J. Garbe, J. M. Gillis, N. R. Petersen, B. W. Podoll and M. R. Stoneman, *J. Phys. Chem. Solids*, 2005, **66**, 882-886.
55. H. M. Chen, C. Maohua and S. Adams, *Phys. Chem. Chem. Phys.*, 2015, **17**, 16494-16506.
56. H.-J. Deiseroth, S.-T. Kong, H. Eckert, J. Vannahme, C. Reiner, T. Zaiß and M. Schlosser, *Angew. Chem. Int. Ed.*, 2008, **47**, 755-758.
57. P. R. Rayavarapu, N. Sharma, V. K. Peterson and S. Adams, *Journal of Solid State Electrochemistry*, 2012, **16**, 1807-1813.
58. S.-T. Kong, H.-J. Deiseroth, C. Reiner, Ö. Gün, E. Neumann, C. Ritter and D. Zahn, *Chem. Eur. J* 2010, **16**, 2198-2206.
59. S. T. Kong, Ö. Gün, B. Koch, H. J. Deiseroth, H. Eckert and C. Reiner, *Chem. Eur. J* 2010, **16**, 5138-5147.
60. O. Pecher, S.-T. Kong, T. Goebel, V. Nickel, K. Weichert, C. Reiner, H.-J. Deiseroth, J. Maier, F. Haarmann and D. Zahn, *Chem. Eur. J*, 2010, **16**, 8347-8354.

61. H.-J. Deiseroth, J. Maier, K. Weichert, V. Nickel, S.-T. Kong and C. Reiner, *Z. Anorg. Allg. Chem.*, 2011, **637**, 1287-1294.
62. F. Stadler and C. Fietzek, *ECS Trans.*, 2010, **25**, 177-183.
63. N. J. J. de Klerk, I. Rosłoń and M. Wagemaker, *Chem. Mater.*, 2016, **28**, 7955-7963.
64. H. Fudong, Y. Jie, Z. Xiangyang and W. Chunsheng, *Adv. Energy Mater.*, 2018, **0**, 1703644.
65. D. A. Ziolkowska, W. Arnold, T. Druffel, M. Sunkara and H. Wang, *ACS Applied Materials & Interfaces*, 2019, DOI: 10.1021/acsami.8b19181.
66. K. H. Park, Q. Bai, D. H. Kim, D. Y. Oh, Y. Zhu, Y. Mo and Y. S. Jung, *Adv. Energy Mater.*, 2018, **8**, 1800035.
67. L. Zhou, K.-H. Park, X. Sun, F. Lalère, T. Adermann, P. Hartmann and L. F. Nazar, *ACS Energy Lett.*, 2018, DOI: 10.1021/acsenergylett.8b01997, 265-270.
68. M. Tatsumisago and A. Hayashi, *Solid State Ion.*, 2012, **225**, 342-34569. N. Machida, H. Maeda, H. Peng and T. Shigematsu, *J. Electrochem. Soc.*, 2002, **149**, A688-A693.
70. A. Hayashi, *J. Ceram. Soc. Jpn.*, 2007, **115**, 110-117.
71. K. Minami, A. Hayashi and M. Tatsumisago, *J. Ceram. Soc. Jpn.*, 2010, **118**, 305-308.
72. M. Tatsumisago, T. Saito and T. Minami, *Thermochimica Acta*, 1996, **280**, 333-341.
73. M. Tatsumisago, T. Saito and T. Minami, *Chemistry Letters*, 2001, **30**, 790-791.

74. M. Tatsumisago, S. Hama, A. Hayashi, H. Morimoto and T. Minami, *Solid State Ion.*, 2002, **154–155**, 635-640.
75. K. Takada, N. Aotani, K. Iwamoto and S. Kondo, *Solid State Ion.*, 1996, **86**, 877-882.
76. R. Komiya, A. Hayashi, H. Morimoto, M. Tatsumisago and T. Minami, *Solid State Ion.*, 2001, **140**, 83-87.
77. A. Hayashi, K. Minami, S. Ujiie and M. Tatsumisago, *J. Non-Cryst. Solids*, 2010, **356**, 2670-2673.
78. H. Yamane, M. Shibata, Y. Shimane, T. Junke, Y. Seino, S. Adams, K. Minami, A. Hayashi and M. Tatsumisago, *Solid State Ion.*, 2007, **178**, 1163-1167.
79. Z. Liu, W. Fu, E. A. Payzant, X. Yu, Z. Wu, N. J. Dudney, J. Kiggans, K. Hong, A. J. Rondinone and C. Liang, *J. Amer. Chem. Soc.*, 2013, **135**, 975-978.
80. R. Makiura, T. Yonemura, T. Yamada, M. Yamauchi, R. Ikeda, H. Kitagawa, K. Kato and M. Takata, *Nat Mater*, 2009, **8**, 476-480.
81. M. Tachez, J.-P. Malugani, R. Mercier and G. Robert, *Solid State Ion.*, 1984, **14**, 181-185.
82. K. Homma, M. Yonemura, T. Kobayashi, M. Nagao, M. Hirayama and R. Kanno, *Solid State Ion.*, 2011, **182**, 53-58.
83. Y. G. Guo, J. S. Lee and J. Maier, *Adv. Mater.*, 2005, **17**, 2815-2819.
84. X. Yao, D. Liu, C. Wang, P. Long, G. Peng, Y.-S. Hu, H. Li, L. Chen and X. Xu, *Nano Lett.*, 2016, DOI: 10.1021/acs.nanolett.6b03448.
85. Q. Zhang, H. Wan, G. Liu, Z. Ding, J. P. Mwizerwa and X. Yao, *Nano Energy*, 2019, **57**, 771-782.

86. A. Banerjee, K. H. Park, J. W. Heo, Y. J. Nam, C. K. Moon, S. M. Oh, S.-T. Hong and Y. S. Jung, *Angew. Chem. Int. Ed.*, 2016, **55**, 9634-9638.
87. H. Wang, Y. Chen, Z. D. Hood, G. Sahu, A. S. Pandian, J. K. Keum, K. An and C. Liang, *Angew. Chem. Int. Ed.*, 2016, **55**, 8551-8555.
88. T. Ohtomo, A. Hayashi, M. Tatsumisago and K. Kawamoto, *J. Mater. Sci.*, 2013, **48**, 4137-4142.
89. G. Liu, D. Xie, X. Wang, X. Yao, S. Chen, R. Xiao, H. Li and X. Xu, *Energy Storage Mater.*, 2018, DOI: <https://doi.org/10.1016/j.ensm.2018.07.008>.
90. Z. Zhang, L. Zhang, X. Yan, H. Wang, Y. Liu, C. Yu, X. Cao, L. van Eijck and B. Wen, *J. Power Sources*, 2019, **410-411**, 162-170.
91. F. D. Han, Y. Z. Zhu, X. F. He, Y. F. Mo and C. S. Wang, *Adv. Energy Mater.*, 2016, **6**, 9.
92. S. Hori, K. Suzuki, M. Hirayama, Y. Kato and R. Kanno, *Frontiers in Energy Research*, 2016, **4**.
93. F. Wu, W. Fitzhugh, L. Ye, J. Ning and X. Li, *Nat. Commun.*, 2018, **9**, 4037.
94. C. Chen and X. Guo, *Acta Chim Slov.*, 2016, **63**, 489.
95. W. D. Richards, L. J. Miara, Y. Wang, J. C. Kim and G. Ceder, *Chem. Mater.*, 2016, **28**, 266-273.
96. J. Haruyama, K. Sodeyama, L. Y. Han, K. Takada and Y. Tateyama, *Chem. Mater.*, 2014, **26**, 4248-4255.
97. A. Sakuda, A. Hayashi and M. Tatsumisago, *Chem. Mater.*, 2010, **22**, 949-956.

98. M. Sumita, Y. Tanaka, M. Ikeda and T. Ohno, *J. Phys. Chem. C*, 2016, **120**, 13332-13339.
99. K. Takada, N. Ohta, L. Q. Zhang, X. X. Xu, B. T. Hang, T. Ohnishi, M. Osada and T. Sasaki, *Solid State Ion.*, 2012, **225**, 594-597.
100. C. Chen and X. Guo, *Acta chimica Slovenica*, 2016, **63**, 489-495.
101. D. Y. Oh, Y. J. Nam, K. H. Park, S. H. Jung, K. T. Kim, A. R. Ha and Y. S. Jung, *Adv. Energy Mater.*, 2019, **0**, 1802927.
102. C. Wagner, *Journal of Physics and Chemistry of Solids*, 1972, **33**, 1051-1059.
103. J. Maier, *Nat Mater*, 2005, **4**, 805-815.
104. J.-F. Wu and X. Guo, *Physical Chemistry Chemical Physics*, 2017, **19**, 5880-5887.
105. K. Takada, *Langmuir*, 2013, **29**, 7538-7541.
106. K. Takada and T. Ohno, *Front. Energy Res.*, 2016, **4**.
107. K. Yoon, J.-J. Kim, W. M. Seong, M. H. Lee and K. Kang, *Scientific reports*, 2018, **8**.
108. W. Zhang, T. Leichtweiß, S. P. Culver, R. Koerver, D. Das, D. A. Weber, W. G. Zeier and J. Janek, *ACS Appl. Mater. Interfaces*, 2017, **9**, 35888–35896.
109. M. Haruta, S. Shiraki, T. Suzuki, A. Kumatani, T. Ohsawa, Y. Takagi, R. Shimizu and T. Hitosugi, *Nano Letters*, 2015, **15**, 1498-1502.
110. N. J. J. de Klerk and M. Wagemaker, *ACS Applied Energy Materials*, 2018, **1**, 5609-5618.

111. J. Haruyama, K. Sodeyama and Y. Tateyama, *ACS Applied Materials & Interfaces*, 2017, **9**, 286-292.
112. Y. Zhu, X. He and Y. Mo, *ACS Applied Materials & Interfaces*, 2015, **7**, 23685-23693.
113. J. Auvergniot, A. Cassel, J.-B. Ledeuil, V. Viallet, V. Seznec and R. Dedryvère, *Chem. Mater.*, 2017, **29**, 3883-3890.
114. W. Zhang, F. H. Richter, S. P. Culver, T. Leichtweiss, J. G. Lozano, C. Dietrich, P. G. Bruce, W. G. Zeier and J. Janek, *ACS Appl. Mater. Interfaces*, 2018, **10**, 22226-22236.
115. R. Koerver, I. Aygün, T. Leichtweiß, C. Dietrich, W. Zhang, J. O. Binder, P. Hartmann, W. G. Zeier and J. Janek, *Chem. Mater.*, 2017, **19**, 5574-5582.
116. K. Takada, T. Ohno, N. Ohta, T. Ohnishi and Y. Tanaka, *ACS Energy Letters*, 2017, **3**, 98-103.
117. N. Ohta, K. Takada, I. Sakaguchi, L. Zhang, R. Ma, K. Fukuda, M. Osada and T. Sasaki, *Electrochemistry Communications*, 2007, **9**, 1486-1490.
118. N. Ohta, K. Takada, L. Zhang, R. Ma, M. Osada and T. Sasaki, *Adv. Mater.*, 2006, **18**, 2226-2229.
119. A. Sakuda, H. Kitaura, A. Hayashi, K. Tadanaga and M. Tatsumisago, *J. Electrochem. Soc.*, 2009, **156**, A27-A32.
120. Y. Zhu, X. He and Y. Mo, *J. Mater. Chem. A*, 2016, **4**, 3253-3266.
121. B. Wang, Y. Zhao, M. N. Banis, Q. Sun, K. R. Adair, R. Li, T.-K. Sham and X. Sun, *ACS Appl. Mater. Interfaces*, 2018, **10**, 1654-1661.

122. B. Wang, J. Liu, M. Norouzi Banis, Q. Sun, Y. Zhao, R. Li, T.-K. Sham and X. Sun, *ACS Appl. Mater. Interfaces*, 2017, **9**, 31786-31793.
123. J. Liu, M. N. Banis, X. Li, A. Lushington, M. Cai, R. Li, T.-K. Sham and X. Sun, *The Journal of Physical Chemistry C*, 2013, **117**, 20260-20267.
124. B. Wang, J. Liu, Q. Sun, R. Li, T.-K. Sham and X. Sun, *Nanotechnology*, 2014, **25**, 504007.
125. X. Meng, J. Liu, X. Li, M. N. Banis, J. Yang, R. Li and X. Sun, *RSC Advances*, 2013, **3**, 7285-7288.
126. Y. Xiao, L. J. Miara, Y. Wang and G. Ceder, *Joule*, 2019, **3**, 1-24.
127. A. Sakuda, H. Kitaura, A. Hayashi, K. Tadanaga and M. Tatsumisago, *J. Electrochem. Soc.*, 2009, **156**, A27-A32.
128. K. Takada, N. Ohta, L. Zhang, K. Fukuda, I. Sakaguchi, R. Ma, M. Osada and T. Sasaki, *Solid State Ion.*, 2008, **179**, 1333-1337.
129. J. H. Woo, J. E. Trevey, A. S. Cavanagh, Y. S. Choi, S. C. Kim, S. M. George, K. H. Oh and S.-H. Lee, *J. Electrochem. Soc.*, 2012, **159**, A1120-A1124.
130. G. Oh, M. Hirayama, O. Kwon, K. Suzuki and R. Kanno, *Chem. Mat.*, 2016, **28**, 2634-2640.
131. S. Ito, S. Fujiki, T. Yamada, Y. Aihara, Y. Park, T. Y. Kim, S.-W. Baek, J.-M. Lee, S. Doo and N. Machida, *J. Power Sources*, 2014, **248**, 943-950.
132. K. Aso, A. Sakuda, A. Hayashi and M. Tatsumisago, *ACS Applied Materials & Interfaces*, 2013, **5**, 686-690.

133. Y. E. Choi, K. H. Park, D. H. Kim, D. Y. Oh, H. R. Kwak, Y.-G. Lee and Y. S. Jung, *ChemSusChem*, 2017, **10**, 2605-2611.
134. D. H. Kim, D. Y. Oh, K. H. Park, Y. E. Choi, Y. J. Nam, H. A. Lee, S.-M. Lee and Y. S. Jung, *Nano Lett.*, 2017, **17**, 3013-3020.
135. C. Wang, Q. Sun, Y. Liu, Y. Zhao, X. Li, X. Lin, M. N. Banis, M. Li, W. Li, K. R. Adair, D. Wang, J. Liang, R. Li, L. Zhang, R. Yang, S. Lu and X. Sun, *Nano Energy*, 2018, **48**, 35-43.
136. D. Y. Oh, Y. J. Nam, K. H. Park, S. H. Jung, S.-J. Cho, Y. K. Kim, Y.-G. Lee, S.-Y. Lee and Y. S. Jung, *Adv. Energy Mater.*, 2015, **5**, 1500865.
137. C. Wang, K. R. Adair, J. Liang, X. Li, Y. Sun, X. Li, J. Wang, Q. Sun, F. Zhao, X. Lin, R. Li, H. Huang, L. Zhang, R. Yang, S. Lu and X. Sun, *Adv. Funct. Mater.*, 2019, **1900392**, DOI:10.1002/adfm.201900392.
138. Y. J. Nam, S. J. Cho, D. Y. Oh, J. M. Lim, S. Y. Kim, J. H. Song, Y. G. Lee, S. Y. Lee and Y. S. Jung, *Nano Letters*, 2015, **15**, 3317-3323.
139. K. H. Park, D. Y. Oh, Y. E. Choi, Y. J. Nam, L. Han, J.-Y. Kim, H. Xin, F. Lin, S. M. Oh and Y. S. Jung, *Adv. Mater.*, 2016, **28**, 1874-1883.
140. D. Y. Oh, D. H. Kim, S. H. Jung, J.-G. Han, N.-S. Choi and Y. S. Jung, *Journal of Materials Chemistry A*, 2017, **5**, 20771-20779.
141. H. Chen, C. Wang, W. Dong, W. Lu, Z. Du and L. Chen, *Nano letters*, 2014, **15**, 798-802.
142. G. Girishkumar, B. McCloskey, A. C. Luntz, S. Swanson and W. Wilcke, *J. Phys. Chem. Lett.*, 2010, **1**, 2193-2203.

143. P. G. Bruce, S. A. Freunberger, L. J. Hardwick and J.-M. Tarascon, *Nat Mater*, 2012, **11**, 19-29.
144. X. L. Ji, K. T. Lee and L. F. Nazar, *Nat. Mater.*, 2009, **8**, 500-506.
145. Y. Sun, N. Liu and Y. Cui, *Nat. Energy*, 2016, DOI: 10.1038/nenergy.2016.71, 16071.
146. Y. Li, W. Zhou, X. Chen, X. Lü, Z. Cui, S. Xin, L. Xue, Q. Jia and J. B. Goodenough, *Proc. Natl. Acad. Sci. U.S.A.*, 2016, DOI: 10.1073/pnas.1615912113.
147. S. Wenzel, S. Randau, T. Leichtweiß, D. A. Weber, J. Sann, W. G. Zeier and J. Janek, *Chem. Mater.*, 2016, **28**, 2400-2407.
148. F. Han, A. S. Westover, J. Yue, X. Fan, F. Wang, M. Chi, D. N. Leonard, N. J. Dudney, H. Wang and C. Wang, *Nat. Energy*, 2019, DOI: 10.1038/s41560-018-0312-z.
149. R. Xu, F. Han, X. Ji, X. Fan, J. Tu and C. Wang, *Nano energy*, 2018, **53**, 958-966.
150. P. Hartmann, T. Leichtweiss, M. R. Busche, M. Schneider, M. Reich, J. Sann, P. Adelhelm and J. r. Janek, *The Journal of Physical Chemistry C*, 2013, **117**, 21064-21074.
151. S. Wenzel, T. Leichtweiss, D. Krüger, J. Sann and J. Janek, *Solid State Ion.*, 2015, **278**, 98-105.
152. S. Wenzel, D. A. Weber, T. Leichtweiss, M. R. Busche, J. Sann and J. Janek, *Solid State Ion.*, 2016, **286**, 24-33.
153. W. D. Richards, L. J. Miara, Y. Wang, J. C. Kim and G. Ceder, *Chem. Mat.*, 2016, **28**, 266-273.

154. A. Schwöbel, R. Hausbrand and W. Jaegermann, *Solid State Ion.*, 2015, **273**, 51-54.
155. S. Wenzel, T. Leichtweiss, D. A. Weber, J. Sann, W. G. Zeier and J. Janek, *ACS Applied Materials & Interfaces*, 2016, **8**, 28216-28224.
156. M. Sakuma, K. Suzuki, M. Hirayama and R. Kanno, *Solid State Ion.*, 2016, **285**, 101-105.
157. T. Kobayashi, A. Yamada and R. Kanno, *Electrochim. Acta*, 2008, **53**, 5045-5050.
158. A. M. Nolan, Y. Zhu, X. He, Q. Bai and Y. Mo, *Joule*, 2018, DOI: <https://doi.org/10.1016/j.joule.2018.08.017>, 1-33.
159. J. Janek and W. G. Zeier, *Nature Energy*, 2016, **1**, 16141.
160. M. Nagao, A. Hayashi, M. Tatsumisago, T. Kanetsuku, T. Tsuda and S. Kuwabata, *Physical Chemistry Chemical Physics*, 2013, **15**, 18600-18606.
161. M. Nagao, A. Hayashi, M. Tatsumisago, T. Kanetsuku, T. Tsuda and S. Kuwabata, *Physical Chemistry Chemical Physics*, 2013, **15**, 18600-18606.
162. C. Wang, Y. Zhao, Q. Sun, X. Li, Y. Liu, J. Liang, X. Li, X. Lin, R. Li, K. R. Adair, L. Zhang, R. Yang, S. Lu and X. Sun, *Nano Energy*, 2018, **53**, 168-174.
163. Y. Gao, D. Wang, Y. C. Li, Z. Yu, T. E. Mallouk and D. Wang, *Angew. Chem. Int. Ed.*, 2018, **57**, 13608-13612.
164. J. Yin, X. Yao, G. Peng, J. Yang, Z. Huang, D. Liu, Y. Tao and X. Xu, *Solid State Ion.*, 2015, **274**, 8-11.

165. H. Tsukasaki, Y. Mori, M. Otoyama, S. Yubuchi, T. Asano, Y. Tanaka, T. Ohno, S. Mori, A. Hayashi and M. Tatsumisago, *Scientific Reports*, 2018, **8**, 6214.
166. F. Strauss, T. Bartsch, L. de Biasi, A. Y. Kim, J. Janek, P. Hartmann and T. Brezesinski, *ACS Energy Lett.*, 2018, DOI: 10.1021/acseenergylett.8b00275, 992-996.
167. R. Koerver, W. Zhang, L. de Biasi, S. Schweidler, A. O. Kondrakov, S. Kolling, T. Brezesinski, P. Hartmann, W. G. Zeier and J. Janek, *Energy Environ. Sci.*, 2018, DOI: 10.1039/C8EE00907D.
168. N. C. Rosero-Navarro, A. Miura and K. Tadanaga, *Journal of Sol-Gel Science and Technology*, 2019, **89**, 303-309.
169. B. Wu, S. Wang, W. J. Evans Iv, D. Z. Deng, J. Yang and J. Xiao, *J. Mater. Chem. A*, 2016, **4**, 15266-15280.
170. J. Betz, G. Bieker, P. Meister, T. Placke, M. Winter and R. Schmuch, *Adv. Energy Mater.*, 2018, **0**, 1803170.
171. H. Z. D., W. Hui, P. A. Samuthira, P. Rui, G. K. D., C. Miaofang, L. Chengdu and X. Younan, *Advanced Energy Materials*, 2018, **8**, 1800014.
172. H. Chen, C. Wang, W. Dong, W. Lu, Z. Du and L. Chen, *Nano Lett.*, 2015, **15**, 798-802.
173. H. Chen, C. Wang, Y. Dai, S. Qiu, J. Yang, W. Lu and L. Chen, *Nano Lett.*, 2015, **15**, 5443-5448.
174. H. Chen, C. Wang, Y. Dai, J. Ge, W. Lu, J. Yang and L. Chen, *Nano Energy*, 2016, **26**, 43-49.

175. X. Li, M. Banis, A. Lushington, X. Yang, Q. Sun, Y. Zhao, C. Liu, Q. Li, B. Wang, W. Xiao, C. Wang, M. Li, J. Liang, R. Li, Y. Hu, L. Goncharova, H. Zhang, T.-K. Sham and X. Sun, *Nature Communications*, 2018, **9**, 4509.
176. C. Wang, H. Chen, W. Dong, J. Ge, W. Lu, X. Wu, L. Guo and L. Chen, *Chemical Communications*, 2014, **50**, 1202-1204.
177. Z. Lin and C. Liang, *Journal of Materials Chemistry A*, 2015, **3**, 936-958.
178. M. Nagao, A. Hayashi and M. Tatsumisago, *Electrochimica Acta*, 2011, **56**, 6055-6059.
179. A. Hayashi, T. Ohtomo, F. Mizuno, K. Tadanaga and M. Tatsumisago, *Electrochemistry Communications*, 2003, **5**, 701-705.
180. T. Kobayashi, Y. Imade, D. Shishihara, K. Homma, M. Nagao, R. Watanabe, T. Yokoi, A. Yamada, R. Kanno and T. Tatsumi, *J. Power Sources*, 2008, **182**, 621-625.
181. T. Yamada, S. Ito, R. Omoda, T. Watanabe, Y. Aihara, M. Agostini, U. Ulissi, J. Hassoun and B. Scrosati, *J. Electrochem. Soc.*, 2015, **162**, A646-A651.
182. Z. Lin, Z. Liu, W. Fu, N. J. Dudney and C. Liang, *Angewandte Chemie*, 2013, **125**, 7608-7611.
183. F. Han, J. Yue, X. Fan, T. Gao, C. Luo, Z. Ma, L. Suo and C. Wang, *Nano Letters*, 2016, **16**, 4521-4527.
184. Z. Lin, Z. Liu, N. J. Dudney and C. Liang, *ACS Nano*, 2013, **7**, 2829-2833.
185. X. Li, J. Liang, X. Li, C. Wang, J. Luo, R. Li and X. Sun, *Energy Environ. Sci.*, 2018, **11**, 2828.

186. K. Kerman, A. Luntz, V. Viswanathan, Y.-M. Chiang and Z. Chen, 2017, **164**, A1731-A1744.
187. J. Schnell, T. Günther, T. Knoche, C. Vieider, L. Köhler, A. Just, M. Keller, S. Passerini and G. Reinhart, *J. Power Sources*, 2018, **382**, 160-175.
188. C. Wang, X. Li, Y. Zhao, M. N. Banis, J. Liang, X. Li, Y. Sun, K. R. Adair, Q. Sun, Y. Liu, F. Zhao, S. Deng, X. Lin, R. Li, Y. Hu, T.-K. Sham, H. Huang, L. Zhang, R. Yang, S. Lu and X. Sun, *Small Methods*, 2019, DOI: 10.1002/smt.201900261, 1900261.
189. N. Machida, J. Kashiwagi, M. Naito and T. Shigematsu, *Solid State Ion.*, 2012, **225**, 354-358.
190. Y. J. Nam, D. Y. Oh, S. H. Jung and Y. S. Jung, *J. Power Sources*, 2018, **375**, 93-101.

Chapter 2

2. Experimental Apparatus and Characterization Techniques

2.1 Experimental Apparatus

Atomic layer deposition (ALD) and molecular layer deposition (MLD) systems.

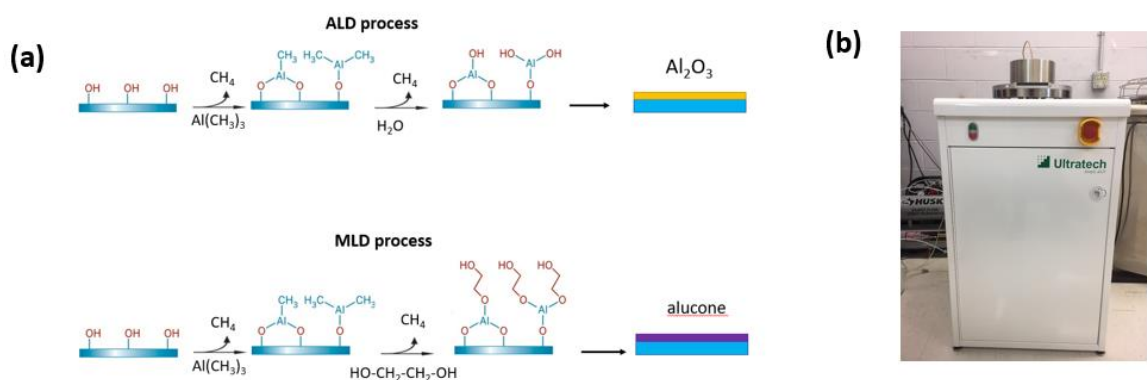


Figure 2- 1 (a) Chemical reaction process of ALD and MLD deposition process. (b) Savannah 200 ALD system (Veeco/carbon nanotube (CNT) division of the Veeco Instruments Inc.).

Atomic layer deposition process is based on two self-limited reactions, by controlling the sequence, purge time, and temperature, a thin film layer can be growth on a substrate with a highly precise thickness controllability. Similar to the ALD, molecular layer deposition also based on the self-limited reactions, but the main difference between MLD and ALD is that MLD layer can synthesize inorganic or organic/inorganic hybrid thin film layer.

2.2 Characterizations Techniques

2.2.1 Physical Characterizations

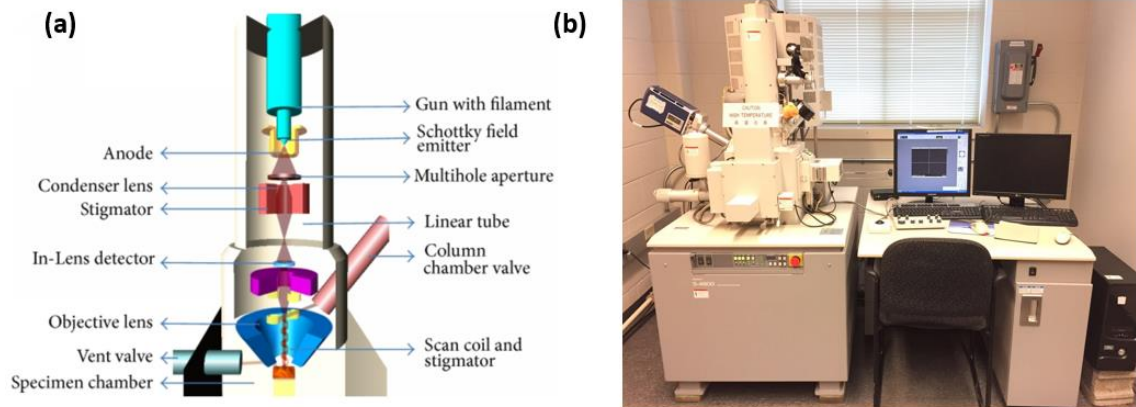


Figure 2- 2 (a) Principle of FE-SEM operations.^[3] (b) An Hitachi S-4800 scanning electron microscopy.

SEM is using high energy electron beam, which has an ultra-small wavelength, to observe the morphology of materials at the nanometer scale. In addition, the high energy electron beam also interacts with samples, generating X-rays, Auger electrons, which can be exploited to retrieve chemical information of samples. The morphologies of the samples in my research were characterized by an Hitachi S4800 Scanning Electron Microscopy at an acceleration voltage of 5 kV, as shown in **Figure 2-2b**.

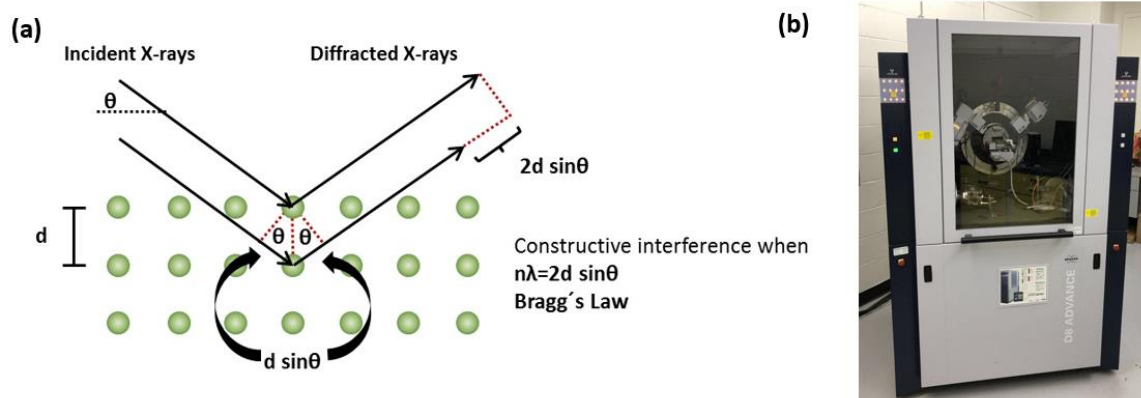


Figure 2- 3 (a) The principle of X-ray diffraction. (b) The Bruker D8 advance diffractometer XRD system.

X-ray diffraction (XRD) is employing X-ray to determine the structure information of samples. As long as the X-ray diffraction follows the Bragg's law, we can observe the diffraction pattern at a certain angle, which is closely related to the atomic arrangement of samples (**Figure 2-3a**). The XRD pattern of my samples in this thesis were collected on a Bruker D8 Advance Diffractometer using Cu $K\alpha$ radiation at 40 kV and 40 mA (As shown in **Figure 2-3b**).

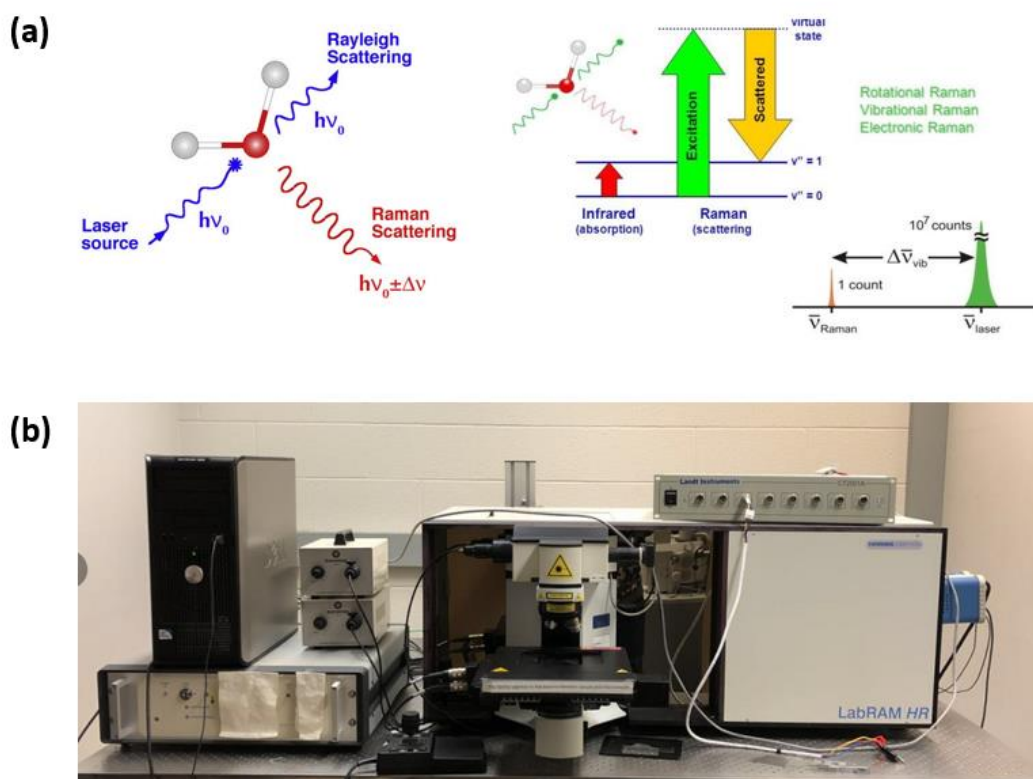


Figure 2- 4 (a) The main principle of Raman spectroscopy.[4] (b) HORIBA Scientific LabRAM HR Raman spectrometer system.

Raman scattering is closely related to the molecular rotation and chemical bond vibration. By determining the Raman scattering, we can obtain the molecular structural information. Raman scattering spectra of my samples in this thesis were recorded using a Nicolet 380 and a HORIBA Scientific LabRAM HR Raman spectrometer system (As shown in **Figure 2-4b**) equipped with a 532.4 nm laser.

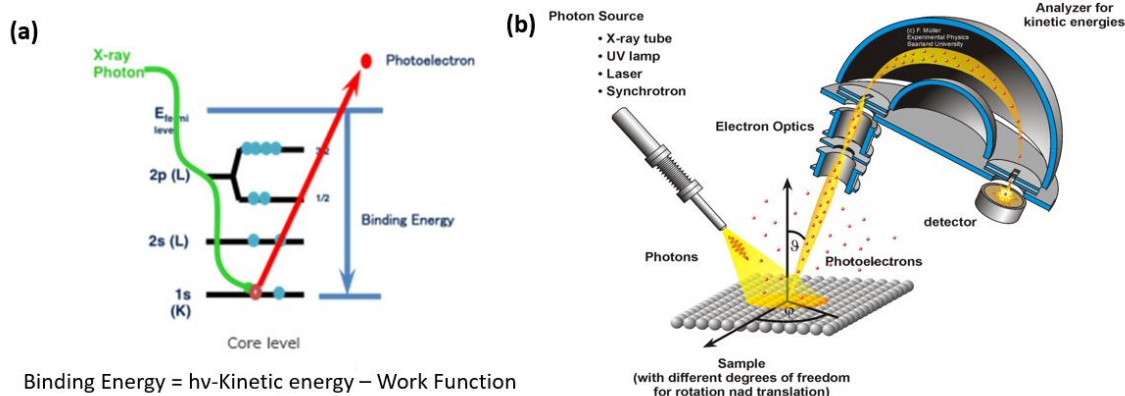


Figure 2- 5 (a) The principles of X-ray photoelectron spectroscopy. (b) Schematic drawing of a typical XPS setup with photon source (X-rays, UV-light, laser or Synchrotron radiation).[5]

X-ray photoelectron spectroscopy (XPS) was used to analyze the chemical composition and bonding by detecting the amount of the escaped electrons from the surface of the samples at a certain excitation energy (**Figure 2-5**). The XPS measurements were carried out in Western Surface Science using an Ar glovebox connected XPS (Kratos AXIS Ultra Spectrometer) system for air-sensitive samples.

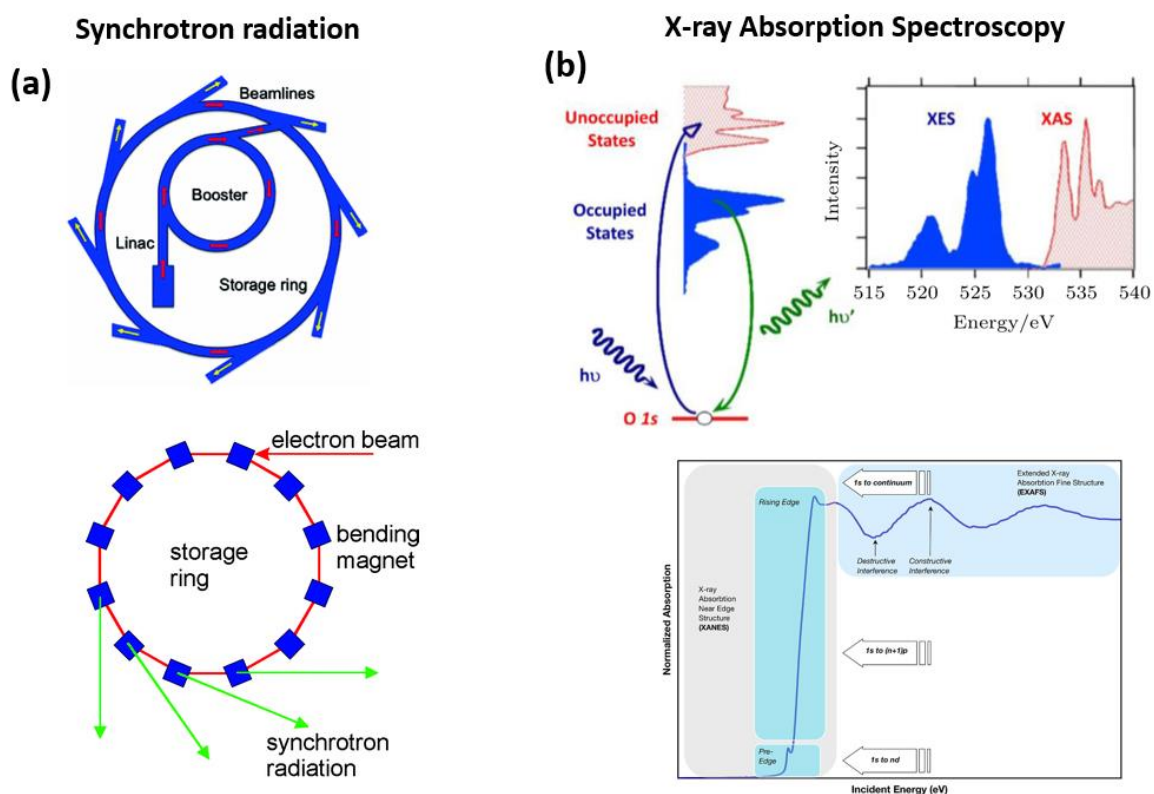


Figure 2- 6 (a) The principle of generating synchrotron radiation. (b) The principle of X-ray absorption spectroscopy (XAS). [6]

Synchrotron radiation is electromagnetic energy emitted by charged particles (e.g., electrons and ions) that are moving at speeds close to that of light when their paths are altered, as by a magnetic field. It is so called because particles moving at such speeds in a variety of particle accelerator that is known as a synchrotron produce electromagnetic radiation of this sort. Bending magnets are used to bend the high-speed electron, then emitting radiation. The radiation produced in this way has a characteristic polarization and the frequencies generated can range over the entire electromagnetic spectrum which is also called continuum radiation (**Figure 2-6a**).

X-ray absorption spectroscopy (XAS) is closely related to the electron transition from occupied states to unoccupied states. By determining the energy change of XAS spectra, we tell the chemical information change of certain elements in the sample. The full

XAS spectrum can be divided into two parts, X-ray absorption near edge structure (XANES) and Extended X-ray Absorption Fine Structure (EXAFS). XANES gives information about the valence state, energy bandwidth and bond angles, while EXAFS yields information about the interatomic distances, near neighbor coordination numbers, and lattice dynamic (**Figure 2-6b**).

2.3 Electrochemical Characterizations

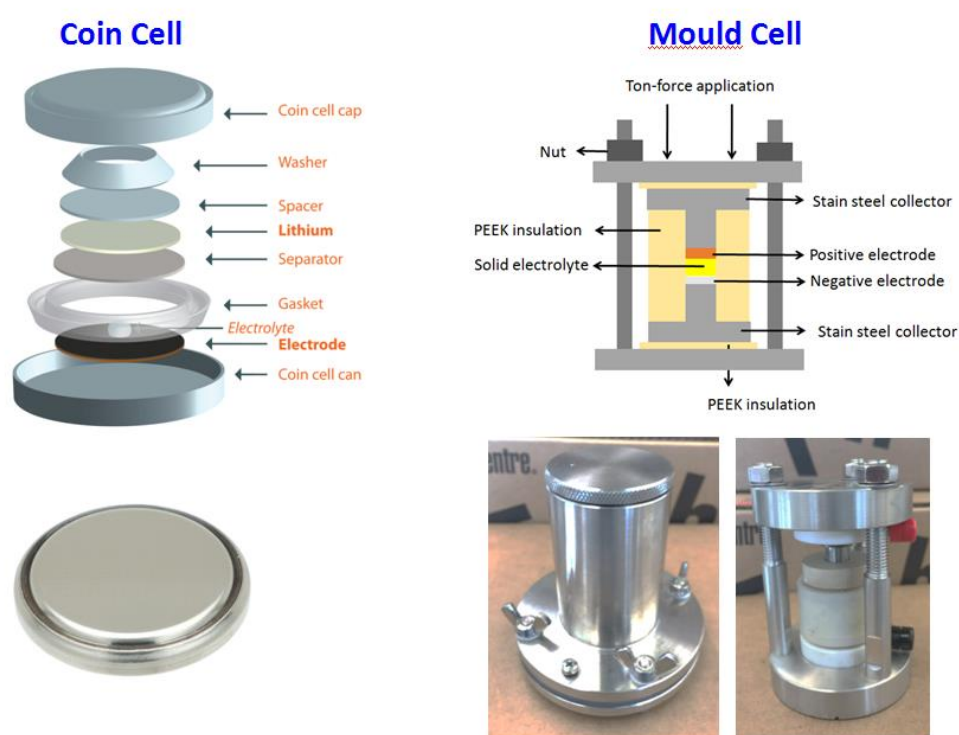


Figure 2- 7 The configurations of a coin cell and a mould cell with their physical pictures.

The coin cell CR2032 was assembled for electrochemical performance analysis. The mould cell is used to test the electrochemical performance of all-solid-state batteries in my thesis.

2.4 References

- [1] http://www.isw.physics.uwo.ca/facilities_techniques/rbs.html
- [2] <https://www.uwo.ca/ssw/services/tof-sims.html>
- [3] Y. Jusman, S. Ng, N. Osman, Investigation of CPD and HMDS Sample Preparation Techniques for Cervical Cells in Developing Computer-Aided Screening System Based on FE-SEM/EDX. 2014. doi:<https://doi.org/10.1155/2014/289817>
- [4] https://www.horiba.com/en_en/raman-imaging-and-spectroscopy/
- [5] <https://epm.univie.ac.at/research/low-dimensional-quantum-solids/methods/>
- [6] William Clegg, Synchrotron chemical crystallography. *J. Chem. Soc., Dalton Trans.*, 2000, 3223-3232

Chapter 3

3 Manipulating Interfacial Nanostructure to Achieve High-Performance All-Solid-State Lithium-Ion Batteries*

All-solid-state lithium-ion batteries (ASSLIBs) have gained substantial attention worldwide due to their intrinsic safety and high energy density. However, the large interfacial resistance of ASSLIBs, which is originated from the interfacial reactions and inferior electrode-electrolyte contact between electrodes and solid electrolytes, dramatically constrains their electrochemical performance.

Here we rationally designed a dual shell interfacial nanostructure to enable high-performance ASSLIBs, in which the inner shell LiNbO_3 suppresses the interfacial reactions while the outer shell $\text{Li}_{10}\text{GeP}_2\text{S}_{12}$ enables intimate electrode-electrolyte contact. As a result, the dual shell structured $\text{Li}_{10}\text{GeP}_2\text{S}_{12}@ \text{LiNbO}_3@ \text{LiCoO}_2$ exhibits a high initial specific capacity of 125.8 mAh.g^{-1} (1.35 mAh.cm^{-2}) with an initial Coulombic efficiency of 90.4 % at 0.1 C and 87.7 mAh.g^{-1} at 1C. More importantly, in-situ X-ray absorption near-edge spectroscopy (XANES) was performed for the first time to reveal the interfacial reactions between $\text{Li}_{10}\text{GeP}_2\text{S}_{12}$ and LiCoO_2 . This dual shell nanostructure demonstrates an ideal interfacial configuration for realizing high-performance ASSLIBs.

***Note: This work has been published.**

Wang, C., Li, X., Zhao, Y., Banis, M. N., Liang, J., Li, X., Sun, Y., Adair, K. R., Sun, Q., Liu, Y., Zhao, F., Deng, S., Lin, X., Li, R., Hu, Y., Sham, T. - K., Huang, H., Zhang, L., Yang, R., Lu, S., Sun, X., Manipulating Interfacial Nanostructure to Achieve High - Performance All - Solid - State Lithium - Ion Batteries. **Small Methods** 2019, 3, 1900261. <https://doi.org/10.1002/smtd.201900261>

3.1 Introduction

Safe and high-energy-density rechargeable lithium-ion batteries are in great demand for large-scale energy storage systems and long-range electric vehicles. Conventional lithium-ion batteries (LIBs), which employ organic liquid electrolytes (LEs), have proven challenging to achieve the desired safety standards due to the flammable nature of the organic LEs. Additionally, the limited electrochemical window of the organic LEs restricts the further improvement of the energy density of conventional LIBs,^[1] especially when coupled with high-voltage cathodes and lithium metal anodes. Under intensive investigation for over two decades, all-solid-state lithium-ion batteries (ASSLIBs) are now regarded as one of the most promising energy storage systems because of their superior safety and great potential to meet the target of high energy density.^[2] As an indispensable component of the ASSLIBs, solid-state electrolytes with high ionic conductivity and wide electrochemical windows are indispensable. Over the past years, significant advances have been made in solid-state electrolytes, such as oxide electrolytes,^[2b, 3] polymer electrolytes,^[4] and sulfide electrolytes (SEs).^[5] Among them, SEs possess high ionic conductivity ($10^{-3} \sim 10^{-2} \text{ S.cm}^{-1}$), particularly $\text{Li}_{9.54}\text{Si}_{1.74}\text{P}_{1.44}\text{S}_{11.7}\text{Cl}_{0.3}$ (25 mS.cm^{-1}),^[2a] $\text{Li}_7\text{P}_3\text{S}_{11}$ (17 mS.cm^{-1}), $\text{Li}_{10}\text{GeP}_2\text{S}_{12}$ (12 mS.cm^{-1}),^[6] and $\text{Li}_{10.35}[\text{Sn}_{0.27}\text{Si}_{1.08}]\text{P}_{1.65}\text{S}_{12}$ (11 S.cm^{-1})^[5a] possess ionic conductivities rivalling that of liquid electrolytes (10.2 mS.cm^{-1}).^[1] However, the electrochemical performance of SE-based ASSLIBs is constrained by the large interfacial resistance, which is originated from the interfacial reactions and lithium deficient space-charge layer as well as the inferior solid-solid contact between electrode materials and SEs.^[2d, 7] With tremendous efforts, various strategies have been proposed to suppress the interfacial resistance, including (i) developing interfacial layers (LiNbO_3 and $\text{Li}_4\text{Ti}_5\text{O}_{12}$) to suppress the interfacial reactions,^[8] (ii) synthesizing soluble solid electrolytes to improve the interfacial contact between electrode materials and SEs,^[9] (iii) designing homogeneous

and compatible interface,^[10] and (iv) using novel solid electrolytes.^[11] However, the electrochemical performance of ASSLIBs is still far behind the standard for practical application.

Inspired by the pioneering success in addressing the challenges of silicon anodes,^[12] sulfur cathodes,^[13] and Li metal anodes^[14] by rational nanostructure design, here we rationally designed a dual shell interfacial nanostructure to enable high-performance ASSLIBs. The inner shell is devised to suppress the interfacial reactions and lithium-deficient space-charge layer (SCL) between electrode materials and SEs. The outer shell is constructed to ensure the intimate solid-solid contact between electrode materials and SEs. As a result, the dual shell structured LGPS@LNO@LCO cathode exhibits a high initial specific capacity of 125.8 mAh g⁻¹ (1.35 mAh.cm⁻²) with an initial coulombic efficiency of 90.4% at 0.1 C and 87.7 mAh.g⁻¹ at 1C. Moreover, the charge and discharge curves of the dual shell structured LGPS@LNO@LCO exactly match those in liquid electrolytes, suggesting the negligible polarization and complete utilization of LCO in ASSLIBs. Additionally, in-situ XANES was performed to reveal the interfacial reactions between LCO and LGPS for the first time. This demonstration shed light on the interfacial nanostructure design to achieve high-performance SE-based ASSLIBs.

3.2 Experimental Procedures

3.2.1 Synthesis of One-Shell LNO@LCO and Dual Shell

Structured LGPS@LNO@LCO.

Commercial LiCoO₂ (LCO) is purchased from Sigma Aldrich. Atomic layer deposition was employed to uniformly deposit 5 nm LiNbO₃ (LNO) on LCO particles, forming one-shell LNO@LCO particles. The ALD procedures were reported previously.^[1] To obtain dual shell LGPS@LNO@LCO particles., 30 mg commercial Li₁₀GeP₂S₁₂ (LGPS)

(purchased from MSE supplies, its room-temperature ionic conductivity is 3.5×10^{-3} S.cm⁻¹) was dispersed in heptane, 70 mg LNO@LCO was added into the heptane solution. After thoroughly mixing them, the dispersant heptane was removed under vacuum at 80 °C overnight. The dual shell LGPS@LNO@LCO is directly used as the cathode of ASSLIBs. The electrochemical impedance spectra were from 7MHz to 0.1Hz with an amplitude of 10 mV. The CV was tested from 1.9V to 3.6V with a scan rate of 0.02 mV.s⁻¹. The GITT was performed with a 5min discharge at 0.1C followed by 2 hours of relaxation.

3.2.2 Characterizations

TEM images were recorded using a Tecnai G2 F20 S-TWIN at 200 kV equipped with EDX (Apollo 40 SDD). SEM images were recorded using a Scanning Electron Microscope (SEM) (FEI Quanta 400 FEG). Synchrotron-based in-situ X-ray absorption was performed at the Canadian Light Source. Synchrotron-based X-ray absorption near edge structure (XANES) was carried out at the Canadian Light Source (CLS). S K-edge XANES was collected using fluorescence yield mode using Si (111) crystals on the Soft X-ray Microcharacterization beamline (SXRBM) at the CLS. For ex-situ XANES experiments, to avoid sample oxidation, the samples are firstly sealed by Mylar polymer thin film in a glove box under the Ar atmosphere and subsequently transferred to the corresponding beamline for further measurements. For operando synchrotron studies, an ambient table setup was used at the SXRMB beamline. The chamber was filled with helium gas to reduce scattering at low energies. Charge-discharge characteristics of operando cells were galvanostatically tested at 0.05 C in the range of 2.0 V-3.6 V (V vs. Li-In) at room temperature using a Landline Battery Tester. The XANES measurements have been conducted at the shortest time around 10-20 min scans at the SXRMB beamline of the Canadian Light Source.

3.2.3 Electrochemical Performance

All of the all-solid-state lithium-ion battery performance was tested by home-made mold cells at room temperature. To evaluate the performance of the pristine LCO in ASSLIBs, just mixing LCO with LGPS with a mass ratio of 70:30 in an agate mortar for 15 min. 80 mg LGPS was compressed at 1.5t first to form a solid-state electrolyte layer. 12 mg cathode composites were then spread on one side of LGPS pellets and further pressed at 3.5t. A piece of indium foil was put on another side of LGPS and pressed at 0.5t. To test the performance of the one-shell LNO@LCO particles in ASSLIBs, 70 mg LNO@LCO was mixed with LGPS in an agate mortar for 15 min, then the LNO@LCO/LGPS composite is used as the cathode of ASSLIBs. The battery assembly procedure is exactly the same as that of pristine LCO-based ASSLIBs. In terms of dual shell structured LGPS@LNO@LCO particles, we directly use it as the cathode of ASSLIBs and follow the above-mentioned procedure to make the ASSLIBs. The test voltage range is from 1.9V to 3.6V. The mass of the active materials in ASSLIBs is 7 mg. 1C is defined utilizing 140 mA.g^{-1} (1.3 mA.cm^{-2}) for all the LCO electrodes.

3.3 Results and Discussion

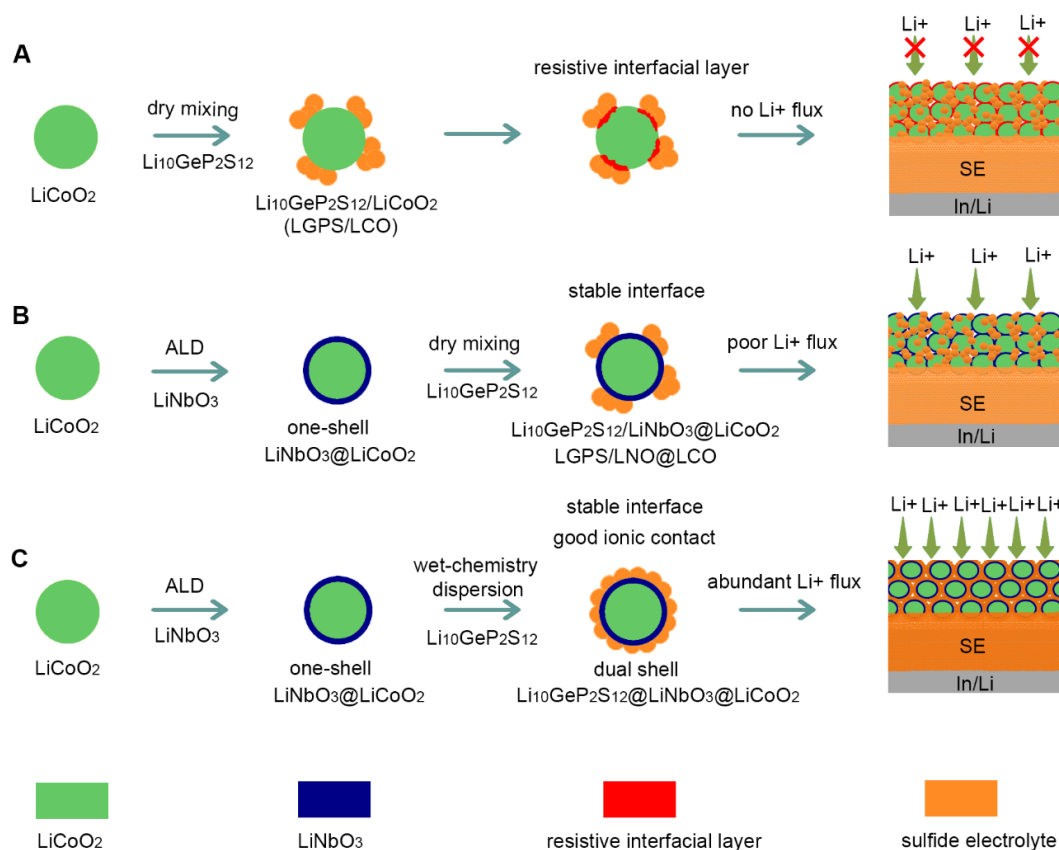


Figure 3-1 Schematic diagram of ASSLIBs with various interfacial nanostructure. (A) LiCoO₂ directly mixed with Li₁₀GeP₂S₁₂ without interfacial design for ASSLIBs. (B) A one-shell LiNbO₃@LiCoO₂ cathode for ASSLIBs. (C) A dual shell LGPS@LNO@LCO for ASSLIBs.

As a proof-of-concept study, the typical active material LiCoO₂, the most well-known solid-state sulfide electrolyte Li₁₀GeP₂S₁₂, and the high ionically conductive interfacial layer LiNbO₃ are chosen, although the concept is not limited to these materials. In general, when directly mixing LCO with LGPS without any interfacial coating, a highly resistive layer will form at the interface between LCO and LGPS during the initial charge process, which intrinsically blocks the Li⁺ transfer.^[8a] Furthermore, a lithium-deficient space-charge layer will form at the interface,^[15] under this scenario, ASSLIBs can be

barely charged due to the significant interfacial resistance in the ASSLIBs (**Figure 3-1A**). With one shell (LNO) isolating the direct contact between LCO and LGPS, the interfacial reactions and lithium-deficient SCL can be suppressed.^[16] Atomic layer deposition is employed to conformally construct the inner layer LNO.^[2d, 17] In this case, ASSLIBs can be operated with a low current, because the interfacial Li^+ flux is limited by insufficient ionic contact between LCO and LGPS (**Figure 3-1B**). In addition, the aggregation of LCO and LGPS particles could lead to the incomplete utilization and serious polarization of LCO in ASSLIBs.^[18] The remedy to this case is to construct a dual shell interfacial configuration. As shown in **Figure 3-1C**, when LGPS with high ionic conductivity is further dispersed on the one-shell LNO@LCO particle via a wet-chemistry dispersion process, intimate solid-solid contact between LGPS and LNO@LCO can be achieved, thus enabling an abundant Li^+ flux across the interface. It should be mentioned that the dispersion process is different from the previous soluble sulfide electrolyte coating, in which a post-annealing process is required to crystallize SEs.^[9a, 9b] In addition, the wet-chemistry dispersion process can be easily developed with other SEs without the post-annealing process. The detailed experimental procedure can be found in the supporting information.

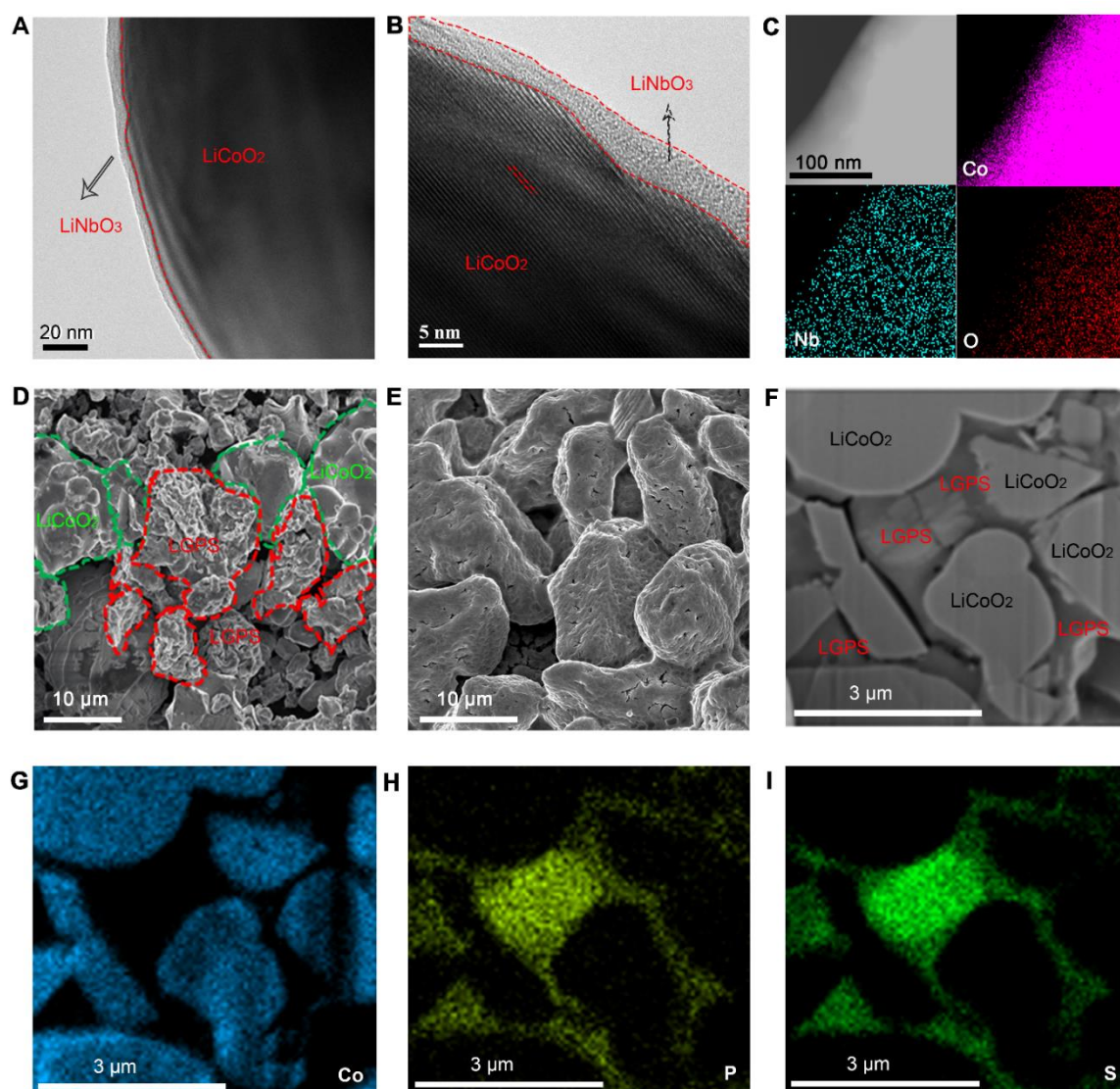


Figure 3-2 Structural and elemental analysis of one-shell LNO@LCO and dual shell LGPS@LNO@LCO. (A) A TEM image of one-shell LNO@LCO particles. (B) a high-resolution TEM image of one-shell LNO@LCO particles. (C) Energy-dispersive X-ray spectroscopic (EDS) mapping of Co, Nb, and O by HAADF-STEM. (D). SEM image of the one-shell LNO@LCO/LGPS electrode. (E) SEM image of the mixture of the dual shell structured LGPS@LNO@LCO electrode. (F) FIB cross-section image of LGPS@LNO@LCO. (G) Co mapping. (H) P mapping. (I) S mapping.

The particle size of the pristine commercial LCO was found to be around 6~15 μm by scanning electron microscopy (SEM) (**Figure 3-S1**). 5 nm LNO was uniformly and conformably coated on the LCO surface by atomic layer deposition (ALD), as confirmed by the transmission electron microscopy (TEM) images in **Figure 3-2A and 3-2B**. The energy dispersive X-ray spectroscopic (EDX) mapping of Co, Nb, and O were detected by high-angle annular dark-field scanning transmission electron microscopy (HAADF-STEM) (**Figure 3-2C**), explicitly confirming the uniform coating of LNO on the LCO surface. It should be mentioned that the interfacial coating in previous works is mainly realized by the sol-gel method,^[8, 19] which cannot guarantee the uniformity and conformality of ALD coatings.^[20] **Figure 3-2D** shows an SEM image of LNO@LCO/LGPS composite synthesized by conventional dry mixing, which clearly shows the aggregation of LCO and LGPS particles and inferior solid-solid contact between LNO@LCO and LGPS. Compared to the LNO@LCO/LGPS composites, the uniform coverage of LGPS on LNO@LCO particles can be seen in the LGPS@LNO@LCO composites (**Figure 3-2E**), implying the dual shell structure of was successfully realized by the wet-chemistry dispersion process. Furthermore, the cross-section image of LGPS@LNO@LCO composites milled by a focused ion beam (FIB) is presented in **Figure 3-2F**. In addition, the corresponding EDX mapping of Co, P, and S are shown in **Figure 3-2G, 3-2H, and 3-2I**, respectively, further confirming that the outer LGPS layer is uniformly and conformally coated on LNO@LCO surfaces. Further EDX mapping images (including Ge mapping and Nb mapping) of LGPS@LNO@LCO can be found in **Figure 3-S2**, which also confirms the LNO shell on the LCO surface. To be the best of our knowledge, this is the first time to demonstrate the LGPS coating on the electrode materials via the wet-chemistry dispersion process.

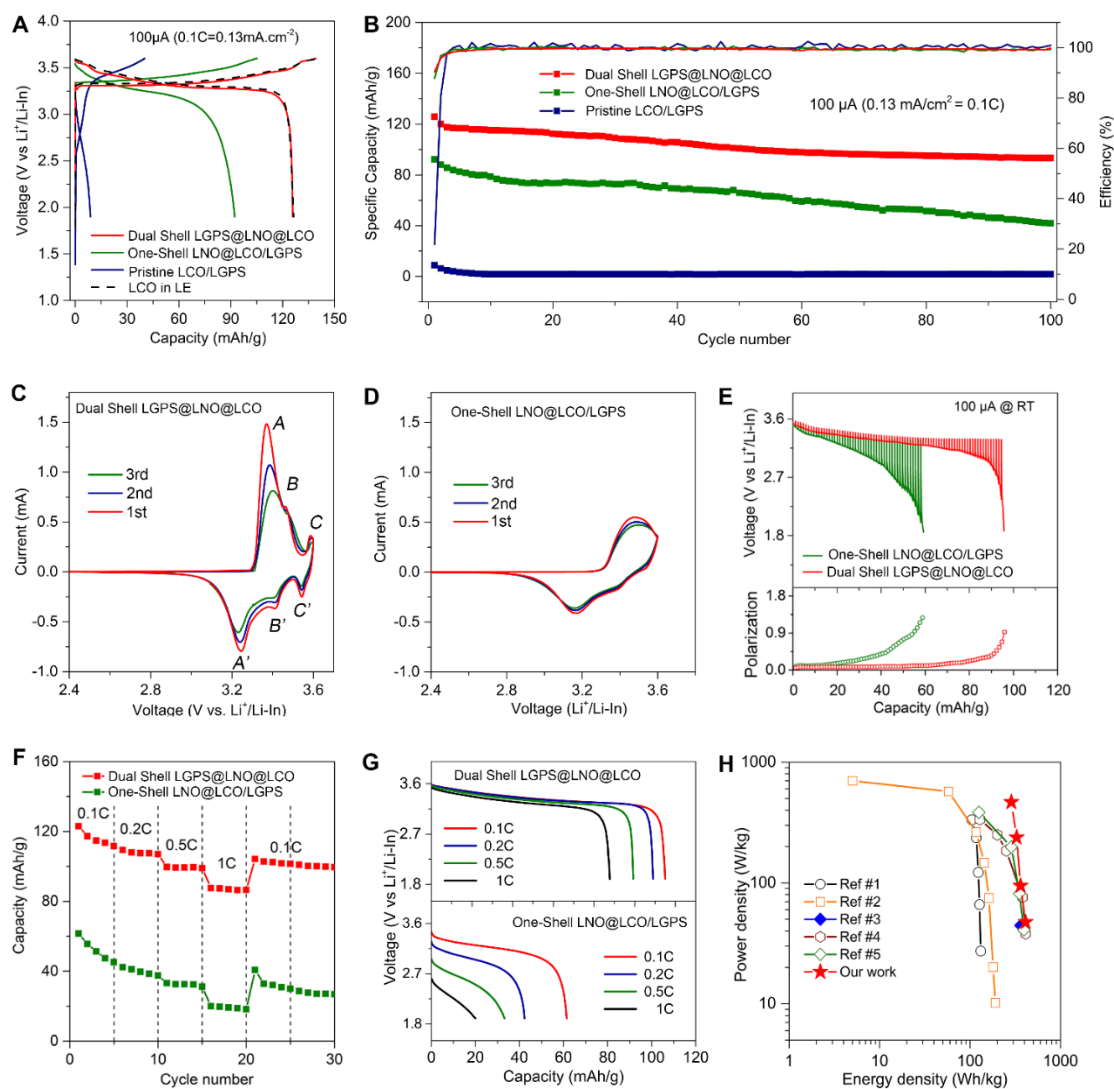


Figure 3-3 Electrochemical performance of ASSLIBs with pristine LCO, one-shell LNO@LCO, and dual-shell structured LGPS@LNO@LCO. (A) Charge-discharge curves. (B) Cycling stability and Coulombic efficiency. (C) CV curves of dual shell structured LGPS@LNO@LCO. (D) CV curves of one-shell LNO@LCO/LGPS electrodes. (E) Galvanostatic Intermittent Titration Technique (GITT). (F) Rate performance. (G) Discharge curves at various current densities. (H) Ragone plot.

The electrochemical performances of ASSLIBs with various interfacial structures were evaluated thoroughly. **Figure 3-3A** exhibits the typical charge-discharge curves of pristine LCO, one-shell LNO@LCO, dual shell structured LGPS@LNO@LCO, and LCO

in liquid electrolytes (LE), respectively. The pristine LCO exhibits an initial charge capacity of 40.1 mAh.g⁻¹ and discharge capacity of 8.8 mAh.g⁻¹ at 0.1C (1C=1.3 mA.cm⁻² = 140 mA.g⁻¹). The initial Coulombic efficiency is only 21.9%. The low Coulombic efficiency and significant polarization indicate serious interfacial reactions during the initial charging process. In addition, the slope at the very beginning of the charge curve is an indicator of a lithium-deficient SCL between LCO and LGPS.^[15, 21] The one-shell LNO@LCO exhibits an initial discharge capacity of 92.2 mAh.g⁻¹ with the Coulombic efficiency of 89.1%. Interestingly, the slope before Li⁺ de-lithiation is totally disappeared, suggesting that the one-shell LNO@LCO can suppress the interfacial reactions and SCL between LCO and LGPS. However, the polarization between charge and discharge curves is still obvious, which is caused by the poor ionic contact between LNO@LCO and LGPS. The dual shell structured LGPS@LNO@LCO presents an initial capacity of 125.8 mAh.g⁻¹ with an initial Coulombic efficiency of 90.4%. It is worth to mention that the charge-discharge curves of the dual shell LGPS@LNO@LCO exactly match those of LCO in liquid electrolytes under the same current density (Figure S3), demonstrating that the dual shell structured LGPS@LNO@LCO can achieve the full utilization of LCO with a negligible polarization in ASSLIBs. The electrochemical impedance spectroscopy (EIS) was performed to analyze the interfacial resistance of pristine LCO, one-shell LNO@LCO, and dual shell structured LGPS@LNO@LCO after the initial charge process (**Figure 3-S4**). The interfacial resistance of the pristine LCO after the first charge process is over 3000 ohms, which is reduced to 150 ohms with LNO inner shell protection, and further reduced to 68 ohms when LGPS is coated on the LNO@LCO particles. The reduction in resistance suggests that the inner shell LNO can suppress the interfacial reactions and the outer shell LGPS can improve the interfacial contact between LNO@LCO and LGPS.

Figure 3-3B shows the cycle stability of pristine LCO, one-shell LNO@LCO, and dual shell structured LGPS@LNO@LCO and the corresponding Coulombic efficiencies

(Figure 3-S5). Pristine LCO shows no capacity after several cycles, which is due to the serious interfacial reactions between pristine LCO and LGPS. Comparatively, the one-shell LNO@LCO shows higher capacity and longer cycle stability. However, the capacity decays rapidly and is still far behind the theoretical capacity of LCO. The reason was believed to be the detachment of LCO from LGPS induced by the volume change upon cycling (Figure S6). The dual shell structured LGPS@LNO@LCO shows a higher capacity of 125.8 mAh.g^{-1} , which can still retain a capacity of 90.3 mAh.g^{-1} after 100 cycles. **Figure 3-3C** presents the cyclic voltammogram (CV) profiles of the dual shell structured LGPS@LNO@LCO and one-shell LNO@LCO, respectively. The three pairs of redox peaks of LGPS@LNO@LCO can be clearly seen. The *A-A'* redox peaks are related to the insulator-metal transition with the coexistence of two distinct hexagonal phases.^[19, 22] The *B-B'* and *C-C'* redox peaks are associated with the phase transition from the hexagonal structure (O3) to the monoclinic structure of LCO.^[22] Comparatively, the CV of LNO@LCO shows obvious polarization and smaller peak currents (**Figure 3-3D**), suggesting the limited Li^+ flux across the interface between LCO and LGPS. The Galvanostatic Intermittent Titration Technique (GITT) was further utilized to analyze the polarization and lithium-ion (Li^+) diffusion efficiency of LNO@LCO and LGPS@LNO@LCO. **Figure 3-3E** shows the GITT curves and polarization curves of LNO@LCO and LGPS@LNO@LCO. Obviously, the polarization of LGPS@LNO@LCO is smaller than that of LNO@LCO. Based on the GITT theoretical analysis, the Li^+ diffusion efficiency of the dual shell LGPS@LNO@LCO electrode is almost 4 orders of magnitude higher than that of one-shell LNO@LCO electrodes (Figure 3-S7 and Table 3-S1), indicating that the contact area between LNO@LCO and LGPS is dramatically enhanced by designing dual shell interfacial structure.

When tested at various current densities, the one-shell LNO@LCO shows limited capacity and large polarization at a high current density (**Figure 3-3F**). Specifically,

one-shell LNO@LCO exhibit a specific capacity of 20.0 mAh.g⁻¹ with a large polarization at 1C, while the dual shell structured LGPS@LNO@LCO presents a capacity of 87.7 mAh.g⁻¹ with a negligible polarization at 1C (**Figure 3-3G**). The reason behind the increased capacity and negligible polarization could be due to the high ionic conductivity (1.2×10^{-3} S.cm⁻¹, **Figure 3-S8**) of the outer shell LGPS. **Figure 3-3H** compares the electrochemical performance with all previously reported results in the Ragone plot. The sources of the data are listed in **Table 3-S2**. It is apparent that the electrochemical performance of the dual shell structured LGPS@LNO@LCO overtakes previous results, especially the power density.^[6a, 8a, 21]

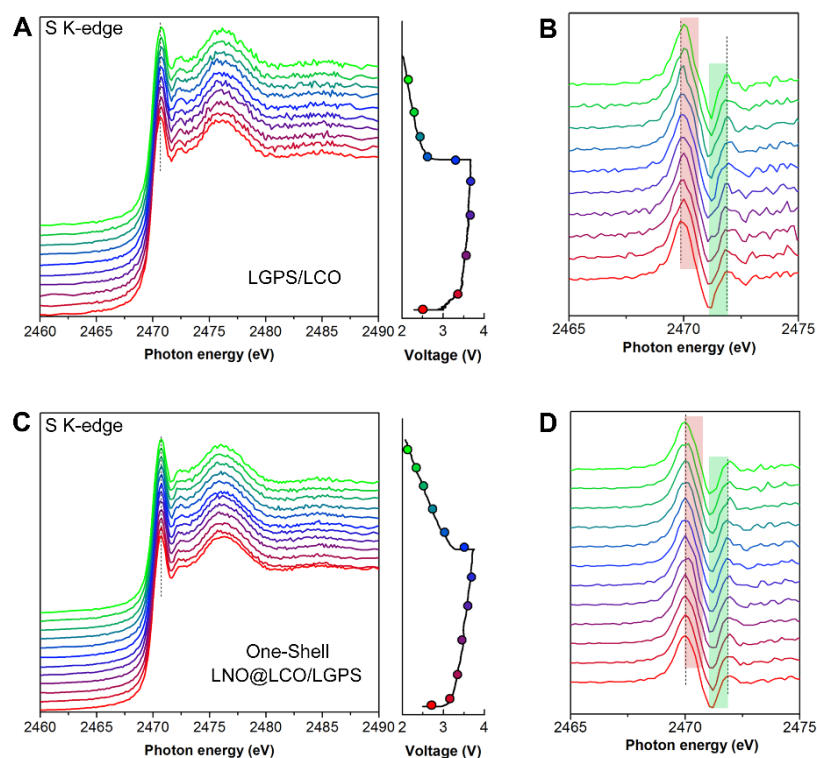


Figure 3-4 In-situ XANES of ASSLIBs during the initial charge-discharge process. (A) S K-edge of the bare LCO/LGPS cathode. (B) The first deviation of the bare LCO/LGPS electrode. (C) S K-edge of the one-shell LNO@LCO/LGPS electrode. (D) The first deviation of the one-shell LNO@LCO/LGPS electrode.

To unveil the interfacial reactions between LCO and LGPS and functionality of the inner

shell LNO, in-situ X-ray absorption near-edge spectroscopy (XANES) was performed. **Figure 3-4A** and **3-4C** present the in-operando sulfur K-edge XANES and the discharge-charge profiles of pristine LCO and one-shell LNO@LCO, respectively. The electrochemical phenomena are completely consistent with the results in Figure 3A. Comparing the S K-edge XANES, the edge jump of the LGPS before the electrochemical reaction is at 2470 eV, which is corresponding to the one level excitation of an electron from the K shell.^[23] Due to the weak signal to noise ratio, the first-order derivation spectra was subtracted in **Figure 3-4B** and **3-4D**. Pristine LCO/LGPS presents a lot of shoulder peaks at 2470 eV (red bar) and 2472 eV (green bar) during the charge-discharge process, while LNO@LCO/LGPS does not, implying that the inner shell LNO can suppress the interfacial reactions between LCO and LGPS. However, the changes in other elements are not clarified, such as phosphorus and germanium. As a remedy, surface-sensitive X-ray photoelectron spectroscopy (XPS) was performed to further examine the chemical information on P, Ge, and S.

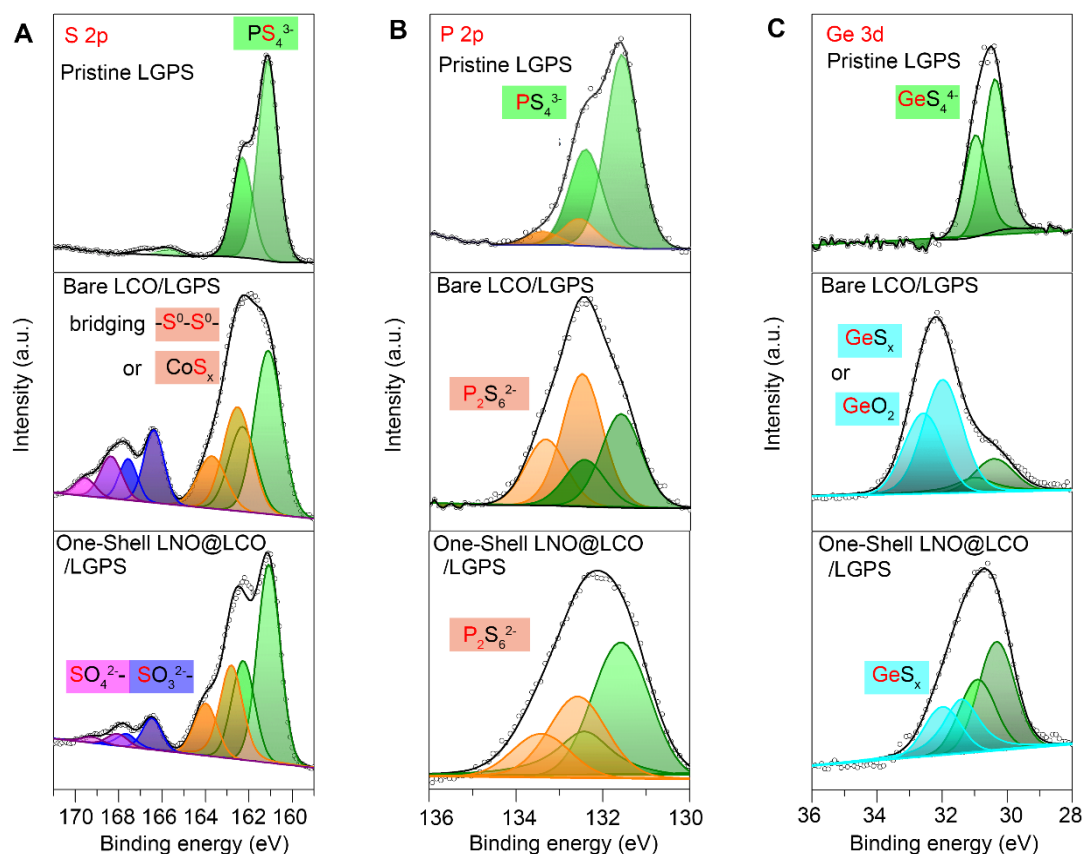


Figure 3-5 Ex-situ XPS characterizations on the pristine LGPS (top), bare LCO/LGPS electrodes after 100 cycles (middle), and one-shell LNO@LCO/LGPS electrodes after 100 cycles (bottom). (A) S 2p spectra, (B) P 2p spectra, (C) Ge 3d spectra.

Figure 3-5 shows the ex-situ XPS results of S 2p, P 2p, and Ge 3d from pristine LGPS, bare LCO/LGPS after 100 cycles, and one-shell LNO@LCO/LGPS after 100 cycles, respectively. The assignment of each peak can be found in Table S3. In S 2p spectra (**Figure 3-5A**), S of LGPS is highly oxidized to $-S-S-$ or CoS_x in comparison with S spectra of pristine LGPS. In addition, sulfite and sulfate species were also detected, which is also caused by the oxidization of LGPS by LCO during the charge-discharge process.^[19, 21] Interestingly, the intensity of oxidization peaks is reduced with the inner LNO shell (**Figure 3-5A**, bottom), suggesting the inner shell LNO can alleviate the oxidization of LCO during the charge-discharge process. **Figure 3-5B** shows the

comparison of P 2p spectra. P 2p spectra of bare LCO/LGPS exhibit more intensive $P_2S_6^{2-}$ peaks, suggesting P of bare LCO/LGSP is highly oxidized after cycling. In LNO@LCO/LGPS samples, the intensity of $P_2S_6^{2-}$ peaks is strongly suppressed by the inner shell LNO protection. Similarly, in terms of Ge 3d spectra (**Figure 3-5C**), the intensity associated with the oxidized species, such as GeS_x and/or GeO_2 , are reduced in the one-shell LNO@LCO samples, implying that the oxidization of Ge of LGPS is also suppressed by the inner shell LNO. All the results explicitly demonstrate that the inner shell can inhibit the oxidization reactions of LGPS but cannot completely suppress the interfacial oxidization reactions due to the intrinsically narrow electrochemical windows of LGPS.^[24]

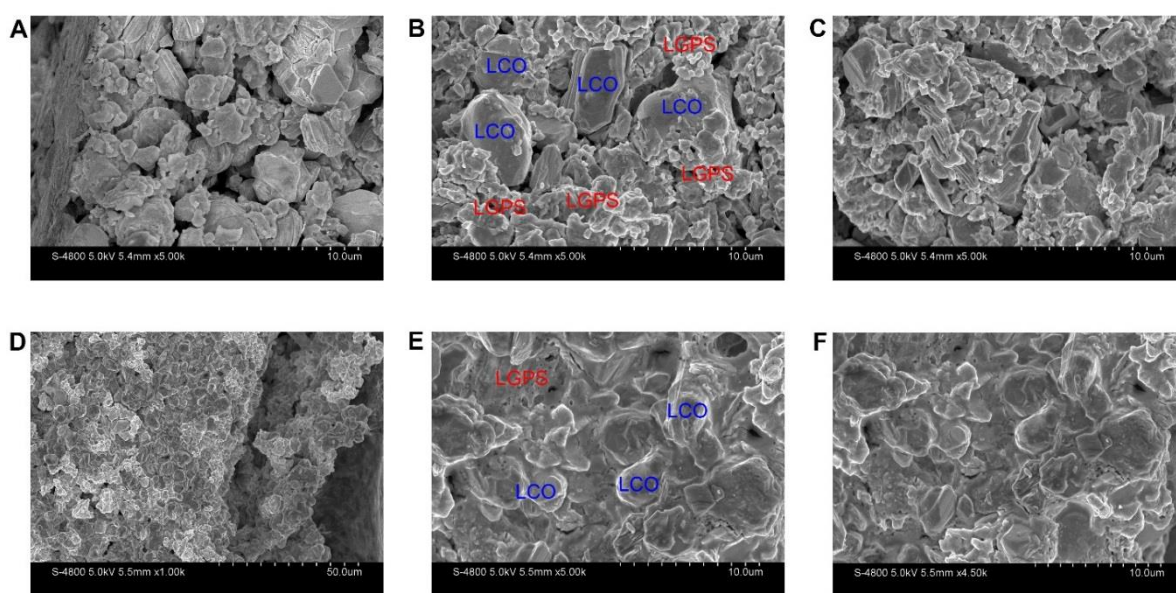


Figure 3-6 (A-C) one-shell LNO@LCO/LGPS electrodes. (D-F) dual shell structured LGPS@LNO@LCO electrodes.

To check the internal microstructure of one-shell LNO@LCO and dual shell LGPS@LNO@LCO, the cross-section of electrodes were examined by SEM. The LNO@LCO electrodes show a lot of pores between LGPS and LNO@LCO, which suggests the contact between LNO@LCO and LGPS is inferior (point-to-point contact,

Figure 3-6 A-C), limiting the Li^+ flux across the interface. As a sharp contrast, the dual shell structured LGPS@LNO@LCO shows favorable contact between LCO and LGPS. All the LNO@LCO particles are well dispersed in the LGPS matrix (**Figure 3-6 D-F**), thus providing abundant Li^+ flux across the interface and guaranteeing the high utilization of LCO. Resultantly, the initial charge-discharge curves, active material utilization, and Coulombic efficiency of dual shell structured LGPS@LNO@LCO exactly match those of LCO operated in LEs. All these results confirm that the dual shell interface could overcome the large interfacial resistance originated from the interfacial reactions and inferior interparticle contact between electrode materials and SEs in ASSLIBs.

3.4 Conclusions

In summary, we rationally designed a dual shell structured LGPS@LNO@LCO for high-performance SE-based ASSLIBs, in which the inner shell LiNbO_3 suppresses the interfacial reactions while the outer shell $\text{Li}_{10}\text{GeP}_2\text{S}_{12}$ enables intimate electrode-electrolyte contact. The interfacial reactions between LGPS and LCO characterized by the in-situ XANES and ex-situ XPS highlight the necessity of inner shell LNO. The outer shell LGPS coating realized by a universal wet-chemistry dispersion process enables the full utilization and negligible polarization of LCO in SE-based ASSLIBs. As a result, the dual shell structured $\text{Li}_{10}\text{GeP}_2\text{S}_{12}@LiNbO_3@LiCoO_2$ exhibits a high initial specific capacity of 125.8 mAh.g^{-1} (1.35 mAh.cm^{-2}) with an initial Coulombic efficiency of 90.4 % at 0.1 C and 87.7 mAh.g^{-1} at 1C. This dual shell nanostructure demonstrates an ideal interfacial configuration for achieving SE-based ASSLIBs with high-energy density and high-power density.

3.5 Acknowledgments

This work was supported by Natural Sciences and Engineering Research Council of Canada (NSERC), Canada Research Chair Program (CRC), Canada Foundation for Innovation (CFI), Ontario Research Fund (ORF), China Automotive Battery Research Institute Co., Ltd., Glabat Solid-State Battery Inc., Canada Light Source (CLS) at University of Saskatchewan, Interdisciplinary Development Initiatives (IDI) by Western University, and University of Western Ontario.

3.6 References

- [1] K. Xu, *Chem. Rev.* **2004**, *104*, 4303-4418.
- [2] aY. Kato, S. Hori, T. Saito, K. Suzuki, M. Hirayama, A. Mitsui, M. Yonemura, H. Iba, R. Kanno, *Nat. Energy* **2016**, *1*, 16030; bF. Han, J. Yue, C. Chen, N. Zhao, X. Fan, Z. Ma, T. Gao, F. Wang, X. Guo, C. Wang, *Joule* **2018**, *2*, 497-508; cJ. Janek, W. G. Zeier, *Nat. Energy* **2016**, *1*, 16141; dY. Zhao, K. Zheng, X. Sun, *Joule* **2018**, 1-22; eG. Zhonghui, S. Huabin, F. Lin, Y. Fangliang, Z. Yi, L. Wei, H. Yunhui, *Adv. Mater.* **2018**, *30*, 1705702; fK. H. Park, Q. Bai, D. H. Kim, D. Y. Oh, Y. Zhu, Y. Mo, Y. S. Jung, *Adv. Energy Mater.* **2018**, *8*, 1800035.
- [3] C. Wang, Q. Sun, Y. Liu, Y. Zhao, X. Li, X. Lin, M. N. Banis, M. Li, W. Li, K. R. Adair, D. Wang, J. Liang, R. Li, L. Zhang, R. Yang, S. Lu, X. Sun, *Nano Energy* **2018**, *48*, 35-43.
- [4] aW. Liu, S. W. Lee, D. Lin, F. Shi, S. Wang, A. D. Sendek, Y. Cui, *Nat. Energy* **2017**, *2*, 17035; bL. Yue, J. Ma, J. Zhang, J. Zhao, S. Dong, Z. Liu, G. Cui, L. Chen, *Energy Storage Mater.* **2016**, *5*, 139-164.

- [5] aY. Sun, K. Suzuki, S. Hori, M. Hirayama, R. Kanno, *Chem. Mater.* **2017**, *29*, 5858-5864; bS. J. Sedlmaier, S. Indris, C. Dietrich, M. Yavuz, C. Dräger, F. von Seggern, H. Sommer, J. Janek, *Chem. Mater.* **2017**, *29*, 1830-1835; cC. Wang, Y. Zhao, Q. Sun, X. Li, Y. Liu, J. Liang, X. Li, X. Lin, R. Li, K. R. Adair, L. Zhang, R. Yang, S. Lu, X. Sun, *Nano Energy* **2018**, *53*, 168-174.
- [6] aN. Kamaya, K. Homma, Y. Yamakawa, M. Hirayama, R. Kanno, M. Yonemura, T. Kamiyama, Y. Kato, S. Hama, K. Kawamoto, A. Mitsui, *Nat. Mater.* **2011**, *10*, 682-686; bS. P. Ong, Y. Mo, W. D. Richards, L. Miara, H. S. Lee, G. Ceder, *Energy Environ. Sci.* **2013**, *6*, 148-156.
- [7] aP. K. Ho, B. Qiang, K. D. Hyeon, O. D. Yang, Z. Yizhou, M. Yifei, J. Y. Seok, *Adv. Energy Mater.* **2018**, *0*, 1800035; bX. Chen, W. He, L.-X. Ding, S. Wang, H. Wang, *Energy Environ. Sci.* **2019**.
- [8] aN. Ohta, K. Takada, L. Zhang, R. Ma, M. Osada, T. Sasaki, *Adv. Mater.* **2006**, *18*, 2226-2229; bN. Ohta, K. Takada, I. Sakaguchi, L. Zhang, R. Ma, K. Fukuda, M. Osada, T. Sasaki, *Electrochem Commun.* **2007**, *9*, 1486-1490.
- [9] aD. H. Kim, D. Y. Oh, K. H. Park, Y. E. Choi, Y. J. Nam, H. A. Lee, S.-M. Lee, Y. S. Jung, *Nano Lett.* **2017**, *17*, 3013-3020; bK. H. Park, D. Y. Oh, Y. E. Choi, Y. J. Nam, L. Han, J.-Y. Kim, H. Xin, F. Lin, S. M. Oh, Y. S. Jung, *Adv. Mater.* **2016**, *28*, 1874-1883; cA. Banerjee, K. H. Park, J. W. Heo, Y. J. Nam, C. K. Moon, S. M. Oh, S.-T. Hong, Y. S. Jung, *Angew. Chem. Int. Ed.* **2016**, *55*, 9634-9638.
- [10] aF. D. Han, T. Gao, Y. J. Zhu, K. J. Gaskell, C. S. Wang, *Adv. Mater.* **2015**, *27*, 3473-3483; bX. Li, J. Liang, X. Li, C. Wang, J. Luo, R. Li, X. Sun, *Energy Environ. Sci.* **2018**, *11*, 2828-2832.

- [11]T. Asano, A. Sakai, S. Ouchi, M. Sakaida, A. Miyazaki, S. Hasegawa, *Adv. Mater.* **2018**, *0*, 1803075.
- [12]C. K. Chan, H. Peng, G. Liu, K. McIlwrath, X. F. Zhang, R. A. Huggins, Y. Cui, *Nat. Nanotech.* **2007**, *3*, 31.
- [13]X. L. Ji, K. T. Lee, L. F. Nazar, *Nat. Mater.* **2009**, *8*, 500-506.
- [14]D. Lin, Y. Liu, Z. Liang, H.-W. Lee, J. Sun, H. Wang, K. Yan, J. Xie, Y. Cui, *Nat. Nanotech.* **2016**, *11*, 626-632.
- [15]K. Takada, N. Ohta, L. Zhang, K. Fukuda, I. Sakaguchi, R. Ma, M. Osada, T. Sasaki, *Solid State Ion.* **2008**, *179*, 1333-1337.
- [16]M. Sumita, Y. Tanaka, M. Ikeda, T. Ohno, *J. Phys. Chem. C* **2016**, *120*, 13332-13339.
- [17]aB. Wang, Y. Zhao, M. N. Banis, Q. Sun, K. R. Adair, R. Li, T.-K. Sham, X. Sun, *ACS Appl. Mater. Interfaces* **2018**, *10*, 1654-1661; bY. Zhao, X. Sun, *ACS Energy Lett.* **2018**, *3*, 899-914.
- [18]aK. Suzuki, N. Mashimo, Y. Ikeda, T. Yokoi, M. Hirayama, R. Kanno, *ACS Appl. Energy Mater.* **2018**, *1*, 2373-2377; bJ. Kim, M. Eom, S. Noh, D. Shin, *J. Power Sources* **2013**, *244*, 476-481.
- [19]W. Zhang, F. H. Richter, S. P. Culver, T. Leichtweiss, J. G. Lozano, C. Dietrich, P. G. Bruce, W. G. Zeier, J. Janek, *ACS Appl. Mater. Interfaces* **2018**, *10*, 22226-22236.
- [20]X. Meng, X.-Q. Yang, X. Sun, *Adv. Mater.* **2012**, *24*, 3589-3615.
- [21]W. Zhang, T. Leichtweiß, S. P. Culver, R. Koerver, D. Das, D. A. Weber, W. G. Zeier, J. Janek, *ACS Appl. Mater. Interfaces* **2017**.

[22] Q. Liu, X. Su, D. Lei, Y. Qin, J. Wen, F. Guo, Y. A. Wu, Y. Rong, R. Kou, X. Xiao, F. Aguesse, J. Bareño, Y. Ren, W. Lu, Y. Li, *Nat. Energy* **2018**, *3*, 936-943.

[23] X. Li, M. Banis, A. Lushington, X. Yang, Q. Sun, Y. Zhao, C. Liu, Q. Li, B. Wang, W. Xiao, C. Wang, M. Li, J. Liang, R. Li, Y. Hu, L. Goncharova, H. Zhang, T.-K. Sham, X. Sun, *Nat. Commun.* **2018**, *9*, 4509.

[24] aF. D. Han, Y. Z. Zhu, X. F. He, Y. F. Mo, C. S. Wang, *Adv. Energy Mater.* **2016**, *6*, 9; bF. Wu, W. Fitzhugh, L. Ye, J. Ning, X. Li, *Nat Commun* **2018**, *9*, 4037.

3.7 Supporting Information

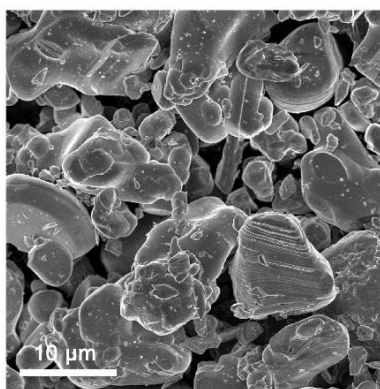


Figure 3-S1. The SEM image of pristine LiCoO₂ particles. The particle size is around 6~15 μm.

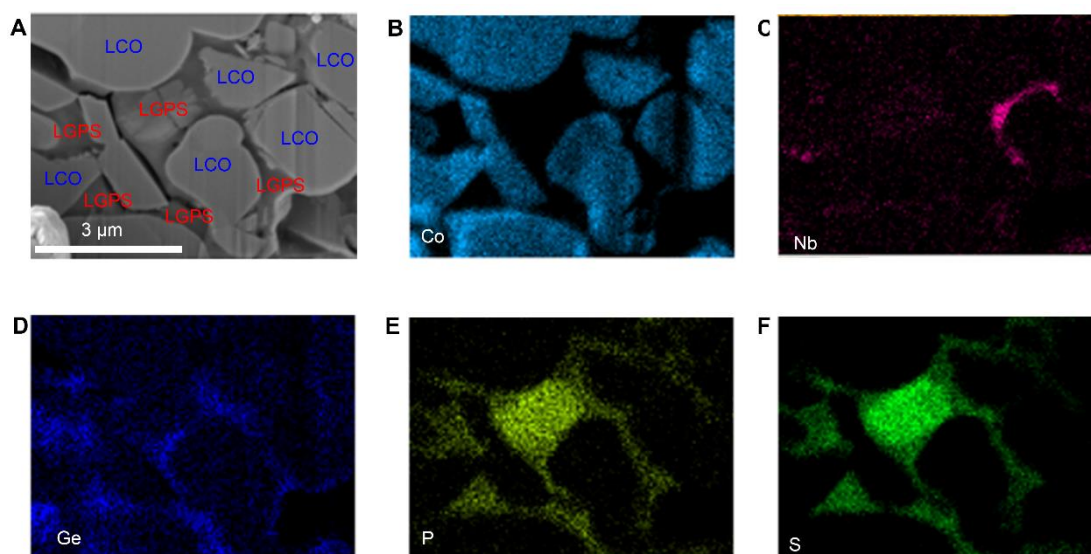


Figure 3-S2. The FIB cross-sectioned image of dual core-shell LGPS@LNO@LCO particles (A) and Co mapping (B), Nb mapping (C), Ge mapping (D), P mapping (E), and S mapping (F). It can be clearly seen that the LNO is conformably coated on LCO and LGPS is uniformly dispersed on LNO@LCO surfaces.

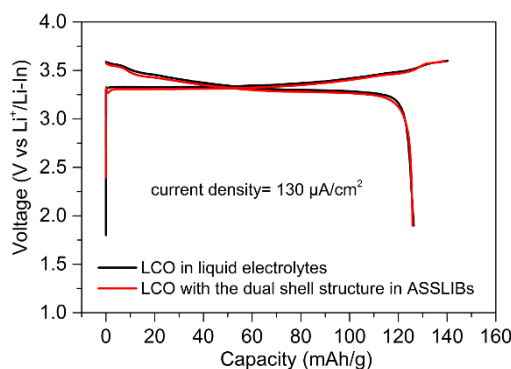


Figure 3-S4. The initial charge-discharge curves of LCO in liquid electrolytes and solid-electrolytes (LGPS). The tested current density is $0.13 \text{ mA}\cdot\text{cm}^{-2}$. The charge-discharge curves of dual shell LGPS@LNO@LCO are exactly the same with that liquid electrolytes, implying the full utilization and negligible polarization of LCO with dual shell interfacial structure in ASSLIBs.

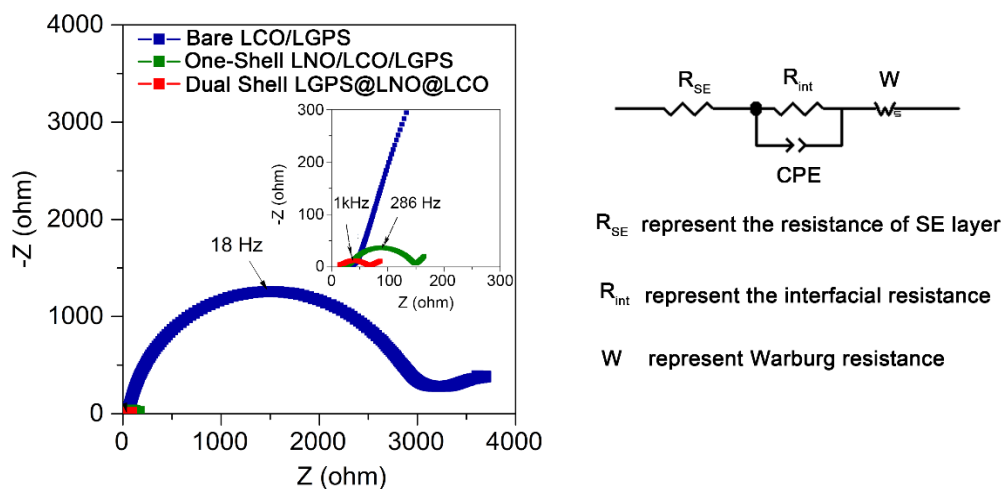


Figure 3-S5. Electrochemical impedance spectra of bare LCO/LGPS, one-shell LNO@LCO/LGPS, and dual shell LGPS@LNO@LCO after the initial charging process. The equivalent circuit shows that the impedance (R_{SE}) at the high frequency is related to the resistance of the solid electrolyte layer and the impedance at the middle frequency is corresponding to the interfacial resistance between LCO and LGPS (R_{int}). The resistance at high frequency is only 20 ohms, which is related to the resistance of the

solid-state LGPS layer. The pristine LCO exhibit a very large interfacial resistance at the middle frequency, which is over 3000 ohms, after the first charge process, indicating that the interfacial reactions between LGPS and LCO are very significant during the first charge process. Interestingly, the interfacial resistance is reduced to 150 ohms with LNO coating, suggesting that the inner shell LNO protection can dramatically suppress the interfacial reactions. Furthermore, the interfacial resistance is reduced to 68 ohms in the dual shell LGPS@LNO@LCO cathode, implying that the LGPS coating can enhance the Li^+ flux across the interface between LNO@LCO and LGPS.

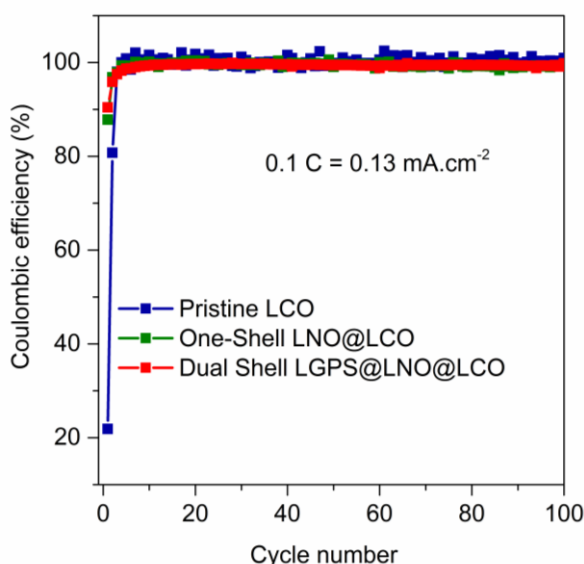


Figure 3-S6. The Coulombic efficiencies (CE) of pristine LCO, one-shell LNO@LCO, and dual shell structured LGPS@LNO@LCO within 100 cycles. The initial Coulombic efficiencies of pristine LCO, one-shell LNO@LCO, and dual shell structured LGPS@LNO@LCO are 21.8%, 89.1%, and 90.4 %, respectively. After 5 cycles, the following CEs tends to be stable. The CEs of one-shell LNO@LCO and dual shell structured LGPS@LNO@LCO are very close, which is about 99.5% to 99.8%.

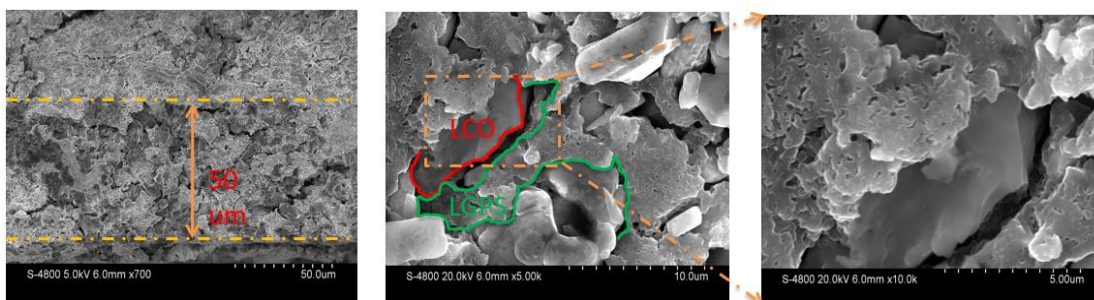


Figure 3-S7. The cross-section of the one-shell LNO@LCO/LGPS electrode after 100 cycles. It can be clearly seen that the volume change of LCO during the charge-discharge cycles could result in the loss contact between LCO and LGPS, thus leading to the capacity loss.

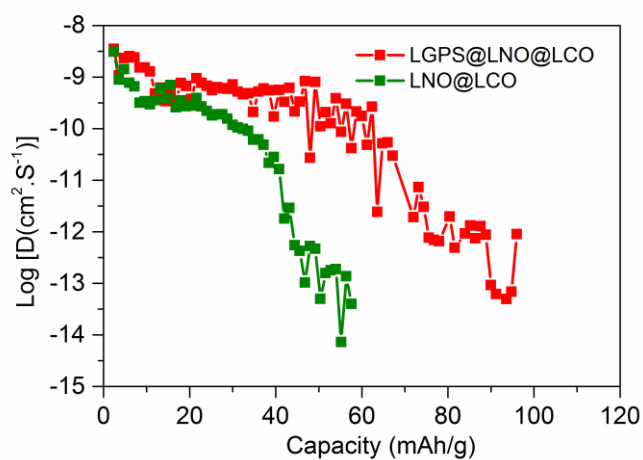


Figure 3-S8. The lithium-ion diffusion efficient calculated by GITT theoretical analysis.

According to the GITT theoretical analysis, Li^+ diffusion coefficient can be calculated by the following equation:

$$D = \frac{4}{\pi\tau} \left(\frac{m_{LCO} V_m}{M_{LCO} S} \right)^2 \left(\frac{\Delta E_s}{\Delta E_t} \right)^2$$

Where D is chemical diffusion coefficient, S is interfacial contact area between LCO and LGPS in our case, τ is pulse duration (300 s in our case), ΔE_s is the steady-state voltage change, ΔE_t is the transient voltage change, m_{LCO} is the mass of the LCO in the cathode composite (7 mg), M_{LCO} is the molecular weight of LiCoO_2 (97.87 g. mol^{-1}), V_m is the molar volume of the sample (LiCoO_2 , $19.56 \text{ cm}^3 \text{ mol}^{-1}$).^[2]

Table 3-S1. The Li^+ diffusion coefficient of LNO@LCO and LGPS@LNO@LCO.

Cathode	Li^+ diffusion coefficient	Specific Capacity (mAh.g^{-1})
Dual core-shell LGPS@LNO@LCO	2.08869×10^{-10}	50.4
Core-shell LNO@LCO	4.96749×10^{-14}	50.4

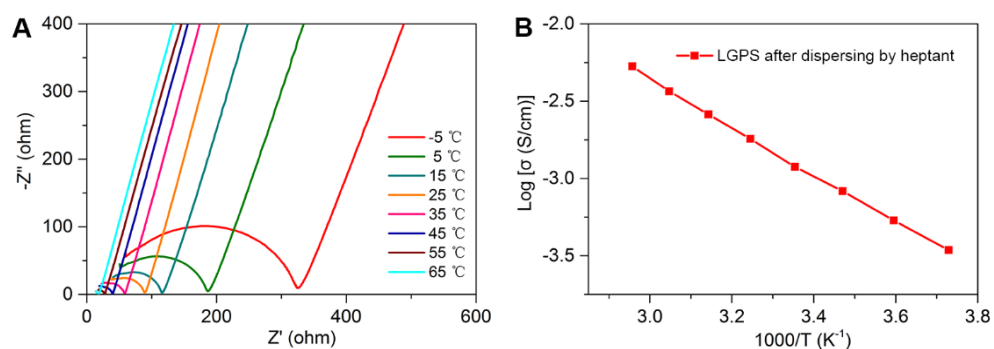


Figure 3-S9. (A) The EIS spectra of LGPS after dispersing by heptane at various temperatures. (B). Arrhenius plot of LGPS after dispersing by heptane. The room-temperature ionic conductivity of LGPS after dispersing by heptane is $1.2 \times 10^{-3} \text{ S.cm}^{-1}$.

Table 3-S2. The references for the Ragone plot.

Name	References
Ref #1	R. Mosthev, B. Johnson, <i>J. Power Sources</i> 2000 , <i>91</i> , 86. ^[3]
Ref #2	K. Takada et al. <i>Adv. Mater.</i> (2006), <i>18</i> , 2226-2229. DOI: 10.1002/adma.200502604. ^[4]
Ref #3	R. Kanno et al. <i>Nat. Mater.</i> (2011), <i>10</i> , 682-686 DOI: 10.1038/NMAT3066. ^[5]
Ref #4	J. Janek et al. <i>ACS Appl. Mater. Interfaces</i> (2017), <i>9</i> , 17835–17845 DOI: 10.1021/acsami.7b01137. ^[6]
Ref #5	Y-S Jung et al. <i>Adv. Mater.</i> (2016), <i>28</i> , 1874–1883. DOI: 10.1002/adma.201505008. ^[2b]

Table 3-S3. The specific area of the high-resolution XPS peaks.

Cathode	Binding Energy	Specific	Peak Assignment	Relative
Bare LCO/LGPS S 2p spectra	S 2p _{3/2} , 161.11 eV	694.585	PS ₄ ³⁻	45.5%
	S 2p _{1/2} , 162.29 eV	369.03		
	S 2p _{3/2} , 162.52 eV	464.78	-S ⁰ -S ⁰⁻ , or CoS _x	30.4%
	S 2p _{1/2} , 163.70 eV	232.79		
	S 2p _{3/2} , 166.38 eV	226.60	SO ₃ ²⁻	14.8%
	S 2p _{1/2} , 167.56 eV	113.30		
	S 2p _{3/2} , 168.37 eV	144.39	SO ₄ ²⁻	9.5%
	S 2p _{1/2} , 169.55 eV	72.19		
LNO@LCO/LGPS S 2p spectra	S 2p _{3/2} , 161.11 eV	757.33	PS ₄ ³⁻	59.5%
	S 2p _{1/2} , 162.29 eV	378.67		
	S 2p _{3/2} , 162.52 eV	399.12	-S ⁰ -S ⁰⁻ , or CoS _x	29.8%
	S 2p _{1/2} , 163.70 eV	199.56		
	S 2p _{3/2} , 166.38 eV	99.51	SO ₃ ²⁻	7.6%
	S 2p _{1/2} , 167.56 eV	49.75		
	S 2p _{3/2} , 168.37 eV	40.51	SO ₄ ²⁻	3.1%
	S 2p _{1/2} , 169.55 eV	20.25		

Bare LCO/LGPS P 2p spectra	P 2p3/2 , 131.58 eV	89.3	PS₄³⁻	36.4%
	P 2p1/2 , 132.42 eV	44.65		
	P 2p3/2 , 132.58 eV	156.4	P₂S₆²⁻	63.6%
	P 2p1/2 , 133.42 eV	78.2		
LNO@LCO/LGPS P 2p spectra	P 2p3/2 , 131.58 eV	223.2	PS₄³⁻	61.3%
	P 2p1/2 , 132.42 eV	111.6		
	P 2p3/2 , 132.58 eV	140.9	P₂S₆²⁻	38.7%
	P 2p1/2 , 133.42 eV	70.45		
Bare LCO/LGPS Ge 3d spectra	Ge 3d5/2 , 30.40 eV	48.44	GeS₂	21.6%
	Ge 3d3/2 , 30.99 eV	32.23		
	Ge 3d5/2 , 31.99 eV	176.21	GeO₂	78.4%
	Ge 3d3/2 , 32.57 eV	117.47		
LNO@LCO/LGPS Ge 3d spectra	Ge 3d5/2 , 30.40 eV	76.78	GeS₂	60.4%
	Ge 3d3/2 , 30.99 eV	51.19		
	Ge 3d5/2 , 31.41 eV	50.28	GeO_x	39.6%
	Ge 3d3/2 , 32 eV	33.52		

The relative ratio of peak area is marked in red (Bare LCO/LGPS) and blue (LNO@LCO/LGPS). It can be clearly seen that the peak area of PS_4^{3-} and GeS_2 is significantly reduced in bare LCO/LGPS, while the peak area of PS_4^{3-} and GeS_2 is partially reduced in LNO@LCO/LGPS, suggesting that the inner shell LNO can inhibit the interfacial reactions between LCO and LGPS to some extent.

References

- [1] B. Wang, Y. Zhao, M. N. Banis, Q. Sun, K. R. Adair, R. Li, T.-K. Sham, X. Sun, *ACS Appl. Mater. Interfaces* **2018**, *10*, 1654-1661.
- [2] aX. H. Rui, N. Ding, J. Liu, C. Li, C. H. Chen, *Electrochimica Acta* **2010**, *55*, 2384-2390; bK. H. Park, D. Y. Oh, Y. E. Choi, Y. J. Nam, L. Han, J.-Y. Kim, H. Xin, F. Lin, S. M. Oh, Y. S. Jung, *Adv. Mater.* **2016**, *28*, 1874-1883.
- [3] R. Moshtev, B. Johnson, *J. Power Sources* **2000**, *91*, 86-91.
- [4] N. Ohta, K. Takada, L. Zhang, R. Ma, M. Osada, T. Sasaki, *Adv. Mater.* **2006**, *18*, 2226-2229.
- [5] N. Kamaya, K. Homma, Y. Yamakawa, M. Hirayama, R. Kanno, M. Yonemura, T. Kamiyama, Y. Kato, S. Hama, K. Kawamoto, A. Mitsui, *Nat. Mater.* **2011**, *10*, 682-686.
- [6] W. Zhang, D. A. Weber, H. Weigand, T. Arlt, I. Manke, D. Schröder, R. Koerver, T. Leichtweiss, P. Hartmann, W. G. Zeier, J. Janek, *ACS Appl. Mater. Interfaces* **2017**, *9*, 17835-17845.

Chapter 4

4. Single Crystal Cathodes Increasing Power and Energy Density of All-Solid-State Batteries*

LiCoO₂ has been widely studied in ASSLIBs, however, its capacity is much lower than mainstream LiNi_xMn_yCo_zO₂ (x+y+z=1, NMC) cathodes. Therefore, high-capacity NMC cathodes should be investigated in ASSLIBs to enable high energy density.

In this work, single-crystal Li(Ni_{0.5}Mn_{0.3}Co_{0.2})O₂ (SC-NMC532) is used as the cathode material for ASSLIBs, which exhibits 6~14 times higher Li⁺ diffusion coefficient than polycrystalline Li(Ni_{0.5}Mn_{0.3}Co_{0.2})O₂ (PC-NMC532). As a result, SC-NMC532 exhibits an initial specific capacity of 151.2 mAh.g⁻¹ while PC-NMC532 shows an initial capacity of only 111.9 mAh.g⁻¹. After 150 cycles, SC-NMC532 retains a capacity of 88.9 mAh.g⁻¹. More impressively, under a high current density of 1.3 mA.cm⁻², SC-NMC532 exhibits a capacity of 82 mAh.g⁻¹, much higher than the 2.1 mAh.g⁻¹ capacity of PC-NMC532. This work demonstrates that single-crystal NMC cathodes could enable both high power density and high energy density in ASSLIBs at room temperature.

*Note: This work will be submitted.

Changhong Wang, Sooyeon Hwang, Jianwen Liang, Xiaona Li, Changtai Zhao, Yipeng Sun, Jiwei Wang, Nathaniel Holmes, Ruying Li, Huan Huang, Shangqian Zhao, Li Zhang, Shigang Lu, Dong Su, and Xueliang Sun, Single Crystal Cathodes Enabling High-Energy and High-Power All-Solid-State Lithium-Ion Batteries. **In preparation.**

4.1 Introduction

Rechargeable lithium-ion batteries (LIBs) are widely used in electric vehicles and portable electronic devices.^{1, 2} However, the use of flammable organic liquid electrolytes with narrow electrochemical windows presents safety challenges and places a constraint on the energy density of LIBs.³ To eliminate safety concerns, replacing liquid electrolytes with inorganic solid-state electrolytes in LIBs is regarded as the ultimate solution. All-solid-state LIBs (ASSLIBs) also allow for increased energy density by employing bi-polar stacking technology and using high-voltage cathodes and lithium metal anodes.⁴⁻⁷ Owing to the significant improvements in safety and energy density, ASSLIBs have attracted considerable attention in recent years.⁸⁻¹⁰

Several challenges hinder the development of ASSLIBs, including (1) insufficient ionic conductivity of solid-state electrolytes,^{11, 12} (2) large interfacial resistance due to poor solid-solid contact and detrimental interfacial reactions,¹³⁻¹⁶ and (3) poor rate performance due to slow lithium-ion (Li^+) kinetics in ASSLIBs.¹⁷⁻¹⁹ With continuous efforts over the past decades, many solid-state electrolytes with high ionic conductivity have been developed. The ionic conductivities of solid-state sulfide electrolytes (SEs), $\text{Li}_{9.54}\text{Si}_{1.74}\text{P}_{1.44}\text{S}_{11.7}\text{Cl}_{0.3}$ ($25 \text{ mS}\cdot\text{cm}^{-1}$)⁴, $\text{Li}_{10}\text{GeP}_2\text{S}_{12}$ (LGPS, $12 \text{ mS}\cdot\text{cm}^{-1}$),²⁰ and $\text{Li}_7\text{P}_3\text{S}_{11}$ ($17 \text{ mS}\cdot\text{cm}^{-1}$)²¹ surpass even that of liquid electrolytes ($10.2 \text{ mS}\cdot\text{cm}^{-1}$).²² Sulfide-based ASSBs are therefore regarded as one of the most promising solid-state battery systems. To address the problem of large interfacial resistance, many soluble SSEs have been reported which, when coated on cathode materials or infiltrated into the electrode sheet, significantly reduce the interfacial resistance between electrodes and SEs.²³⁻²⁹ In addition, various interfacial buffer layers (i.e. LiNbO_3 , LiTaO_3) have been developed to effectively prevent the interfacial reactions between oxide cathodes and SEs.^{15, 30, 31}

In contrast to the tremendous effort toward improving the ionic conductivity of SEs and

suppressing interfacial resistance, few attempts have been made to improve the rate capability of ASSLIBs. In this work, we explore the electrochemical performance of single-crystal $\text{Li}(\text{Ni}_{0.5}\text{Mn}_{0.3}\text{Co}_{0.2})\text{O}_2$ (SC-NMC532) in SE-based ASSBs for the first time. It is found that the Li^+ diffusion coefficient of SC-NMC532 is 6~14 times higher than that of polycrystalline (PC) NMC532. As a result, SC-NMC532 demonstrates a higher discharge capacity and significantly improved rate performance when compared to PC-NMC532. This work suggests that using single-crystal NMC could enable both high energy density and high power density ASSLIBs.

4.2 Experiments and Characterizations

4.2.1 Surface Modification of SC-NMC532 and PC-NMC532

Stoichiometric amounts of lithium acetate (LiCO_2CH_3 , Sigma-Aldrich, 99.99%), niobium(V) ethoxide ($\text{Nb}(\text{OCH}_2\text{CH}_3)_5$, Sigma-Aldrich, 99.95%, trace metals basis), and tantalum(V) butoxide ($\text{Ta}(\text{OCH}_2\text{CH}_2\text{CH}_2\text{CH}_3)_5$, Sigma-Aldrich, 99.99%, trace metals basis) were dissolved in absolute ethanol (Sigma-Aldrich, >99.8%, GC) and stirred magnetically for 2 hours. The mass fraction of LNTO sol-gel in absolute ethanol was diluted to 10%. 2 g of single-crystal $\text{LiNi}_{0.5}\text{Mn}_{0.3}\text{Co}_{0.2}\text{O}_2$ (SC-NMC532) or polycrystalline $\text{LiNi}_{0.5}\text{Mn}_{0.3}\text{Co}_{0.2}\text{O}_2$ (PC-NMC532) (supplied from the China Automotive Battery Research Institute) was dispersed into 5ml absolute ethanol. 2 wt% LNTO was then added to the NMC532 solution. After magnetically stirring for 2 hours, the solution was dried at 80°C. The powder was further dried under vacuum at 100°C overnight and annealed in air at 450°C for 2 hours. The samples are identified as LNTO@NMC532, and LNTO@PC-NMC532, respectively.

4.2.2 Characterizations

Transmission electron microscopy (TEM) was performed with a JEM-2100 operated at

200 kV. Scanning Transmission Electron Microscopy (STEM)-Energy Dispersive Spectroscopy (EDS) mapping was done with an FEI Talos F200X TEM (operated at 200 keV) equipped with an energy dispersive X-ray spectrometer. Scanning Electron Microscope (SEM) images were recorded with an SEM-4800. Powder X-ray diffraction (XRD) patterns were collected on a Bruker AXS D8 Advance with Cu K α radiation ($\lambda = 1.54178 \text{ \AA}$) and a special holder to avoid exposure to air during tests.

4.2.3 Assembly of ASSLIBs

70 mg of LNT@SC-NMC532 and 30 mg of commercial Li₁₀GeP₂S₁₂ (LGPS) (purchased from MSE supplies) were mixed to serve as the cathode composite. 80 mg of LGPS was first pressed at 1 MPa. 12 mg of cathode composite was then uniformly spread on one side of the LGPS layer and compressed at 350 MPa. A piece of indium foil was positioned on the other side of LGPS and pressed at 100 MPa. Then the battery rested for 3 hours before electrochemical testing. The electrochemical impedance spectra were recorded from 7 MHz to 0.1 Hz with an amplitude of 10 mV. CV was performed from 1.9V to 3.8V with a scan rate of 0.02 mV.s⁻¹. GITT tests were performed with a 5 min discharge at 0.1C followed by 2 hours of relaxation. The mass loading of NMC532 was 10.7 mg.cm⁻². 1C is defined at 0.13 mA.cm⁻². All electrochemical performance tests were performed at room temperature by a LAND electrochemical analysis system.

4.3. Results and Discussion

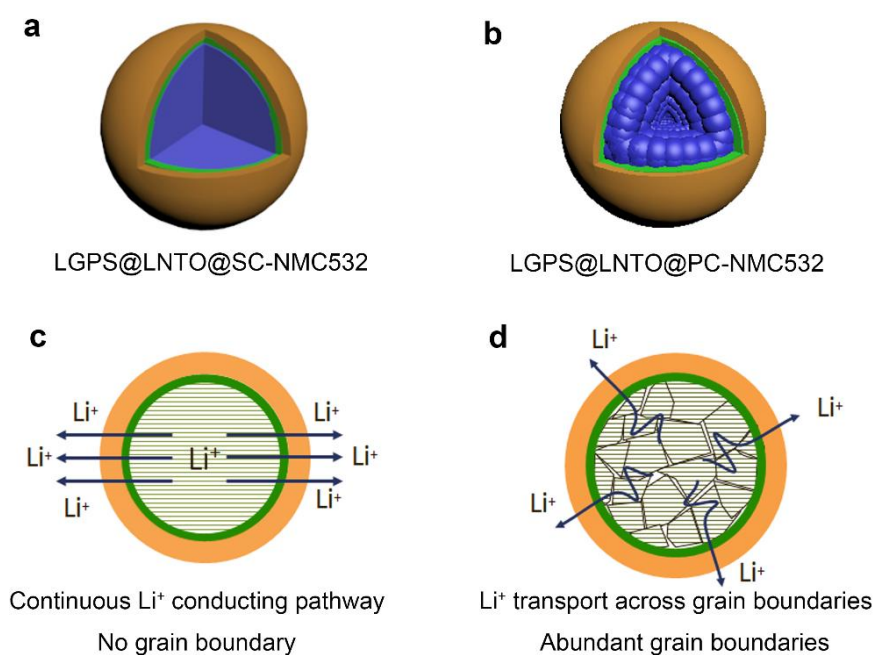


Figure 4-1 (a) Illustration of SC-NMC532 in SE-based ASSBs. (b) Illustration of PC-NMC532 in SE-based ASSBs. (c) A cross-sectional image of LGPS@LNTO@SC-NMC532, in which Li⁺ has a continuous conducting pathway. (d) A cross-sectional image of LGPS@LNTO@PC-NMC532, in which Li⁺ is transported across many grain boundaries.

$\text{Li}_{10}\text{GeP}_2\text{S}_{12}$ (LGPS), which exhibits a high ionic conductivity of $3.5 \times 10^{-3} \text{ S.cm}^{-1}$ (Figure 4-S1), was used as the solid-state electrolyte for this study. To prevent interfacial reactions between the oxide cathode and SE, an interfacial layer of LiNbTaO_3 (LNTO) was inserted between the NMC532 and LGPS (Figure 4-1a and 4-1b). Unlike in liquid cells, the solid-state electrolyte LGPS only contacts the NMC532 through solid-solid contact. PC-NMC532 cathodes possess many grain boundaries within each micro-spherical particle, requiring Li⁺ to pass through many grain boundaries before reaching the solid-state electrolyte (Figure 4-1d). In contrast, SC-NMC532 cathodes do

not contain grain boundaries, thus providing continuous Li^+ conduction pathways (**Figure 4-1c**). SC-NMC532 is therefore believed to possess faster Li^+ kinetics than PC-NMC532 in ASSLIBs.

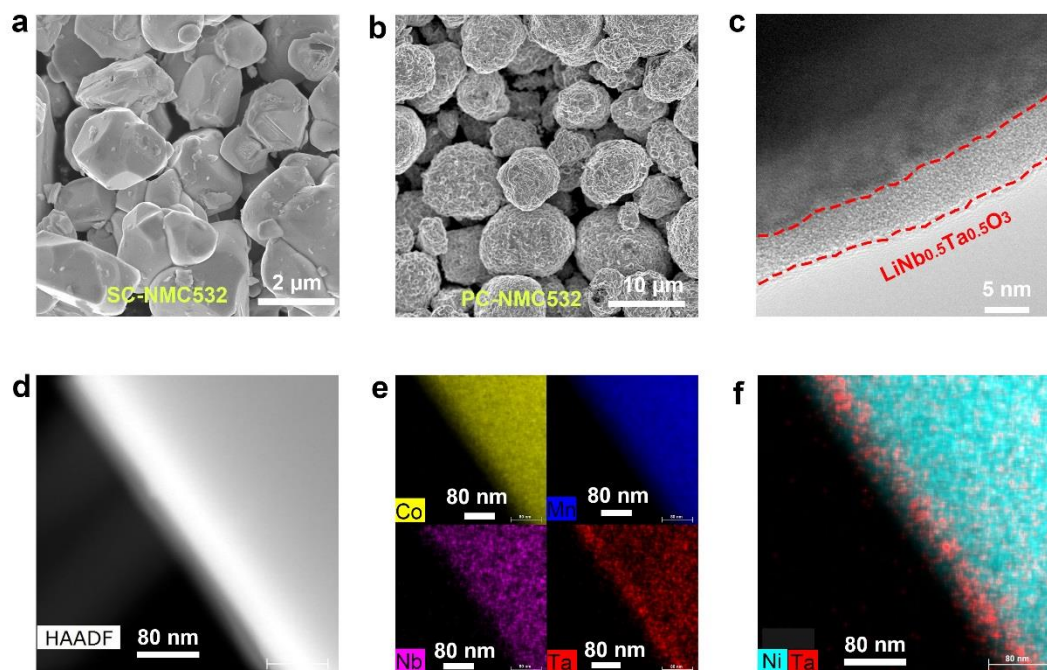


Figure 4-2 Structural Characterization of LNTO@SC-NMC532 and LNTO@PC-NMC532. (a) An SEM image of LNTO@SC-NMC532. (b) An SEM image of LNTO@PC-NMC532. (c) HRTEM image of LNTO@SC-NMC532. (d) HAADF image of LNTO@SC-NMC532 and (e) Co, Mn, Nb, and Ta mapping. (f) A combination of Ni and Ta elemental maps of LNTO@SC-NMC532 acquired with STEM-EDX.

To verify this assumption, LNTO-coated SC-NMC532 and LNTO-coated NMC532 were prepared, scanning electron microscopy (SEM) images of which are presented in **Figure 4-2a** and **4-2b** respectively. The SC-NMC532 samples are single particles with a diameter of about 2~10 μm while the PC-NMC532 samples are secondary microspheres with a diameter of approximately 2~15 μm . The thickness of the LNTO interfacial

coating layer was about 7 nm, as revealed by the scanning transmission electron microscopy (STEM) image in **Figure 4-2c**. To confirm the uniformity of the LNTO coating, SEM-energy dispersive X-ray spectroscopy elemental mappings of Ni, Co, Mn, Nb, and Ta are presented in **Figure 4-S2**. The uniform mapping of Nb and Ta on the SC-NMC532 implies the presence of a uniform LNTO layer. The high-angle annular dark-field (HAADF) image of LNTO-coated SC-NMC532 (**Figure 4-2d**) and STEM-energy dispersive X-ray spectroscopy elemental maps of Co, Mn, Nb, and Ta (**Figure 4-2e**) also indicate a homogenous distribution of all elements. In addition, the combined map of Ni and Ta in the LNTO-coated SC-NMC532 shows that Ta has a strong signal at the edge (**Figure 4-2f**), further suggesting that the LNTO was uniformly coated on the SC-NMC532. X-ray diffraction (XRD) patterns of LNTO-coated SC-NMC532 and LNTO-coated PC-NMC532 are compared in **Figure 4-S3**. No LNTO diffraction patterns are detected, indicating that the LNTO coating is amorphous. Interestingly, the (104) peak for SC-NMC532 at 44.6° is split, a typical characteristic of single-crystal NMC cathodes caused by the separation of $K_{\alpha 1}$ and $K_{\alpha 2}$ reflected from the (104) lattice plane in SC-NMC532.³²⁻³⁴

The electrochemical performance of SC-NMC532 and PC-NMC532 in SE-based ASSLIBs was first tested under a current density of 0.1C (1C=1.3 mA.cm⁻²). SC-NMC532 demonstrated a charge capacity of 180.2 mAh.g⁻¹ and a discharge capacity of 151.2 mAh.g⁻¹ with an initial Coulombic efficiency of 83.9% (**Figure 4-3a**). Comparatively, PC-NMC532 displayed a discharge capacity of only 111.9 mAh.g⁻¹. In addition, the discharge plateau of SC-NMC532 is much higher than that of PC-NMC532, indicating that SC-NMC532 possesses faster Li⁺ kinetics than PC-NMC532. Furthermore, an electrochemical impedance spectroscopy (EIS) analysis (**Figure 4-S4**) reveals the charge transfer resistance of SC-NMC532 to be about 181 Ω , which is significantly lower than that of PC-NMC532 (463 Ω). The EIS analysis provides further evidence of improved Li⁺ kinetics in SC-NMC532.

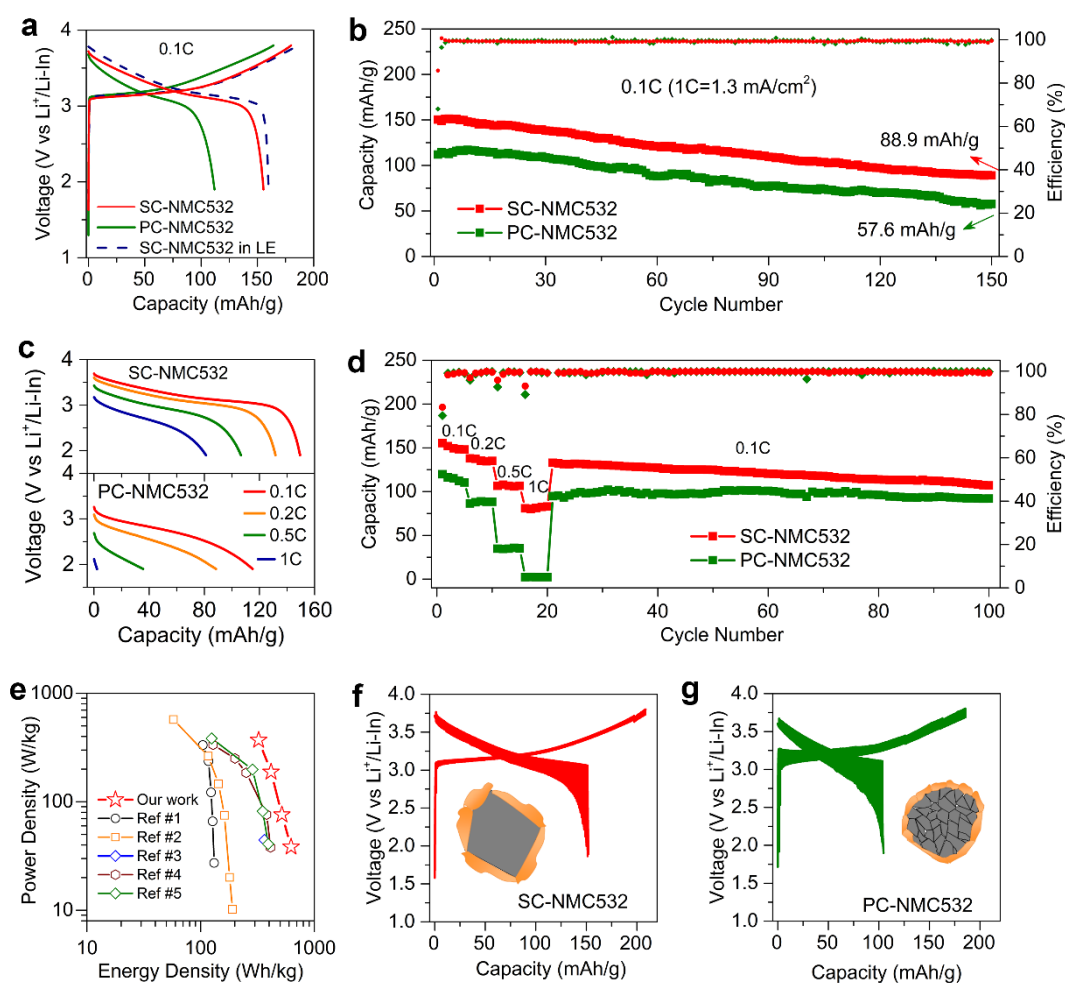


Figure 4-3 Electrochemical Performance of LNTO@SC-NMC532 and LNTO@PC-NMC532. (a) Initial charge/discharge curves of SC-NMC532, PC-NMC532, and pristine SC-NMC532 in the conventional liquid electrolyte (LE). (b) Cycling stability of SC-NMC532 and PC-NMC532. (c) Discharge curves of SC-NMC532 and PC-NMC532 under various current densities. (d) Rate performance of SC-NMC532 and PC-NMC532. (e) The Ragone plots of SC-NMC632-based ASSLIBs and previously reported ASSLIBs. (f) Charging-discharging GITT curves of SC-NMC532. (g) Charging-discharging GITT curves of PC-NMC532.

Figure 4-3b displays the cycling stability of SC-NMC532 and PC-NMC532. After 150 cycles, the SC-NMC532 retains a specific capacity of 88.9 mAh.g⁻¹ while PC-NMC532 retains a specific capacity of only 57.6 mAh.g⁻¹. The corresponding decay rate of SC-NMC532 is 0.35%, which is slightly lower than that of PC-NMC532 (0.44%). The good cycling stability indicates that the interfacial LNT0 coating effectively suppresses interfacial reactions. The cyclic voltammetry (CV) profiles for SC-NMC532 and PC-NMC532 clearly show the redox peaks of Ni²⁺/Ni⁴⁺ and Ni³⁺/Ni⁴⁺ at around 3.3V (vs. Li⁺/Li-In) (**Figure 4-S5**). The overlapping of the oxidation/reduction peaks implies that SC-NMC532 has good electrochemical reversibility in SE-based ASSLIBs. The peak currents of SC-NMC532 are higher than those of PC-NMC532, and the polarization of SC-NMC532 is less than that of PC-NMC532. These findings are consistent with the charge/discharge curves in **Figure 4-3a**.

The rate performance of SC-NMC532 and PC-NMC532 from 0.1C to 1C is presented in **Figure 4-3d** and the corresponding discharge curves at various C-rates are depicted in **Figure 4-3c**. PC-NMC532 cannot be discharged at 1C due to significant voltage hysteresis (**Figure 4-3e**), while SC-NMC532 shows a discharge capacity of 82 mAh.g⁻¹ at 1C. It should be mentioned that the inferior rate-performance of polycrystalline NMC cathodes as tabulated in **Table 4-S1**, has been reported multiple times prior to this work^{18, 35, 36}. **Figure 4-3e** displays the Ragone plots of SC-NMC532-based ASSLIBs and previously reported promising ASSLIBs at room temperature. Detailed references are listed in **Table 4-S2**. Obviously, SC-NMC532-based ASSLIBs offer the highest energy density and power density, suggesting that the high theoretical power density of ASSLIBs will be more readily realized by using single-crystal NMC cathodes instead of polycrystalline.

The disparity in rate-performance between SC-NMC532 and PC-NMC532 strongly suggests that SC-NMC532 has faster Li⁺ kinetics than PC-NMC532 in ASSLIBs. To

quantify the Li^+ diffusion coefficients, both SC-NMC532 and PC-NMC532 were tested during the initial charge/discharge process using the galvanostatic intermittent titration technique (GITT) (Figure 4-3g and 4-3h). Both the polarization and Li^+ diffusion coefficients of SC-NMC532 and PC-NMC532 are calculated based on the initial charge and discharge process separately and discussed in Figure 4-4.

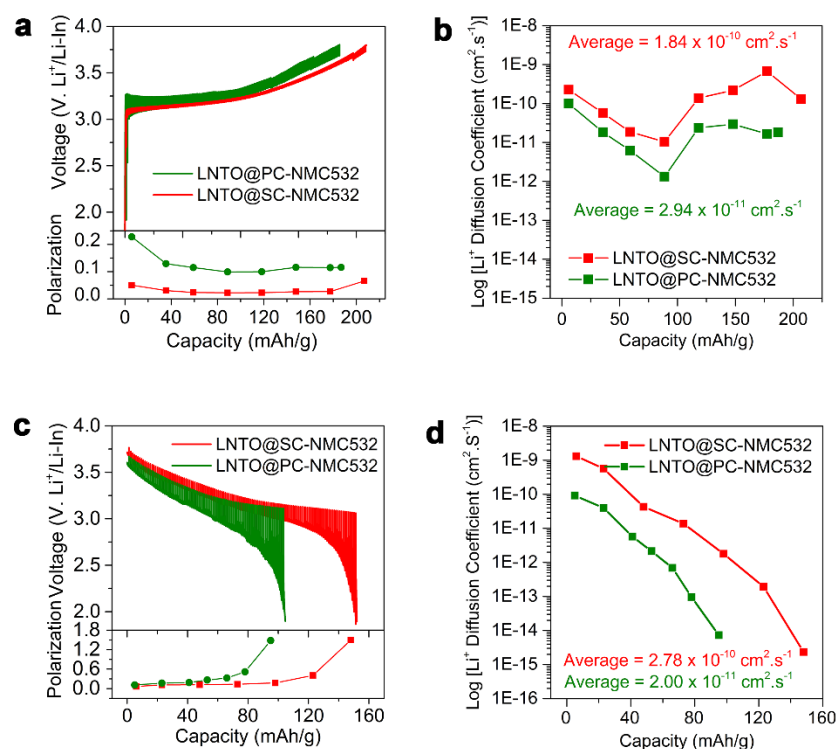


Figure 4-4 Quantification of Li^+ diffusion coefficients of SC-NMC532 and PC-NMC532 during the initial charge/discharge process. (a) Comparison of the GITT behavior and polarization curves during the initial charge process. (b) Li^+ diffusion coefficients of LNT0@SC-NMC532 and LNT0@PC-NMC532 at different charge states. (c) Comparison of GITT behavior and polarization curves during the initial discharge process. (d) Li^+ diffusion coefficients of LNT0@SC-NMC532 and LNT0@PC-NMC532 at different discharge states.

Based on the GITT results, the Li^+ diffusion coefficient can be calculated with the equation:^{23, 37}

$$D_{\text{Li}^+} = \frac{4}{\pi\tau} \left(\frac{m_{\text{NMC532}} V_{\text{NMC532}}}{M_{\text{NMC532}} S} \right)^2 \left(\frac{\Delta E_s}{\Delta E_\tau} \right)^2 \quad (1)$$

where τ is the relaxation time (2 hours), m_{NMC532} is the actual mass of SC-NMC532 in the electrode composite, V_{NMC532} is the molar volume of SC-NMC532 ($20.73 \text{ cm}^3 \cdot \text{mol}^{-1}$), M_{NMC532} is the molar mass of the host materials SC-Li(Ni_{0.5}Mn_{0.3}Co_{0.2})O₂ ($96.58 \text{ g} \cdot \text{mol}^{-1}$), ΔE_s the steady-voltage change after 2 hours of relaxation and ΔE_τ is the change in the transient-voltage change after a 5 min discharge process at $0.13 \text{ mA} \cdot \text{cm}^{-2}$.

Figure 4-4a compares the GITT curve and electrochemical polarization of SC-NMC532 and PC-NMC532 during the charging process. The electrochemical polarization of SC-NMC532 is less than 50 mV while that of PC-NMC532 is over 110 mV. The average Li^+ diffusion coefficient of SC-NMC532 is $1.84 \times 10^{-10} \text{ cm}^2 \cdot \text{s}^{-1}$ during the initial charge process, 6.25 times higher than that of PC-NMC532 ($2.94 \times 10^{-11} \text{ cm}^2 \cdot \text{s}^{-1}$) (**Figure 4-4b**). **Figure 4-4c** shows the GITT profile and polarization voltage of SC-NMC532 and PC-NMC532 during the initial discharging process. The discharging polarization voltage of SC-NMC532 ($< 180 \text{ mV}$) is also smaller than that of PC-NMC532 ($\sim 300 \text{ mV}$). The increased polarization at the end of the discharge process is due to the saturation of Li^+ sites in the NMC532 crystal structure.³⁸ The average Li^+ diffusion coefficient for SC-NMC532 ($2.78 \times 10^{-10} \text{ cm}^2 \cdot \text{s}^{-1}$) during the discharge process is almost 13.9 times higher than that of LNT@PC-NMC532 ($2.00 \times 10^{-11} \text{ cm}^2 \cdot \text{s}^{-1}$). Overall, SC-NMC532 exhibits a Li^+ diffusion coefficient of 6~14 times higher than PC-NMC532 in ASSLIBs. Single-crystal NMC cathodes, therefore, have the potential to enable simultaneously high energy-density and power-density ASSLIBs at room temperature.

4.4. Conclusions

In summary, we systematically evaluated the electrochemical performance of SC-NMC532 in SE-based ASSLIBs. SC-NMC532 exhibits a Li^+ diffusion coefficient of 6~14 times higher than PC-NMC532. Consequently, SC-NMC532 exhibits an initial specific capacity of 151.2 mAh.g^{-1} and retains a specific capacity of 88.9 mAh.g^{-1} after 150 cycles. More importantly, SC-NMC532 exhibits a specific capacity of 82 mAh.g^{-1} under a high current density of 1.3 mA.cm^{-2} while PC-NMC532 only shows 2.1 mAh.g^{-1} . This work demonstrates that single-crystal NMC cathodes present a new avenue toward ASSLIBs with high energy density and high power density at room temperature.

4.5 Acknowledgements

This work was supported by Natural Sciences and Engineering Research Council of Canada (NSERC), Canada Research Chair Program (CRC), Canada Foundation for Innovation (CFI), Ontario Research Fund, China Automotive Battery Research Institute Co., Ltd, Glatat Solid-State Battery Inc., the Canada Light Source at University of Saskatchewan (CLS), Interdisciplinary Development Initiatives (IDI) by Western University, and University of Western Ontario. J.L. and X. L. thank the support of Mitacs Elevate Postdoctoral Fellowship. C.W. appreciates the funding support of the Mitacs Accelerate Fellowship. This research used resources of the Center for Functional Nanomaterials, which is a U.S. DOE Office of Science Facility, at Brookhaven National Laboratory under Contract No. DE-SC0012704.

4.6 References

1. Y. Zhao, K. Zheng and X. Sun, *Joule*, 2018, 1-22.
2. J. W. Choi and D. Aurbach, *Nat. Rev. Mater.*, 2016, **1**, 16013.
3. T. Famprakis, P. Canepa, J. A. Dawson, M. S. Islam, and C. Masquelier, *Nat. Mater.*, 2019, DOI: 10.1038/s41563-019-0431-3, doi:<https://doi.org/10.1038/s41563-41019-40431-41563>.
4. Y. Kato, S. Hori, T. Saito, K. Suzuki, M. Hirayama, A. Mitsui, M. Yonemura, H. Iba, and R. Kanno, *Nat. Energy*, 2016, **1**, 16030.
5. Y. Shen, Y. Zhang, S. Han, J. Wang, Z. Peng and L. Chen, *Joule*, 2018.
6. L. Liu, J. Xu, S. Wang, F. Wu, H. Li and L. Chen, *eTransportation*, 2019, **1**, 100010.
7. C. Wang, Y. Zhao, Q. Sun, X. Li, Y. Liu, J. Liang, X. Li, X. Lin, R. Li, K. R. Adair, L. Zhang, R. Yang, S. Lu and X. Sun, *Nano Energy*, 2018, **53**, 168-174.
8. A. Manthiram, X. Yu and S. Wang, *Nat. Rev. Mater.*, 2017, **2**, 16103.
9. J. Li, C. Ma, M. Chi, C. Liang, and N. J. Dudney, *Advanced Energy Materials*, 2015, **5**, 1401408.
10. C. Wang, Q. Sun, Y. Liu, Y. Zhao, X. Li, X. Lin, M. N. Banis, M. Li, W. Li, K. R. Adair, D. Wang, J. Liang, R. Li, L. Zhang, R. Yang, S. Lu and X. Sun, *Nano Energy*, 2018, **48**, 35-43.
11. Y. Wang, W. D. Richards, S. P. Ong, L. J. Miara, J. C. Kim, Y. Mo and G. Ceder, *Nat Mater*, 2015, **14**, 1026-1031.

12. X. Li, J. Liang, J. Luo, M. Norouzi Banis, C. Wang, W. Li, S. Deng, C. Yu, F. Zhao, Y. Hu, T.-K. Sham, L. Zhang, S. Zhao, S. Lu, H. Huang, R. Li, K. R. Adair and X. Sun, *Energy Environ. Sci.*, 2019, DOI: 10.1039/C9EE02311A.
13. W. D. Richards, L. J. Miara, Y. Wang, J. C. Kim and G. Ceder, *Chem. Mater.*, 2016, **28**, 266-273.
14. Y. Zhu, X. He and Y. Mo, *J. Mater. Chem. A*, 2016, **4**, 3253-3266.
15. C. Wang, X. Li, Y. Zhao, M. N. Banis, J. Liang, X. Li, Y. Sun, K. R. Adair, Q. Sun, Y. Liu, F. Zhao, S. Deng, X. Lin, R. Li, Y. Hu, T.-K. Sham, H. Huang, L. Zhang, R. Yang, S. Lu and X. Sun, *Small Methods*, 2019, **1900261**, DOI:10.1002/smt.201900261.
16. Q. Zhang, D. Cao, Y. Ma, A. Natan, P. Aurora and H. Zhu, *Advanced Materials*, **0**, 1901131.
17. F. Strauss, T. Bartsch, L. de Biasi, A. Y. Kim, J. Janek, P. Hartmann, and T. Brezesinski, *ACS Energy Lett.*, 2018, DOI: 10.1021/acseenergylett.8b00275, 992-996.
18. R. Koerver, I. Aygün, T. Leichtweiß, C. Dietrich, W. Zhang, J. O. Binder, P. Hartmann, W. G. Zeier, and J. Janek, *Chem. Mater.*, 2017, **19**, 5574-5582.
19. N. Ohta, K. Takada, L. Zhang, R. Ma, M. Osada, and T. Sasaki, *Adv. Mater.*, 2006, **18**, 2226-2229.
20. N. Kamaya, K. Homma, Y. Yamakawa, M. Hirayama, R. Kanno, M. Yonemura, T. Kamiyama, Y. Kato, S. Hama, K. Kawamoto, and A. Mitsui, *Nat. Mater.*, 2011, **10**, 682-686.
21. H. Lee, P. Oh, J. Kim, H. Cha, S. Chae, S. Lee, and J. Cho, *Adv. Mater.*, 2019, **31**, 1900376.

22. K. Xu, *Chem. Rev.*, 2004, **104**, 4303-4418.
23. K. H. Park, D. Y. Oh, Y. E. Choi, Y. J. Nam, L. Han, J.-Y. Kim, H. Xin, F. Lin, S. M. Oh, and Y. S. Jung, *Adv. Mater.*, 2016, **28**, 1874-1883.
24. K. H. Park, Q. Bai, D. H. Kim, D. Y. Oh, Y. Zhu, Y. Mo and Y. S. Jung, *Adv. Energy Mater.*, 2018, **8**, 1800035.
25. D. H. Kim, D. Y. Oh, K. H. Park, Y. E. Choi, Y. J. Nam, H. A. Lee, S.-M. Lee and Y. S. Jung, *Nano Lett.*, 2017, **17**, 3013-3020.
26. A. Sakuda, K. Kuratani, M. Yamamoto, M. Takahashi, T. Takeuchi, and H. Kobayashi, *J. Electrochem. Soc.*, 2017, **164**, A2474-A2478.
27. Y. J. Nam, D. Y. Oh, S. H. Jung and Y. S. Jung, *J. Power Sources*, 2018, **375**, 93-101.
28. C. Wang, K. R. Adair, J. Liang, X. Li, Y. Sun, X. Li, J. Wang, Q. Sun, F. Zhao, X. Lin, R. Li, H. Huang, L. Zhang, R. Yang, S. Lu and X. Sun, *Adv. Funct. Mater.*, 2019, **1900392**, DOI:10.1002/adfm.201900392.
29. A. Miura, N. C. Rosero-Navarro, A. Sakuda, K. Tadanaga, N. H. H. Phuc, A. Matsuda, N. Machida, A. Hayashi, and M. Tatsumisago, *Nat. Rev. Chem.*, 2019, **3**, 189-198.
30. S. P. Culver, R. Koerver, W. G. Zeier and J. Janek, *Adv. Energy Mater.*, 2019, **9**, 1900626.
31. Y. Xiao, L. J. Miara, Y. Wang and G. Ceder, *Joule*, 2019, **3**, 1-24.
32. H. Li, J. Li, X. Ma, and J. R. Dahn, *J. Electrochem. Soc.*, 2018, **165**, A1038-A1045.

33. J. Li, H. Li, W. Stone, R. Weber, S. Hy, and J. R. Dahn, *J. Electrochem. Soc.*, 2017, **164**, A3529-A3537.
34. J. Li, A. R. Cameron, H. Li, S. Glazier, D. Xiong, M. Chatzidakis, J. Allen, G. A. Botton, and J. R. Dahn, *J. Electrochem. Soc.*, 2017, **164**, A1534-A1544.
35. H. Tsukasaki, M. Otoyama, Y. Mori, S. Mori, H. Morimoto, A. Hayashi, and M. Tatsumisago, *J. Power Sources*, 2017, **367**, 42-48.
36. M. A. Kraft, S. Ohno, T. Zinkevich, R. Koerver, S. P. Culver, T. Fuchs, A. Senyshyn, S. Indris, B. J. Morgan, and W. G. Zeier, *J. Amer. Chem. Soc.*, 2018, **140**, 16330-16339.
37. X. H. Rui, N. Ding, J. Liu, C. Li, and C. H. Chen, *Electrochim. Acta*, 2010, **55**, 2384-2390.
38. X. H. Rui, N. Yesibolati, S. R. Li, C. C. Yuan and C. H. Chen, *Solid State Ion.*, 2011, **187**, 58-63.

4.7 Supporting Information

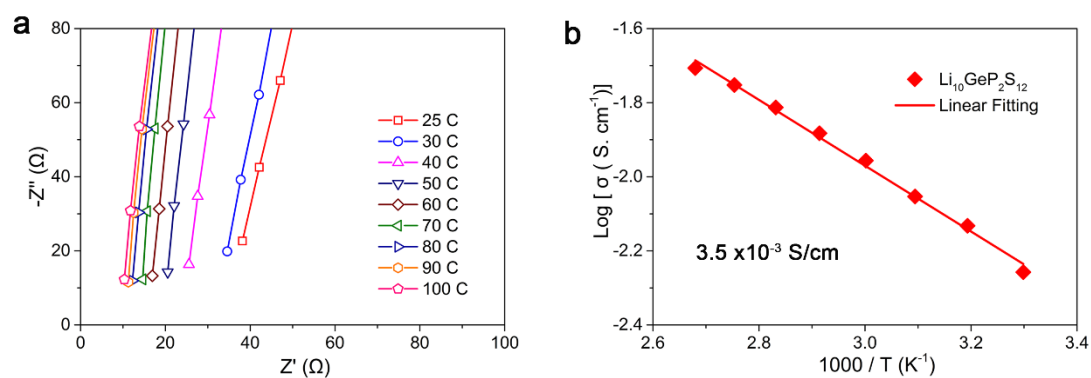


Figure 4-S1. The EIS spectra of $\text{Li}_{10}\text{GeP}_2\text{S}_{12}$ and corresponding Arrhenius plot. The room-temperature ionic conductivity of LGPS is $3.5 \times 10^{-3} \text{ S.cm}^{-1}$.

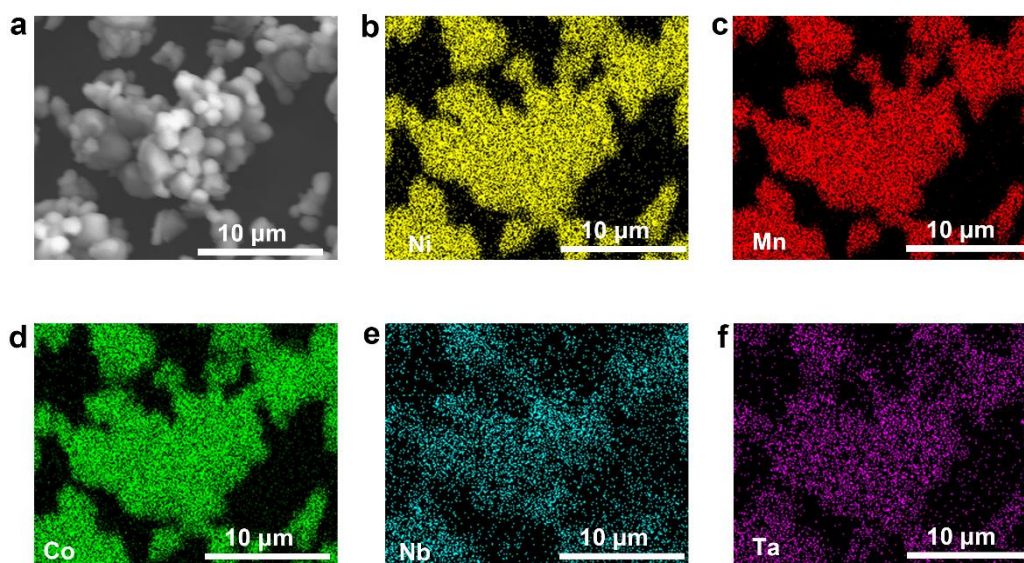


Figure 4-S2. SEM-EDX mapping of LNTO-coated SC-NMC532. (a) SEM image. (b) Ni mapping. (c) Mn mapping. (d) Co mapping. (e) Nb mapping. (f) Ta mapping.

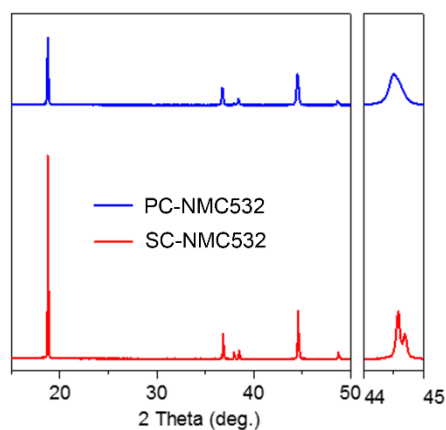


Figure 4-S3. XRD patterns of LNTO-coated SC-NMC532 and LNTO-coated PC-NMC532. The (104) peak at 44.6° for SC-NMC532 is split. This is caused by the separation of $K_{\alpha 1}$ and $K_{\alpha 2}$ reflected from the (104) lattice plane¹ and is characteristic of single-crystal NMC cathodes.¹⁻⁴

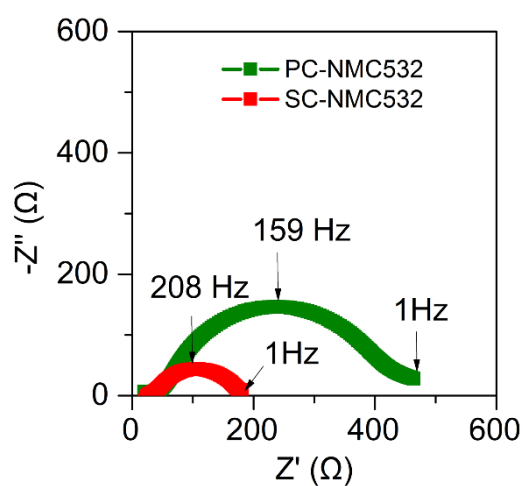


Figure 4-S4. EIS results of SC-NMC532 and PC-NMC532 after first charging to 3.8V. The internal resistance of SC-NMC532 is 181 Ω , much lower than that of PC-NMC532 (463 Ω).

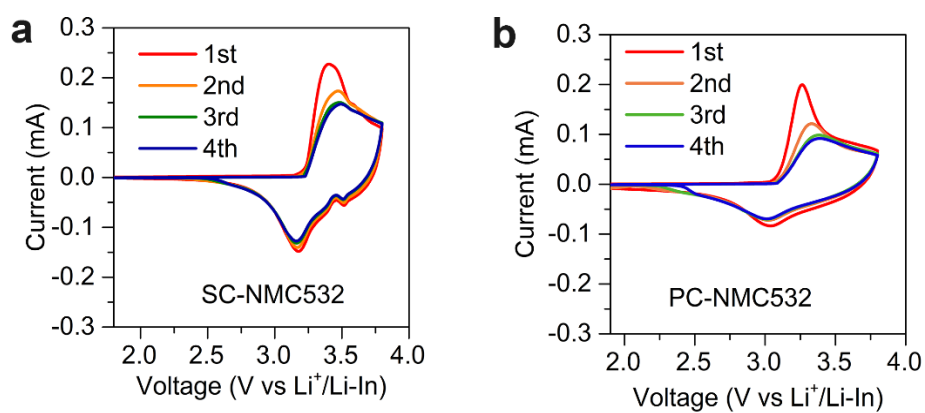


Figure 4-S5. (a) CV profiles of SC-NMC532. (b) CV curves of PC-NMC532.

Table 4-S1. Comparison of the rate performance of various cathodes in SE-based ASSLIBs.

<i>Cathode Composites</i>	<i>Active material loading</i>	<i>Rate definition</i>	<i>Capacity at 1C</i>	<i>Reference</i>
<i>LiNbO₃-coated NMC622</i>	<i>6.4 mg.cm⁻²</i>	<i>1 C = 0.4 mA.cm⁻²</i>	<i>50 mAh.g⁻¹</i>	<i>Ref 1.⁵</i>
<i>Li₂ZrO₃-coated NCA</i>	<i>6.8 mg.cm⁻²</i>	<i>1C = 1 mA.cm⁻²</i>	<i>70 mAh.g⁻¹</i>	<i>Ref⁶</i>
<i>NMC811</i>	<i>10.7 mg.cm⁻²</i>	<i>1C = 2.14 mA.cm⁻²</i>	<i>0 mAh.g⁻¹</i>	<i>Ref.⁷</i>
<i>NMC622</i>	<i>34 mg.cm⁻²</i>	<i>1C = 6.84 mA.cm⁻²</i>	<i>45 mAh.g⁻¹ (at 60°C)</i>	<i>Ref.⁸</i>

<i>LiNb_{0.5}Ta_{0.5}O₃-coated SC-NMC532</i>	<i>10.7 mg.cm⁻²</i>	<i>1 C = 1.3 mAcm⁻²</i>	<i>82 mAh.g⁻¹</i>	<i>This work</i>
---	--------------------------------	--	------------------------------	------------------

Single-crystal NMC532 shows an outstanding discharge capacity of 82 mAh.g⁻¹ at 1C at room temperature, the highest value reported so far.

Table 4-S2 The references for the Ragone plot.

Name	References
Ref #1	R. Mosthev, B. Johnson, <i>J. Power Sources</i> 2000 , <i>91</i> , 86. ⁹
Ref #2	K. Takada et al. <i>Adv. Mater.</i> (2006), <i>18</i> , 2226-2229. DOI: 10.1002/adma.200502604. ¹⁰
Ref #3	R. Kanno et al. <i>Nat. Mater.</i> (2011), <i>10</i> , 682-686 DOI: 10.1038/NMAT3066. ¹¹
Ref #4	J. Janek et al. <i>ACS Appl. Mater. Interfaces</i> (2017), <i>9</i> , 17835–17845 DOI: 10.1021/acsami.7b01137. ¹²
Ref #5	<i>Y-S Jung et al. Adv. Mater.</i> (2016), <i>28</i> , 1874–1883. DOI: 10.1002/adma.201505008. ¹³

References

1. J. Li, A. R. Cameron, H. Li, S. Glazier, D. Xiong, M. Chatzidakis, J. Allen, G. A. Botton, and J. R. Dahn, *J. Electrochem. Soc.*, 2017, **164**, A1534-A1544.
2. S.-K. Jung, H. Gwon, J. Hong, K.-Y. Park, D.-H. Seo, H. Kim, J. Hyun, W. Yang and K. Kang, *Adv. Energy Mater.*, 2014, **4**, 1300787.
3. J. Li, H. Li, W. Stone, R. Weber, S. Hy, and J. R. Dahn, *J. Electrochem. Soc.*, 2017, **164**, A3529-A3537.
4. H. Li, J. Li, X. Ma, and J. R. Dahn, *J. Electrochem. Soc.*, 2018, **165**, A1038-A1045.
5. D. Y. Oh, D. H. Kim, S. H. Jung, J.-G. Han, N.-S. Choi and Y. S. Jung, *J. Mater. Chem. A*, 2017, **5**, 20771-20779.
6. S. Ito, S. Fujiki, T. Yamada, Y. Aihara, Y. Park, T. Y. Kim, S.-W. Baek, J.-M. Lee, S. Doo and N. Machida, *J. Power Sources*, 2014, **248**, 943-950.
7. R. Koerver, I. Aygün, T. Leichtweiß, C. Dietrich, W. Zhang, J. O. Binder, P. Hartmann, W. G. Zeier, and J. Janek, *Chem. Mater.*, 2017, **19**, 5574-5582.
8. M. A. Kraft, S. Ohno, T. Zinkevich, R. Koerver, S. P. Culver, T. Fuchs, A. Senyshyn, S. Indris, B. J. Morgan, and W. G. Zeier, *J. Am. Chem. Soc.*, 2018, **140**, 16330-16339.
9. R. Moshtev and B. Johnson, *J. Power Sources*, 2000, **91**, 86-91.
10. N. Ohta, K. Takada, L. Zhang, R. Ma, M. Osada, and T. Sasaki, *Adv. Mater.*, 2006, **18**, 2226-2229.
11. N. Kamaya, K. Homma, Y. Yamakawa, M. Hirayama, R. Kanno, M. Yonemura, T. Kamiyama, Y. Kato, S. Hama, K. Kawamoto, and A. Mitsui, *Nat. Mater.*, 2011, **10**, 682-686.

12. W. Zhang, D. A. Weber, H. Weigand, T. Arlt, I. Manke, D. Schröder, R. Koerver, T. Leichtweiss, P. Hartmann, W. G. Zeier, and J. Janek, *ACS Appl. Mater. Interfaces*, 2017, **9**, 17835-17845.
13. K. H. Park, D. Y. Oh, Y. E. Choi, Y. J. Nam, L. Han, J.-Y. Kim, H. Xin, F. Lin, S. M. Oh, and Y. S. Jung, *Adv. Mater.*, 2016, **28**, 1874-1883.

Chapter 5

5. Deciphering Oxygen Release of Single-Crystal NMC532 and Its Effect on Sulfide-based ASSLIBs*

As revealed in Chapter 4, single-crystal NMC532 can simultaneously enable the high-power density and high energy density of ASSLIBs at room temperature as long as the interfacial resistance is successfully suppressed by an interfacial coating layer. However, the root cause of the large interfacial resistance and the functionality of the interfacial coating layer has not been well-understood.

In this work, we further investigated the underlying mechanism of interfacial reactions between single-crystal $\text{LiNi}_{0.5}\text{Mn}_{0.3}\text{Co}_{0.2}\text{O}_2$ (SC-NMC532) and sulfide electrolytes. It is found that the oxygen loss from SC-NMC532 contributes to significant oxidation of the sulfide electrolyte $\text{Li}_{10}\text{GeP}_2\text{S}_{12}$ upon cycling. In addition, the structural degradation from a layered structure to a rock-salt structure further impedes interfacial Li^+ transport in ASSLIBs. Fortunately, an interfacial coating is demonstrated to be effective in preventing oxygen release and interfacial structure change, successfully mitigating the large interfacial resistance of ASSLIBs. As a result, $\text{LiNb}_{0.5}\text{Ta}_{0.5}\text{O}_3$ -coated SC-MC532 exhibits an initial specific capacity of 161.4 mAh.g^{-1} , which remains at 92.1 mAh.g^{-1} after 300 cycles. This work provides new insights into the large interfacial resistance of ASSLIBs and presents new opportunities to design high-performance ASSLIBs.

***Note:** This work is ready for submission

Changhong Wang, Sooyeon Hwang, Jianwen Liang, Xiaona Li, Yipeng Sun, Sankha Mukherjee, Nathaniel Holme, Mohammad Norouzi Banis, Changtai Zhao, Ruying Li, Huan Huang, Shangqian Zhao, Li, Zhang, Shigang Lu, Chandra Veer Singh, Dong Su, and Xueliang Sun. Understanding Oxygen Release from Layered Oxide Cathodes in Sulfide-based All-Solid-State Batteries. **Ready for submission**

5.1 Introduction

All-solid-state lithium-ion batteries (ASSLIBs) are attracting worldwide attention due to their significantly improved safety, energy density, and cycling life.^{1, 2} However, several challenges hinder the development of ASSLIBs, including (1) insufficient ionic conductivity of solid-state inorganic electrolytes, and (2) large interfacial resistance originating from detrimental interfacial reactions and poor solid-solid contact between inorganic solid-state electrolytes and electrode materials. With the continuous efforts over the past decades, a lot of solid-state sulfide electrolytes (SEs) with high ionic conductivity reported, such as $\text{Li}_{9.54}\text{Si}_{1.74}\text{P}_{1.44}\text{S}_{11.7}\text{Cl}_{0.3}$ ($25 \text{ mS}\cdot\text{cm}^{-1}$)³ and $\text{Li}_{10}\text{GeP}_2\text{S}_{12}$ (LGPS, $12 \text{ mS}\cdot\text{cm}^{-1}$),⁴ $\text{Li}_7\text{P}_3\text{S}_{11}$ ($17 \text{ mS}\cdot\text{cm}^{-1}$)⁵. Their ionic conductivities are even greater than that of liquid electrolytes ($10.2 \text{ mS}\cdot\text{cm}^{-1}$).⁶ Therefore, SE-based ASSLIBs is regarded as one of the most promising solid-state battery systems. However, the detrimental interfacial reactions and insufficient solid-solid contact between electrode materials and SEs significantly suppress the electrochemical performance of SE-based ASSLIBs.⁷⁻¹⁰ To address these challenges, many soluble SSEs have been developed, which can coat cathode materials or infiltrate into the electrode sheet to significantly improve the solid-solid contact in ASSLIBs.¹¹⁻¹⁶ In addition, various interfacial buffer layers (i.e. LiNbO_3 , LiTaO_3) have been engineered to prevent interfacial reactions between electrode materials and SEs.^{9, 17, 18} With remarkable progress in improving ionic conductivity and suppressing interfacial resistance, SE-based ASSLIBs have been demonstrated with the high power density and high energy density throughout a wide temperature window.¹⁹⁻²⁴ In contrast to the many efforts made toward improving electrochemical performance, little work has been committed to developing an understanding of the interfacial reaction mechanisms between oxide cathodes and SEs, particularly between high-capacity 3d-transition-metal oxide cathodes and sulfide electrolytes.

Oxygen electrochemical/chemical activity has been widely reported in liquid cells featuring 3d-transition-metal oxide cathodes, particularly in layered NMC ($\text{Li}[\text{Ni}_x\text{Co}_y\text{Mn}_z]\text{O}_2$, $x+y+z=1$) cathodes and Li-rich cathodes.²⁵⁻²⁹ The lattice oxygen loss results in voltage and capacity fading as well as a phase transformation from a layered structure to a spinel and/or rock-salt structure.²⁶⁻³³ To date, these challenges have not been explored in the context of ASSLIBs.

In this work, we investigated the interfacial reaction mechanisms and near-surface structural change between single-crystal $\text{LiNi}_{0.5}\text{Mn}_{0.3}\text{Co}_{0.2}\text{O}_2$ (SC-NMC532) and sulfide electrolyte $\text{Li}_{10}\text{GeP}_2\text{S}_{12}$ (LGPS), by X-ray photoelectron spectroscopy and high-resolution transmission electron microscopy (HRTEM). It was found that oxygen release from layered SC-NMC532 is a trigger for detrimental interfacial reactions, which in turn induce the structural change from a layered structure to a rock-salt structure. Both the oxidation of SEs and the structural change are responsible for the large interfacial resistance of ASSLIBs. As a remedy, interface modification has been demonstrated to be effective in suppressing oxygen release and preventing structural change. $\text{LiNb}_{0.5}\text{Ta}_{0.5}\text{O}_3$ (LNTO)-coated SC-NMC532 exhibits an initial specific capacity of 161.4 $\text{mAh}\cdot\text{g}^{-1}$ and remains at 92.1 $\text{mAh}\cdot\text{g}^{-1}$ after 300 cycles. This work provides new insights into the large interfacial resistance of SE-based ASSLIBs and sheds light on new opportunities for achieving high-performance ASSLIBs.

5.2 Experimental Sections

5.2.1 Surface Modification of SC-NMC532

Stoichiometric amounts of lithium acetate (LiCO_2CH_3 , Sigma-Aldrich, 99.99%), niobium(V) ethoxide ($\text{Nb}(\text{OCH}_2\text{CH}_3)_5$, Sigma-Aldrich, 99.95%, trace metals basis), and tantalum(V) butoxide ($\text{Ta}(\text{OCH}_2\text{CH}_2\text{CH}_2\text{CH}_3)_5$, Sigma-Aldrich, 99.99%, trace metals

basis) were dissolved in absolute ethanol (Sigma-Aldrich, >99.8%, GC) and stirred magnetically for 2 hours. The mass fraction of LNTO sol-gel in absolute ethanol was diluted to 10%. 2 g of single-crystal $\text{LiNi}_{0.5}\text{Mn}_{0.3}\text{Co}_{0.2}\text{O}_2$ (SC-NMC532) (supplied from the China Automotive Battery Research Institute) was dispersed into 5ml of absolute ethanol. 2 wt% LNTO was then added to the SC-NMC532 solution. After magnetically stirring for 2 hours, the solution was dried at 80°C. The powder was further dried under vacuum at 100°C overnight and annealed in air at 450°C for 2 hours. The samples are identified as LNTO@NMC532.

5.2.2 Characterizations

Transmission electron microscopy (TEM) was performed with a JEM-2100 operated at 200 kV. Scanning Transmission Electron Microscopy (STEM)-Energy Dispersive Spectroscopy (EDS) mapping was done with an FEI Talos F200X TEM (operated at 200 keV) equipped with an energy dispersive X-ray spectrometer. HAADF-STEM imaging and electron energy loss spectroscopy (EELS) analysis were performed with a Hitachi HD2700C with a probe corrector. Scanning Electron Microscope (SEM) images were recorded with an SEM-4800. Powder X-ray diffraction (XRD) patterns were collected on a Bruker AXS D8 Advance with $\text{Cu K}\alpha$ radiation ($\lambda = 1.54178 \text{ \AA}$) and a special holder to avoid exposure to air during tests. The X-ray photoelectron spectroscopy (XPS) data were collected with a monochromatic $\text{Al K}\alpha$ source (1486.6 eV) using a Kratos AXIS Nova Spectrometer. X-ray absorption near edge structure (XANES) measurements were carried out at the Canadian Light Source (CLS). Mn K-edge XANES data was collected using fluorescence yield mode on the soft X-ray characterization beamline (SXRMB) at the CLS30. To avoid effects from air exposure, all samples were sealed with Mylar film attached to Al film.

5.2.3 Assembly of ASSLIBs

70 mg of LNTO@SC-NMC532 and 30 mg of commercial $\text{Li}_{10}\text{GeP}_2\text{S}_{12}$ (LGPS) (purchased from MSE supplies) were mixed to serve as the cathode composite. 80 mg of LGPS was first pressed at 1 MPa. 12 mg of cathode composite was then uniformly spread on one side of the LGPS layer and compressed at 350 MPa. A piece of indium foil was positioned on the other side of the LGPS and pressed at 100 MPa. The battery was rest for 3 hours before electrochemical testing. The electrochemical impedance spectra were recorded from 7 MHz to 0.1 Hz with an amplitude of 10 mV. The mass loading of NMC532 was 10.7 mg.cm^{-2} . 1C is defined as 0.13 mA.cm^{-2} . All electrochemical performance tests were performed at room temperature by a LAND electrochemical analysis system.

5.2.4 DFT Calculation

All calculations were carried out within the DFT framework as implemented in the Vienna Ab Initio Simulation Package (VASP). The projector augmented-wave pseudopotentials were used to describe the interaction between ions and electrons, and the exchange-correlation effects were treated using the Perdew–Burke–Ernzerhof (PBE) functional under the generalized gradient approximation (GGA) (generalized gradient approximation made simple). Herein, the electronic configurations for the PAW potentials were $1s^22s^1$ for Li, $2s^22p^4$ for O, $3d^84s^1$ for Co, $3d^94s^1$ for Ni and $3d^64s^1$ for Mn. The cutoff energy of the plane waves was 500 eV and the Brillouin zone integrations were performed using a Monkhorst–Pack scheme with a $2 \times 2 \times 2$ k-point mesh (Special points for Brillouin-zone integrations). For the $\text{LiNi}_{0.5}\text{Mn}_{0.3}\text{Co}_{0.2}\text{O}_2$ structure, a Python program (See Supporting Information) was employed to generate 30 different configurations based on a $5 \times 2 \times 1$ supercell consisting of 120 atoms and determine the most energetically stable configuration by structural optimization. Ab

initio molecular dynamics (AIMD) simulations were also performed to ascertain the thermodynamic stabilities of NMC532 structures. AIMD simulations were carried out at 300 K using the Nose thermostat over 2 ps (a unified formulation of the constant temperature molecular-dynamics methods). For the density of state (DOS) calculations, we adopted a DFT+U method to model the Coulombic repulsion between localized electrons in transition metals (first-principles calculations of the electronic structure and spectra of strongly correlated systems: the LDA+U method). The optimized values of Hubbard U values for Ni, Mn, and Co were taken as found to be 6.7, 4.2 and 4.91 eV, respectively, based on the previous study.¹ The energy and force convergence limits were set to be 1×10^{-5} eV/atom and 1×10^{-5} eV/Å, respectively. The VESTA package was used to visualize the different structures (VESTA: a three-dimensional visualization system for electronic and structural analysis).

5.3 Results and Discussion

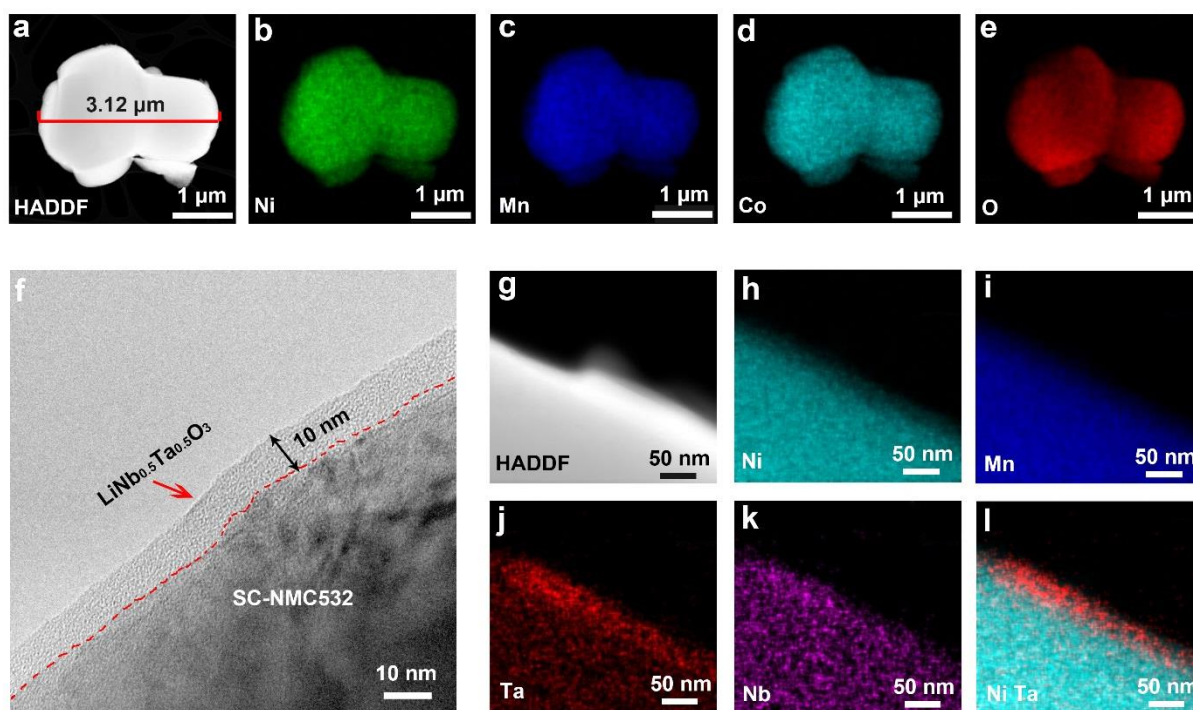


Figure 5-1 HR-TEM images of pristine SC-NMC532 and LNTO@SC-NMC532. (a) HAADF image of single-crystal NMC532. (b) Ni, (c) Mn, (d) Co, (e) O elemental maps of SC-NMC532 acquired with STEM-EDX. (f) Bright-field TEM image of $\text{LiNb}_{0.5}\text{Ta}_{0.5}\text{O}_3$ coating on SC-NMC532. (g) HADDF image of LNTO@SC-NMC532. (h) Ni, (i) Mn, (j) Ta, (k) Nb, (l) a combination of Ni and Ta mapping results obtained from LNTO@SC-NMC532 with STEM-EDX.

Figure 5-1a to **5-1e** show the scanning transmission electron microscopy energy dispersive X-ray spectroscopy (STEM-EDX) image and the Ni, Co, Mn, and O elemental maps of pristine SC-NMC532 with an average particle size of 3 μm , demonstrating a homogenous distribution of all elements. To suppress the interfacial reactions between SC-NMC532 and PC-NMC532 and the sulfide electrolyte $\text{Li}_{10}\text{GeP}_2\text{S}_{12}$ (LGPS), an interfacial layer of LiNbTaO_3 (LNTO) is put between the SC-NMC532 and LGPS (labeled as LNTO@SC-NMC532). The thickness of the conformal LNTO coating is 10 nm, as displayed in **Figure 5-1f**. The STEM-EDX elemental maps of LNTO@SC-NMC532 are displayed in **Figure 5-1g** to **g-1l**. Ta has a strong signal at the edge, further suggesting the LNTO was uniformly coated on SC-NMC532.

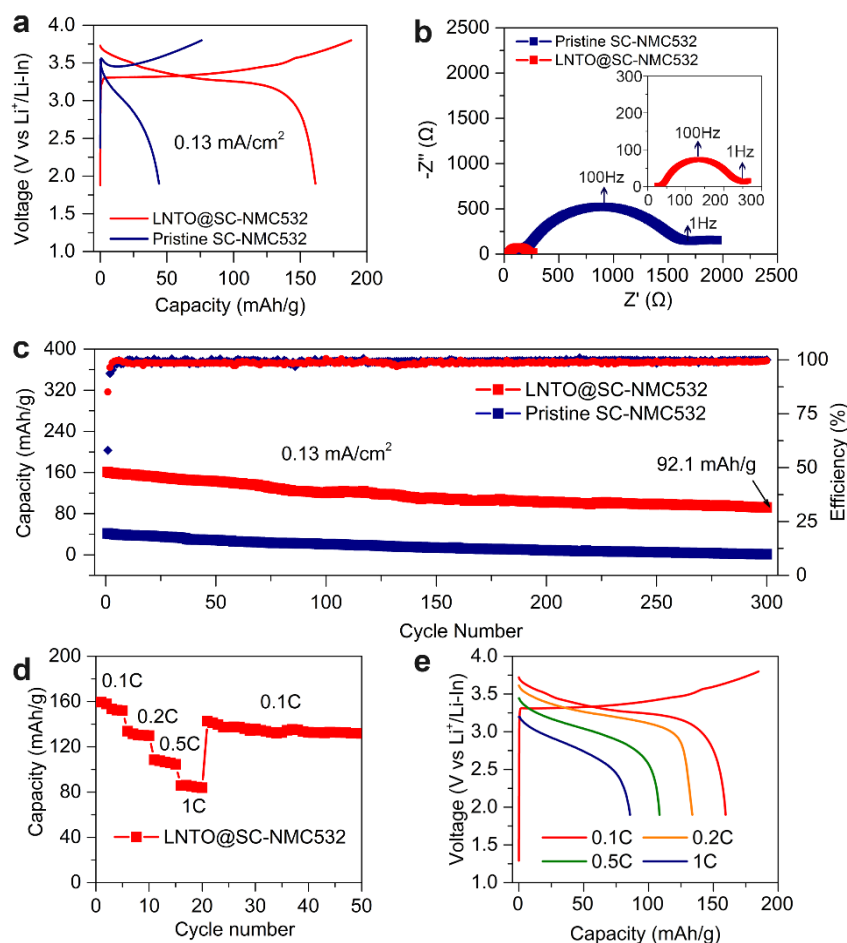


Figure 5-2 Electrochemical Performance of pristine SC-NMC532 and LNT0@SC-NMC532. (a) Comparison of the charge/discharge curves of pristine SC-NMC532 and LNT0@SC-NMC532. (b) EIS of bare SC-NMC532 and LNT0@SC-NMC532 after initially charging to 3.8V. (c) Cycling stability of pristine SC-NMC532 and LNT0@-SC-NMC532. (d) Rate performance of LNT0@SC-NMC532. (e) Charging/Discharging curves under different current densities.

The electrochemical performances of pristine SC-NMC532 and LNT0@SC-NMC532 in SE-based ASSLIBs were first tested under a current density of 0.1C ($1C=1.3 \text{ mA}\cdot\text{cm}^{-2}$), bare SC-NMC532 can be only charged to $76.0 \text{ mAh}\cdot\text{g}^{-1}$ and discharged to $41.4 \text{ mAh}\cdot\text{g}^{-1}$ due to the obvious overpotential caused by the interfacial reactions between SC-NMC532

and LGPS (**Figure 5-2a**), while LNTO@SC-NMC532 can be charged to 188.2 mAh.g⁻¹ and discharged to 161.4 mAh g⁻¹, indicating that LNTO interfacial coating layer can effectively suppress the interfacial resistance resulting from the interfacial reactions between LGPS and SC-NMC532. Furthermore, the initial Coulombic efficiency (CE) (54.5%) of bare SC-NMC532 is also enhanced to 85.1% by introducing interfacial coating layer LNTO, which is close to that of liquid-based cells (85.8%) (Figure S3). Furthermore, the interfacial resistances of bare SC-NMC532 and LNTO@SC-NMC532 were confirmed by electrochemical impedance spectroscopy (EIS) (**Figure 5-2b**). The interfacial resistance between bare SC-NMC532 and LGPS is as large as 1400 Ω, which is effectively reduced to 200 Ω with LNTO interfacial coating.

Figure 5-2c exhibits the cycling stability of bare SC-NMC532 and LNTO@SC-NMC532. After 300 cycles, the capacity of bare SC-NMC532 is only 1.2 mAh.g⁻¹ with a decay rate per cycling of 1.2%. Comparatively, the specific capacity of LNTO@SC-NMC532 which remains at 92.1 mAh.g⁻¹ after 300 cycles. The corresponding decay rate is 0.18%, which about 10 times lower than bare SC-NMC532. The improved cycling stability indicates that the interfacial coating layer LNTO is stable upon cycling. **Figure 5-2d** shows the rate-performance of LNTO@SC-NMC532 from 0.1C to 1C. LNTO@SC-NMC532 shows a discharge capacity of 82 mAh.g⁻¹ at 1C. It should be mentioned that the rate-performance of LNTO@SC-NMC532 outperforms a lot of previous reports,²⁴⁻²⁶ as tabulated in **Table 5-S1**.

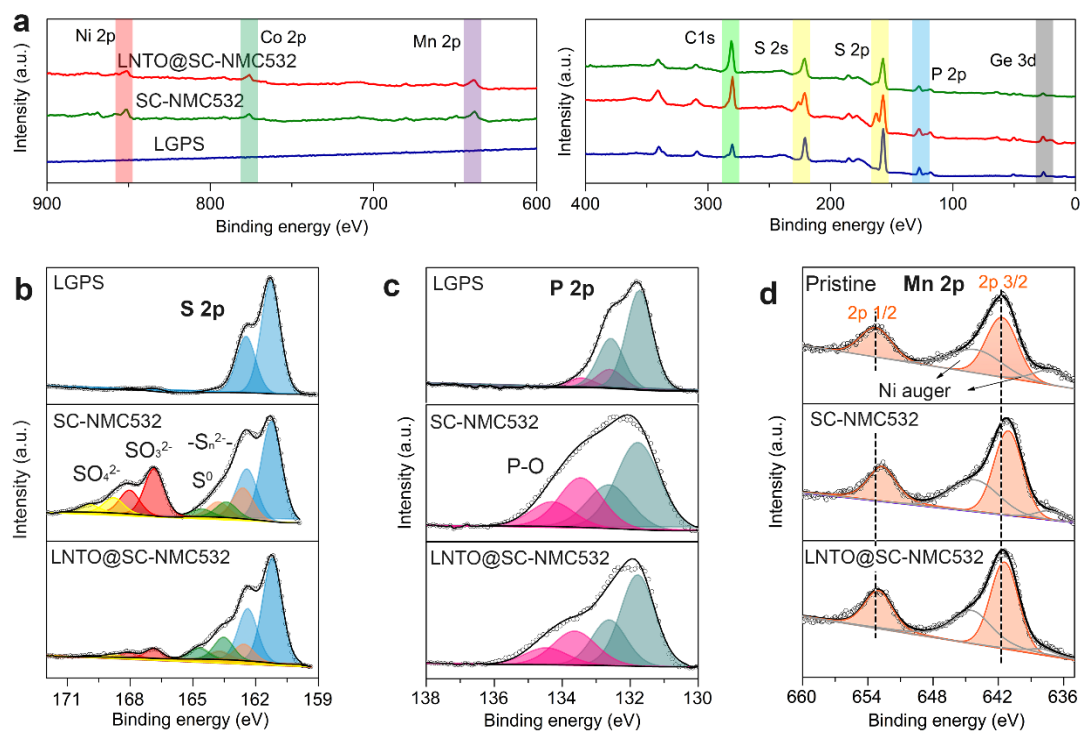


Figure 5-3 XPS Spectra of LGPS, SC-NMC532/LGPS electrode after 100 cycles, and LNTO@SC-NMC532 electrode after 100 cycles. (a) full survey. (b) S 2p spectra. (c) P 2p spectra. (d) Mn 2p spectra.

X-ray photoelectron spectroscopy (XPS) was employed to probe the interfacial reactions between SC-NMC532 and LGPS after cycling. **Figure 5-3a** shows the full surveys of pristine LGPS, SC-NMC532/LGPS after 100 cycles, and LNTO@SC-NMC532 after 100 cycles, in which elements such as P, S, Ge, Ni, Co, Mn are clearly detected. Interestingly, the S 2p and P 2p peaks of SC-NMC532/LGPS and LNTO@SC-NM532 became are considerably different after cycling (highlighted by yellow). **Figure 5-3b** displays the high-resolution S 2p spectra from two samples and pristine LGPS. LGPS only shows a pair of peaks at 161.26 eV, which is corresponding to the PS₄³⁻. Comparatively, SC-NMC532/LGPS after 100 cycles shows a lot of additional peaks at the higher binding energy. The additional peaks between 162 eV and 165 eV can be assigned to the polysulfides, such as S⁰ or -S_n⁻ (n≥2), indicating LGPS is oxidized by SC-NMC532 during the cycling.²⁴ More interestingly, the strong peaks of sulfates SO₃²⁻ (166.8eV)

and SO_4^{2-} (168.8 eV) are clearly observed, suggesting the oxygen in NMC532 reacts with S of LGPS, thus forming SO_4^{2-} and SO_3^{2-} species.²⁷ With the LNTO interfacial coating layer, the intensity of the SO_4^{2-} and SO_3^{2-} peaks is greatly suppressed, suggesting the interfacial coating layer can prevent the interfacial reactions between SC-NMC532 and LGPS. **Figure 5-3c** presents high-resolution P 2p spectra of pristine LGPS, SC-NMC532 after 100 cycles, and LNTO@SC-NMC532 after 100 cycles. Compared to the P 2p spectra of pristine LGPS, the P 2p spectra of SC-NMC532/LGPS shows additional peaks at higher binding energy, which indicates the formation of PO_4^{3-} . The intensity of P-O peaks is decreased with the LNTO interfacial coating layer, suggesting that P-O formation is due to the interfacial reactions between SC-NMC532 and LGPS, which can be suppressed by LNTO interfacial coating layer. XPS results clearly demonstrate that new species such as SO_4^{2-} , SO_3^{2-} and PO_4^{3-} are formed at the interface between SC-NMC532 and LGPS after cycling. Actually, these oxygen-containing species are commonly observed in different oxide cathode/sulfide-based ASSLIBs, including LCO/LGPS,²⁷ LCO/Li₆PS₅Cl, NMC811/Li₃PS₄. However, the underlying reason has not been well-studied.

Now the question is where the oxygen comes from. We assumed that oxygen comes from SC-NMC532 during cycling. To test this assumption, Mn⁴⁺ change of NMC cathodes after cycling was further verified by X-ray absorption spectroscopy because the reduction of Mn ions is normally accompanied by the oxygen evolution of NMC cathodes.²⁸ As shown in **Figure 5-3d**, comparing to the pristine SC-NMC532 in which the oxidation state Mn is Mn⁴⁺, the Mn 2p spectra of SC-NMC532 after 100 cycles are shifted to lower binding energy, indicating Mn⁴⁺ is reduced. With the interfacial coating layer, Mn reduction can be mitigated. Furthermore, X-ray absorption spectroscopy (XAS) was also performed to probe the Mn valent state change. (**Figure 5-S6**). Clearly, the Mn⁴⁺ is reduced after 100 cycles, implying the oxygen evolution from NMC cathodes can contribute to the formation of SO_4^{2-} , SO_3^{2-} and PO_4^{3-} at the interface in ASSLIBs.

Fortunately, the Mn reduction can be effectively mitigated by adding interfacial coating layer LNTO.

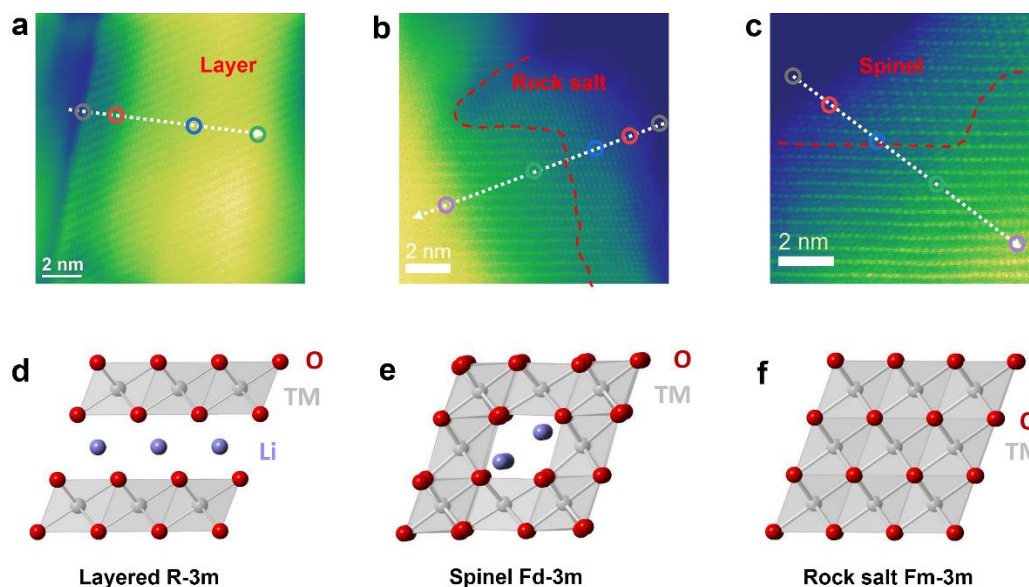


Figure 5-4 Interfacial structure change and chemical evolution of SC-NMC532. (a) HAADF-STEM image of pristine SC-NMC532. (b) HAADF-STEM image of SC-NMC532-after 100 cycles. (c) HAADF-STEM image of LNTO@SC-NMC532 after 100 cycles. (d) Illustration of a layered R-3m structure. (e) Illustration of a spinel Fd-3m structure. (f) Illustration of a rock-salt structure.

To investigate the structural changes at the surface of SC-NMC532, HAADF-STEM images were acquired. To avoid the contamination during imaging, the sulfide electrolytes at the interface were totally removed by ethanol. As displayed in **Figure 5-4a**, the well-defined layered structure of SC-NMC532 was observed. STEM-EELS line scan of Mn $L_{2,3}$ edge presents the oxidation state of Mn is homogeneous over the sample. After 100 cycles in SE-based ASSLIBs, the reduction of Mn was found from the surface to the inner layered structure (**Figure 5-4b**), suggesting the oxygen evolution of SC-NMC532. More obviously, the interfacial layered structure was changed to a rock-salt structure after cycling (**Figure 5-4g** and **5-4h**). The surface reconstruction is

also associated with the oxygen evolution of SC-NMC532.²⁹⁻³¹ With the interfacial coating layer, Mn reduction is alleviated (**Figure 5-4e** and **5-4f**). A couple of nanometers thick spinel layer was found at LNT0@SC-NMC532 (**Figure 5-4i**) but considering that the average oxidation state of transition metals is lower at rock-salt than spinel, we can infer that oxygen loss and interface reconstruction can be alleviated by interface coating.

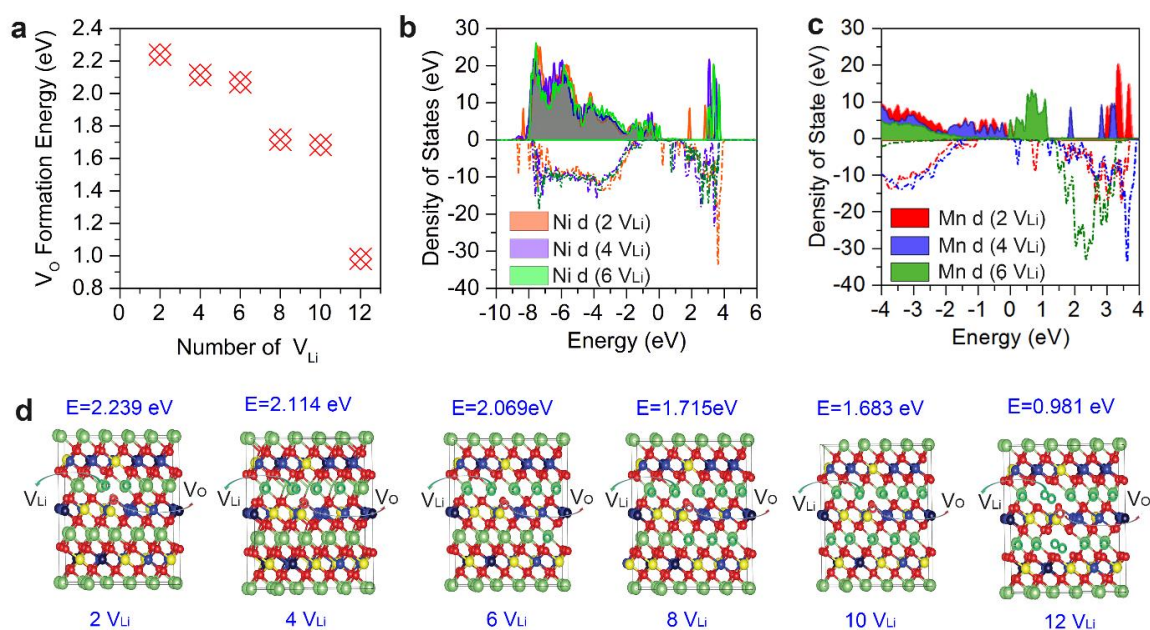


Figure 5-5 First-principles calculation to determine the formation energy of oxygen vacancies in SC-NMC532. (a) The formation energy of oxygen vacancies as a function of Li vacancy numbers. (b) The comparison of Ni d states after removing Li atoms from the supercell. (c) The comparison of Mn d states after removing Li atoms from the supercell. The Fermi level is set to be 0 eV. (d) Illustration of oxygen vacancies in $\text{LiNi}_{0.5}\text{Mn}_{0.3}\text{Co}_{0.2}\text{O}_2$ supercells under different Li vacancy contents.

In general, Li vacancies (V_{Li}) vacancies are generated during the charging and discharging of SC-NMC532. Oxygen vacancies (V_O) is associated with the loss of lattice oxygen. Density functional theory calculations were performed to study the energetics of oxygen vacancy (V_O) formation in SC-NMC532 and its dependence on Li

vacancy concentration (V_{Li}). **Figure S4** shows the formation energy of oxygen vacancies as a function of V_{O} concentration. It can be seen that at the pristine state (no de-lithiation) of SC-NMC532 the formation energy of V_{O} is 2.05 eV, which monotonically increases with the concentration of V_{O} . This indicates that the generation of V_{O} is energetically difficult at the beginning of charging. Contrastingly, with Li vacancies generated in the lattices (during cycling), the formation energy of V_{O} reduces monotonically (**Figure 5a** and **Figure 5d**). For example, with 12 V_{Li} , the formation energy of V_{O} is only 0.981 eV, which indicates that the continued formation of V_{Li} the generation of V_{O} becomes increasingly favorable under high-voltages. In addition, the d states in Ni shift to higher energy with the generation of Li vacancies, suggesting that the Ni^{2+} in the pristine SC-NMC532 is oxidized (**Figure 5b**). This observation is consistent with the fact that the de-lithiation of NMC cathodes is accompanied by $\text{Ni}^{2+}/\text{Ni}^{4+}$ and $\text{Ni}^{3+}/\text{Ni}^{4+}$ oxidation. On the contrary, the d states in Mn shift towards lower energy levels with the generation of Li vacancies (**Figure 5c**), suggesting that Mn tends to be reduced with the loss of lattice oxygen. This observation is again supported by the Mn XPS and XAS results discussed above. These results further demonstrate that oxygen loss in SC-NMC532 occurs at high charging states and induces near-surface structure change, which in turn accounts for the large interfacial resistance of ASSLIBs.

5.4. Conclusions

We demonstrated in this work that the oxygen release from SC-NMC532 contributes to the detrimental interfacial reactions between LGPS and SC-NMC532, which was validated by XPS and DFT calculations. The oxygen loss during cycling also induces a structural change from a layered structure to a rock-salt structure, as observed by HADDF-STEM and verified by XANES. This structural change also impedes interfacial Li^+ transport. As a remedy, the interfacial coating is demonstrated to be effective in suppressing the oxygen loss and interfacial structural change, thereby

mitigating interfacial reactions and eliminating interfacial resistance. LNTO-coated SC-MC532 exhibits an initial specific capacity of 161.4 mAh.g⁻¹, which remains at 92.1 mAh.g⁻¹ after 300 cycles. Moreover, a high discharge capacity of 82 mAh.g⁻¹ was demonstrated at current density of 1C (1C= 1.3 mA.cm⁻²). This work provides new insights into the large interfacial resistance of ASSLIBs and presents new opportunities to design high-performance ASSLIBs.

5.5 Acknowledgements

This work was supported by Natural Sciences and Engineering Research Council of Canada (NSERC), Canada Research Chair Program (CRC), Canada Foundation for Innovation (CFI), Ontario Research Fund, China Automotive Battery Research Institute Co., Ltd, Glabat Solid-State Battery Inc., the Canada Light Source at University of Saskatchewan (CLS) and University of Western Ontario. J.L. and X. L. thank the support of Mitacs Elevate Postdoctoral Fellowship. C.W. appreciates the funding support of the Mitacs Accelerate Fellowship. This research used resources of the Center for Functional Nanomaterials, which is a U.S. DOE Office of Science Facility, at Brookhaven National Laboratory under Contract No. DE-SC0012704.

5.6 Author Contribution

X. Sun supervised the whole project. C. Wang conceived the idea and designed all the experiments and characterizations. M. Jiang, Sankha Mukherjee, and C. Singh conducted the first-principles calculations. S. H. and D. S. helped with TEM characterization and analysis. J. L. and X. L. interpreted the experimental results. M. Banis and Y. Sun helped with synchrotron characterization. C. Z., Y. S. and J. W. discussed all the experimental results. N. H. polished the language. R. L helped with purchasing all the chemicals. C. W. wrote the manuscript. All the authors discussed

the results and commented on the manuscript.

5.7 References

1. A. Manthiram, X. Yu and S. Wang, *Nat. Rev. Mater.*, 2017, **2**, 16103.
2. J. Li, C. Ma, M. Chi, C. Liang, and N. J. Dudney, *Advanced Energy Materials*, 2015, **5**, 1401408.
3. Y. Kato, S. Hori, T. Saito, K. Suzuki, M. Hirayama, A. Mitsui, M. Yonemura, H. Iba, and R. Kanno, *Nat. Energy*, 2016, **1**, 16030.
4. N. Kamaya, K. Homma, Y. Yamakawa, M. Hirayama, R. Kanno, M. Yonemura, T. Kamiyama, Y. Kato, S. Hama, K. Kawamoto, and A. Mitsui, *Nat. Mater.*, 2011, **10**, 682-686.
5. H. Lee, P. Oh, J. Kim, H. Cha, S. Chae, S. Lee, and J. Cho, *Adv. Mater.*, 2019, **31**, 1900376.
6. K. Xu, *Chem. Rev.*, 2004, **104**, 4303-4418.
7. W. D. Richards, L. J. Miara, Y. Wang, J. C. Kim and G. Ceder, *Chem. Mater.*, 2016, **28**, 266-273.
8. Y. Zhu, X. He and Y. Mo, *J. Mater. Chem. A*, 2016, **4**, 3253-3266.
9. C. Wang, X. Li, Y. Zhao, M. N. Banis, J. Liang, X. Li, Y. Sun, K. R. Adair, Q. Sun, Y. Liu, F. Zhao, S. Deng, X. Lin, R. Li, Y. Hu, T.-K. Sham, H. Huang, L. Zhang, R. Yang, S. Lu and X. Sun, *Small Methods*, 2019, **1900261**, DOI:10.1002/smtd.201900261.
10. Q. Zhang, D. Cao, Y. Ma, A. Natan, P. Aurora and H. Zhu, *Advanced Materials*, **0**, 1901131.

11. K. H. Park, D. Y. Oh, Y. E. Choi, Y. J. Nam, L. Han, J.-Y. Kim, H. Xin, F. Lin, S. M. Oh, and Y. S. Jung, *Adv. Mater.*, 2016, **28**, 1874-1883.
12. K. H. Park, Q. Bai, D. H. Kim, D. Y. Oh, Y. Zhu, Y. Mo and Y. S. Jung, *Adv. Energy Mater.*, 2018, **8**, 1800035.
13. D. H. Kim, D. Y. Oh, K. H. Park, Y. E. Choi, Y. J. Nam, H. A. Lee, S.-M. Lee and Y. S. Jung, *Nano Lett.*, 2017, **17**, 3013-3020.
14. A. Sakuda, K. Kuratani, M. Yamamoto, M. Takahashi, T. Takeuchi, and H. Kobayashi, *J. Electrochem. Soc.*, 2017, **164**, A2474-A2478.
15. Y. J. Nam, D. Y. Oh, S. H. Jung and Y. S. Jung, *J. Power Sources*, 2018, **375**, 93-101.
16. S. P. Culver, R. Koerver, W. G. Zeier and J. Janek, *Adv. Energy Mater.*, 2019, **9**, 1900626.
17. Y. Xiao, L. J. Miara, Y. Wang and G. Ceder, *Joule*, 2019, **3**, 1-24.
18. N. Ohta, K. Takada, L. Zhang, R. Ma, M. Osada, and T. Sasaki, *Adv. Mater.*, 2006, **18**, 2226-2229.
19. F. Mizuno, A. Hayashi, K. Tadanaga and M. Tatsumisago, *Adv. Mater.*, 2005, **17**, 918-921.
20. N. Ohta, K. Takada, I. Sakaguchi, L. Zhang, R. Ma, K. Fukuda, M. Osada, and T. Sasaki, *Electrochem commun.*, 2007, **9**, 1486-1490.
21. W. D. Richards, T. Tsujimura, L. J. Miara, Y. Wang, J. C. Kim, S. P. Ong, I. Uechi, N. Suzuki, and G. Ceder, *Nature Communications*, 2016, **7**, 11009.

22. E. Rangasamy, Z. Liu, M. Gobet, K. Pilar, G. Sahu, W. Zhou, H. Wu, S. Greenbaum, and C. Liang, *J. Amer. Chem. Soc.*, 2015, **137**, 1384-1387.
23. X. Li, J. Liang, J. Luo, M. Norouzi Banis, C. Wang, W. Li, S. Deng, C. Yu, F. Zhao, Y. Hu, T.-K. Sham, L. Zhang, S. Zhao, S. Lu, H. Huang, R. Li, K. R. Adair, and X. Sun, *Energy & Environmental Science*, 2019, **12**, 2665-2671.
24. R. Koerver, I. Aygün, T. Leichtweiß, C. Dietrich, W. Zhang, J. O. Binder, P. Hartmann, W. G. Zeier, and J. Janek, *Chem. Mater.*, 2017, **19**, 5574-5582.
25. H. Tsukasaki, M. Otoyama, Y. Mori, S. Mori, H. Morimoto, A. Hayashi, and M. Tatsumisago, *J. Power Sources*, 2017, **367**, 42-48.
26. M. A. Kraft, S. Ohno, T. Zinkevich, R. Koerver, S. P. Culver, T. Fuchs, A. Senyshyn, S. Indris, B. J. Morgan, and W. G. Zeier, *J. Amer. Chem. Soc.*, 2018, **140**, 16330-16339.
27. W. Zhang, F. H. Richter, S. P. Culver, T. Leichtweiss, J. G. Lozano, C. Dietrich, P. G. Bruce, W. G. Zeier, and J. Janek, *ACS Appl. Mater. Interfaces*, 2018, **10**, 22226-22236.
28. S.-K. Jung, H. Gwon, J. Hong, K.-Y. Park, D.-H. Seo, H. Kim, J. Hyun, W. Yang and K. Kang, *Adv. Energy Mater.*, 2014, **4**, 1300787.
29. F. Lin, I. M. Markus, D. Nordlund, T.-C. Weng, M. D. Asta, H. L. Xin, and M. M. Doeff, *Nat. Commun.*, 2014, **5**, 3529.
30. J. Lee, J. K. Papp, R. J. Clément, S. Sallis, D.-H. Kwon, T. Shi, W. Yang, B. D. McCloskey, and G. Ceder, *Nat. Commun.*, 2017, **8**, 981.
31. E. Hu, X. Yu, R. Lin, X. Bi, J. Lu, S. Bak, K.-W. Nam, H. L. Xin, C. Jaye, D. A. Fischer, K. Amine and X.-Q. Yang, *Nat. Energy*, 2018, **3**, 690-698.

5.8 Supporting Information

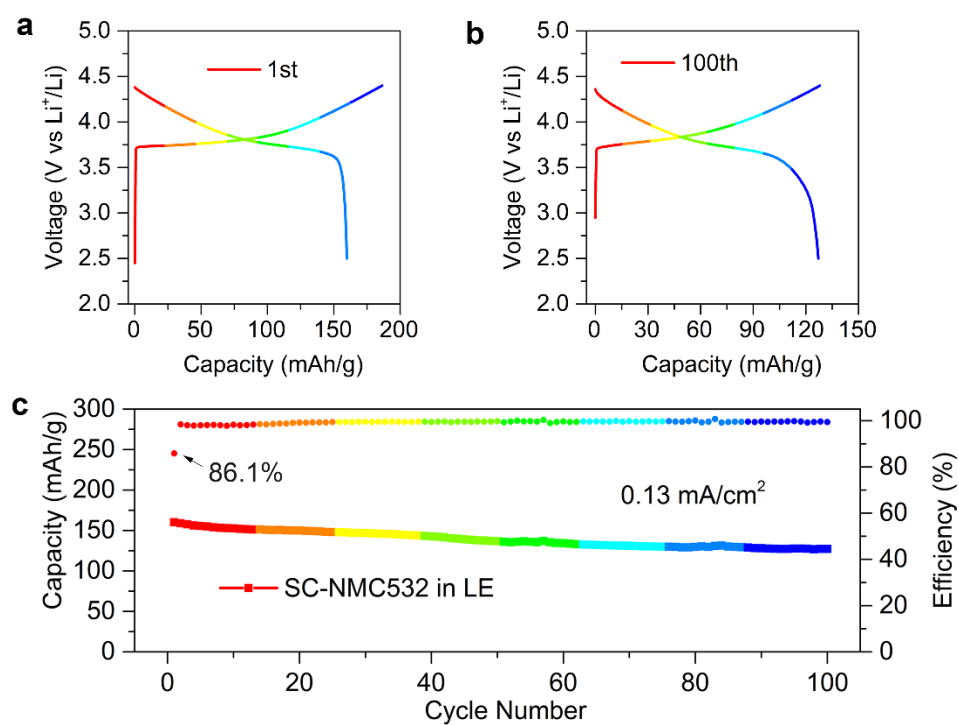


Figure 5-S1. Electrochemical performance of SC-NMC532 in liquid electrolytes. (a) Initial charge/discharge curves. (b) Charge/discharge curves at the 100th cycle. (c) Cycling stability of SC-NMC532 in liquid cells at a current density of 0.13 mA.cm⁻².

Table 5-S1. Comparison of the rate performance of various cathodes in SE-based ASSLIBs.

Cathode Composites	Active material loading	Rate definition	Capacity at 1C	Reference
LiNbO ₃ -coated NMC622	6.4 mg.cm ⁻²	1 C = 0.4 mA.cm ⁻²	50 mAh.g ⁻¹	Ref 1. ²
Li ₂ ZrO ₃ -coated NCA	6.8 mg.cm ⁻²	1C= 1 mA.cm ⁻²	70 mAh.g ⁻¹	Ref ³
NMC811	10.7 mg.cm ⁻²	1C= 2.14mA.cm ⁻²	0 mAh.g ⁻¹	Ref. ⁴
NMC622	34 mg.cm ⁻²	1C=6.84 mA.cm ⁻²	45 mAh.g ⁻¹ (at 60°C)	Ref. ⁵
LiNb_{0.5}Ta_{0.5}O₃-coated SC-NMC532	10.7 mg.cm⁻²	1 C = 1.3 mAcm⁻²	82 mAh.g⁻¹	This work

Single-crystal NMC532 shows an outstanding discharge capacity of 82 mAh.g⁻¹ at 1C at room temperature, the highest value reported so far.

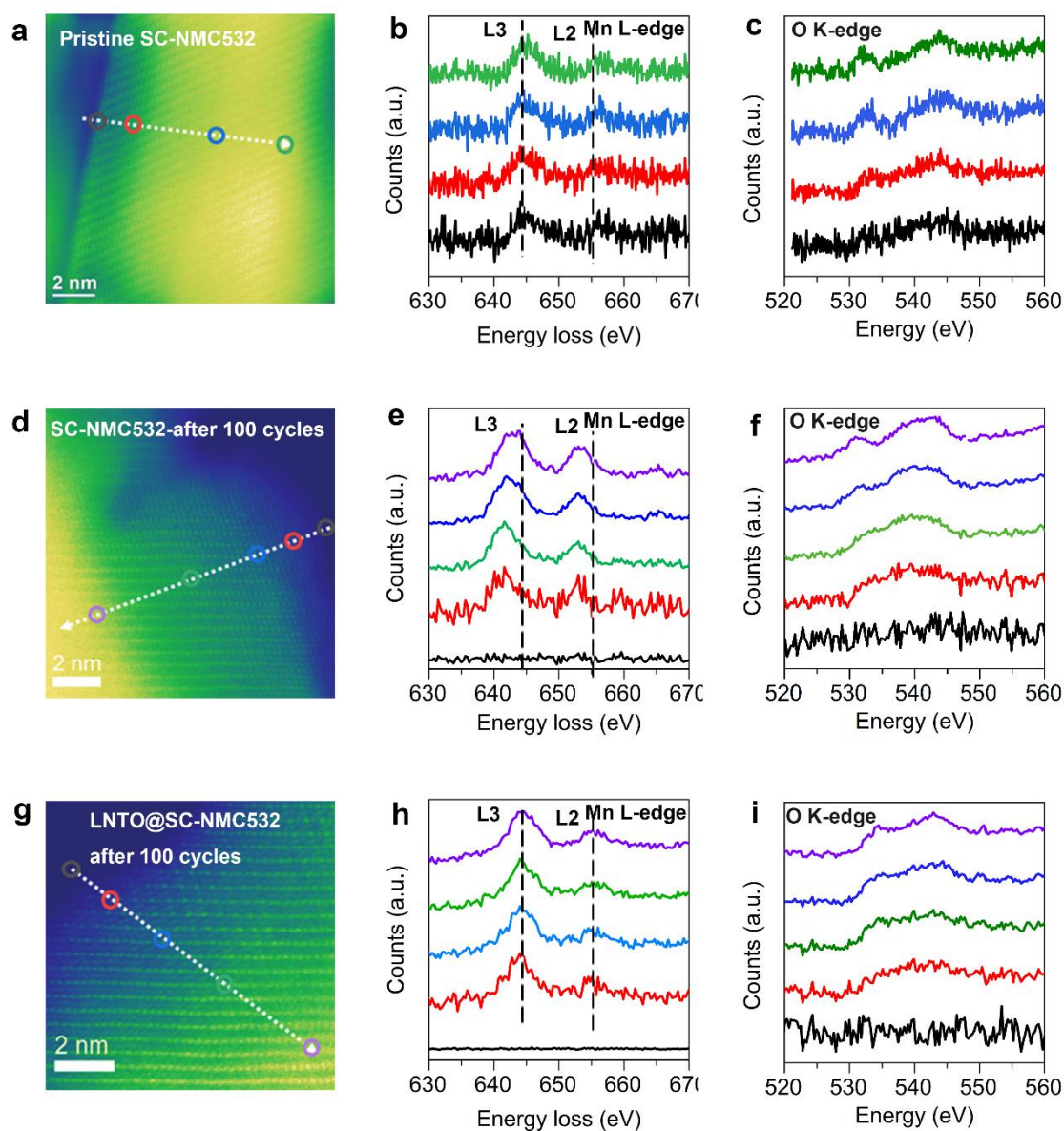


Figure 5-S2. Interfacial structure change and chemical evolution of SC-NMC532. (a, b, c) HR-TEM image of pristine SC-NMC532 and the corresponding EELS spectra of Mn 2p and O 1s (d, e, f) HR-TEM image of SC-NMC532-after 100 cycles and the corresponding EELS spectra of Mn 2p and O 1s. (g, h, i) HR-TEM image of LNT0@SC-NMC532 after 100 cycles and the corresponding EELS spectra of Mn 2p and O 1s.

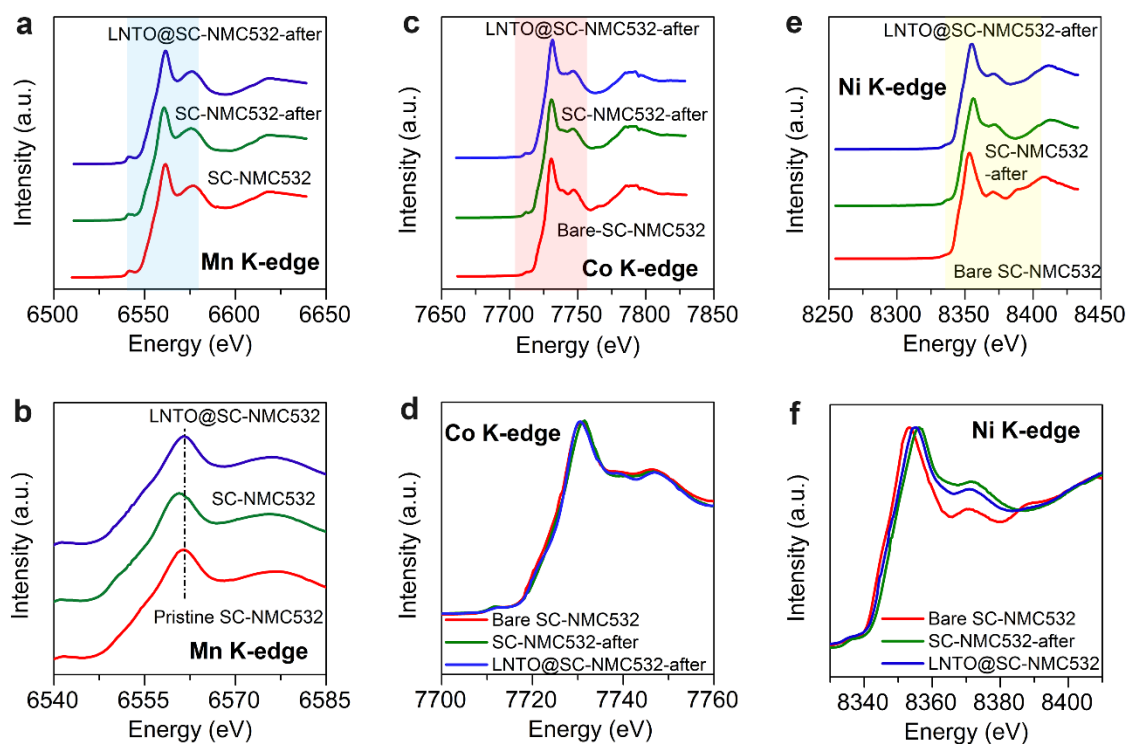


Figure 5-S3 X-ray absorption spectroscopy (XAS) of bare SC-NMC532, SC-NMC532 after 100 cycles, and LNT0@SC-NMC532-after 100 cycles. (a) and (b) Mn K-edge, (c) and (d) Co K-edge. (e) and (f) Ni K-edge.

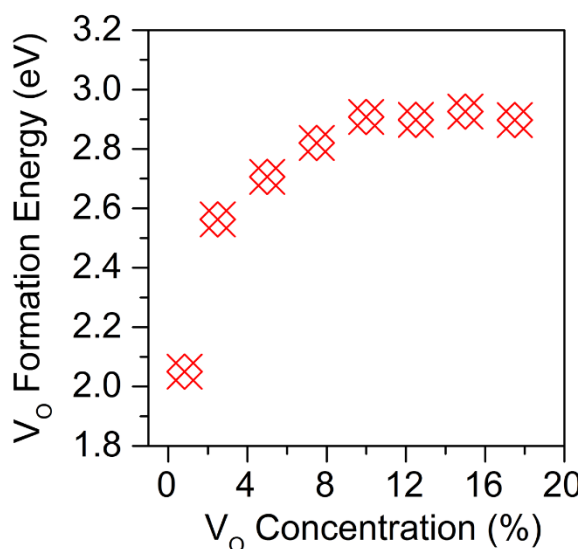


Figure 5-S4. The formation energy of oxygen vacancies as a function of oxygen vacancy concentration.

References.

1. Xu, R., Sun, H., de Vasconcelos, L.S. & Zhao, K. Mechanical and Structural Degradation of LiNi_xMn_yCo_zO₂ Cathode in Li-Ion Batteries: An Experimental Study. *J. Electrochem. Soc.* **164**, A3333-A3341 (2017).
2. Oh, D.Y. et al. Single-step wet-chemical fabrication of sheet-type electrodes from solid-electrolyte precursors for all-solid-state lithium-ion batteries. *J. Mater. Chem. A* **5**, 20771-20779 (2017).
3. Ito, S. et al. A rocking chair type all-solid-state lithium-ion battery adopting Li₂O–ZrO₂ coated LiNi_{0.8}Co_{0.15}Al_{0.05}O₂ and a sulfide-based electrolyte. *J. Power Sources* **248**, 943-950 (2014).

4. Koerver, R. et al. Capacity fade in solid-state batteries: interphase formation and chemomechanical processes in nickel-rich layered oxide cathodes and lithium thiophosphate solid electrolytes. *Chem. Mater.* **19**, 5574-5582 (2017).
5. Kraft, M.A. et al. Inducing High Ionic Conductivity in the Lithium Superionic Argyrodites $\text{Li}_{6+x}\text{P}_{1-x}\text{Ge}_x\text{S}_5\text{I}$ for All-Solid-State Batteries. *J. Am. Chem. Soc.* **140**, 16330-16339 (2018).

Chapter 6

6. Unraveling Interfacial Ion Transport in All-Solid-State Lithium-Ion Batteries*

Based on our previous studies, an interfacial coating layer is indispensable to successfully achieve high-performance all-solid-state lithium-ion (Li^+) batteries (ASSLIBs). However, the kinetics of Li^+ transport across the coating layer itself has not been studied yet.

Here we engineered the interfacial coating layer ($\text{LiNb}_{0.5}\text{Ta}_{0.5}\text{O}_3$) with different Li^+ conductivity. By relating the electrochemical performance of ASSLIBs to the ionic conductivity of the interfacial coating, it is found that increasing the ionic conductivity of the interfacial coating layer can significantly improve the electrochemical performance of ASSLIBs. Most importantly, the critical interfacial ionic conductivity of approximately $3.87 \times 10^{-5} \text{ S}\cdot\text{cm}^{-1}$ is required for ASSLIBs to achieve the comparable electrochemical performance with that of liquid cells. Notably, $\text{LiNi}_{0.5}\text{Mn}_{0.3}\text{Co}_{0.2}\text{O}_2$ with the highest ion-conductive interfacial coating can exhibit an initial capacity of $152 \text{ mAh}\cdot\text{g}^{-1}$ at 0.1 C and $88 \text{ mAh}\cdot\text{g}^{-1}$ at 1 C . This work suggests that apart from suppressing interfacial reactions, enhancing the Li^+ -conducting capability of the interfacial coating layer is also imperative for achieving high-performance SE-based ASSLIBs.

***Note:** This work has been submitted.

Changhong Wang, Jianwen Liang, Yang Zhao, Xiaona Li, Sooyeon Hwang, Keegan Adair, Yulong Liu, Xia Li, Sixu Deng, Xiaofei Yang, Ruying Li, Huan Huang, Li, Zhang, Shigang Lu, Dong Su, and Xueliang Sun. Revealing Interfacial Ion Transport Kinetics in All-Solid-State Lithium-Ion Batteries. **Submitted.**

6.1. Introduction

All-solid-state lithium-ion batteries (ASSLIBs) have gained worldwide attention in recent years due to their improved safety feature and energy density over conventional LIBs with flammable liquid organic electrolytes.¹⁻³ However, the commercialization of ASSLIBs has been hindered by several challenges. First, developing solid-state electrolyte with high ionic conductivity and good electrochemical stability.⁴ Second, overcoming large interfacial resistance for lithium-ion (Li^+) transport in ASSLIBs.^{5, 6} Besides, developing cost-effective manufacturing protocol is also very crucial for the successful commercialization of ASSLIBs.^{7, 8} The first challenge has been well addressed by developing high Li^+ -conductive solid-state sulfide electrolytes (SEs), such as $\text{Li}_{9.54}\text{Si}_{1.74}\text{P}_{1.44}\text{S}_{11.7}\text{Cl}_{0.3}$ (25 $\text{mS}\cdot\text{cm}^{-1}$),⁹ $\text{Li}_7\text{P}_3\text{S}_{11}$ (17 $\text{mS}\cdot\text{cm}^{-1}$), $\text{Li}_{10}\text{GeP}_2\text{S}_{12}$ (12 $\text{mS}\cdot\text{cm}^{-1}$),¹⁰ $\text{Li}_{10.35}[\text{Sn}_{0.27}\text{Si}_{1.08}]\text{P}_{1.65}\text{S}_{12}$ (11 $\text{mS}\cdot\text{cm}^{-1}$),¹¹ $\text{Li}_{6+x}\text{P}_{1-x}\text{Ge}_x\text{S}_5\text{I}$ (18 $\text{mS}\cdot\text{cm}^{-2}$),¹² and $\text{Na}_{2.88}\text{Sb}_{0.88}\text{W}_{0.12}\text{S}_4$ (32 $\text{mS}\cdot\text{cm}^{-1}$).¹³ Although SEs with high ionic conductivity have been successfully developed, SE-based ASSLIBs demonstrate dissatisfactory electrochemical performance due to large interfacial resistance. The large interfacial resistance is mainly caused by severe interfacial reactions and the insufficient solid-solid contact between oxide cathodes and SEs.¹⁴⁻¹⁶ In order to suppress the interfacial resistance, soluble SEs in organic solvents (i.e. $\text{Li}_2\text{S}-\text{P}_2\text{S}_5$ ¹⁷, $\text{Li}_6\text{PS}_5\text{Cl}$,¹⁸ $\text{Li}_6\text{PS}_5\text{Br}$ ¹⁹, $\text{LiI}-\text{LiSnS}_4$ ²⁰, Na_3SbS_4 ²¹) are developed to coat oxide cathodes, thus dramatically improving the solid-solid contact.^{4, 7, 22} On the other hand, the necessity of an interfacial coating layer (i.e. LiNbO_3 ,^{23, 24} $\text{Li}_4\text{Ti}_5\text{O}_{12}$,²⁵ $\text{Li}_2\text{O}-\text{ZrO}_2$,²⁶ or $\text{Li}_{0.35}\text{La}_{0.5}\text{Sr}_{0.05}\text{TiO}_3$ ²⁷) to suppress interfacial reactions between oxide cathodes and SEs has been confirmed by lots of experiments and theoretical calculations.²⁸⁻³⁰ However, the kinetics of Li^+ transport across the interfacial coating layer has not been fully understood yet.

In this work, we purposely manipulated the ionic conductivity of an interfacial coating layer $\text{LiNb}_{0.5}\text{Ta}_{0.5}\text{O}_3$ (LNTO), aiming at investigating the effect of interfacial ionic

conductivity on SE-based ASSLIBs. LNTO with different Li⁺-conductivities was successfully coated on single-crystal LiNi_{0.5}Mn_{0.3}Co_{0.2}O₂ (NMC532) via tuning post-annealing temperature. It is found that NMC532 coated with low Li⁺-conductive LNTO shows a low Li⁺ diffusivity of $1.11 \times 10^{-11} \text{ cm}^2 \cdot \text{s}^{-1}$ while NMC532 coated with high Li⁺-conductive LNTO exhibits the high Li⁺ diffusivity of $1.36 \times 10^{-10} \text{ cm}^2 \cdot \text{s}^{-1}$, suggesting that improving the ionic conductivity of the interfacial coating layer can significantly boost Li⁺ diffusion kinetics in SE-based ASSLIBs. The high Li⁺-conductive LNTO-coated NMC532 shows a high initial capacity of 152 mAh.g⁻¹ at 0.1 C and 107.5 mAh.g⁻¹ at 1C at room temperature. This work manifests that improving the ionic conductivity of the interfacial coating layer can accelerate Li⁺ transport across the cathode/SE interface, which is of great importance toward high-performance SE-based ASSLIBs.

6.2 Experimental Section

6.2.1 Synthesis of LiNb_{0.5}Ta_{0.5}O₃ (LNTO)

Stoichiometric amounts of lithium acetate (LiCO₂CH₃, Sigma-Aldrich, 99.99%), niobium(V) ethoxide (Nb(OCH₂CH₃)₅, Sigma-Aldrich, 99.95%, trace metals basis), and tantalum(V) butoxide (Ta(OCH₂CH₂CH₂CH₃)₅, Sigma-Aldrich, 99.99%, trace metals basis) were dissolved in absolute ethanol (Sigma-Aldrich, >99.8%, GC) and stirred magnetically for 2 hours. Then dry the homogeneous sol at 80°C. After further drying the sol at 100°C under vacuum for overnight. The LiNb_{0.5}Ta_{0.5}O₃ powder was obtained. Then LiNb_{0.5}Ta_{0.5}O₃ powder was annealed in air at 350°C, 450°C, and 550°C for 2 hours, respectively. To determine the ionic conductivity of 100 mg LiNb_{0.5}Ta_{0.5}O₃ was pressed as a pellet around 350 MPa, then two pieces of indium foil were attached to both sides of the pellet. The pressure of 50 MPa was further applied to ensure the solid-solid contact between the indium foil and the LNTO pellet. The electrochemical impedance spectra

were from 7MHz to 0.1Hz with an amplitude of 10 mV.

6.2.2 Synthesis of LNTO@NMC532.

The mass fraction of LNTO so-gel in absolute ethanol was diluted to 10%. 2 g single-crystal $\text{LiNi}_{0.5}\text{Mn}_{0.3}\text{Co}_{0.2}\text{O}_2$ (NMC532) (supplied from China automotive battery research institute) was dispersed into 5ml absolute ethanol. And then 2 wt% LNTO was added into the NMC532 solution. After magnetically stirring 2 hours, the solution was dry at 80°C. Then LNTO@NMC532 was further dried under vacuum at 100°C for overnight. Then LNTO@NMC532 was annealed in air at 350°C, 450°C, and 550°C for 2 hours, respectively. The samples were labeled at LNTO@NMC532-350, LNTO@NMC532-450, and LNTO@NMC532-550, respectively.

6.2.3 Characterizations

TEM analysis was performed on a transmission electron microscopy (TEM; JEM-2100, 200 kV). Scanning Transmission Electron Microscopy (STEM)-Energy Dispersive Spectroscopy (EDS) mapping was done by an FEI Talos F200X TEM (operated at 200 keV) equipped with an energy dispersive X-ray spectrometer. SEM images were recorded using a Scanning Electron Microscope (SEM-4800) a Bruker D8 diffractometer, using Cu K α radiation. X-ray diffraction (XRD) was employed to obtain XRD patterns.

6.2.4 Assembly of All-Solid-State Lithium-Ion Batteries

70 mg LNTO@LCO and 30 mg commercial $\text{Li}_{10}\text{GeP}_2\text{S}_{12}$ (LGPS) (purchased from MSE supplies, its room-temperature ionic conductivity is $3.5 \times 10^{-3} \text{ S}\cdot\text{cm}^{-1}$) was mixed as the cathode composites. 80 mg LGPS was pressed at 1 MPa first. Then 12 mg cathode composite was uniformly spread on one side of the LGPS layer and compressed at 350 MPa. A piece of indium foil was attached to the other side of LGPS and pressed at 100

MPa. Then the battery was retested for 6 hours before electrochemical testing. The electrochemical impedance spectra were from 7MHz to 0.1Hz with an amplitude of 10 mV. The CV was tested from 1.9V to 3.8V with a scan rate of 0.02 mV.s⁻¹. The GITT was performed with a 5 min discharge at 0.1C followed by 2 hours of relaxation. The mass loading of NMC532 is 10.7 mg.cm⁻². 1C is defined at 0.13 mA.cm⁻². All the electrochemical performance was tested at room temperature by the LAND electrochemical analysis system.

6.3. Results and Discussion

6.3.1 Synthesis of Interfacial LiNb_{0.5}Ta_{0.5}O₃ (LNTO) with Different Ionic Conductivities.

LNTO has a low electrical conductivity (10⁻¹¹ S.cm⁻¹) and wide electrochemical window,^{30, 31} which is beneficial for suppressing interfacial reactions at the cathode/SE interface and providing good interfacial stability upon cycling. Most interestingly, the ionic conductivity of LNTO can be tuned by altering post-annealing temperature,³¹⁻³³ which provides us a unique platform for studying the effect of interfacial coating layer ionic conductivity on the electrochemical performance of SE-based ASSLIBs. First LNTO was synthesized by a sol-gel method.³⁴ Thermogravimetry (TG) and differential scanning calorimetry (DSC) was employed to determine the annealing temperature of LNTO in air. As shown in TG-DSC curves (**Figure 6-S1**), the organic species of Nb and Ta precursors are decomposed in air before 350°C. Three exothermic peaks are shown at 380 °C, 410 °C, and 427 °C, which implies the formation of LNTO nanocrystals.^{31, 35} No any exothermic peak is observed after 450°C. Therefore, LNTO powder was thermally treated at 350 °C, 450 °C, and 550 °C in air for 2 hours to obtain different ionic conductivity, respectively. The detailed experimental procedure can be found in Supporting Information. X-ray diffraction (XRD) patterns in **Figure 6-1a**

indicates that LNT0 annealed at 350 °C, 450 °C and 550 °C is amorphous, partially crystallized, and fully crystallized, respectively. The ionic conductivities of LNT0 annealed at 350 °C, 450°C, and 550°C are 13.2 $\mu\text{S cm}^{-1}$, 38.7 $\mu\text{S cm}^{-1}$, and 2.43 $\mu\text{S cm}^{-1}$, respectively, as evaluated by electrochemical impedance spectroscopy (EIS) (Figure 6-1b, 6-1c). The same relationship between the ionic conductivity and crystallinity of LNT0 has also been found in early references.^{31, 36}

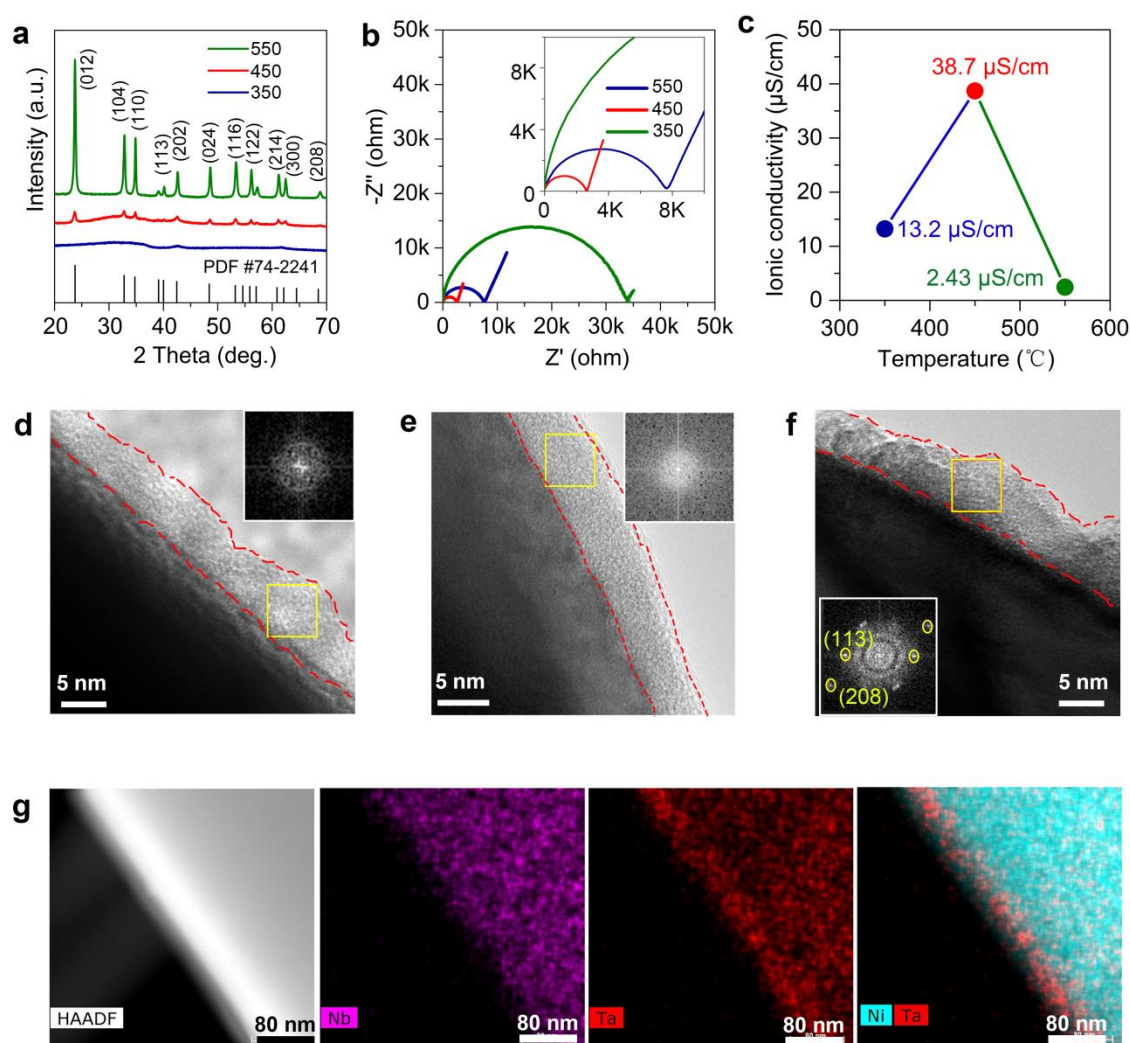


Figure 6-1 Characterizations on $\text{LiNb}_{0.5}\text{Ta}_{0.5}\text{O}_3$ (LNT0) and LNT0@NMC532. (a) XRD patterns of $\text{LiNb}_{0.5}\text{Ta}_{0.5}\text{O}_3$ (LNT0) annealed at various temperatures. (b) EIS profile of LNT0 after annealing at different temperatures. (c) The ionic

conductivity of LNTO annealing at different temperatures. (d) TEM image of LNTO@NMC532 annealed at 350°C. (e) TEM image of LNTO@NMC532 annealed at 450°C. (f) TEM image of LNTO@NMC532 annealed at 550°C. (g) STEM-EDX mapping of Nb, Ta and Ni-Ta combination.

To interpose the LNTO interfacial layer at the cathode/SE interface, LNTO sol-gel was coated on single-crystal $\text{LiNi}_{0.5}\text{Mn}_{0.3}\text{Co}_{0.2}\text{O}_2$ (NMC532) followed by the same annealing procedures as mentioned above. These LNTO-coated NMC532 cathodes are labeled as LNTO@NMC532-350, LNTO@SC-NMC532-450, and LNTO@NMC532-550, respectively. High-resolution transmission electron microscopy (HRTEM) was performed to inspect the crystallinity, thickness, and uniformity of the LNTO interfacial layer. **Figure 6-1d, 6-1e,** and **6-1f** exhibit the TEM images and corresponding fast Fourier transform (FFT) patterns (inset) of LNTO@NMC532-350, LNTO@NMC532-450, and LNTO@NMC532-550, respectively. All the thickness of the LNTO interfacial layer on NMC532 is consistently 5 nm. The LNTO interfacial layers annealed at 350 °C and 450 °C does not show FFT patterns, indicating the LNTO interfacial layer is in an amorphous state. While LNTO interfacial layer annealed at 550 °C clearly exhibits an FFT pattern, indicating the crystalline LNTO layer is formed on the NMC532 surface. By increasing the annealing temperature, the crystallinity of LNTO is enhanced, which is in good agreement with the XRD result of LNTO. Representative scanning TEM (STEM)-energy-dispersive X-ray (EDX) mapping of LNTO@NMC532-450 is present in **Figure 6-1g**, verifying the uniformity and conformality of LNTO interfacial layer on NMC532 surface. To further confirm that LNTO is fully covered on NMC532 at a macroscopic perspective, scanning electron microscopy (SEM) coupled with EDX was performed. As displayed in **Figure 6-S2, 6-S3,** and **6-S4**, the uniform distribution of Nb and Ta on all the NMC532 particles demonstrates all NMC532 particles are fully covered by LNTO. **Figure 6-S5** shows the XRD patterns of LNTO@NMC532 after heating under different temperatures. The

unchanged (003) peaks suggest that interfacial coating LNTO does not diffuse into the NMC532 lattice during the annealing process. The same thickness, same chemical composition, and full coverage of LNTO on NMC532 particles serve as a reliable foundation for investigating the effect of interfacial ionic conductivity on SE-based ASSLIBs.

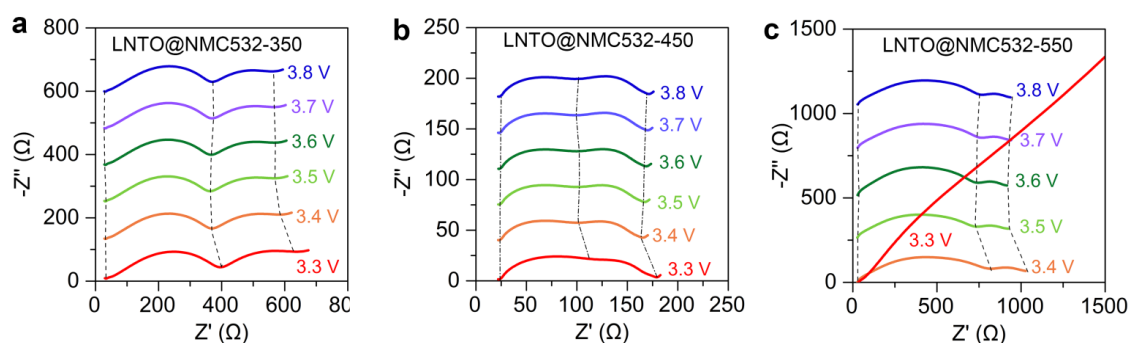


Figure 6-2 EIS profiles of ASSLIBs being charged at different cut-off voltages. (a) LNTO@NMC532-350, (b) LNTO@NMC532-450, (c) LNTO@NMC532-550.

To confirm that interfacial coating layer LNTO suppresses interfacial reactions between NMC532 and SEs, ex-situ EIS was conducted to examine the interfacial resistance change during the initial charge process, upon which most of interfacial reactions occur.^{37, 38} **Figure 6-2a, 6-2b, and 6-2c** present the EIS profiles of LNTO@NMC532-based ASSLIBs being charged at various cut-off voltages from 3.3 V to 3.8 V. All the EIS profiles mainly consist of two semi-circles except for the first EIS profile (a slope) of LNTO@NMC532-550 charging to 3.3V. The slope is caused by the large polarization that retards the de-lithiation process of LNTO@NMC532-550 even being charged to 3.3 V. In general, the high-frequency semicircle of EIS profiles is corresponding to the cathode interfacial resistance and grain boundary resistance of SEs, while the low-frequency semicircle represents the anode interfacial resistance.^{37, 39} The unnoticeable change of cathode interfacial resistance strongly suggest that the interfacial coating LNTO successfully prevents the interfacial reactions between NMC532 and SEs.

Among them, LNT0@NMC532-450 exhibits the smallest interfacial resistance while LNT0@NMC532-550 shows the largest interfacial resistance, which hints that the high Li^+ -conductive coating layer is beneficial for interfacial Li^+ transport in SE-based ASSLIBs. The further discussion of interfacial resistance will be made in the next part.

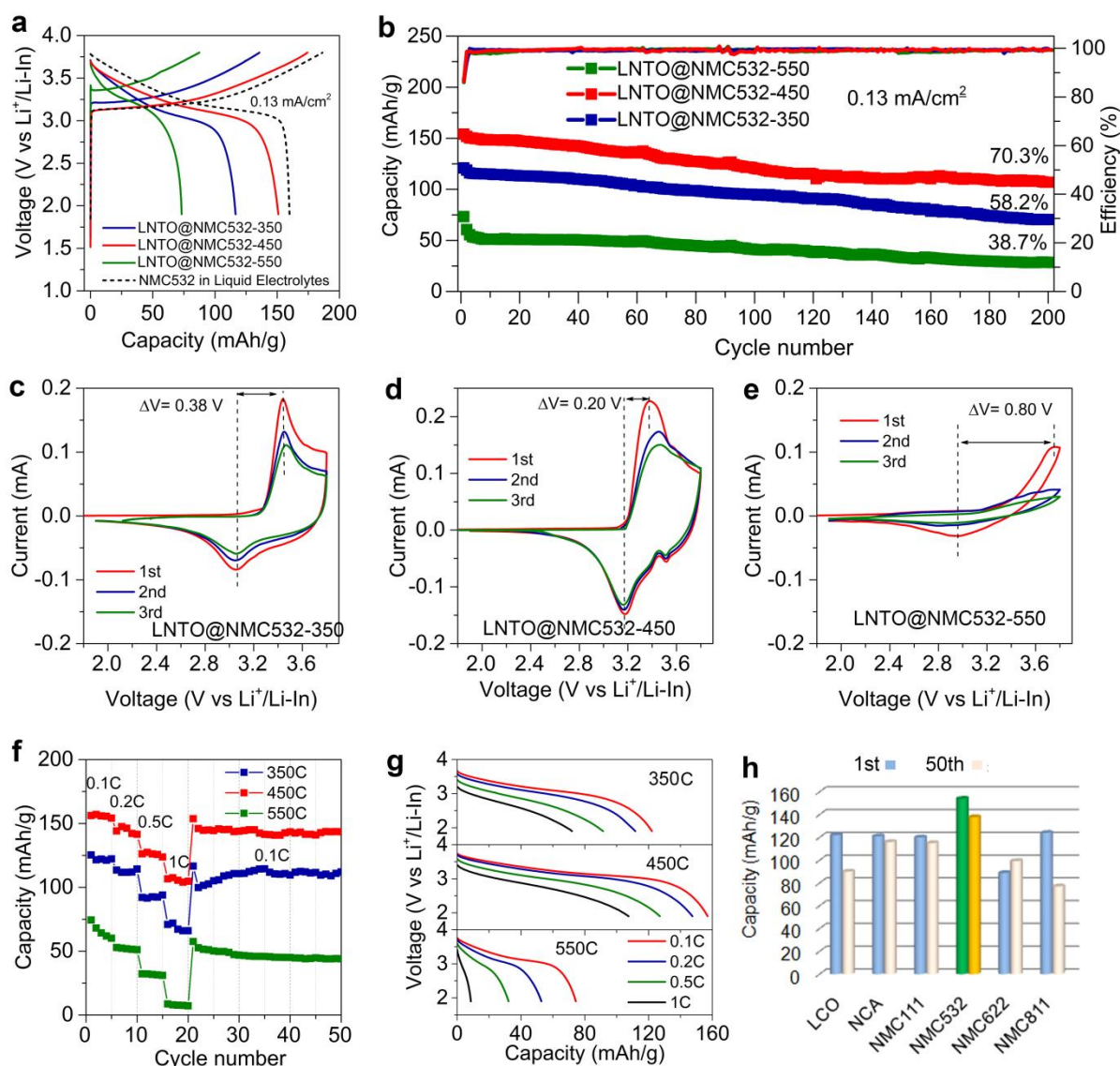


Figure 6-3 Electrochemical performance of LNT0@SC-NMC532-based ASSLIBs.

(a) the comparison of the charge-discharge curves of LNT0@NMC532-350, LNT0@NMC532-450, and LNT0@NMC532-550. (b) The cycling stability and Coulombic efficiency of LNT0@NMC532-350, LNT0@NMC532-450, and

LNT@NMC532-550. (c) CV profiles of LNT@NMC532-350. (d) CV profiles of LNT@NMC532-450. (e) CV profiles of LNT@NMC532-550. (f) Rate performance of LNT@NMC532-350, LNT@NMC532-450, and LNT@NMC532-550. (g) Discharge curves with different current densities of LNT@NMC532-350, LNT@NMC532-450, and LNT@NMC532-550. (h) The comparison of electrochemical performance with previous results related to SE-based ASSLIBs.

6.3.2 Electrochemical Performance of LNT@NMC532-based ASSLIBs

To fairly evaluate the electrochemical performance of these three cathodes in SE-based ASSLIBs, typical $\text{Li}_{10}\text{GeP}_2\text{S}_{12}$ (LGPS) was selected as the solid-state electrolyte due to its high ionic conductivity of $(2.8 \text{ mS}\cdot\text{cm}^{-1})$.⁴⁰ **Figure 6-3a** shows their initial charge/discharge curves at a current density of $130 \mu\text{A}\cdot\text{cm}^{-2}$ (0.1C). The initial de-lithiation voltage (3.25 V vs $\text{Li}^+/\text{Li-In}$) and polarization of LNT@NMC532-450 are discernibly smaller than those of the other two cathodes. At the initial stage of charging, the initial de-lithiation voltage of LNT@NMC532-450 overlaps with that of NMC532-based liquid cells at the same current density, suggesting that highly Li^+ -conductive LNTO interfacial layer can enable the interfacial Li^+ transport as fast as that in liquid cells. The initial discharge curve of LNT@NMC532 is slightly lower than that of liquid cells, which is probably due to the volume change-induced physical contact loss between NMC532 and LGPS, as revealed in previous work.^{37, 41}

The initial discharge capacity of LNT@NMC532-450 is $152 \text{ mAh}\cdot\text{g}^{-1}$, higher than those of LNT@NMC532-350 ($120.9 \text{ mAh}\cdot\text{g}^{-1}$) and LNT@NMC532-550 ($73.2 \text{ mAh}\cdot\text{g}^{-1}$). The initial Coulombic efficiency of LNT@NMC532-350, LNT@NMC532-450, and LNT@NMC532-550 is 87.14%, 86.68%, and 85.98%, respectively, which are close to

that of NMC532-based liquid cells (85.79%) (**Figure 6-S6**). The high initial Coulombic efficiency of three cathodes hints that interfacial reactions between NMC532 and LGPS have been successfully suppressed by the LNTO coating layer, which is fully consistent with the EIS results discussed in Figure 2. The capacity retention after 200 cycles of LNTO@NMC532-350, LNTO@NMC-532-450, and LNTO@NMC532-550 is around 58.2%, 70.3%, and 38.7%, respectively (**Figure 6-3b**). The average Coulombic efficiency of LNTO@NMC532-450 is 99.2% after the second cycle.

Furthermore, cyclic voltammetry (CV) curves of LNTO@NMC532-350, LNTO@NMC532-450, and LNTO@NMC532-550 were compared in **Figure 6-3c**, **6-3d**, and **6-3e**, respectively. It can be seen that the oxidation/reduction peak currents of LNTO@NMC532-450 and LNTO@NMC532-350 are larger than that of LNTO@NMC532-550, which is consistent with their higher initial discharge capacity. In addition, the polarization voltage (0.20 V) between oxidization and reduction peaks of LNTO@NMC532-450 is much smaller than those of LNTO@NMC532-350 (0.38 V) and LNTO@NMC532-550 (0.80V), further verifying that LNTO@NMC532-450 possess the best reversibility and the fastest Li^+ transport kinetics.

The rate-performance of LNTO@NMC532-350, LNTO@NMC532-450, and LNTO@NMC532-550 were also compared (**Figure 6-3f**) and their corresponding curves at 0.1C, 0.2C, 0.5C, and 1C are present in **Figure 6-3g**. Remarkably, LNTO@NMC532-450 demonstrates the best rate of performance. Even at 1C, the specific capacity keeps at 107.5 mAh.g^{-1} . In contrast, the LNTO@NMC532-550 displays the capacity of 8.6 mAh.g^{-1} at 1C. Comparing the best electrochemical performance of LNTO@NMC-532-450 with those previously reported electrochemical performances of SE-based ASSLIBs,^{12, 37, 42-44} both the specific capacity and capacity retention outperforms most of the previously reported results (**Figure6- 3h**) (**Table 6-S1**).

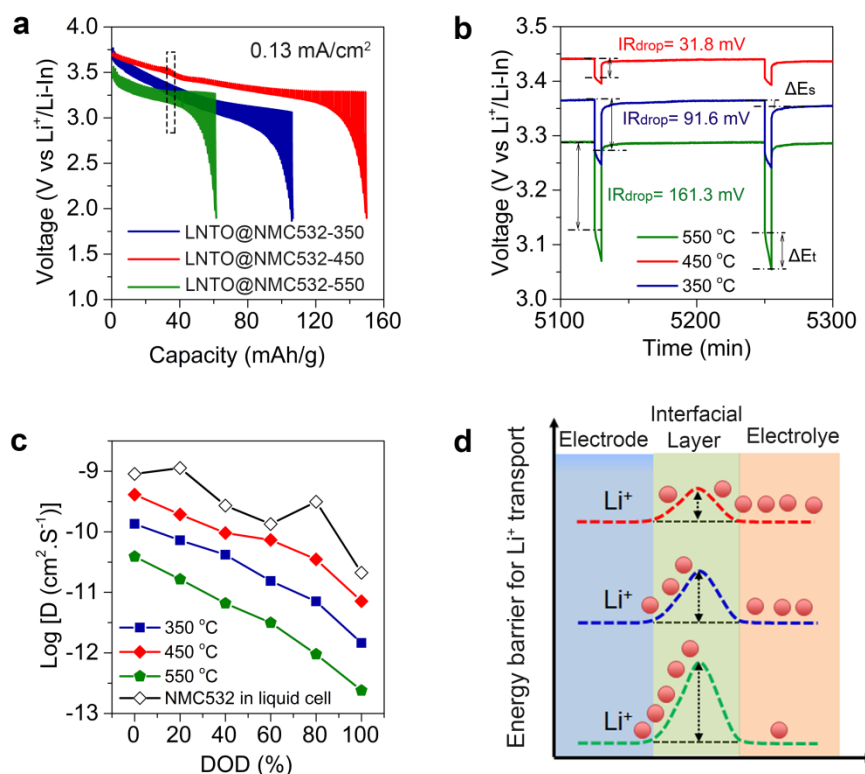


Figure 6-4 Analysis of Li⁺ transport kinetics. (a) Initial discharging GITT profiles of LNTO@NMC532-350, LNTO@NMC532-450, and LNTO@NMC532-550. (b) Typical GITT curves marked with IR drop. (c) Li⁺ diffusion coefficient of LNTO@NMC532-350, LNTO@NMC532-450, and LNTO@NMC532-550 as a function of depth of discharge (DOD). (d) Schematics of Li⁺ transport across the electrode-electrolyte interface with different energy barriers.

6.3.3 Quantifying Li⁺ Diffusivity of LNTO@NMC532

To gain insights into the Li⁺ kinetics behind the electrochemical performance difference, Li⁺ diffusion kinetics of LNTO@NMC532 in SE-based ASSLIBs was further analyzed by galvanostatic intermittent titration technique (GITT), because an interfacial coating layer has a profound impact on Li⁺ diffusivity of electrode materials, as widely studied in liquid cells.⁴⁵⁻⁵² **Figure 6-4a** displays the typical discharging GITT curves of the

LNT@NMC532-350, LNT@NMC532-450, and LNT@NMC532-550 at 0.1 C. Obviously, LNT@NMC532-450 shows the lowest polarization among them, indicating the fastest Li⁺ kinetics.⁴⁷ In addition, the voltage drop (IR_{drop}) after the current interruption is closely related to the Li⁺ transport resistance inside the solid-state batteries. Typically, the IR_{drop} of LNT@SC-NMC532-450 is only 31.8 mV (**Figure 6-4b**), which is approximately 3 times lower than that of LNT@SC-NMC532-350 (91.6 mV) and 5 times lower than that of LNT@SC-NMC532-550 (161.3 mV). The Li⁺ diffusivity of these LNT@NMC532 electrodes can be quantitatively calculated according to the equation:⁴⁶

$$D_{\text{Li}^+} = \frac{4}{\pi\tau} \left(\frac{m_{\text{NMC532}} V_{\text{NMC532}}}{M_{\text{NMC532}} S} \right)^2 \left(\frac{\Delta E_s}{\Delta E_\tau} \right)^2 \quad (1)$$

Where τ is the relaxation time (2 hours), m_{NMC532} is the mass of SC-NMC532 in the electrode composite. V_{NMC532} is the molar volume of SC-NMC532 (20.73 cm³.mol⁻¹), M_{NMC532} is the molar mass of host materials, for the discharge process, the host material is SC-Li_{0.3}(Ni_{0.5}Mn_{0.3}Co_{0.2})O₂ (91.66 g.mol⁻¹). ΔE_s is the steady-voltage change after 2 hours of relaxation. ΔE_τ is the change in the transient-voltage change after 5 min discharge process at 0.13 mA.cm⁻². ΔE_s and ΔE_τ were illustrated in **Figure 6-4b**.

Figure 6-4c compares the Li⁺ diffusivity of LNT@NMC532-350, LNT@NMC532-450, and LNT@NMC532-550 as a function of the different depth of discharge (DOD). In general, the Li⁺ diffusion coefficient decreases with the increase of DOD, which is accompanied by the saturation of Li⁺ sites in NMC532 upon the discharge, thus the Li⁺ concentration gradient gradually decreases upon discharge.^{49, 51} Comparatively, the average Li⁺ diffusivity of LNT@NMC532-350, LNT@NMC532-450, and LNT@NMC532-550 in ASSLIBs are 4.55×10^{-11} cm².s⁻¹, 1.36×10^{-10} cm².s⁻¹, and 1.11×10^{-11} cm².s⁻¹, respectively, which are lower than that of liquid cells (4.62×10^{-10} cm².s⁻¹) (**Figure 6-S7**), indicating that the coating

layer slows down the Li^+ transport in solid-state batteries. However, the Li^+ diffusivity of LNT0@NMC532-450 and LNT0@NMC532-350 are approximately 12 and 4 times faster than that of LNT0@NMC532-550, demonstrating that improving the ionic conductivity of coating layer significantly boost the Li^+ transport kinetics in solid-state batteries.

Interfacial Li^+ transport kinetics was further verified by EIS. In EIS profiles (**Figure 6-S8**) the inception is related to the resistance of solid electrolytes layer, the semi-circle at the high-frequency region is related to the interfacial resistance between NMC532 and LGPS and grain boundary resistance of LGPS, as simulated by the equivalent circuits inserted in **Figure 6-S8(d)**.²³ The interfacial resistance of LNT0@NMC532-450 is 124 Ω , while the interfacial resistances of LNT0@NMC532-350 and LNT0@NMC532-550 are 369 Ω and 672 Ω , respectively. High ionic conductivity of LNT0 coated on NMC532 exhibits the lowest interfacial resistance, as shown in **Figure 6-S8(b)**, confirming that the LNT0 with a higher interfacial ionic conductivity can significantly reduce the interfacial resistance. Both the GITT and EIS analyses consistently demonstrate that high Li^+ -conductive LNT0 coated NMC532 exhibits fast Li^+ diffusion kinetics while low Li^+ -conductive LNT0 coated NMC532 manifests sluggish Li^+ diffusion kinetics in solid-state batteries. Therefore, enhancing the ionic conductivity of the interfacial coating layer can significantly accelerate the interfacial Li^+ transport kinetics, which in turn improves the electrochemical performance of SE-based ASSLIBs.

Figure 6-4d illustrates Li^+ transport across the interfacial coating with different energy barriers. The high interfacial ionic conductivity of the interfacial coating layer can conduct Li^+ fast at the interface, which is corresponding to a low energy barrier for interfacial Li^+ transport. In contrast, the low interfacial ionic conductivity of the interfacial layer conducts Li^+ very slow, thus showing a high energy barrier for interfacial Li^+ transport. Detailed and in-depth discussion about the Li^+ transport process in a

solid-state battery can be found in **Figure 6-S9**.

6.4. Conclusions

In this work, we manipulated the ionic conductivity of the interfacial coating layer by tuning post-annealing temperature and investigated its effect on the electrochemical performance of SE-based ASSLIBs for the first time. It is found that the ionic conductivity of the interfacial coating layer determines the Li⁺ diffusion kinetics in SE-based ASSLIBs and increasing the ionic conductivity of the interfacial coating layer can significantly accelerate the interfacial Li⁺ transport. The oxide cathode NMC532 coated with the highest Li⁺-conductive LNTO exhibits the highest Li⁺ diffusion coefficient of $1.36 \times 10^{-10} \text{ cm}^2\cdot\text{S}^{-1}$. Resultantly, the LNO@NMC532 demonstrates a high capacity of 152 mAh.g⁻¹ at 0.1 C and 107.5 mAh.g⁻¹ at 1C. This work suggests that enhancing the ionic conductivity of the interfacial coating layer is essential for developing high-performance SE-based ASSLIBs.

6.5 Acknowledgments

This work was supported by Natural Sciences and Engineering Research Council of Canada (NSERC), Canada Research Chair Program (CRC), Canada Foundation for Innovation (CFI), Ontario Research Fund (ORF), China Automotive Battery Research Institute Co., Ltd., Glabat Solid-State Battery Inc., Canada Light Source (CLS) at University of Saskatchewan, Interdisciplinary Development Initiatives (IDI) by Western University, and University of Western Ontario. Dr. J. Liang, Dr. X. Li, and Dr. X. L. thank the funding support of Mitacs Elevate Postdoctoral Fellowships. Dr. S. Deng and C. Wang appreciates the funding support from Mitacs Accelerate Fellowships. Part of electron microscopy work was conducted at the Center for Functional Nanomaterials,

which is a U.S. DOE Office of Science Facility, at Brookhaven National Laboratory under Contract No. DE-SC0012704.

6.6 Author Contributions

X. Sun supervised the project. C. Wang conceived this idea, synthesized the electrodes, tested the electrochemical performances, performed characterization and wrote this manuscript. S. Hwang and D. Su helped with TEM characterization. R. Li helped with SEM and purchased all the chemicals. All authors discussed the results and commented on the manuscript.

6.7 References

1. S. Xia, X. Wu, Z. Zhang, Y. Cui and W. Liu, *Chem*, 2019, DOI: 10.1016/j.chempr.2018.11.013, 1-33.
2. X.-B. Cheng, C.-Z. Zhao, Y.-X. Yao, H. Liu and Q. Zhang, *Chem*, 2019, **5**, 74-96.
3. Y. Zhao, K. Zheng and X. Sun, *Joule*, 2018, 1-22.
4. A. Miura, N. C. Rosero-Navarro, A. Sakuda, K. Tadanaga, N. H. H. Phuc, A. Matsuda, N. Machida, A. Hayashi and M. Tatsumisago, *Nat. Rev. Chem.*, 2019, **3**, 189-198.
5. H. Lee, P. Oh, J. Kim, H. Cha, S. Chae, S. Lee and J. Cho, *Adv. Mater.*, 2019, **31**, 1900376.
6. S. P. Culver, R. Koerver, W. G. Zeier and J. Janek, *Adv. Energy Mater.*, 2019, **9**, 1900626.

7. K. H. Park, Q. Bai, D. H. Kim, D. Y. Oh, Y. Zhu, Y. Mo and Y. S. Jung, *Adv. Energy Mater.*, 2018, **8**, 1800035.
8. T. Ates, M. Keller, J. Kulisch, T. Adermann and S. Passerini, *Energy Storage Materials*, 2019, **17**, 204-210.
9. Y. Kato, S. Hori, T. Saito, K. Suzuki, M. Hirayama, A. Mitsui, M. Yonemura, H. Iba and R. Kanno, *Nat. Energy*, 2016, **1**, 16030.
10. N. Kamaya, K. Homma, Y. Yamakawa, M. Hirayama, R. Kanno, M. Yonemura, T. Kamiyama, Y. Kato, S. Hama, K. Kawamoto and A. Mitsui, *Nat. Mater.*, 2011, **10**, 682-686.
11. Y. Sun, K. Suzuki, S. Hori, M. Hirayama and R. Kanno, *Chem. Mater.*, 2017, **29**, 5858-5864.
12. M. A. Kraft, S. Ohno, T. Zinkevich, R. Koerver, S. P. Culver, T. Fuchs, A. Senyshyn, S. Indris, B. J. Morgan and W. G. Zeier, *J. Am. Chem. Soc.*, 2018, **140**, 16330-16339.
13. A. Hayashi, N. Masuzawa, S. Yubuchi, F. Tsuji, C. Hotehama, A. Sakuda and M. Tatsumisago, *Nat. Commun.*, 2019, **10**, 5266.
14. P. K. Ho, B. Qiang, K. D. Hyeon, O. D. Yang, Z. Yizhou, M. Yifei and J. Y. Seok, *Adv. Energy Mater.*, 2018, **0**, 1800035.
15. X. Fan, X. Ji, F. Han, J. Yue, J. Chen, L. Chen, T. Deng, J. Jiang and C. Wang, *Sci. Adv.*, 2018, **4**, 9245.
16. X. Li, J. Liang, X. Li, C. Wang, J. Luo, R. Li and X. Sun, *Energy Environ. Sci.*, 2018, **11**, 2828.
17. S. Teragawa, K. Aso, K. Tadanaga, A. Hayashi and M. Tatsumisago, *J. Power*

Sources, 2014, **248**, 939-942.

18. D. H. Kim, D. Y. Oh, K. H. Park, Y. E. Choi, Y. J. Nam, H. A. Lee, S.-M. Lee and Y. S. Jung, *Nano Lett.*, 2017, **17**, 3013-3020.

19. S. Yubuchi, M. Uematsu, C. Hotehama, A. Sakuda, A. Hayashi and M. Tatsumisago, *J. Mater. Chem. A*, 2019, **7**, 558-566.

20. K. H. Park, D. Y. Oh, Y. E. Choi, Y. J. Nam, L. Han, J.-Y. Kim, H. Xin, F. Lin, S. M. Oh and Y. S. Jung, *Adv. Mater.*, 2016, **28**, 1874-1883.

21. A. Banerjee, K. H. Park, J. W. Heo, Y. J. Nam, C. K. Moon, S. M. Oh, S.-T. Hong and Y. S. Jung, *Angew. Chem. Int. Ed.*, 2016, **55**, 9634-9638.

22. S. Yubuchi, M. Uematsu, M. Deguchi, A. Hayashi and M. Tatsumisago, *ACS Applied Energy Materials*, 2018, **1**, 3622-3629.

23. N. Ohta, K. Takada, I. Sakaguchi, L. Zhang, R. Ma, K. Fukuda, M. Osada and T. Sasaki, *Electrochem. Commun.*, 2007, **9**, 1486-1490.

24. C. Wang, X. Li, Y. Zhao, M. N. Banis, J. Liang, X. Li, Y. Sun, K. R. Adair, Q. Sun, Y. Liu, F. Zhao, S. Deng, X. Lin, R. Li, Y. Hu, T.-K. Sham, H. Huang, L. Zhang, R. Yang, S. Lu and X. Sun, *Small Methods*, 2019, **1900261**, doi:10.1002/smtd.201900261.

25. N. Ohta, K. Takada, L. Zhang, R. Ma, M. Osada and T. Sasaki, *Adv. Mater.*, 2006, **18**, 2226-2229.

26. T. Shi, Q. Tu, Y. Tian, Y. Xiao, L. J. Miara, O. Kononova and G. Ceder, *Advanced Energy Materials*, 2019, **n/a**, 1902881.

27. D. Cao, Y. Zhang, A. M. Nolan, X. Sun, C. Liu, J. Sheng, Y. Mo, Y. Wang and H. Zhu, *Nano Lett.*, 2019, DOI: 10.1021/acs.nanolett.9b02678.

28. S. P. Culver, R. Koerver, W. G. Zeier and J. Janek, *Adv. Energy Mater.*, 2019, **0**, 1900626.
29. Y. Xiao, L. J. Miara, Y. Wang and G. Ceder, *Joule*, 2019, doi.org/10.1016/j.joule.2019.02.006.
30. Y. Zhu, X. He and Y. Mo, *J. Mater. Chem. A*, 2016, **4**, 3253-3266.
31. A. M. Glass, K. Nassau and T. J. Negran, *J Appl Phys*, 1978, **49**, 4808-4811.
32. S. Lanfredi and A. C. M. Rodrigues, *J Appl Phys*, 1999, **86**, 2215-2219.
33. C. Yada, C. E. Lee, D. Laughman, L. Hannah, H. Iba and B. E. Hayden, *J. Electrochem. Soc*, 2015, **162**, A722-A726.
34. W. Zhang, D. A. Weber, H. Weigand, T. Arlt, I. Manke, D. Schröder, R. Koerver, T. Leichtweiss, P. Hartmann, W. G. Zeier and J. Janek, *ACS Appl. Mater. Interfaces*, 2017, **9**, 17835-17845.
35. N. Özer and C. M. Lampert, *Sol. Energy Mater Sol. Cells*, 1995, **39**, 367-375.
36. H. Aono, N. Imanaka and G.-y. Adachi, *Accounts Chem. Res.*, 1994, **27**, 265-270.
37. R. Koerver, I. Aygün, T. Leichtweiß, C. Dietrich, W. Zhang, J. O. Binder, P. Hartmann, W. G. Zeier and J. Janek, *Chem. Mater.*, 2017, **19**, 5574-5582.
38. K. Takada, N. Ohta, L. Zhang, K. Fukuda, I. Sakaguchi, R. Ma, M. Osada and T. Sasaki, *Solid State Ion.*, 2008, **179**, 1333-1337.
39. A. Y. Kim, F. Strauss, T. Bartsch, J. H. Teo, T. Hatsukade, A. Mazilkin, J. Janek, P. Hartmann and T. Brezesinski, *Chem. Mater.*, 2019, DOI: 10.1021/acs.chemmater.9b02947.

40. C. Wang, K. R. Adair, J. Liang, X. Li, Y. Sun, X. Li, J. Wang, Q. Sun, F. Zhao, X. Lin, R. Li, H. Huang, L. Zhang, R. Yang, S. Lu and X. Sun, *Adv. Funct. Mater.*, 2019, **1900392**, DOI:10.1002/adfm.201900392.
41. R. Koerver, W. Zhang, L. de Biasi, S. Schweidler, A. O. Kondrakov, S. Kolling, T. Brezesinski, P. Hartmann, W. G. Zeier and J. Janek, *Energy Environ. Sci.*, 2018, DOI: 10.1039/C8EE00907D.
42. A. Sakuda, H. Kitaura, A. Hayashi, M. Tatsumisago, Y. Hosoda, T. Nagakane and A. Sakamoto, *Chem. Lett.*, 2012, **41**, 260-261.
43. S. Ito, S. Fujiki, T. Yamada, Y. Aihara, Y. Park, T. Y. Kim, S.-W. Baek, J.-M. Lee, S. Doo and N. Machida, *J. Power Sources*, 2014, **248**, 943-950.
44. N. Machida, J. Kashiwagi, M. Naito and T. Shigematsu, *Solid State Ion.*, 2012, **225**, 354-358.
45. X. H. Rui, N. Yesibolati, S. R. Li, C. C. Yuan and C. H. Chen, *Solid State Ion.*, 2011, **187**, 58-63.
46. X. H. Rui, N. Ding, J. Liu, C. Li and C. H. Chen, *Electrochim. Acta*, 2010, **55**, 2384-2390.
47. J. Li, X. Xiao, Y.-T. Cheng and M. W. Verbrugge, *J. Phys. Chem. Lett.*, 2013, **4**, 3387-3391.
48. S. Shi, P. Lu, Z. Liu, Y. Qi, L. G. Hector, H. Li and S. J. Harris, *J. Am. Chem. Soc.*, 2012, **134**, 15476-15487.
49. R. Amin and Y.-M. Chiang, *J. Electrochem. Soc.*, 2016, **163**, A1512-A1517.
50. J. S. Park, A. U. Mane, J. W. Elam and J. R. Croy, *ACS Omega*, 2017, **2**, 3724-3729.

51. Y. J. Kim, H. Kim, B. Kim, D. Ahn, J.-G. Lee, T.-J. Kim, D. Son, J. Cho, Y.-W. Kim and B. Park, *Chem. Mater.*, 2003, **15**, 1505-1511.
52. J.-Y. Liang, X.-X. Zeng, X.-D. Zhang, P.-F. Wang, J.-Y. Ma, Y.-X. Yin, X.-W. Wu, Y.-G. Guo and L.-J. Wan, *J. Am. Chem. Soc.*, 2018, **140**, 6767-6770.

6.8 Supporting Information

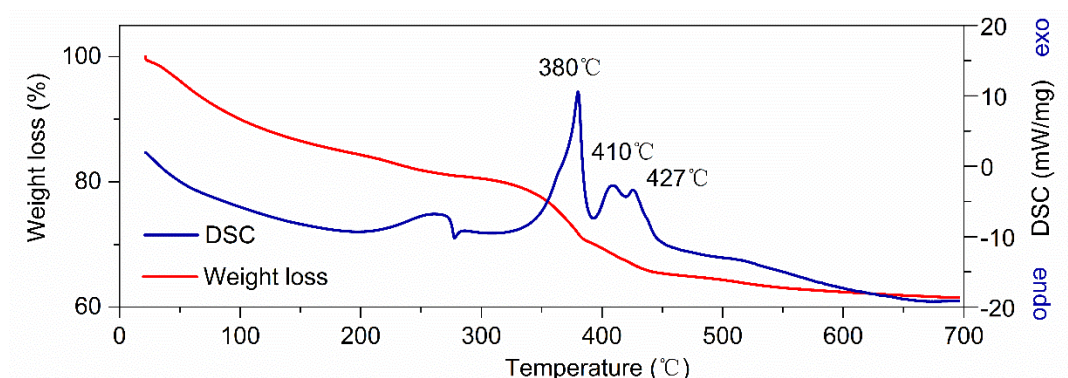


Figure 6-S1. TGA-DSC analysis of Li-Nb-Ta-O sol-gel under the air atmosphere. Before 350°C, the weight loss is due to the burn of organic species in air. The exothermic peaks between 360 °C to 450 °C are due to the phase-transition reactions of $\text{LiNb}_{0.5}\text{Ta}_{0.5}\text{O}_3$. After 450°C, it was believed to growth of nanograins of LNTO.

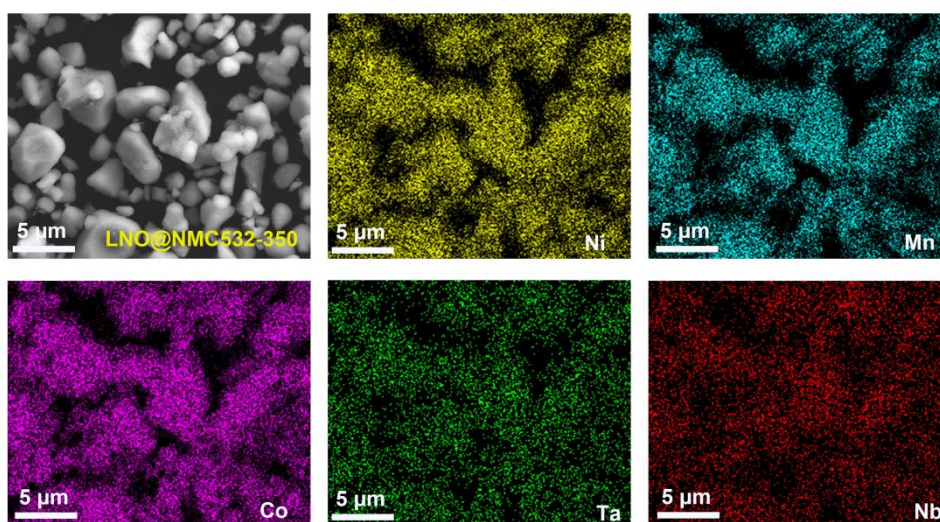


Figure 6-S2. SEM image and corresponding EDX mapping of LNTO@NMC532-350

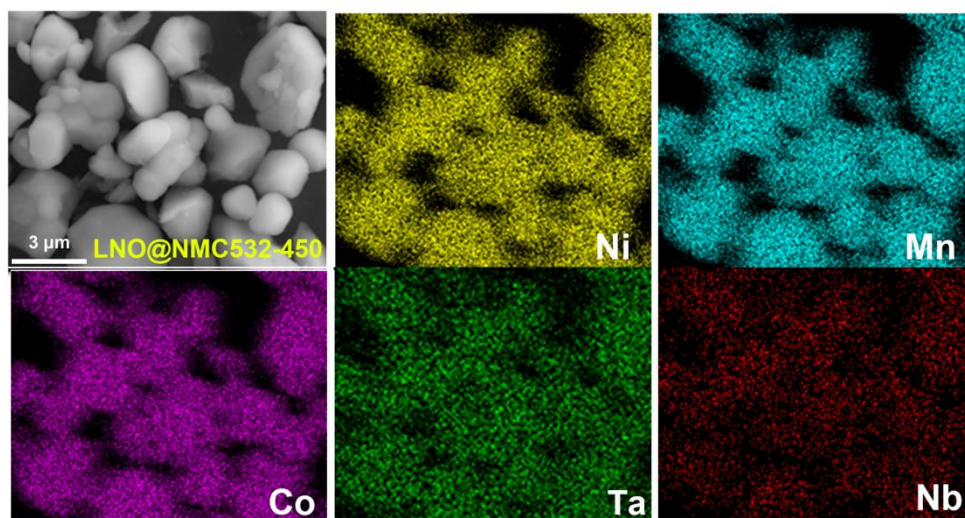


Figure 6-S3. SEM image and corresponding EDX mapping of LNT0@NMC532-450

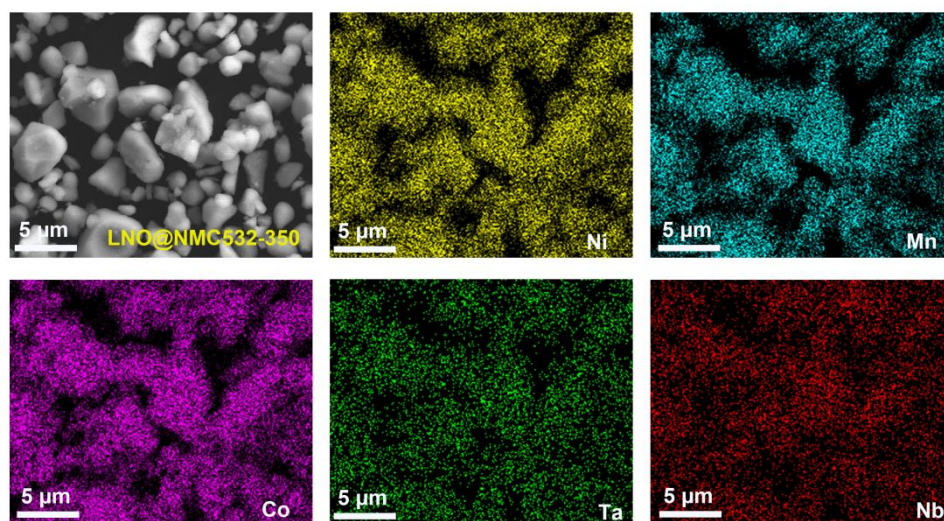


Figure6- S4. SEM image and corresponding EDX mapping of LNT0@NMC532-550

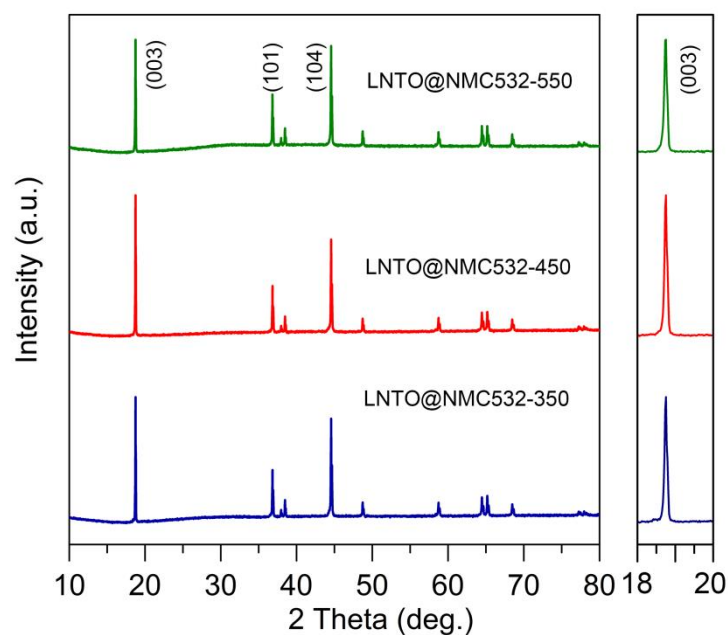


Figure 6-S5. XRD patterns of LNTO@NMC532-350, LNTO@NMC532-450, and LNTO@NMC532-550. The invisible change of (003) peak hints that LNTO does not diffuse into the NMC532 lattice during the high-temperature annealing process.

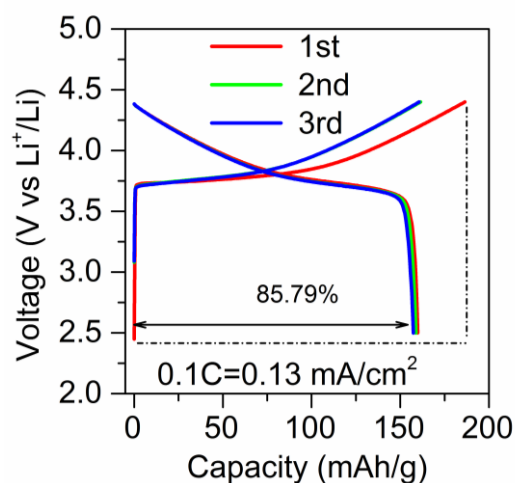


Figure 6-S6. Charge/discharge curves of NMC532 in liquid cells at the current density of $0.13 \text{ mA}\cdot\text{cm}^{-2}$.

Table 6-S1. The comparison of specific capacity in the references with results demonstrated in this work

<i>Cathode</i>	<i>Capacity at the 1st cycle</i>	<i>Capacity at the 50th</i>	<i>References</i>
<i>LiFePO₄</i>	<i>110</i>	<i>N/A</i>	<i>Ref1¹</i>
<i>LCO</i>	<i>126</i>	<i>103</i>	<i>Ref2²</i>
<i>NCA</i>	<i>121</i>	<i>116</i>	<i>Ref³</i>
<i>NMC111</i>	<i>120</i>	<i>115</i>	<i>Ref 3⁴</i>
<i>NMC532</i>	<i>154</i>	<i>137.8</i>	<i>This work</i>
<i>NMC622</i>	<i>88.8</i>	<i>99.3</i>	<i>Ref6⁵</i>
<i>NMC811</i>	<i>124</i>	<i>77</i>	<i>Ref7⁶</i>

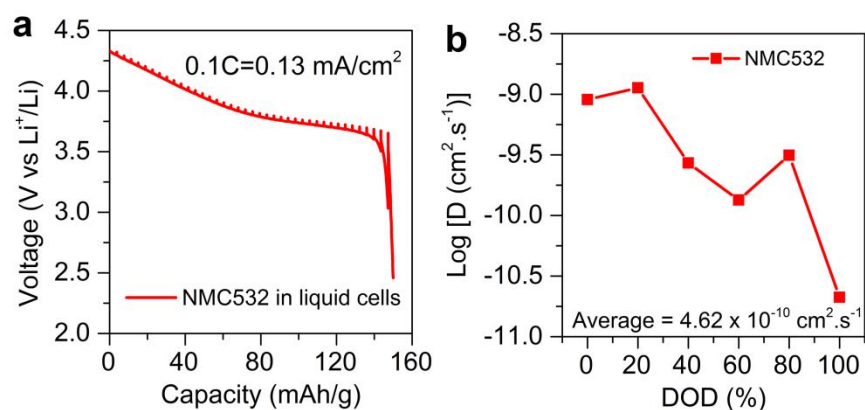


Figure 6-S7. (a) GITT discharge curve of NMC532 in liquid cells. (b) Li⁺ diffusion coefficients of NMC532 as the function of depth of discharge (DOD).

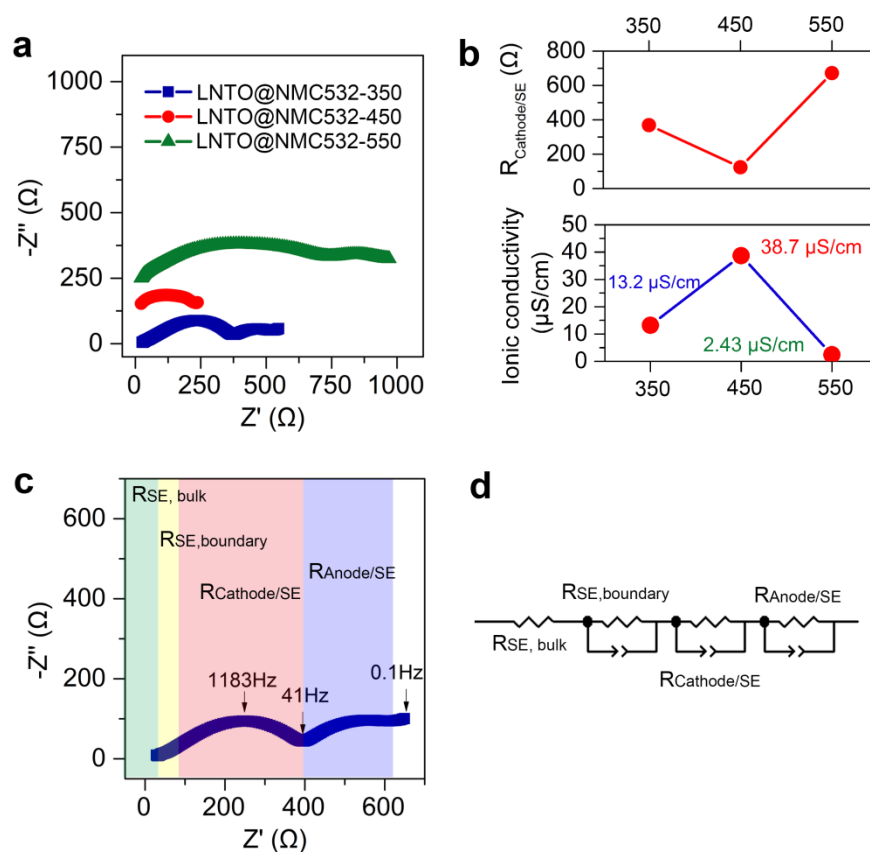


Figure 6-S8. (a) EIS profiles of LNT0@NMC532-350, LNT0@NMC532-450, and LNT0@NMC532-550 after first charging, respectively. (b) The cathode interfacial resistance of LNT0@NMC532-350, LNT0@NMC532-450, and LNT0@NMC532-550. (c) Assignment of typical EIS results. (d) The corresponding equivalent circuit.

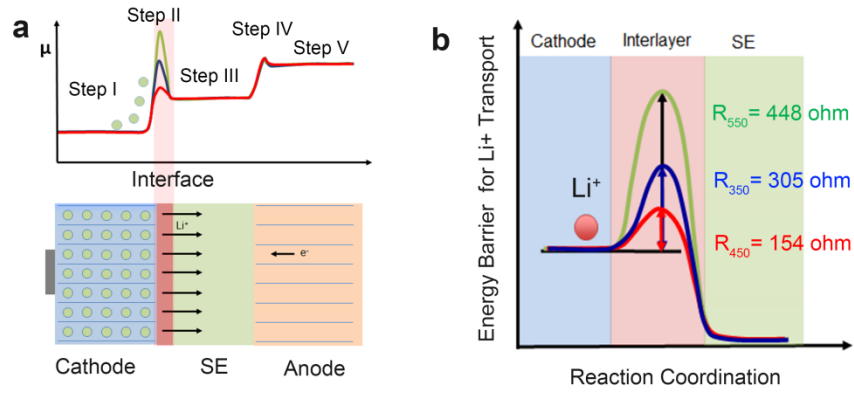


Figure 6-S9. Illustration of Li⁺ transport process in an all-solid-state lithium-ion battery. (a) Five key steps of Li⁺ transport in ASSLIBs. (b) Li⁺ transport across the interfacial coating layer with different energy barriers.

In general, Li⁺ transport in a solid-state battery can be divided into five distinguishable steps (**Figure 6-S9a**),^{7, 8} Step I: Li⁺ diffusion inside the layered cathode structure (Step I: $\frac{1}{R_{cathode}}$), Step II: Li⁺ across cathode-SE interface, which is determined by the ionic conductivity of cathode electrolyte interphases (CEI) ($\frac{1}{R_{CEI}}$), Step III: Li⁺ transport in the solid-state electrolyte layer, corresponding to the ionic conductivity of SEs ($\frac{1}{R_{SE}}$), Step IV: Li⁺ across the SEI layer at the anode interface ($\frac{1}{R_{SEI}}$), representing by ionic conductivity of SEI layer, and Step V: Li⁺ diffusion in an anode material ($\frac{1}{R_{SEI}}$). Thus, the consumed energy for Li⁺ transport in a solid-state battery (E_{total}) can be expressed as below, given that E_{total} is in reverse proportion to the total ionic conductivity ($\frac{1}{\sigma_{total}}$).

$$E_{total} \propto \frac{1}{\sigma_{total}} = \frac{1}{\frac{1}{R_{Cathode} + R_{CEI} + R_{SE} + R_{SEI} + R_{Anode}}} = R_{Cathode} + R_{CEI} + R_{SE} + R_{SEI} + R_{Anode} \quad (2)$$

In step I, layered single-crystal NMC532 has good electronic conductivity in our case, thus the electron percolation in the cathode composite is faster than Li⁺ transport, thus

electrochemical reactions mainly occurred at the interface between SC-NMC532 and LGPS. In addition, both the electric field and Li^+ concentration gradient inside the cathode materials can drive Li^+ to move. Moreover, the Li^+ diffusivity of NMC532 in liquid cells is about 10^{-8} to 10^{-10} $\text{cm}^2 \cdot \text{S}^{-1}$,⁹ which is also faster than Li^+ diffusion at the interface ($R_{\text{cathode}} \ll R_{\text{CEI}}$). Therefore, Step I would not be the limiting step. Furthermore, LGPS using the SE layer possesses a high ionic conductivity of 10^{-3} to 10^{-2} $\text{S} \cdot \text{cm}^{-1}$. And the indium foil was used as the reference electrode, which is stable against SE. Thus Li^+ transport across the SEI layer and indium layer should not be the limiting step either. Therefore, R_{SE} , R_{SEI} , and R_{anode} can be negligible in our case. All the things considered, equation 2 can simply be expressed as below.

$$E_{\text{total}} = E_{\text{decisive}} \propto \frac{1}{\sigma_{\text{CEI}}} = R_{\text{CEI}} \quad (3)$$

That is to say, Li^+ transport across the cathode-SE interface is the determining process, which greatly affects the energy consumed in a solid-state battery. The higher the R_{CEI} , the more energy required to conduct Li^+ back and forward (**Figure 6-S9b**). The smaller the R_{CEI} , the less energy consumed for interfacial Li^+ transport. In electrochemistry, solid-state batteries with a small R_{CEI} can exhibit high areal capacity and great rate-performance. Therefore, enhancing the ionic conductivity of the interfacial coating layer is highly demanded for achieving high-performance ASSLIBs with high areal capacity and fast charge/discharge capability.

References

1. A. Sakuda, H. Kitaura, A. Hayashi, M. Tatsumisago, Y. Hosoda, T. Nagakane and A. Sakamoto, *Chem. Lett.*, 2012, **41**, 260-261.

2. C. Wang, X. Li, Y. Zhao, M. N. Banis, J. Liang, X. Li, Y. Sun, K. R. Adair, Q. Sun, Y. Liu, F. Zhao, S. Deng, X. Lin, R. Li, Y. Hu, T.-K. Sham, H. Huang, L. Zhang, R. Yang, S. Lu and X. Sun, *Small Methods*, 2019, **0**, 1900261.
3. S. Ito, S. Fujiki, T. Yamada, Y. Aihara, Y. Park, T. Y. Kim, S.-W. Baek, J.-M. Lee, S. Doo and N. Machida, *J. Power Sources*, 2014, **248**, 943-950.
4. N. Machida, J. Kashiwagi, M. Naito, and T. Shigematsu, *Solid State Ion.*, 2012, **225**, 354-358.
5. M. A. Kraft, S. Ohno, T. Zinkevich, R. Koerver, S. P. Culver, T. Fuchs, A. Senyshyn, S. Indris, B. J. Morgan, and W. G. Zeier, *J. Am. Chem. Soc.*, 2018, **140**, 16330-16339.
6. R. Koerver, I. Aygün, T. Leichtweiß, C. Dietrich, W. Zhang, J. O. Binder, P. Hartmann, W. G. Zeier, and J. Janek, *Chem. Mater.*, 2017, **19**, 5574-5582.
7. T. R. Jow, S. A. Delp, J. L. Allen, J.-P. Jones and M. C. Smart, *J. Electrochem. Soc.*, 2018, **165**, A361-A367.
8. Y. Li, K. Leung, and Y. Qi, *Acc. Chem. Res.*, 2016, **49**, 2363-2370.
9. R. Amin and Y.-M. Chiang, *J. Electrochem. Soc.*, 2016, **163**, A1512-A1517.

Chapter 7

7. Eliminating Interfacial Resistance in All-Inorganic Batteries by In-situ Interfacial Growth of Li_3InCl_6 *

As revealed in Chapter 6, the interfacial Li^+ -conductivity of the coating layer determines the electrochemical performance of ASSLIBs. The ionic conductivity of traditional oxide coating materials is quite low ($\leq 10^{-5} \text{ S.cm}^{-1}$). Therefore, increasing the ionic conductivity of an interfacial coating layer is critical for realizing high-performance ASSLIBs.

In this work, we successfully eliminate the interfacial resistance of ASSLIBs by in-situ interfacial growth of a highly Li^+ -conductive halide electrolyte (Li_3InCl_6 , 1.5 mS.cm^{-1}) on LiCoO_2 (LCO). Owing to strong interfacial interaction and excellent interfacial compatibility, the interfacial resistance is as low as $0.13 \text{ } \Omega.\text{cm}^{-2}$. Consequently, LCO with 15wt% LIC exhibits a high initial capacity of 131.7 mAh.g^{-1} at 0.1C ($1\text{C}=1.3 \text{ mA.cm}^{-2}$) and can be cycled up to 4C at room temperature. The discharge capacity retains 90.3 mAh.g^{-1} after 200 cycles. More importantly, a high areal capacity of 6 mAh.cm^{-2} is realized with a high LCO loading of 48.7 mg.cm^{-2} . This work offers a new route toward the development of high-energy-density and high-power-density ASSIBs without interfacial obstacles.

***Note:** This work has been submitted

Changhong Wang, Jianwen Liang, Ming Jiang, Xiaona Li, Sankha, Mukherjee, Keegan Adair, Matthew Zheng, Yang Zhao, Feipeng, Zhao, Shuming Zhang, Ruying Li, Huan Huang, Shangqian Zhao, Li Zhang, Shigang Lu, Chandra Veer Singh, and Xueliang Sun. Eliminating Interfacial Resistance in All-Inorganic Solid-State Batteries by In-situ Interfacial Growth of Halide Electrolytes. **Advanced Energy Materials**. Submitted.

7.1 Introduction

All-inorganic solid-state batteries (AISSBs) have received considerable attention in recent years because of their significant advantages in safety and energy density over liquid cells.^[1] However, there are several main challenges impeding the development of AISSBs,^[1d] including (1) insufficient ionic conductivity of inorganic solid-state electrolytes (ISEs);^[2] (2) large interfacial resistance between electrode materials and SEs, which originates from poor solid-solid contact and undesirable interfacial reactions; (3) lithium dendrite growth in ISEs. With the continuous efforts over the past years, various ISEs have been developed with high ionic conductivity, such as sulfide electrolytes ($\text{Li}_{10}\text{GeP}_2\text{S}_{12}$,^[2] 12 mS.cm⁻², $\text{Li}_{9.54}\text{Si}_{1.74}\text{P}_{1.44}\text{S}_{11.7}\text{Cl}_{0.3}$,^[3] 25 mS.cm⁻²), their ionic conductivity even surpass those of conventional liquid electrolytes and gel polymers.^[4] To suppress the lithium dendrite growth in ISEs, various effective strategies have also been proposed, such as interface modification and chemical composition tuning of SEs.^[5]

In contrast to the tremendous success in developing highly lithium-ion (Li^+)-conductive ISEs and suppressing lithium dendrite growth in ISEs, the large interfacial resistance between electrode materials and ISEs has not been successfully addressed yet. Until now, sulfide-based AISSBs suffer from detrimental interfacial reactions between sulfide electrolytes and oxide cathodes because of the narrow electrochemical windows of sulfide electrolytes.^[6] To suppress the interfacial reactions, interfacial coating such as LiNbO_3 , LiTaO_3 , and $\text{Li}_4\text{Ti}_5\text{O}_{12}$ is indispensable.^[7] Unfortunately, the uniformity of these interfacial at the interface is hard to control. Although advanced atomic layer deposition can significantly improve the uniformity of the interfacial coating layer.^[6a] The low ionic conductivity ($10^{-6} \sim 10^{-9}$ S.cm⁻¹) of these interfacial coating materials significantly limits the Li^+ transport in AISSBs,^[7c, 8] which is several orders of magnitude lower than those of sulfide and oxide electrolytes themselves. Obviously, the large interfacial resistance between the oxide cathodes and ISEs becomes the primary challenge in

AISSBs. Therefore, finding innovative strategies to reduce the interfacial resistance in AISSBs is of great importance.

Inspired by the high ionic conductivity of halide electrolytes (Li_3MX_6 , $\text{M}=\text{Y}$, In et al, $\text{X}=\text{Cl}$, Br) and their excellent stability against high-voltage cathodes,^[9] here we report an in-situ interfacial growth of halide electrolytes (Li_3InCl_6 , LIC) on electrode materials (LiCoO_2 , LCO) from aqueous solution for the first time. Three-dimensional (3D) continuous Li^+ conduction pathway can be successfully constructed within LIC@LCO electrodes with as little as 15 wt% LIC (30 wt% SEs in most previous studies), thus ensuring the high energy density of AISSBs. Benefiting from the wide electrochemical windows and high ionic conductivity ($1.5 \text{ mS}\cdot\text{cm}^{-1}$) of LIC as well as the strong interfacial interaction, the interfacial resistance between LCO and LIC is successfully reduced to $0.13 \text{ }\Omega\cdot\text{cm}^{-2}$. As a result, the LIC@LCO-15wt% electrode exhibits a high initial discharge capacity of $131.7 \text{ mAh}\cdot\text{g}^{-1}$ with an initial Coulombic efficiency of 92.7% at 0.1C. The energy density of AISSBs is up to $512 \text{ Wh}\cdot\text{kg}^{-1}$. Even at a high rate of 4C ($5.2 \text{ mA}\cdot\text{cm}^{-2}$), $28.5 \text{ mAh}\cdot\text{g}^{-1}$ can be obtained, which corresponds to $1300\text{W}\cdot\text{kg}^{-1}$. More importantly, a high areal capacity of $6.0 \text{ mAh}\cdot\text{cm}^{-2}$ can be realized with a high LCO loading of $48.7 \text{ mg}\cdot\text{cm}^{-2}$. This work provides a promising route to eliminate the interfacial resistance between oxide cathodes and ISEs toward high-energy-density and high-power-density AISSBs.

7.2 Experimental Section

7.2.1 In-situ Synthesis of Li_3InCl_6 @ LiCoO_2 Electrodes

Lithium chloride (LiCl , Alfa Aesar, 99.9%) and indium chloride (InCl_3 , Alfa Aesar, 99.99%) with a stoichiometric molar ratio of 3:1 were weighed and dissolved in deionized water at ambient environment. Then lithium cobalt oxide (LiCoO_2 , LCO, Alfa Aesar,

98%, $0.5\text{m}^2\cdot\text{g}^{-1}$) was then added to the aqueous solution. The solution was then dried in air at $100\text{ }^\circ\text{C}$ to obtain a dry powder. Finally, the dry powder was transferred into a vacuum oven and heated $200\text{ }^\circ\text{C}$ for 5 hours. The electrode was labeled as LIC@LCO. The mass ratio of LCO in LIC@LCO composites is controlled at 85 wt%, 90 wt%, and 95 wt%. The pure Li_3InCl_6 (LIC) electrolyte was also synthesized following the same procedure without adding LCO active materials.

7.2.2 Characterizations

The morphologies of LIC@LCO composites and LIC solid electrolytes were characterized by a Hitachi S-4800 field emission scanning electron microscopy (SEM) equipped with energy dispersive spectroscopy (EDS). X-ray diffraction (XRD) patterns were performed on a Bruker AXS D8 Advance with a $\text{Cu K}\alpha$ radiation ($\lambda = 1.54178\text{ \AA}$) at room temperature with air-tight holder to avoid air exposure. The data were collected by scanning 1s per step with a step width of 0.02 from 10° to 80° (2θ). The data for the X-ray refinement were collected on Bruker AXS D8 Advance with a $\text{Cu K}\alpha$ radiation. The data were collected by scanning 5s per step with one step of 0.02° from 10 to 90° (2θ). For in-situ Raman test, 10 mg LIC@LCO-15wt% composites were used as the working electrode, In foils was used as the reference electrode, the testing current is $100\text{ }\mu\text{A}$. The In L_3 -edge and Cl K-edge X-ray absorption near edge structure (XANES) spectra were collected using fluorescence yield mode on the soft X-ray micro characterization beamline (SXRMB) at the Canadian Light Source (CLS). All samples were covered with Mylar film attached to Al film and sealed before transforming to the vacuum chamber to avoid air exposure.

7.2.3 Electrochemical Performances

All the solid-state batteries are prepared inside an Ar-filled glove box and tested by

home-made mold cells at room temperature. First, 80 mg Li_3InCl_6 powder was placed into a polytetrafluoroethylene (PTFE) die with a diameter of 10 mm and pressed at 1 ton. Then, 12 mg of the cathode composite powder (i.e. LIC@LCO-15wt%) were dispersed on one side of the LIC pellet and pressed at 1 ton again. Then a piece of Li-In foil was attached to another side of LIC pellets. To avoid the possible influence of redox conversion between In^{3+} and In, a thin layer of $\text{Li}_{10}\text{GeP}_2\text{S}_{12}$ was used on the surface of In-Li anode. The mass loading of LCO in LIC@LCO-15wt%-based ASSBs is $13 \text{ mg}\cdot\text{cm}^{-2}$. To demonstrate high areal capacity, 45 mg LIC@LCO-15wt% was put in ASSBs, in which the mass loading of LCO is $48.73 \text{ mg}\cdot\text{cm}^{-2}$. All ASSBs were tested within the voltage range of 2.5-3.6 V (vs. Li^+/LiIn) using a Land cyler (Wuhan, China) at room temperature. Cyclic voltammetry (CV) measurement using versatile multichannel potentiostat 3/Z (VMP3) was performed from 2.5~3.6 (vs. $\text{Li}^+/\text{Li-In}$) at 0.1 mV s^{-1} . To measure the ionic conductivity of Li_3InCl_6 , 100 mg LIC electrolytes were pressed at 3.5 tons and carbon powder was used as the ion-blocking electrode. The electrochemical impedance spectra were from 7 MHz to 1 Hz with an amplitude of 10 mV. The GITT was performed with a 5min discharge at 0.1C followed by 2 hours of relaxation.

7.2.4 DFT Calculation

All calculations were carried out within the DFT framework as implemented in the Vienna *Ab Initio* Simulation Package (VASP). The projector augmented-wave pseudopotentials were used to describe the interaction between ions and electrons, and the exchange-correlation effects were treated using the Perdew–Burke–Ernzerhof (PBE) functional under the generalized gradient approximation (GGA).¹ Herein, the electronic configurations for the PAW potentials were $1s^22s^1$ for Li, $2s^22p^4$ for O, $3d^84s^1$ for Co, $3s^23p^5$ for Cl and $5s^25p^1$ for In. We used the DFT+U method and rigorously optimized the Hubbard U parameter for Co 3d states.² The lattice parameters and bandgaps for

different magnitude of U is presented in **Table 7-S5**. A U parameter of 4 eV was found to be suitable which is consistent with previous reports. The lattice parameters of LiCoO_2 (LCO) and Li_3InCl_6 (LIC) were optimized using a Monkhorst–Pack grid k-points of $8 \times 8 \times 2$ and $4 \times 4 \times 4$, respectively, whereas as kinetic energy cutoffs 500 eV and 450 eV were used. The VESTA package was used to visualize the various bulk, surface and interface structures.³

For surface calculations, the van der Waals (vdW) correction function proposed by Grimme was adopted, which can well describe the long-range vdW interaction.⁴ The vacuum space in the z -direction was about 15 Å to avoid the interaction between neighboring. The k-point mesh was set to be $4 \times 2 \times 1$ for individual LCO and LIC surface slabs. The surface energies were calculated using the following expression, $E_{surf} = (E_{slab} - nE_{bulk}) / 2S$, where E_{surf} is the surface energy, E_{slab} is the energy of the slab containing n units of LCO and LIC, E_{bulk} is the bulk energy per unit, and S is the area of the surface. As for the LCO/LIC interface calculation, the electric field in VASP was realized by adding an artificial dipole sheet at the center of the simulation cell. All the atoms of hybrid heterostructures were optimized until the total energies converged to below 10^{-4} eV and the forces acting on atoms were less than 10^{-2} eV/Å. The Monkhorst–Pack grids of k-point mesh were set to be $2 \times 2 \times 1$ for LCO/LIC interface. Furthermore, the binding energy was determined using the expression, $E_B = E_{LCO/LIC} - (E_{LCO} + E_{LIC})$, where $E_{LCO/LIC}$, E_{LCO} and E_{LIC} represent the total energy of the LCO/LIC interface, LCO and LIC surface slabs under the applied voltage.

7.3 Results and Discussion

7.3.1 Synthesis and Characterization of LIC and LIC@LCO

The in-situ interfacial growth of LIC on LCO is schematically shown in **Figure 7-1a**. InCl_3 and LiCl with a stoichiometric ratio of 1:3 were dissolved in deionized water, forming a transparent $\text{Li}_3\text{InCl}_6 \cdot n\text{H}_2\text{O}$ solution. Subsequently, LiCoO_2 was added into the transparent solution. After evaporation of water solution under 100°C , the obtained dry powder was transferred to a vacuum oven and heated at 200°C for 5 hours to dehydrate $\text{Li}_3\text{InCl}_6 \cdot n\text{H}_2\text{O}$. Then yielded Li_3InCl_6 -coated LiCoO_2 (LIC@LCO) cathode composites were used for AISSBs directly. Detailed synthesis procedures can be found in Supplementary Information. It should be noted that the thickness of the LIC layer can be adjusted by controlling the LIC-to-LCO ratio. In general, the less ISE content in the electrode composite, the higher the energy density of batteries. However, too little ISEs in electrode composites limits the ionic contact between electrode materials and ISEs. Therefore, the best ratio between LIC and LCO requires optimization. As shown in **Figure 7-S1**, LCO's surface is not fully covered with 5 wt% LIC but can be completely coated with 10 wt% LIC. With 15% LIC (**Figure 7-1b** and **7-1c**), not only is the surface covered but also the gap between LCO particles is fully filled, thus constructing 3D continuous Li^+ conduction pathways in the cathode composites (labeled as LIC@LCO-15wt%) (**Figure 7-S1i**). **Figure 7-1b** and **7-1d** present the SEM image of LIC@LCO-15wt% and its corresponding energy-dispersive X-ray spectroscopy (EDX) elemental mapping of O and Cl, respectively, confirming the uniform distribution of LCO in the LIC matrix. To check the solid-solid contact beneath the surface, a cross-section of LIC@LCO-15wt% was fabricated by focused ion beam (FIB) and the corresponding EDS mapping of Co, O, In, Cl is displayed in **Figure 7-1e** and **7-1g**, respectively, showing that LCO is surrounded by LIC with 3D continuous Li^+ percolation networks.

Furthermore, X-ray diffraction (XRD) was also conducted to determine the crystallinity of the LIC layer. As displayed in **Figure 7-S2**, all the LIC@LCO electrodes exhibit strong XRD patterns associated with LCO. In addition, a small peak (131) at 34.3°C originating from the LIC is identified in LIC@LCO-15wt% and LIC@LCO-10wt% while 5% LIC@LCO does not show the (131) peak due to the lower amount of LIC on the LCO surface, suggesting that the crystalline LIC is successfully coated on LCO.

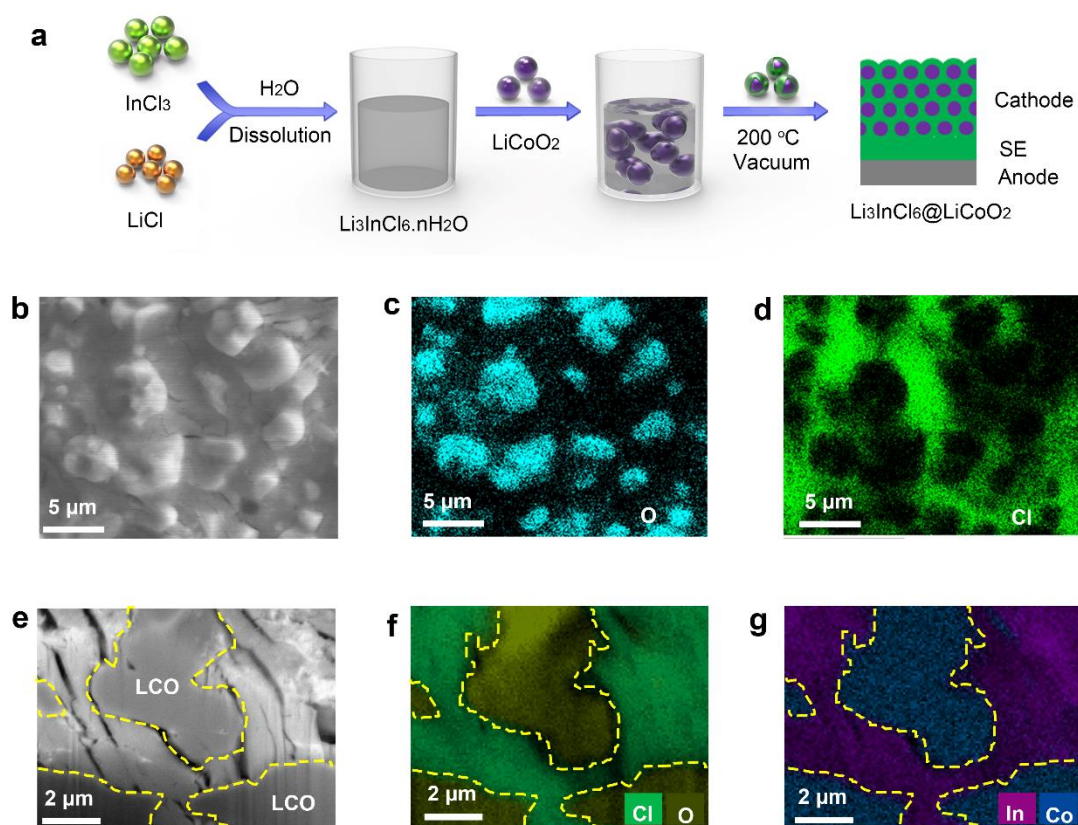


Figure 7-1 (a) Illustration of the in-situ synthesis of Li_3InCl_6 on LiCoO_2 (LIC@LCO). (b) SEM image of LIC@LCO-15wt%. (c) Elemental O mapping. (d) Elemental Cl mapping. (e) Cross-sectional SEM image of LIC@LCO-15wt%. (f) Elemental Cl and O combined mapping. (g) Elemental In and Co combined mapping.

LIC used as the ISE layer in AISSBs was also synthesized following the same method.

As determined by electrochemical impedance spectroscopy (EIS) in Figure 7-S3a and 7-S3b, the ionic conductivity of LIC is $1.5 \text{ mS}\cdot\text{cm}^{-1}$ at 25°C and the activation energy is 0.35 eV , which is comparable to current-mainstream oxide and sulfide electrolytes.^[10] In addition, the primary particle size of LIC is approximately $300\sim 500 \text{ nm}$ (Fig. S3c-3de). **Figure 7-S4a** shows the slow-scanned XRD pattern and Rietveld refinement results, showing that LIC has monoclinic unit cell (C2/m(12), ICSD No.04-009-9027) with the cell parameters of $a=6.39980 \text{ \AA}$, $b=11.06670 \text{ \AA}$, $c=6.37880 \text{ \AA}$, $\alpha=\gamma=90.0000^\circ$, $\beta=109.7915^\circ$. Furthermore, **Figure 7-S4b to 7-S3d** presents the crystal structure of LIC, displaying that LIC consists of InCl_6 octahedra and LiCl_6 octahedra with a rock salt structure. The detailed structural parameters are tabulated in **Table 7-S1**. The high ionic conductivity and low activation energy of LIC is due to high Li^+ vacancy content (33.3%) in its distorted monoclinic rock-salt structure.^[9a]

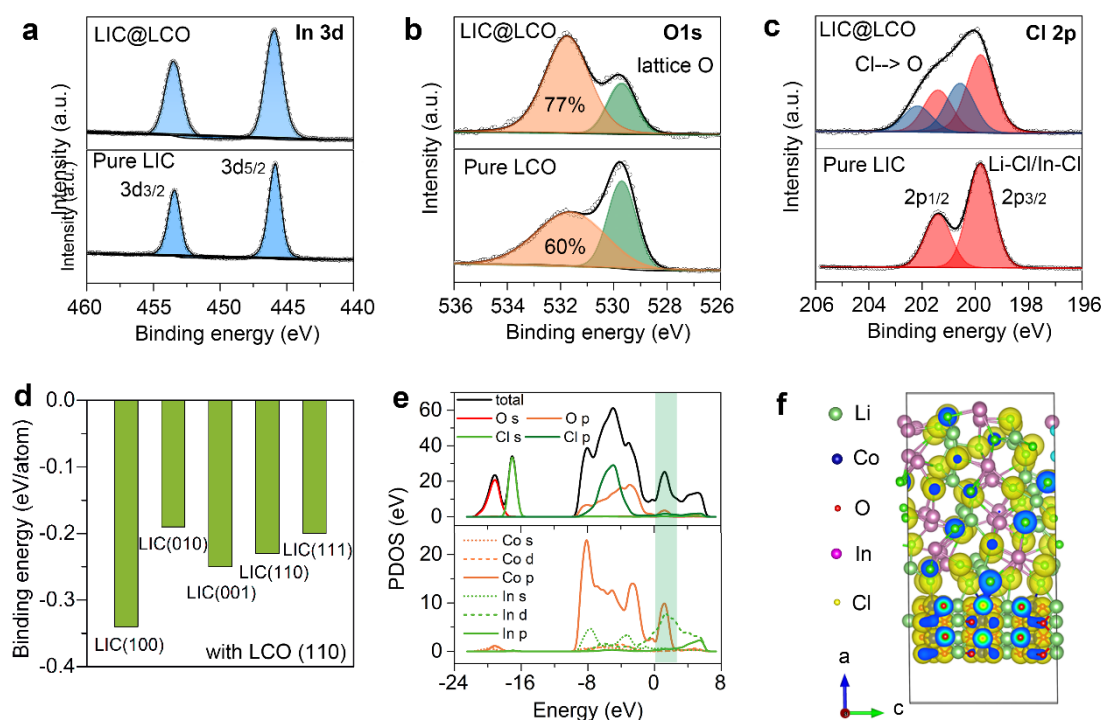


Figure 7-2 Chemical Interaction between LIC and LCO. XPS spectra of LIC@LCO-15wt%. (a) In 3d spectra. (b) O 1s spectra. (c) Cl 2p spectra. (d) The binding energy between the LCO (110) and different LIC surfaces. (e) PDOS of s, p,

d orbitals of O, Cl, In, and Co. (f) Differential charge density of the LCO(110)/LIC(100) interface.

7.3.2 Interfacial Interaction between LIC and LCO

X-ray photoelectron spectroscopy (XPS) was performed to analyze the interface interaction between LIC and LCO. In 3d_{5/2} and In 3d_{3/2} peaks are located at 446.2 eV and 453.8 eV, respectively, which corresponds to the In³⁺ bonding state of LIC (**Figure 7-2a**).^[9c, 11] There is no energy shift found in the In 3d spectra between LIC@LCO and pure LIC, suggesting that the chemical states of In on LIC@LCO surface are exactly the same as that in pristine LIC. This observation also indicates the successful synthesis of LIC on the LCO surface. For the O 1s spectra (**Figure 7-2b**), the green peak at 529.7 eV is characteristic of O atoms in the LCO crystal lattice,^[12] while the orange peak at relatively higher binding energy of 531.7 eV is associated with oxygen-containing species or dangling oxygen bonds at the LCO surface.^[12] Interestingly, the intensity of the orange peaks increases from 60% to 77% in LIC@LCO, suggesting that more oxygen-rich species are formed at the LIC/LCO interface, which may be a result of the interfacial interaction between LIC and LCO. In Cl 2p spectra (**Figure 7-2c**), pure LIC only shows a pair of red peaks (Cl 2p_{3/2} and Cl 2p_{1/2}) at 199.6 eV and 201.2 eV, respectively, which are associated with In-Cl and/or Li-Cl bonds in LIC. However, a pair of blue peaks at higher binding energy (200.6 eV and 202.2 eV) are found after coating LIC on LCO, implying that Cl of LIC is involved in the interfacial interaction between LIC and LCO. Based on the O1s and Cl 2p spectra, we presumed that the O of LCO interacts with the Cl of LIC at the LIC@LCO interface.

To verify this assumption, a density functional theory (DFT) calculation was performed. The surface of LCO and LIC are shown in **Figure 7-S5** and their energies are

summarized in **Table 7-S2**. The experimental measurements and previous DFT simulations indicate the existence of energetically favored (110)-oriented LCO surface.^[13] Furthermore, (110) surfaces in LCO particles provide Li⁺ conduction paths along the $\langle 110 \rangle$ directions.^[13b, 13c] Therefore, we selected (110) face as a representative surface of LCO and the surface energy of LCO(110) was calculated to be 10.60 eV.nm⁻². **Figure 7-2d** displays the binding energies between the LCO (110) and different LIC faces, which indicates that LCO has high binding energy with LIC and the strongest binding energy of -0.34 eV/atom is found between the LCO(110) and LIC (100) (**Table 7-S3**). **Figure 7-2e** shows the partial density of state (PDOS) of Co, In, Cl, and O, respectively. The absence of an energy gap at the Fermi level indicates the good electronic conductivity of LIC@LCO composites. In addition, the p orbital overlap of Cl and O indicates the interaction between Cl and O, as highlighted by the green shadow region. Furthermore, the differential charge density of the LCO(110)/LIC(100) interface clearly showed the charge overlap of Cl and O at the interface (**Figure 7-2f**), indicative of the Cl and O coordination between LIC and LCO. It is believed that the strong interfacial interaction is beneficial for the intimate solid-solid ionic contact and long-term electrochemical cycling stability.

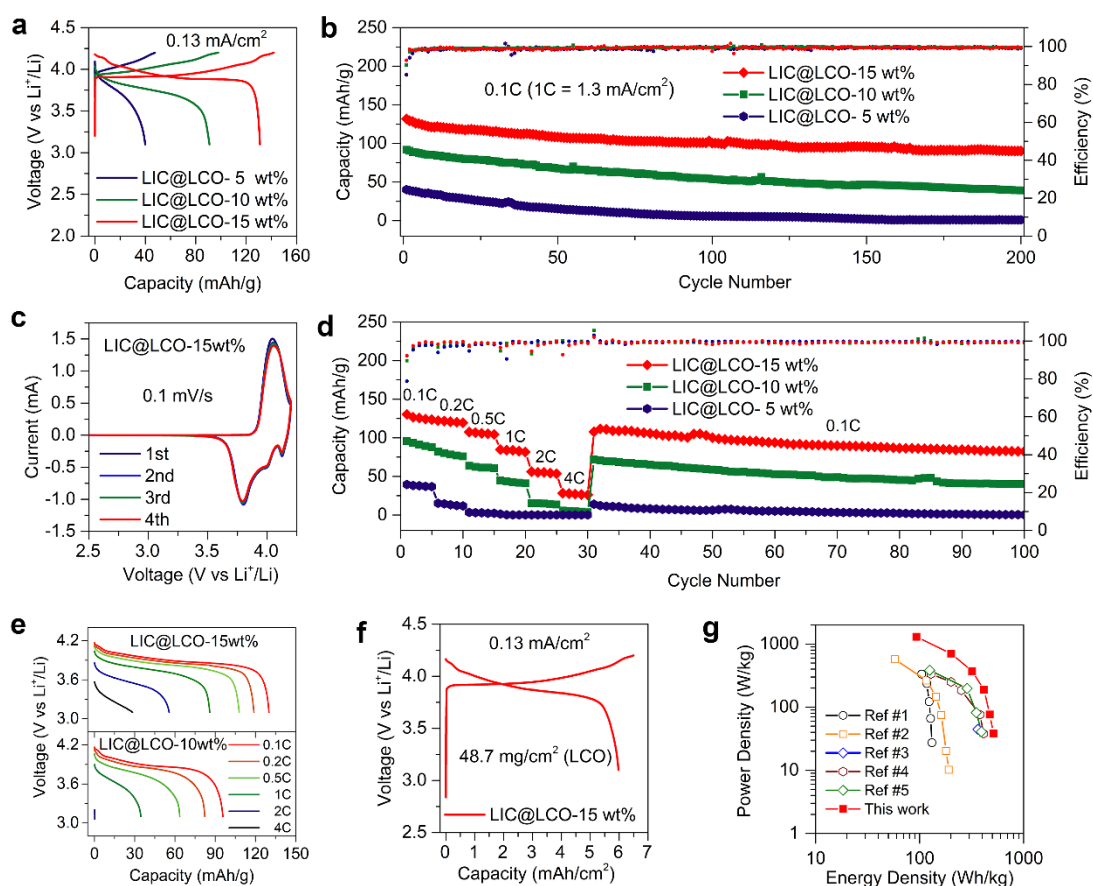


Figure 7-3 Electrochemical performance of LIC@LCO electrodes. (a) initial charge/discharge curves of LIC@LCO electrodes with various ratios. (b) Cycling stability. (c) CV curves. (d) Rate Performance of LIC@LCO. (e) Discharge curves of LIC@LCO-15wt% and LIC@LCO-10wt% under various current densities. (g) Charge/discharge curves of high-loading LIC@LCO electrodes. (g) Ragone plot

7.3.3 Electrochemical Performance of LIC@LCO

LIC@LCO-based AISSBs were evaluated at 0.1C ($1C = 1.3 \text{ mA}\cdot\text{cm}^{-2}$) at room temperature due to high ionic conductivity of LIC ($1.5 \text{ mS}\cdot\text{cm}^{-1}$). The initial charge and discharge curves are presented in **Figure 7-3a**. With the increase of the LIC-to-LCO

ratio, the polarization between charge and discharge curves is suppressed and the discharge capacity is significantly increased. With 15wt% LIC, the initial charge capacity is 142.1 mAh.g⁻¹ and the initial discharge capacity is 131.7 mAh.g⁻¹ with an initial Coulombic efficiency of 92.7%. The corresponding energy density is up to 513 Wh.kg⁻¹. It should be highlighted that the charge/discharge curves are overlapping with those of LCO in liquid electrolytes at the same current density of 0.13 mA.cm⁻² (**Figure 7-S6**), implying the full utilization of LCO in AISSB with ultrafast interfacial Li⁺ conduction as fast as that in liquid cells.^[6a] With 10wt% and 5wt% LIC, LCO discharges at 90.9 mAh.g⁻¹ and 39.9 mAh.g⁻¹, respectively. To determine the change in the interfacial resistance, in-situ EIS was performed on LIC@LCO-15wt% electrodes during the initial charge/discharge process (**Figure 7-S7**). The first semi-circle at the high-frequency region represents the resistance of the LIC layer, which is close to 78 Ω. The resistance of the LIC layer does not undergo obvious change, implying the excellent stability of LIC upon cycling. The small semi-circle at the middle frequency represents the interfacial resistance between LIC@LCO,^[9b] which is 6.8 Ω (0.13 Ω.cm⁻²).^[9b] It should be mentioned that the ultra-small interfacial resistance is significantly smaller than those of sulfide/oxide-based AISSBs, which generally shows the interfacial resistance at hundreds or thousands of ohms,^[5c, 14] suggesting that LIC@LCO-15wt% electrodes have the fastest interfacial Li⁺ transport among all the AISSBs reported so far.^[3, 5c, 14-15] The middle-frequency semi-circle keeps stable during the initial charge/discharge process, indicating that no interfacial reactions occurred between LIC and LCO upon cycling, which is due to the wide electrochemical window (up to 4.3V vs. Li⁺/Li) of LIC.^[9a]

Figure 7-3b displays the cycling performance of LIC@LCO with different LIC contents. After 200 cycles, LIC@LCO with 15 wt% LIC keeps at 90.3 mAh.g⁻¹ with a CE of 99.3% while the LIC@LCO with 10 wt% LIC only remains at 39.1 mAh.g⁻¹ and LIC@LCO with 5 wt% LIC cannot be reversibly charged/discharged. **Figure 7-3c** shows the CV curves of LIC@LCO with 15 wt% LIC. The overlap of CV curves also indicates the

stable cycling performance of LIC@LCO in AISSBs. **Figure 7-3d** displays the rate-performance LIC@LCO with 15 wt% LIC. Even at 4C ($5.2 \text{ mA}\cdot\text{cm}^{-2}$), LIC@LCO still shows a capacity of $28.5 \text{ mAh}\cdot\text{g}^{-1}$. **Figure 7-3e** displays the corresponding discharge curves under different current densities. The corresponding power density of LIC@LCO-15wt% is up to $1300 \text{ W}\cdot\text{kg}^{-1}$. Considering the high-loading electrode ($13 \text{ mg}\cdot\text{cm}^{-2}$) in AISSBs, the rate-performance of LIC@LCO is astonishing.^[16]

To determine the Li^+ kinetics of LIC@LCO-15wt%, which is closely related to the power density of AISSBs, the galvanostatic intermittent titration technique (GITT) was performed. The charge/discharge GITT curves, the small polarization curves, and the high Li^+ diffusion coefficient ($\sim 10^{-9} \text{ cm}^2\cdot\text{S}^{-1}$) are presented in **Figure 7-S8**. The high Li^+ diffusion coefficient is even comparable with that in liquid cells.^[17] That's why LIC@LCO-15wt% demonstrates a high rate performance up to 4C. The fast Li^+ kinetics of LIC@LCO-15wt% is ascribed to the intimate solid-solid contact, small interfacial resistance as well as excellent interfacial compatibility. To meet the standards required for practical applications, a high real capacity of LIC@LCO of $6 \text{ mAh}\cdot\text{cm}^{-2}$ is also demonstrated with a high LCO loading of $48.7 \text{ mg}\cdot\text{cm}^{-2}$ (**Figure 7-3f**). **Figure 7-3g** compares the power density and energy density of LIC@LCO-based AISSBs with all previously reported results in the Ragone plot.^[2, 6a, 7a, 18] The sources of the data are listed in **Table 7-S4**. It is apparent that LIC@LCO-15wt% demonstrated the highest both energy density and power density of AISSBs.

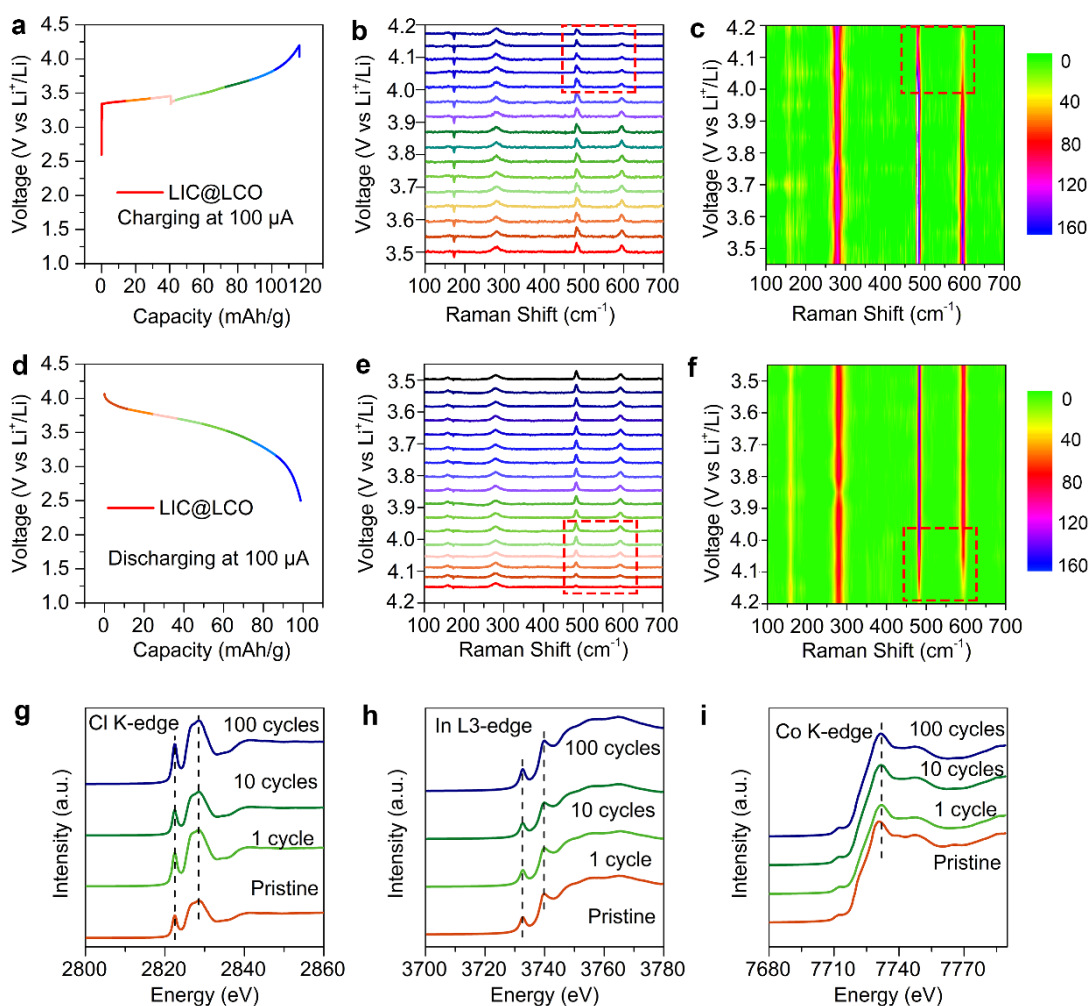


Figure 7-4 In situ/operando Raman and ex-situ XAS spectra of LIC@LCO-15wt% in AISSBs. (a) Charging curves of LIC@LCO electrodes at the current density of 0.13 mA.cm⁻². (b) Raman spectra of the LIC@LCO electrode during the charging process. (c) Contour plot of LIC@LCO during the charging process. (d) Discharging curves of LIC@LCO electrodes at the current density of 0.13 mA.cm⁻². (e) Raman spectra of LIC@LCO electrodes during the discharging process. (f) Contour plot of LIC@LCO during the discharging process. (g) XAS of Cl K-edge. (h) XAS of In L3-edge. (i) XAS of Co K-edge.

In-situ/operando Raman spectroscopy was performed to examine the interfacial stability between LIC and LCO upon cycling. The LIC@LCO electrode can be successfully charged to 118 mAh.g⁻¹ (**Figure 7-4a**). LIC shows a broad peak at 191 cm⁻¹ and a sharp and strong peak of 269 cm⁻¹, while LCO shows 478 cm⁻¹ and 596 cm⁻¹, which are ascribed to E_g and A_{1g} vibrational modes of LCO, respectively.^[19] These four peaks are clearly detected and remain stable until 4.0V (**Figure 7-4b**). The intensity of LiCoO₂ peaks begins to decrease after 4.0V (highlighted by red dash line), while LIC peaks remain the same, suggesting that the LIC is stable even at the high cut-off voltage (**Figure 7-4b**). The contour plot of LIC@LCO during the charging process in **Figure 7-4c** clearly shows the intensity decrease of peaks at 478 cm⁻¹ and 596 cm⁻¹ after charging to 4.0V, which corresponds to the de-lithiation of LCO upon charging.^[19] No new peaks are detected, suggesting the excellent interfacial stability between LIC and LCO. **Figure 7-4d** shows the discharge capacity of 100 mAh.g⁻¹. **Figure 7-4e** shows the Raman spectra of LIC@LCO during the discharge process, the reduced peaks at 478 cm⁻¹ and 596 cm⁻¹ gradually recover from 4.2V to 4.0V and remain the same afterward, suggesting Li⁺ is reversibly intercalated into the LCO layered structure. During the whole discharge process, LIC peaks remain the same, implying LIC is stable against LCO during the electrochemical cycling process.

Furthermore, ex-situ X-ray absorption spectroscopy was performed to investigate the interfacial stability between LIC and LCO. **Figure 7-4g** and **7-4h** display the Cl K-edge and In L3-edge of LIC@LCO-15wt%, respectively. Compared to the pristine Cl K-edge and In L3-edge, the Cl K-edge and In L3-edge of LIC@LCO-15wt% undergo no change even after 100 cycles, suggesting excellent interfacial stability during the electrochemical cycling. **Figure 7-4i** shows the XAS spectra of Co K-edge, which also remains the same after the first cycle, implying the excellent electrochemical stability. The slight difference between the pristine Co K-edge and that after 1 cycle is ascribed to the electrochemical activation process in the initial cycle. The in-situ Raman and ex-situ

XAS analysis strongly confirmed the excellent interfacial compatibility between LCO and LIC.

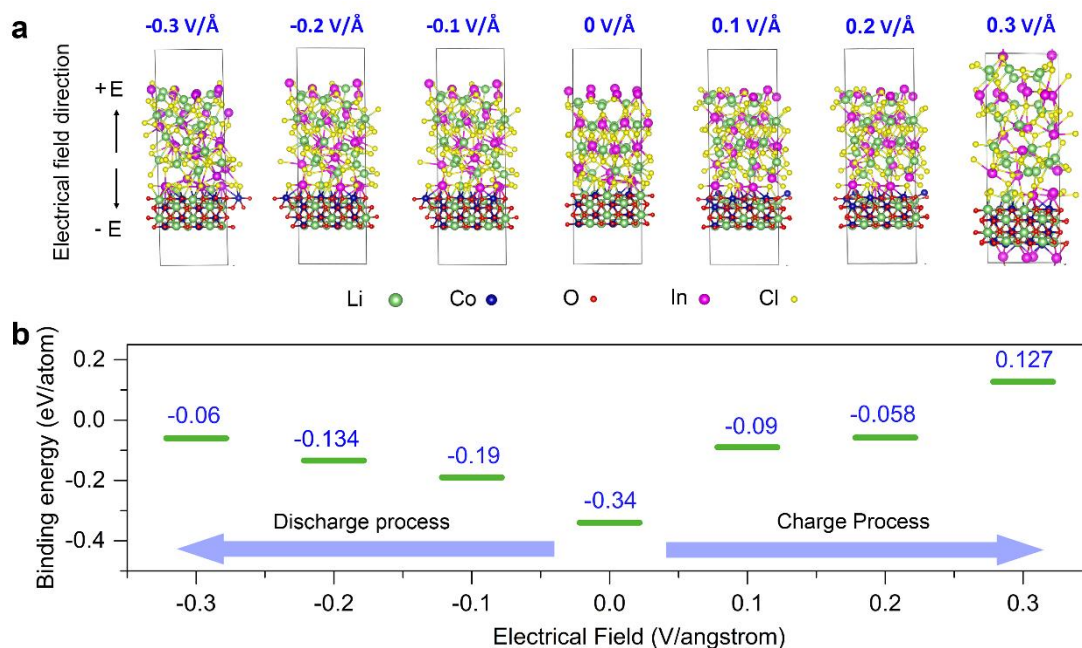


Figure 7-5 (a) Illustration of schematic view of LCO(110)/LIC(100) interface under the electrical field of $-0.3\text{V}/\text{\AA}$, $-0.2\text{V}/\text{\AA}$, $-0.1\text{V}/\text{\AA}$, $0\text{V}/\text{\AA}$, $0.1\text{V}/\text{\AA}$, $0.2\text{V}/\text{\AA}$, and $0.3\text{V}/\text{\AA}$. (b) The variation of binding energy of LCO(110)/LIC(100) interface as a function of electric field strength.

To gain insights into the interfacial stability between LCO and LIC during the charging/discharging process, we simulated the binding energies of LCO(110)/LIC(100) and their interfacial structure change under external electric fields (**Figure 7-5**). During the charging (from $0\text{ V}/\text{\AA}$ to $-0.3\text{ V}/\text{\AA}$) and discharging process (from $-0.3\text{ V}/\text{\AA}$ to $0\text{ V}/\text{\AA}$) (**Figure 7-5b**), the interaction between LCO and LIC becomes more and more weaker, which is caused by the structural change of LIC, especially under high electric field of $\pm 0.3\text{V}/\text{\AA}$ (**Figure 7-5a**). The simulation is consistent with the electrochemical window ($2.38 \sim 4.3\text{V}$ vs Li^+/Li) of LIC.^[9a] Fortunately, here LCO is reversibly cycled between 3.1V and 4.2V , in which LIC is stable and the binding energy between LCO and LIC is

high, thus explaining the ultra-long cycling stability and small interfacial resistance of LIC@LCO-15wt% (discussed in Figure 3).

7.4 Conclusions

Here, we reported an in-situ interfacial growth of halide electrolytes (Li_3InCl_6 , LIC) on electrode materials (LiCoO_2 , LCO) directly aqueous solution, which successfully eliminated the interfacial resistance of AISSBs. To the best of our knowledge, this is the first time to demonstrate the in-situ synthesis of solid-state halide electrolytes on electrode materials without interfacial modification. There are several outstanding advantages of the in-situ interfacial growth of Li_3InCl_6 on electrodes for AISSBs. First, in-situ interfacial growth of LIC on LCO can form intimate solid-solid contact, thus constructing 3D Li^+ transport pathways in LIC@LCO cathode composites. Second, no interfacial modification on LCO is required due to the wide electrochemical windows of LIC.^[9a] Third, LIC possesses a high ionic conductivity of $1.5 \text{ mS}\cdot\text{cm}^{-1}$ and excellent chemical/electrochemical stability against LCO,^[9a, 20] thus showing an ultra-small interfacial resistance of $0.13 \text{ }\Omega\cdot\text{cm}^{-2}$. The interfacial resistance is several orders of magnitude lower than those of mainstream sulfide/oxide-based AISSBs.^[5a, 10a, 21] Moreover, the Li^+ diffusion coefficient is up to $10^{-9} \text{ cm}^2\cdot\text{S}^{-1}$, which is even comparable to that of liquid cells. Therefore, LIC@LCO electrodes exhibited a high rate performance of 4C. The corresponding powder density is $1300 \text{ W}\cdot\text{kg}^{-1}$, which overtakes previous results. Last but not least, 30% of solid electrolytes are mixed in cathode composites in most previous references.^[2-3, 22] In our case, as less as 15wt% LIC is dispersed into cathode composites, which enables the high energy density ($513 \text{ Wh}\cdot\text{kg}^{-1}$) of AISSBs.

In summary, we successfully eliminated the interfacial resistance of AISSBs by in-situ interfacial growth of LIC on LCO. A strong interfacial interaction between LCO and LIC was found by XPS and DFT calculations, which is beneficial for the long-term

cycling stability of AISSBs. Benefiting from the high ionic conductivity (1.5 mS.cm^{-1}) of LIC, intimate solid-solid contact, and excellent interfacial stability, the interfacial resistance between LIC and LCO is as low as $0.13 \text{ }\Omega.\text{cm}^{-2}$. Resultantly, the LIC@LCO-15wt% electrode exhibited a high initial discharge capacity of 131.7 mAh.g^{-1} with an initial Coulombic efficiency of 92.7 % at 0.1C. After 200 cycles, a capacity of 90.3 mAh.g^{-1} can be retained. Furthermore, the high rate performance (28.5 mAh.g^{-1} at 4C) was achieved due to the high Li^+ diffusion coefficient. Moreover, a high areal capacity of LIC@LCO up to 6 mAh.cm^{-2} was demonstrated with a high mass loading of 48.7 mg.cm^{-2} (LCO). This facile approach offers a new route to overcome longstanding interfacial challenges in AISSBs, enabling high-energy-density and high-power-density AISSBs at room temperature.

7.5 Acknowledgements

This work was supported by Natural Sciences and Engineering Research Council of Canada (NSERC), Canada Research Chair Program (CRC), Canada Foundation for Innovation (CFI), Ontario Research Fund, China Automotive Battery Research Institute Co., Ltd, Glabat Solid-State Battery Inc., the Canada Light Source at University of Saskatchewan (CLS), Interdisciplinary Development Initiatives (IDI) by Western University, and University of Western Ontario. J.L. and X. L. thank the support of Mitacs Elevate Postdoctoral Fellowship. C.W. appreciates the funding support of the Mitacs Accelerate Fellowship.

7.6 Author contributions

C. W. and J. L. equally contributed to this work and designed all the experiments and characterizations. M. J. and S. M. performed theoretical calculations. X. L. help with halide electrolyte synthesis. K. A. and M. B. helped with synchrotron characterizations.

R. L helped with purchasing all the chemicals. C. W. wrote the manuscript. All the authors discussed the results and commented on the manuscript. C. S. supervised the theoretical calculations. The whole project was supervised by X. S.

7.7 References

- [1] aA. Manthiram, X. Yu, S. Wang, *Nat. Rev. Mater.* **2017**, *2*, 16103; bT. Famprakis, P. Canepa, J. A. Dawson, M. S. Islam, C. Masquelier, *Nat. Mater.* **2019**, doi:<https://doi.org/10.1038/s41563-41019-40431-41563>; cJ. Li, C. Ma, M. Chi, C. Liang, N. J. Dudney, *Adv. Energy Mater.* **2015**, *5*, 1401408; dY. Zhao, K. Zheng, X. Sun, *Joule* **2018**, 1-22.
- [2] N. Kamaya, K. Homma, Y. Yamakawa, M. Hirayama, R. Kanno, M. Yonemura, T. Kamiyama, Y. Kato, S. Hama, K. Kawamoto, A. Mitsui, *Nat. Mater.* **2011**, *10*, 682-686.
- [3] Y. Kato, S. Hori, T. Saito, K. Suzuki, M. Hirayama, A. Mitsui, M. Yonemura, H. Iba, R. Kanno, *Nat. Energy* **2016**, *1*, 16030.
- [4] K. Xu, *Chem. Rev.* **2004**, *104*, 4303-4418.
- [5] aC. Wang, Y. Zhao, Q. Sun, X. Li, Y. Liu, J. Liang, X. Li, X. Lin, R. Li, K. R. Adair, L. Zhang, R. Yang, S. Lu, X. Sun, *Nano Energy* **2018**, *53*, 168-174; bH. Fudong, Y. Jie, Z. Xiangyang, W. Chunsheng, *Adv. Energy Mater.* **2018**, *0*, 1703644; cZ. Zhang, S. Chen, J. Yang, J. Wang, L. Yao, X. Yao, P. Cui, X. Xu, *ACS Appl. Mater. Interfaces* **2017**, *10*, 2556-2565; dH. Xu, Y. Li, A. Zhou, N. Wu, S. Xin, Z. Li, J. B. Goodenough, *Nano Lett.* **2018**, *18*, 7414-7418; eJ. Liang, X. Li, Y. Zhao, L. V. Goncharova, G. Wang, K. R. Adair, C. Wang, R. Li, Y. Zhu, Y. Qian, *Adv. Mater.* **2018**, *30*, 1804684.
- [6] aC. Wang, X. Li, Y. Zhao, M. N. Banis, J. Liang, X. Li, Y. Sun, K. R. Adair, Q. Sun, Y. Liu, F. Zhao, S. Deng, X. Lin, R. Li, Y. Hu, T.-K. Sham, H. Huang, L. Zhang, R. Yang, S. Lu, X. Sun, *Small Methods* **2019**, *1900261*, DOI:10.1002/smtd.201900261;

- bF. D. Han, Y. Z. Zhu, X. F. He, Y. F. Mo, C. S. Wang, *Adv. Energy Mater.* **2016**, *6*, 9.
- [7] aN. Ohta, K. Takada, L. Zhang, R. Ma, M. Osada, T. Sasaki, *Adv. Mater.* **2006**, *18*, 2226-2229; bK. Takada, N. Ohta, L. Q. Zhang, X. X. Xu, B. T. Hang, T. Ohnishi, M. Osada, T. Sasaki, *Solid State Ion.* **2012**, *225*, 594-597; cY. Xiao, L. J. Miara, Y. Wang, G. Ceder, *Joule* **2019**, doi.org/10.1016/j.joule.2019.02.006.
- [8] aB. Wang, J. Liu, M. Norouzi Banis, Q. Sun, Y. Zhao, R. Li, T.-K. Sham, X. Sun, *ACS Appl. Mater. Interfaces* **2017**, *9*, 31786-31793; bB. Wang, Y. Zhao, M. N. Banis, Q. Sun, K. R. Adair, R. Li, T.-K. Sham, X. Sun, *ACS Appl. Mater. Interfaces* **2018**, *10*, 1654-1661.
- [9] aS. Wang, Q. Bai, A. M. Nolan, Y. Liu, S. Gong, Q. Sun, Y. Mo, *Angew. Chem. Int. Ed.* **2019**, [10.1002/anie.201901938](https://doi.org/10.1002/anie.201901938); bT. Asano, A. Sakai, S. Ouchi, M. Sakaida, A. Miyazaki, S. Hasegawa, *Adv. Mater.* **2018**, *0*, 1803075; cX. Li, J. Liang, J. Luo, M. Norouzi Banis, C. Wang, W. Li, S. Deng, C. Yu, F. Zhao, Y. Hu, T.-K. Sham, L. Zhang, S. Zhao, S. Lu, H. Huang, R. Li, K. R. Adair, X. Sun, *Energy Environ. Sci.* **2019**; dS. Muy, J. Voss, R. Schlem, R. Koerver, S. J. Sedlmaier, F. Maglia, P. Lamp, W. G. Zeier, Y. Shao-Horn, *iScience* **2019**, *16*, 270-282; eX. Sun, X. Li, J. Liang, N. Chen, J. Luo, K. Adair, C. Wang, M. Norouzi Banis, T.-K. Sham, L. Zhang, S. Zhao, S. Lu, H. Huang, R. Li, *Angewandte Chemie International Edition*, *0*.
- [10] aL. Zhou, K.-H. Park, X. Sun, F. Lalère, T. Adermann, P. Hartmann, L. F. Nazar, *ACS Energy Lett.* **2018**, 265-270; bM. A. Kraft, S. Ohno, T. Zinkevich, R. Koerver, S. P. Culver, T. Fuchs, A. Senyshyn, S. Indris, B. J. Morgan, W. G. Zeier, *J. Am. Chem. Soc.* **2018**, *140*, 16330-16339.
- [11] M.-C. Nguyen, M. Jang, D.-H. Lee, H.-J. Bang, M. Lee, J. K. Jeong, H. Yang, R. Choi, *Sci. Rep.* **2016**, *6*, 25079.

- [12] J. Qian, L. Liu, J. Yang, S. Li, X. Wang, H. L. Zhuang, Y. Lu, *Nat. Commun.* **2018**, *9*, 4918.
- [13] aL. Dahéron, H. Martinez, R. Dedryvère, I. Baraille, M. Ménétrier, C. Denage, C. Delmas, D. Gonbeau, *J. Phys. Chem. C* **2009**, *113*, 5843-5852; bY. Shao-Horn, L. Croguennec, C. Delmas, E. C. Nelson, M. A. O'Keefe, *Nat. Mater.* **2003**, *2*, 464-467; cJ. Haruyama, K. Sodeyama, Y. Tateyama, *ACS Appl. Mater. Interfaces* **2017**, *9*, 286-292.
- [14] aX. Han, Y. Gong, K. Fu, X. He, G. T. Hitz, J. Dai, A. Pearse, B. Liu, H. Wang, G. Rubloff, Y. Mo, V. Thangadurai, E. D. Wachsman, L. Hu, *Nat. Mater.* **2017**, *16*, 572-579; bW. J. Li, M. Hirayama, K. Suzuki, R. Kanno, *Solid State Ion.* **2016**, *285*, 136-142; cX. Yao, D. Liu, C. Wang, P. Long, G. Peng, Y.-S. Hu, H. Li, L. Chen, X. Xu, *Nano Lett.* **2016**; dW. Zhang, F. H. Richter, S. P. Culver, T. Leichtweiss, J. G. Lozano, C. Dietrich, P. G. Bruce, W. G. Zeier, J. Janek, *ACS Appl. Mater. Interfaces* **2018**, *10*, 22226-22236.
- [15] R. Koerver, F. Walther, I. Aygun, J. Sann, C. Dietrich, W. Zeier, J. Janek, *J. Mater. Chem. A* **2017**.
- [16] Y. Kuang, C. Chen, D. Kirsch, L. Hu, *Adv. Energy Mater.* **2019**, *0*, 1901457.
- [17] aL. Sun, Z. Zhang, X. Hu, H. Tian, Y. Zhang, X. Yang, *J. Electrochem. Soc* **2019**, *166*, A1793-A1798; bQ. Liu, X. Su, D. Lei, Y. Qin, J. Wen, F. Guo, Y. A. Wu, Y. Rong, R. Kou, X. Xiao, F. Aguesse, J. Bareño, Y. Ren, W. Lu, Y. Li, *Nat. Energy* **2018**, *3*, 936-943.
- [18] aW. Zhang, D. A. Weber, H. Weigand, T. Arlt, I. Manke, D. Schröder, R. Koerver, T. Leichtweiss, P. Hartmann, W. G. Zeier, J. Janek, *ACS Appl. Mater. Interfaces* **2017**,

- 9, 17835-17845; bK. H. Park, D. Y. Oh, Y. E. Choi, Y. J. Nam, L. Han, J.-Y. Kim, H. Xin, F. Lin, S. M. Oh, Y. S. Jung, *Adv. Mater.* **2016**, *28*, 1874-1883.
- [19]E. Flores, P. Novák, E. J. Berg, *Front. Energy Res.* **2018**, *6*.
- [20]S. P. Culver, R. Koerver, W. G. Zeier, J. Janek, *Adv. Energy Mater.* **2019**, *0*, 1900626.
- [21]aC. Wang, K. R. Adair, J. Liang, X. Li, Y. Sun, X. Li, J. Wang, Q. Sun, F. Zhao, X. Lin, R. Li, H. Huang, L. Zhang, R. Yang, S. Lu, X. Sun, *Adv. Funct. Mater.* **2019**, *1900392*, DOI:10.1002/adfm.201900392; bK. N. Wood, K. X. Steirer, S. E. Hafner, C. Ban, S. Santhanagopalan, S.-H. Lee, G. Teeter, *Nat. Commun.* **2018**, *9*, 2490; cC. Wang, Q. Sun, Y. Liu, Y. Zhao, X. Li, X. Lin, M. N. Banis, M. Li, W. Li, K. R. Adair, D. Wang, J. Liang, R. Li, L. Zhang, R. Yang, S. Lu, X. Sun, *Nano Energy* **2018**, *48*, 35-43.
- [22]B. Wu, S. Wang, W. J. Evans Iv, D. Z. Deng, J. Yang, J. Xiao, *J. Mater. Chem. A* **2016**, *4*, 15266-15280.

7.8 Supplementary Information

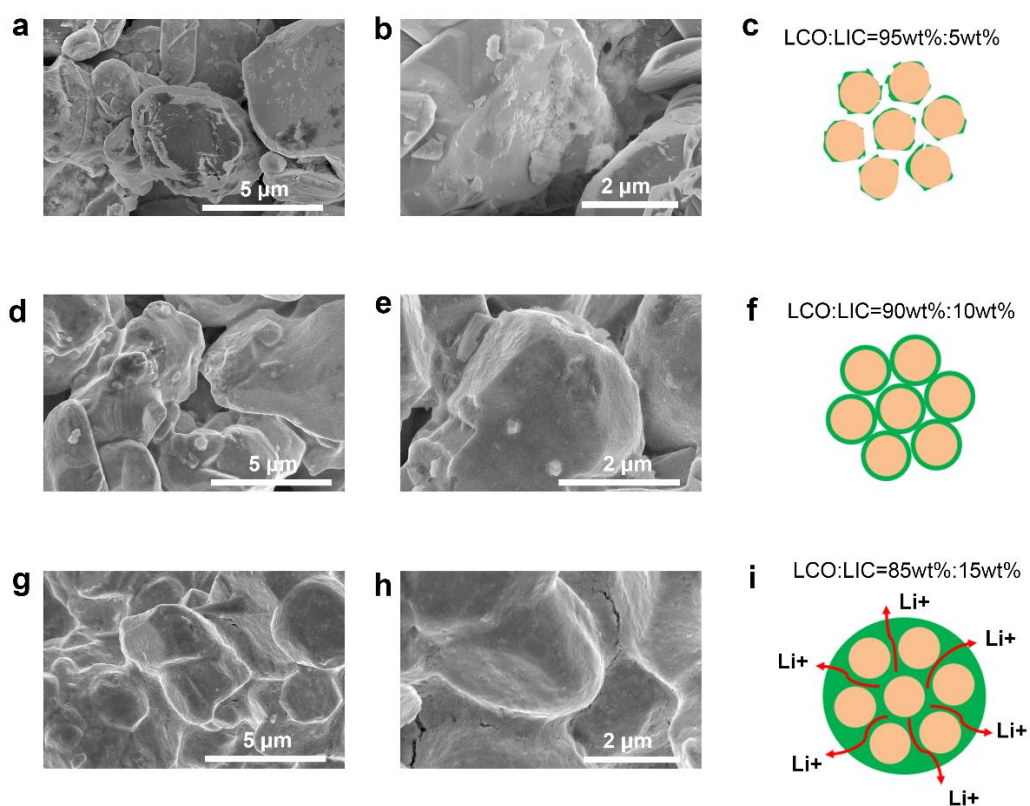


Figure 7-S1. (a) and (b) SEM images of LIC@LCO-5wt%, in which Li^+ conduction is constrained due to the uneven distribution of LIC on the LCO surface. (c) Schematic illustration of LIC distribution on the LCO surface.

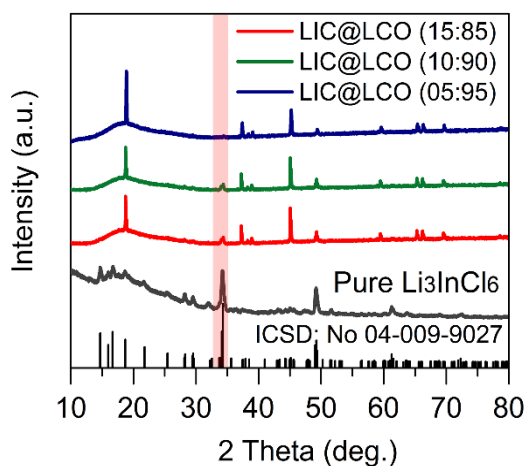


Figure 7-S2. XRD pattern of LIC@LCO with different LIC content.

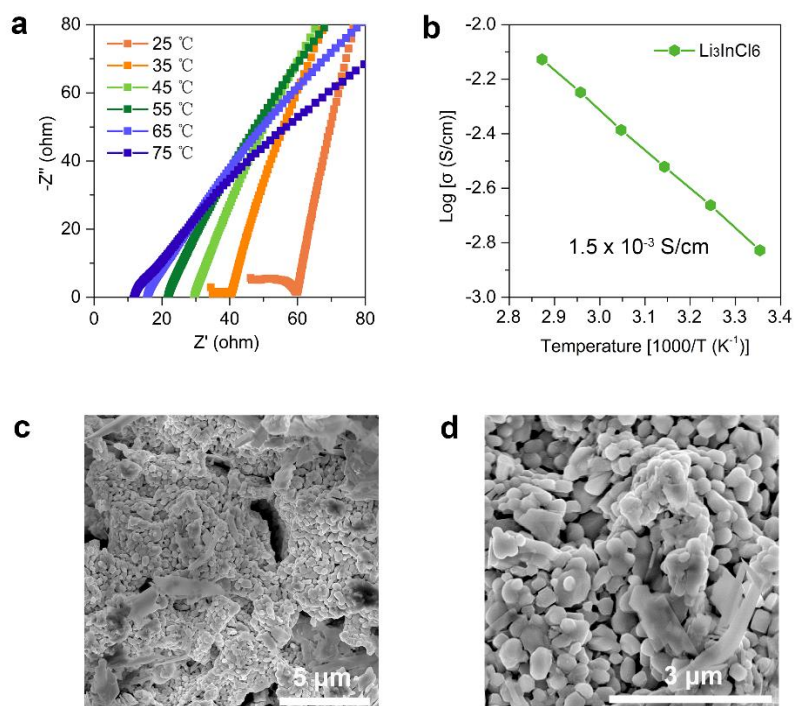


Figure 7-S3. (a) EIS spectra of LIC at various temperatures. (b) Arrhenius plot of LIC. The ionic conductivity of LIC is $1.5 \times 10^{-3} \text{ S.cm}^{-1}$ at RT and $5.2 \times 10^{-3} \text{ S.cm}^{-1}$ at 65°C . (d, e) SEM images of LIC powder, which shows that the size of LIC particles is about 300 ~500 nm.

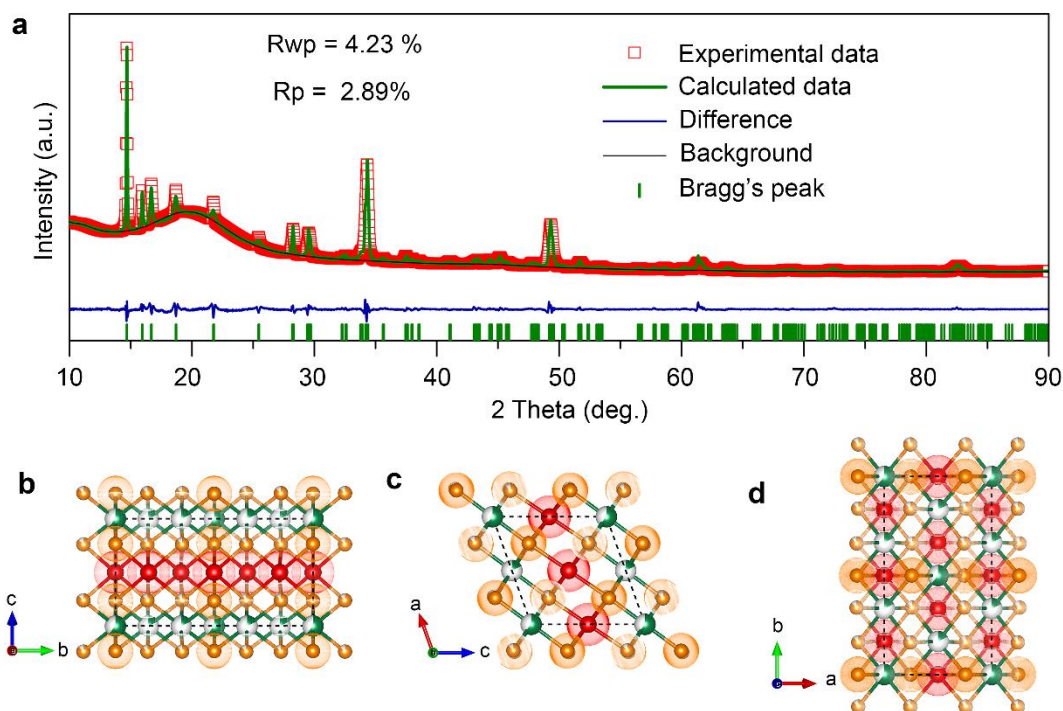
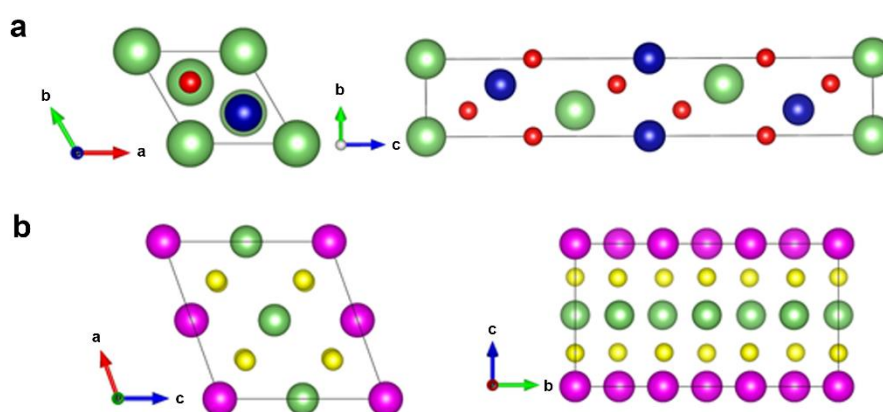


Figure 7-S4. (a) Slow-scanned XRD pattern and Rietveld refinement result of Li_3InCl_6 . (b-d) Crystal structure of Li_3InCl_6 in different directions. Li atom: red sphere, Cl atom: yellow sphere, In atom and In vacancy: green sphere. The XRD patterns of LIC could be indexed well with the distorted rock-salt structure in monoclinic the space group $C2/m$ (12) (ICSD No. 04-009-9027). $a = 6.39980 \text{ \AA}$, $b = 11.06670 \text{ \AA}$, $c = 6.37880 \text{ \AA}$, $\alpha = \gamma = 90.0000^\circ$, $\beta = 109.7915^\circ$, unit cell volume = 425.090402 \AA^3 .

Table 7-S1. Structure Parameters of Li_3InCl_6 .(Rwp = 4.23%, Rp=2.89%, Radiation: Cu α , $\lambda_1 = 1.5406 \text{ \AA}$, $\lambda_2 = 1.5444 \text{ \AA}$)

Atom	Site	x	y	z	Occ.	U	Sym.
Cl(1)	8j	0.24210	0.16220	0.23880	1.000	0.039	1
Cl(2)	4i	0.24500	0.00000	-0.23380	1.000	0.073	m
In(1)	4g	0.00000	0.33330	0.00000	0.180	0.317	2
In(2)	2a	0.00000	0.00000	0.00000	0.610	0.010	2/m
Li(1)	2d	0.50000	0.0000	0.50000	1.000	13.108	2/m
Li(2)	4h	0.0000	0.16830	0.50000	1.000	34.181	2

**Figure 7-S5.** Schematic view of (a) LiCoO_2 and (b) Li_3InCl_6 . Green, blue, red, yellow and pink spheres represent the Li, Co, O, Cl and In atoms,

respectively.

Table 7-S2. The lattice parameters and surface energies for LCO and LIC surfaces.

	a (Å)	b (Å)	E _{surf} (eV/nm ²)
LCO (110)	4.94	14.17	10.60
LIC (100)	11.27	6.56	7.57
LIC (010)	6.40	18.16	16.52
LIC (001)	6.75	11.47	20.46
LIC (110)	6.56	6.52	14.37
LIC f(111)	6.38	10.16	9.15

The surface energies are calculated by

$$E_{surf} = (E_{slab} - nE_{bulk})/2S$$

The formation energy of the LCO (110) surface is calculated to 10.60 eV.nm⁻². The LIC (100) surface is easier to form because of its lowest surface energy of 7.57 eV.nm⁻².

Table 7-S3. The lattice parameter and binding energy for the LCO/LIC interface.

	a (Å)	b (Å)	E_B (eV/atom)
LCO(110)/LIC(100)	9.52	13.47	- 0.34
LCO(110)/LIC(010)	5.44	16.17	- 0.19
LCO(110)/LIC(001)	5.00	13.66	- 0.25
LCO(110)/LIC(110)	5.17	13.48	- 0.23
LCO(110)/LIC(111)	5.02	27.98	- 0.20

The binding energies are calculated by

$$E_b = E_{AB} - (E_A + E_B)$$

The binding energy of the LCO(110)/LIC(100) interface is determined to be -0.34 eV/atom, indicating that this interface is more likely to form.

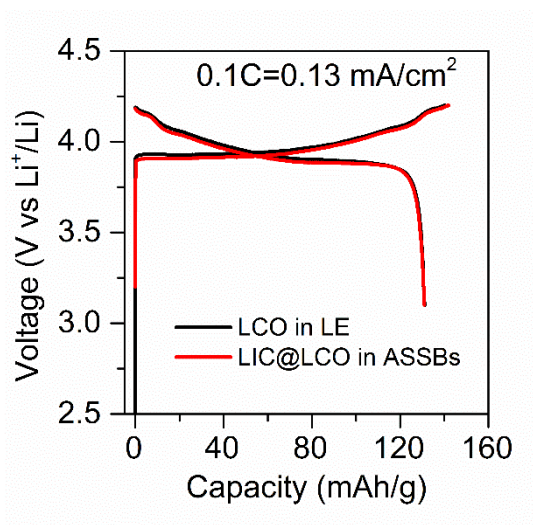


Figure 7-S6. The initial charge/discharge curves of LCO in liquid cells and LIC@LCO-15wt% in ASSLIBs at the current density of 0.13 mA.cm⁻². The overlapping of the charge/discharge curves suggests the full utilization of LCO in ASSBs and the ultra-small interfacial resistance as in liquid cells for Li⁺ transport.

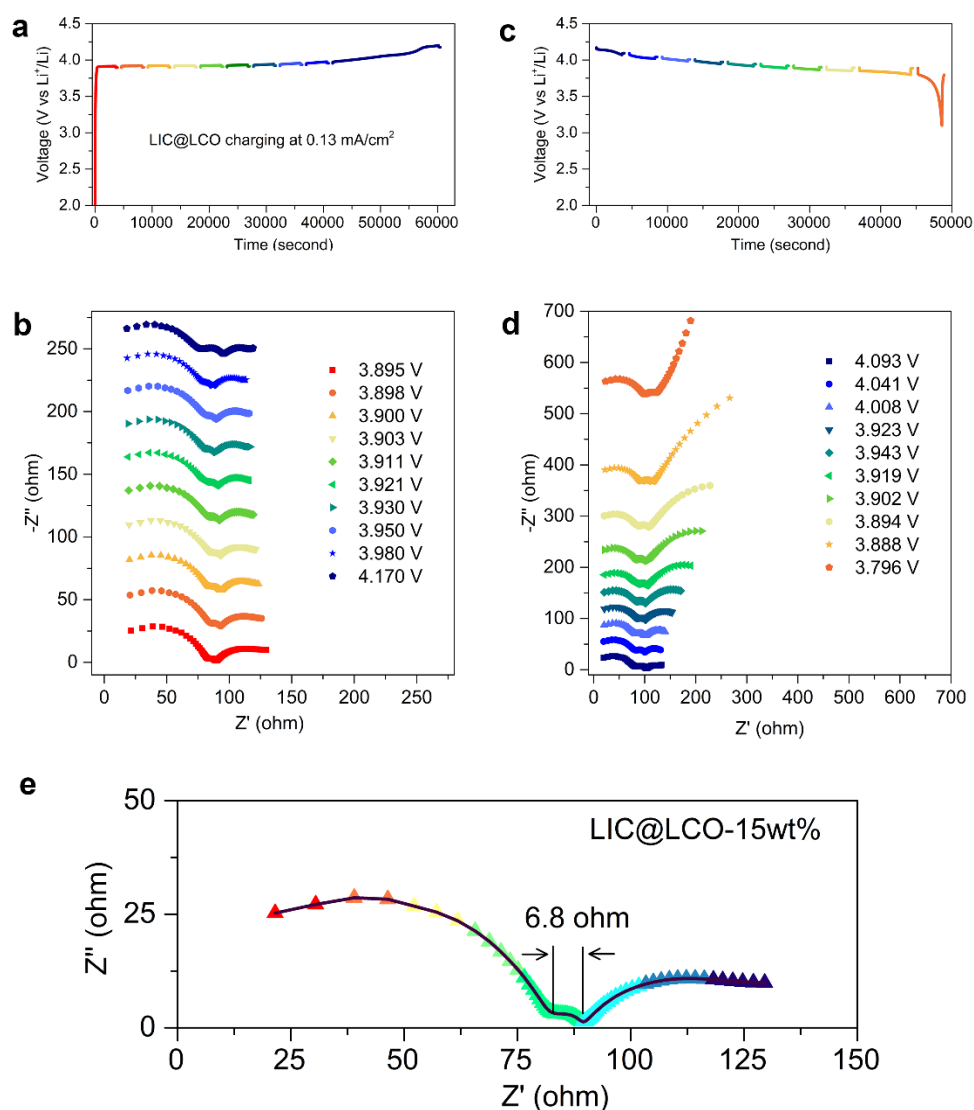


Figure 7-S7. In-situ EIS spectra of LIC@LCO electrodes during the initial charge/discharge process. (a) initial charge curves at 0.1C. (b) EIS spectra at different charge states. (c) discharge curves at 0.1C. (d) EIS spectra at different discharge states. (e) Typical EIS spectra of LIC@LCO-15wt%. The semi-circle at the middle frequency is the total interfacial resistance (6.8 Ω) between LCO and LIC.⁵ The specific area of LCO is 5 cm².mg⁻¹. Thus the interfacial resistance between LCO and LIC is 0.13 Ω .cm⁻².

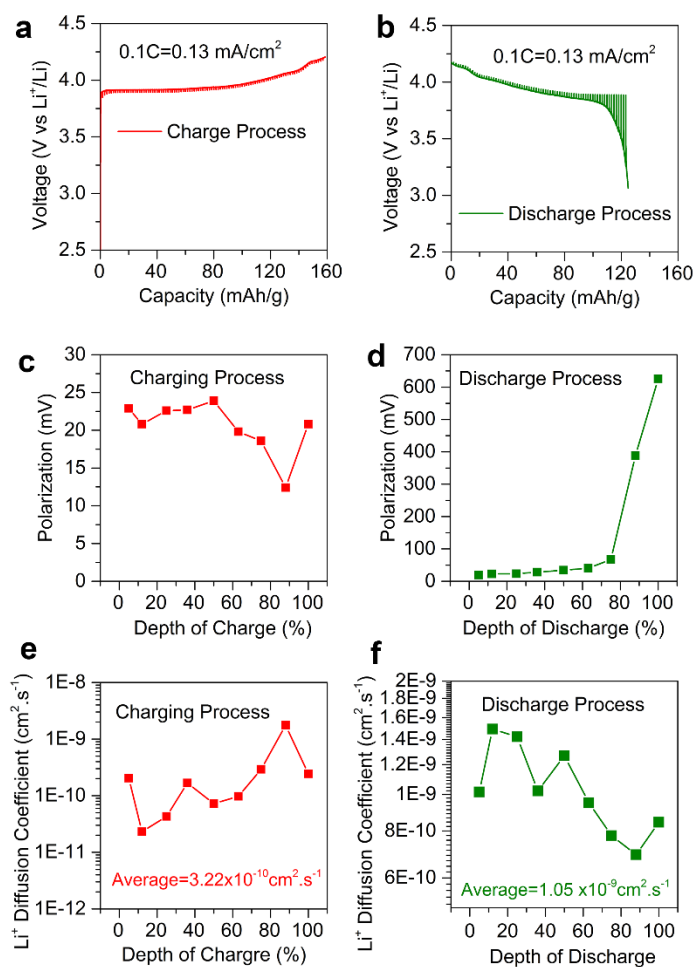


Figure 7-S8. (a) GITT charging curve of LIC@LCO-15wt% at 0.1C. (a) GITT discharging curve of LIC@LCO-15wt% at 0.1C. (c) The polarization of LIC@LCO-15wt% during the initial charge process at 0.1C. (d) The polarization of LIC@LCO-15wt% during the initial discharge process at 0.1C. (e) Li^+ diffusion coefficient at the different depths of charge determined by GITT. (f) Li^+ diffusion coefficient at the different depths of discharge determined by GITT.

According to the GITT theoretical analysis, Li^+ diffusion coefficient can be calculated by the following equation:

$$D = \frac{4}{\pi\tau} \left(\frac{m_{LCO} V_m}{M_{LCO} S} \right)^2 \left(\frac{\Delta E_s}{\Delta E_t} \right)^2$$

Where D is chemical diffusion coefficient, S is interfacial contact area between LCO and LGPS in our case, τ is pulse duration (300 s in our case), ΔE_s is the steady-state voltage change, ΔE_t is the transient voltage change, m_{LCO} is the mass of the LCO in the cathode composite (10.2 mg), M_{LCO} is the molecular weight of LiCoO_2 (97.87 g. mol⁻¹). For the discharge process, M_{LCO} is the molecular weight of $\text{Li}_{0.5}\text{CoO}_2$ (94.4 97.87 g. mol⁻¹). V_m is the molar volume of the sample (LiCoO_2 , 19.56 cm³ mol⁻¹).⁶

Table 7-S4. The references for the Ragone plot.

Name	References
Ref #1	R. Mosthev, B. Johnson, <i>J. Power Sources</i> 2000 , <i>91</i> , 86. ⁷
Ref #2	K. Takada et al. <i>Adv. Mater.</i> (2006), <i>18</i> , 2226-2229. DOI: 10.1002/adma.200502604. ⁸
Ref #3	R. Kanno et al. <i>Nat. Mater.</i> (2011), <i>10</i> , 682-686 DOI: 10.1038/NMAT3066. ⁹
Ref #4	J. Janek et al. <i>ACS Appl. Mater. Interfaces</i> (2017), <i>9</i> , 17835–17845 DOI: 10.1021/acsami.7b01137. ¹⁰
Ref #5	<i>Y-S Jung et al. Adv. Mater.</i> (2016), <i>28</i> , 1874–1883. DOI: 10.1002/adma.201505008. ⁶

Table 7-S5. The lattice parameters and bandgap of LiCoO₂ under different U values. We adopted 4 eV for the Hubbard U value of Co 3d state in the present study.¹¹

U	a (Å)	c (Å)	Bandgap (eV)
1	2.85	14.07	1.00
2	2.84	14.11	1.38
3	2.84	14.14	1.77
4	2.83 2.83^a	14.17 14.04^a	2.13 2.22^a
5	2.81	14.20	2.51

References

1. Perdew, J.P., Burke, K. & Ernzerhof, M. Generalized gradient approximation made simple. *Physical review letters* **77**, 3865 (1996).
2. Anisimov, V.I., Aryasetiawan, F. & Lichtenstein, A. First-principles calculations of the electronic structure and spectra of strongly correlated systems: the LDA+ U method. *Journal of Physics: Condensed Matter* **9**, 767 (1997).
3. Momma, K. & Izumi, F. VESTA: a three-dimensional visualization system for electronic and structural analysis. *Journal of Applied Crystallography* **41**, 653-658 (2008).

4. Grimme, S. Semiempirical GGA-type density functional constructed with a long-range dispersion correction. *Journal of computational chemistry* **27**, 1787-1799 (2006).
5. Asano, T. et al. Solid Halide Electrolytes with High Lithium-Ion Conductivity for Application in 4 V Class Bulk-Type All-Solid-State Batteries. *Adv. Mater.* **0**, 1803075 (2018).
6. Park, K.H. et al. Solution-processable glass LiI-Li₄SnS₄ superionic conductors for all-solid-state Li-ion batteries. *Adv. Mater.* **28**, 1874-1883 (2016).
7. Moshtev, R. & Johnson, B. State of the art of commercial Li-ion batteries. *J. Power Sources* **91**, 86-91 (2000).
8. Ohta, N. et al. Enhancement of the high-rate capability of solid-state lithium batteries by nanoscale interfacial modification. *Adv. Mater.* **18**, 2226-2229 (2006).
9. Kamaya, N. et al. A lithium superionic conductor. *Nat. Mater.* **10**, 682-686 (2011).
10. Zhang, W. et al. Interfacial Processes and Influence of Composite Cathode Microstructure Controlling the Performance of All-Solid-State Lithium Batteries. *ACS Appl. Mater. Interfaces* **9**, 17835-17845 (2017).
11. Haruyama, J., Sodeyama, K., Han, L.Y., Takada, K. & Tateyama, Y. Space-Charge Layer Effect at Interface between Oxide Cathode and Sulfide Electrolyte in All-Solid-State Lithium-Ion Battery. *Chem. Mater.* **26**, 4248-4255 (2014).

Chapter 8

8. Stabilizing Interface between $\text{Li}_{10}\text{SnP}_2\text{S}_{12}$ and Li Metal by Molecular Layer Deposition*

Besides the success made at the cathode interface, suppressing interfacial reactions and lithium dendrite growth between Li metal and solid-state sulfide electrolytes (SEs) is of great importance to high-energy-density all-solid-state lithium metal batteries (ASSLMBs).

In this work, molecular layer deposition (MLD) is employed for the first time to develop an inorganic-organic hybrid interlayer (alucone) at the interface between the Li metal and SEs. It is found that the alucone layer can serve as an artificial solid electrolyte interphase (SEI). As a result, interfacial reactions between Li and SEs are significantly suppressed by intrinsically blocking electron transfer at the interface. In addition, lithium dendrites are also suppressed. Coupled with a LiCoO_2 cathode, ASSLMBs with 30 MLD cycles of alucone on Li metal exhibit a high initial capacity of 120 mAh g^{-1} and can retain a capacity of 60 mAh g^{-1} after 150 cycles. This work exemplifies the use of MLD to stabilize the interface between SEs and Li metal for ASSLMBs.

***Note:** This work has been published in Nano Energy.

Changhong Wang, Yang Zhao, Qian Sun, Xia Li, Yulong Liu, Jianwen Liang, Xiaona Li, Xiaoting Lin, Ruying Li, Keegan R Adair, Li Zhang, Rong Yang, Shigang Lu, Xueliang Sun, Stabilizing interface between $\text{Li}_{10}\text{SnP}_2\text{S}_{12}$ and Li metal by molecular layer deposition. *Nano Energy*, 2018, 53, 168-174.

8.1 Introduction

All-solid-state lithium metal batteries (ASSLMBs) have gained increasing interest in recent years due to their superior safety and higher energy density over those of state-of-the-art lithium-ion batteries.[1, 2] To realize ASSLMBs, the development of solid-state electrolytes is essential. Currently, there are three main categories of solid-state electrolytes under development, including lithium-ion-conductive polymer electrolytes, inorganic lithium-ion-conductive ceramics and their composites as hybrid electrolytes.[3, 4] Among the inorganic ceramics, sulfide electrolytes (SEs) are attracting increasing interest due to their outstanding ionic conductivity ($>10^{-3}$ S/cm). For example, $\text{Li}_{9.54}\text{Si}_{1.74}\text{P}_{1.44}\text{S}_{11.7}\text{Cl}_{0.3}$ shows an ionic conductivity of 25 mS cm^{-1} , [5] which is almost two times higher than that of conventional liquid electrolytes (10.2 mS cm^{-1}). [6] On the other hand, Li metal is considered as the ultimate choice among all the possible anodes for solid-state lithium batteries due to its highest theoretical capacity of $3,860 \text{ mAh g}^{-1}$, or $2,061 \text{ mAh cm}^{-3}$ and lowest electrochemical potential (-3.040 V versus the standard hydrogen electrode), ASSLMBs with high energy density can be achieved. [4, 7, 8]

However, two major challenges hinder the direct use of Li metal in ASSLMBs. Firstly, lithium dendrite formation can lead to short circuits and poses serious safety concerns. Secondly, the interface instability between Li metal and SEs leads to large interfacial resistance for Li-ion (Li^+) conduction. Over the past decades, several promising strategies have been proposed to enable the use of Li metal in ASSLMBs: (1) using Li-Metal alloys instead of pure Li metal anodes, such as Li-In and Li-Al alloys. [9, 10] (2) double layer electrolytes with distinct properties, in which using relatively stable SEs against Li metal can improve the interfacial stability, [11, 12] and (3) protective layers on the Li metal surface, [13-15] such as LiH_2PO_4 [16] and Al_2O_3 , [17] to engineer the interface. However, many of these strategies have drawbacks such as sacrificing the

electrochemical potential of Li metal, lowering the overall energy density, and difficulty in achieving uniform thin film coatings.

In this work, we use molecular layer deposition (MLD) for the first time to develop an inorganic-organic hybrid interlayer (alucone) at the interface between the SEs and Li metal. It was found that the alucone layer can serve as an artificial solid electrolyte interphase (SEI), intrinsically blocking the electron transfer at the anode interface, thus completely suppressing the interfacial reactions between Li and SEs. Moreover, lithium dendrite formation was also suppressed by the MLD coating. In light of the molecular structure of coatings, the inorganic-organic hybrid MLD coating has improved mechanical properties over that of purely inorganic coatings such as Al_2O_3 , which is beneficial for the accommodation of the stress/strain caused by the volume change of electrodes. Coupled with a LiCoO_2 cathode, ASSLMBs with the Li metal protected by alucone exhibit smaller polarization, higher capacity, and longer cycle life than those with bare Li metal. The underlying reasons are believed to be the suppression of interfacial reactions and lithium dendrite formation, thus guaranteeing the long-term cyclability of ASSLMBs. This work exemplifies the use of MLD to stabilize the interface between SEs and Li for ASSLMBs.

8.2 Experimental Section

8.2.1 Li Preparation

A fresh Li foil was used directly. Molecular layer deposition (MLD) of Alucone coatings was conducted in a Gemstar-8 ALD system (Arradiance, USA) directly connected with the argon-filled glove box. Alucone was directly deposited on the as-prepared foil at 85°C by alternatively introducing trimethylaluminum (TMA) and ethylene glycol (EG) as precursors. The MLD process is performed as a sequence of

TMA pulse/purge/EG pulse/purge sequence with the time of 0.01 s/40 s/0.01 s/70 s, respectively. The different cycle numbers of 10, 30 and 50 MLD alucone coating on Li foils are named 10alucone Li, 30alucone Li, and 50alucone Li, respectively. For comparison, Al₂O₃ was performed using TMA and H₂O as precursors at 85°C by ALD.

8.2.2 Electrochemical Measurements

The electrochemical analysis was performed in CR2032 coin-type cells. Li₁₀SnP₂S₁₂ was purchased from NEI corporation. The symmetric cells with a configuration of Li/Li₁₀SnP₂S₁₂/Li were assembled in an ultra-pure argon-filled glove box. The Li stripping/plating studies were carried out in an Arbin BT-2000 battery test system at room temperature. Constant current densities were applied to the electrodes during repeated stripping/plating while the potential was recorded over time. Electrochemical impedance analysis was performed on a biologic electrochemical station with a frequency range from 1000 kHz to 100 m Hz with an amplitude of 10 mV. Cathode composites were mixed with LiCoO₂, Li₁₀SnP₂S₁₂, and acetylene black with a ratio of 60:34:6. To assemble all-solid-state lithium metal batteries, the 80 mg Li₁₀SnP₂S₁₂ was pelletized under 1 ton using a pelletizer with a diameter of 1/2 inch. Then 10 mg cathode composites were put on the side of Li₁₀SnP₂S₁₂ and then pressed at 3 tons. Finally, Li foil was put on another side of Li₁₀SnP₂S₁₂ and pressed at 0.5 tons. All the ASSLMBs were tested with the cut-off voltages from 2.5 V to 4.5 V.

8.2.3 Characterizations

The morphology of materials was analyzed by a Hitachi S-4800 field emission SEM equipped with EDX. XRD patterns were scanned using a Bruker D8 diffractometer, using Cu K α radiation. X-ray photoelectron spectroscopy was performed using Thermo Scientific ESCALAB 250Xi with Al K α -radiation. The pressure in the analysis chamber

was typically 2×10^{-9} torr during acquisition. Raman spectra were collected using the laser with a wavelength of 532 nm.

8.3 Results and Discussion

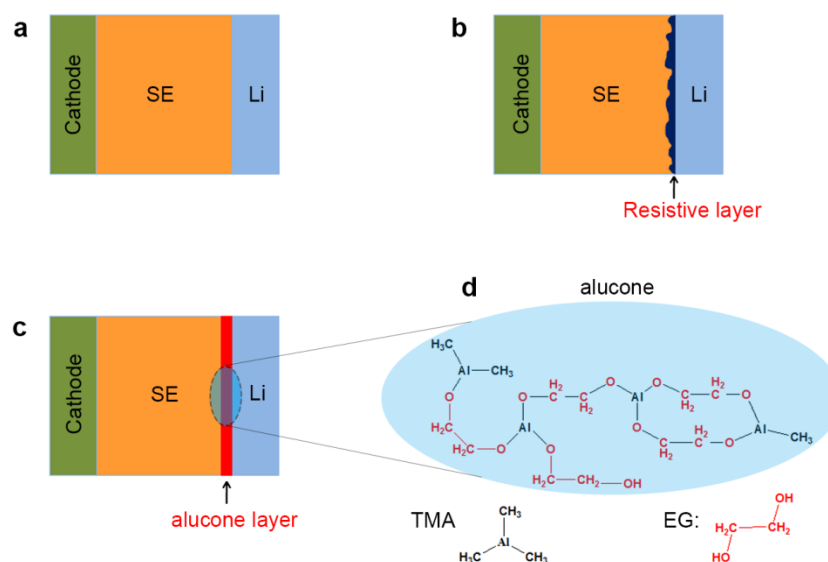


Figure 8-1 Schematic illustration of SE-based ASSLMBs. (a) SE-based ASSLMBs. (b) The resistive layer at the interface between Li and SEs. (c) Alucone layer on the Li surface. (d) The chemical structure of alucone deposited by MLD.

The configuration of all-solid-state lithium metal batteries (ASSLMBs) is illustrated in **Figure 8-1a**, which is consisted of Li metal, SEs, and a cathode. Generally, once bare Li directly contacts with SEs, a resistive layer forms at the interface due to the chemical instability of SEs against highly reactive Li metal (**Figure 8-1b**).^[16, 18] Here, we employed MLD to introduce an inorganic-organic hybrid thin film (alucone) at the interface (**Figure 8-1c**). The chemical structure of polymeric alucone films is present in **Figure 8-1d**, which was deposited on the Li surface by MLD using the precursors of trimethylaluminum (*TMA*) and ethylene glycol (EG).^[19, 20] The morphology of Li foils was checked by scanning electron microscopy (SEM). As shown in Figure S1, there

is no obvious change on the Li metal surface after the MLD process. X-ray photoelectron spectroscopy (XPS) was used to confirm the alucone thin film on the Li surface, Al, Li, C, and O peaks were clearly detected on the Li surface after 30 MLD cycles (**Figure 8-S2**), which are originated from the polymeric alucone layer. It should be mentioned that the thickness of the MLD thin film can be controlled at the atomic/molecular level through the self-limiting reactions between two precursors. Based on our previous study, the growth rate of alucone on Li metal foils is 0.3~0.5 nm per cycle.[20, 21] The different thickness of the alucone coating on Li metal is listed in **Table 8-S1**. A detailed MLD coating process can be found in the experimental section. The alucone thin film has an abundant ether bond (–O–), which is effectively helpful for Li^+ transport,[22] thus serving as artificial solid-electrolyte interphase (SEI) on Li surface after lithiation. SEI is known as a good lithium-ion conductor but an electronic insulator.[23] Thus interfacial reactions between Li metal and SEs could be suppressed by blocking electron transfer between Li and SEs. Furthermore, MLD coatings generally have a lower elastic modulus than pure inorganic coatings, which is beneficial for the accommodation of stress/strain caused by the volume change of electrodes during cycling.[20, 21, 24]

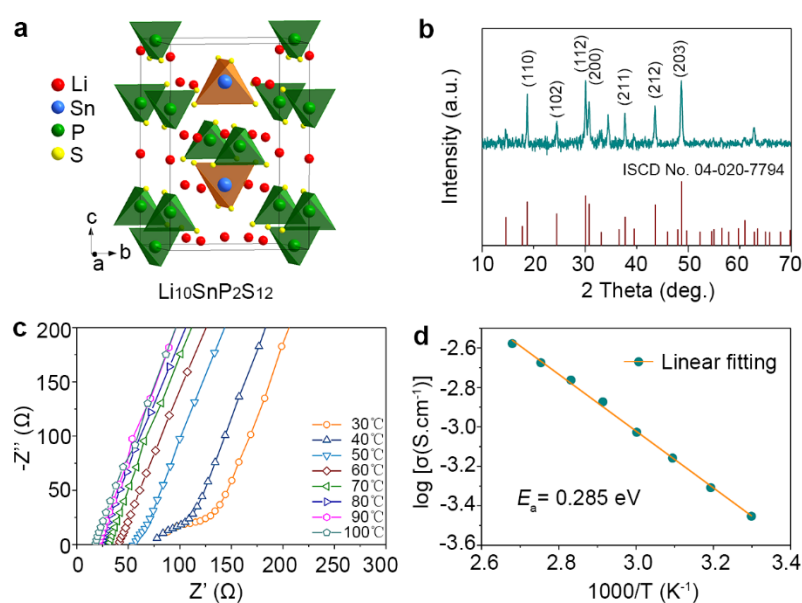


Figure 8-2 Characterizations of $\text{Li}_{10}\text{SnP}_2\text{S}_{12}$ (LSPS). (a) Crystal structure of LSPS. (b) XRD pattern of as-prepared LSPS. (c) EIS profiles of LSPS at various temperatures. (d) Arrhenius plot of LSPS conductivity.

In terms of SEs, a member of LMPS family- $\text{Li}_{10}\text{SnP}_2\text{S}_{12}$ (LSPS)-was selected, which is favorable for its satisfactory ion conductivity and low cost for practical application.[25-27] The crystal structure framework of LSPS consists of $(\text{Sn}_{0.5}\text{P}_{0.5})\text{S}_4$ tetrahedra, PS_4 tetrahedra, LiS_6 octahedra, and LiS_4 tetrahedra (**Figure 8-2a** and **Figure 8-S3**).[25, 26] LSPS has a one-dimensional conduction path along the c-axis.[28] In addition, the *thio*-LiSICON structure of LSPS is evidenced by X-ray diffraction (XRD) patterns (**Figure 8-2b**). Based on the electrochemical impedance spectroscopy (EIS) measurement, the ionic conductivity of $\text{Li}_{10}\text{SnP}_2\text{S}_{12}$ is 3.12×10^{-4} S/cm at room temperature (**Figure 8-2c**). According to the Nernst-Einstein equation $\sigma(T) = A\exp(-E_A/k_B T)$, where σ is the ionic conductivity at a certain temperature, A is the pre-exponential factor, T is the temperature in Kelvin, k_B is the Boltzmann constant, E_A is the activation energy of Li^+ hopping between two adjacent sites,[29] LSPS possesses an activation energy of 0.285 eV (**Figure 8-2d**). In addition, the morphology of LSPS was also examined by scanning electron microscopy (SEM) (**Figure 8-S4**). The particle size of LSPS varies from a few hundred nanometers to several micrometers. The large particle seems to be the aggregation of the small LSPS particles.

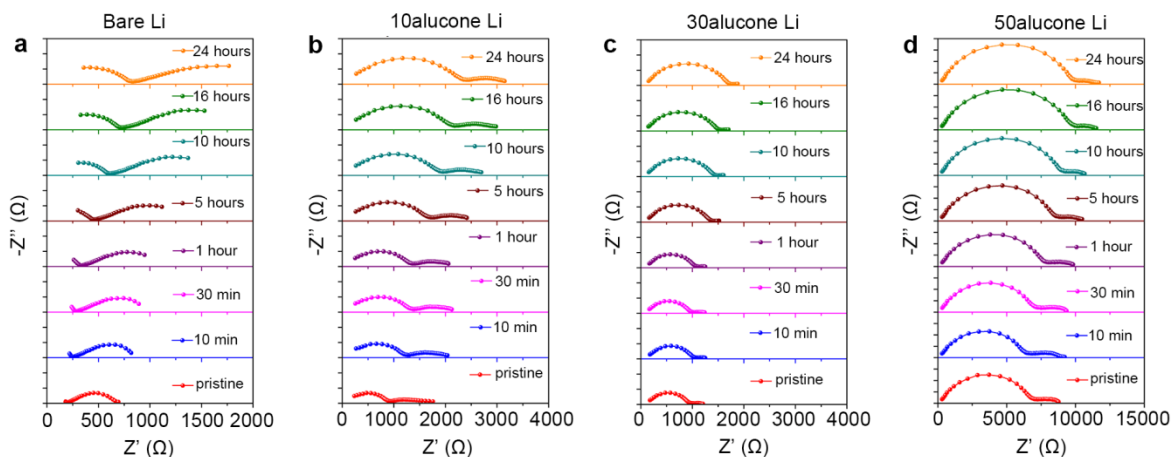


Figure 8-3 Electrochemical impedance spectra of Li symmetric cells. (a) Time-dependent EIS spectra of bare Li-LSPS-Li. (b) Time-dependent EIS spectra of 10alucone Li-LSPS-Li. (c) Time-dependent EIS spectra of 30alucone Li-LSPS-Li. (d) Time-dependent EIS spectra of 50alucone Li-LSPS-Li.

By co-axial pressing, LSPS can be easily pressed into pellets because of its low elastic modulus. Furthermore, to evaluate the interface stability between LSPS and Li metal, Li symmetric cells with a structure of Li/LSPS/Li were fabricated and then the EIS was conducted as a function of time. In Nyquist plots of Li symmetric cells, there are two typical EIS spectra.[30, 31] One consists of a high-frequency semicircle and a finite-length Warburg impedance at low frequencies (**Figure 8-S5a**).[30] These characteristics are typical for mixed ion-electron conductor (MCI, an acronym for mixed conductor interphases). Another one is characteristic of a single semicircle at high frequency, which indicates the formation of ion-conducting SEI at the interface (**Figure 8-S5b**). A detailed explanation is included in the SI.[30] Nyquist plots of Li/LSPS/Li symmetric cells mainly consists of a high-frequency semicircle with a finite-length Warburg impedance (**Figure 83a**), which indicates the interface between Li and LSPS is a mixed ion-electron conductor. Both interfacial resistance (R_{int}) and Warburg impedance (W_s) increase significantly within 24 hours, indicating the growth of mixed conductor interphase (MCI) caused by the noticeable interfacial reactions between Li and LSPS. With alucone coating on Li metal, the Nyquist plot mainly shows a single semicircle at the high frequency, indicating that the interface between LSPS and alucone-coated Li metal is an ion-conducting SEI layer (**Figure 8-3b, 8-3c, and 8-3d**). More interestingly, in the case of 10 cycles alucone (10alucone) coating on Li metal, R_{int} is still increasing within 24 hours (**Figure 8-3b**), implying that 10alucone could not completely suppress the interfacial reactions between Li and LSPS. However, in the case of 30 cycles alucone (30alucone) coating on Li metal, R_{int} is almost stable and the total resistance is minimized (**Figure 8-3c**), indicating that the remarkable interfacial reactions between

LSPS and pristine Li are well suppressed. Nevertheless, in the case of 50 cycles alucone (50alucone), the overall resistance is almost 10 k Ω (**Figure 8-3d**), implying that the thicker alucone coating blocks the ion migration at the interface. From the EIS results, it can be concluded that 30alucone coating on Li metal can serve as an effective ion-conducting SEI interphase and effectively suppress the interfacial reactions.

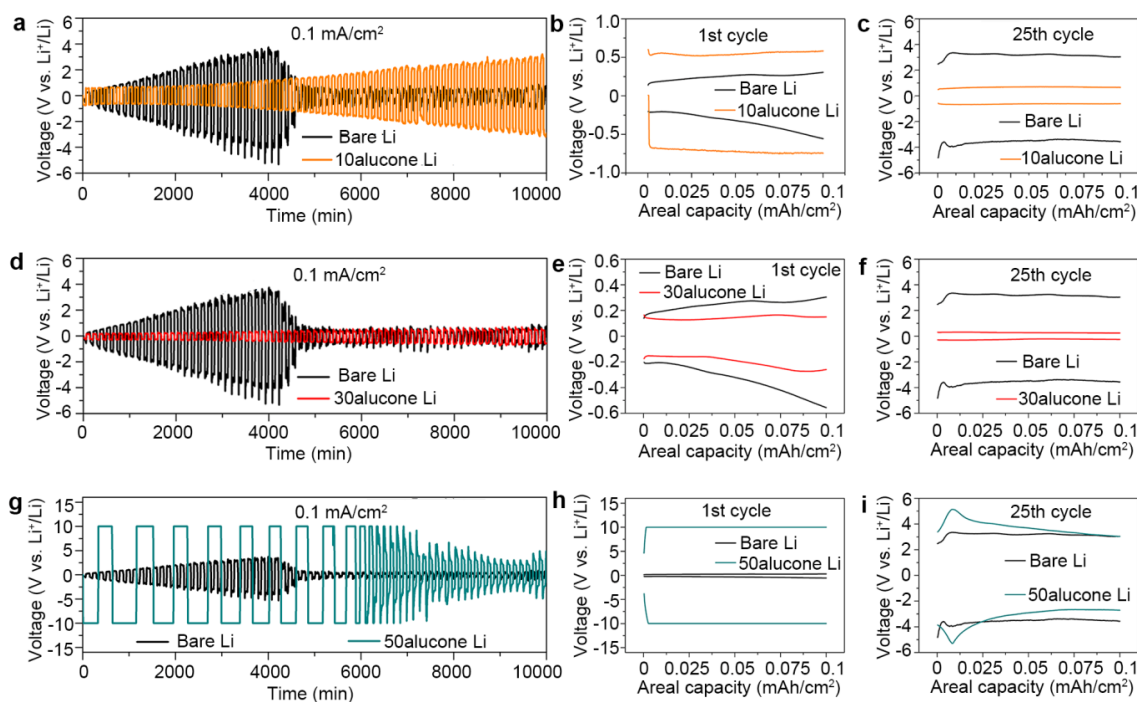


Figure 8-4 Comparison of Li^+ plating/stripping behavior of Li symmetric cells at a current density of 0.1 mA cm^{-2} with an areal capacity of 0.1 mAh cm^{-2} . (a) 10 cycles alucone (10alucone Li) versus bare Li. (b,c) Voltage profiles of the 10alucone Li and the bare Li foil in the 1st cycle and the 25th cycle, respectively. (d) 30 cycles alucone (30alucone Li) versus bare Li. (e, f) Voltage profiles of the 30alucone Li and the bare Li foil in the 1st cycles and the 25th cycle, respectively. (g) 50 cycles alucone (50alucone Li) versus the bare Li. (h,i) Voltage profiles of the 50alucone Li and the bare Li foil in the 1st cycle and the 25th cycle, respectively.

Furthermore, to study the electrochemical stability and reversibility of Li metal against

LSPS, Li symmetric cells were discharged and charged at a constant current (0.1 mA cm^{-2}) with an areal capacity of 0.1 mAh cm^{-2} . Without any coating, the over-potential of Li^+ plating/stripping is greatly increasing (**Figure 8-4a**), indicating that bare Li metal phenomenally reacts with LSPS, resulting in highly resistive interphase at the interface. After 4000 minutes, the over-potential increases to 3.6V and the short circuit happens, which is related to the unlimited formation of the highly resistive interphase and lithium dendrites. Using 10 cycles of alucone coating, the short circuit is suppressed within 10000 minutes. However, the over-potential of Li^+ plating/stripping of 10alucone coated Li is still increased to 3.4V, which means that 10alucone coating cannot suppress the interfacial reactions between SEs and Li metal. The plateau of Li^+ plating/stripping at the 1st cycle and 25th cycle are present in **Figure 8-4b** and **Figure 8-4c**, showing the first charge process has a large over-potential at the first cycle, which indicates that Li^+ need to overcome an energy barrier before nucleation.[32] Interestingly, in the case of 30alucone Li, the over-potential of Li^+ plating/stripping almost keeps less than 0.5V within 10000 minutes (**Figure 8-4d**), strongly indicating the stable electrochemical process at the anode interface between Li metal and LSPS. Again, no short circuit appears. These results are nicely consistent with the EIS results above-mentioned. Compared the Li^+ plating/stripping plateau at the first cycle and 25th cycle, it also can be clearly seen that the over-potential is much lower than that of the control sample, as shown in **Figure 8-4e** and **Figure 8-4f**. To gain insight into the chemical valent evolution of Sn in LSPS, X-ray photoelectron spectroscopy (XPS) was conducted after 25 cycles. As displayed in Figure S6, the Sn 3d spectra exhibited spin-orbit doublet peaks at 486.76 eV ($\text{Sn}^{4+}3d_{5/2}$) and 495.22 eV ($\text{Sn}^{4+} 3d_{3/2}$).[33] Without any coating, the main peaks shift to low binding energy, indicating that Sn^{4+} was reduced to Sn^{2+} . [33] With 30alucone coating, the main peaks of Sn 3d stay at the same energy position as those of pristine LSPS. The XPS results strongly suggest that MLD coating can effectively overcome the interfacial reactions between LSPS and Li metal.

When the MLD coating cycles increase to 50 cycles, there is a large over-potential at the very beginning, as present in Figure 4g, indicating that 50alucone thin film is too thick for Li^+ hopping during the initial plating and stripping process (**Figure 8-4h**). Interestingly, the over-potential is decreased after 10 cycles and reach the same level at the 25 cycles (**Figure 8-4i**), which means the alucone layer could be lithiated, serving as artificial SEI. In addition, the alucone thin film is electronically insulative, thus the interfacial reactions between Li and LSPS can be totally suppressed as long as the thickness is optimized.

To demonstrate the necessity to build an inorganic-organic hybrid coating, purely inorganic Al_2O_3 with different thicknesses was also deposited by ALD on the Li metal surface with TMA and water as a comparison. EIS spectra of the symmetric cells were recorded as a function of time (**Figure 8-S7**). The interface between LSPS and Li metal with 10 or 25 cycles Al_2O_3 is a mixed ion-electron conductor interphase, while the interface is an ion-conducting interphase in the case of 50 and 200 cycles Al_2O_3 . The results confirm that the thickness of the coating layer also plays an important role in forming different categories of the interface layer.

Furthermore, Li symmetrical cells with Al_2O_3 -coated Li were also charged and discharged at a constant current density of $0.1 \text{ mA}\cdot\text{cm}^{-2}$ (**Figure 8-S8**). The over-potential of Li^+ plating/stripping still keeps increasing over time, indicating the interfacial reactions between Li and LSPS were not well inhibited. The underlying reason is believed to be that Li-ion conductive LiAlO_x thin film, which is resulted from the lithiation of Al_2O_3 , [34, 35] possesses a very high elastic modulus. Therefore, the LiAlO_x thin film cannot accommodate the large stress/strain caused by Li^+ plating/stripping. Comparatively, the organic-inorganic hybrid coating layer deposited by MLD (alucone) is much more effective than the organic coating layer (Al_2O_3) deposited by ALD in terms of the suppression of lithium dendrites and interfacial reactions.

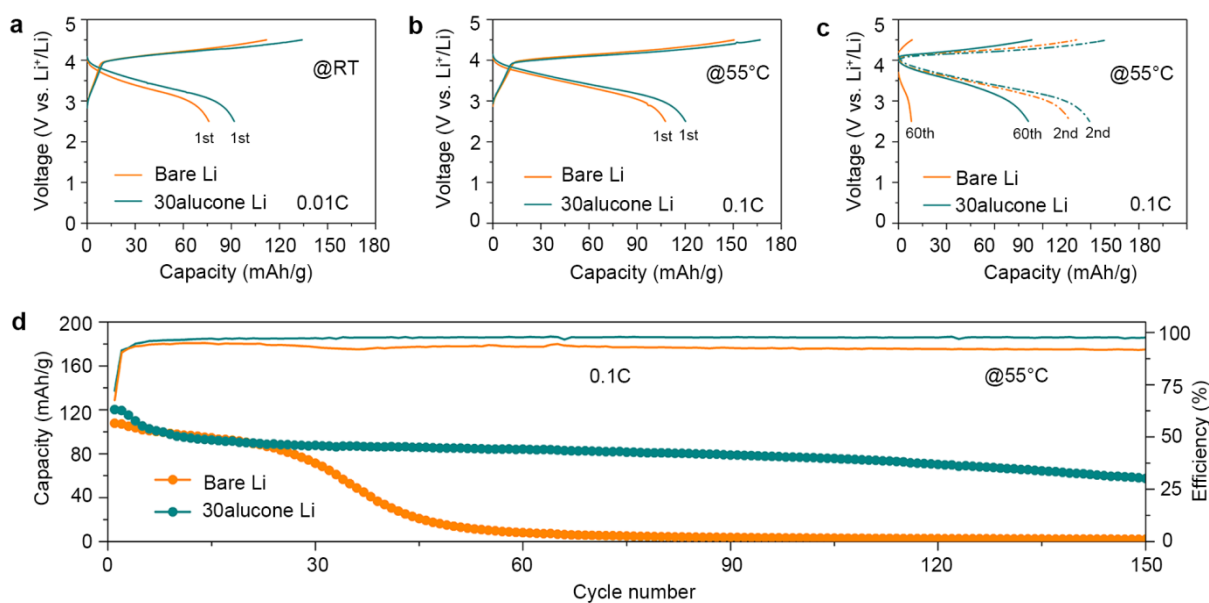


Figure 8-5 Electrochemical performance of all-solid-state lithium metal batteries. (a) Initial charge-discharge curves of LiCoO₂-based ASSLMBs at 0.01C at room temperature. (b) Initial charge-discharge curves of LiCoO₂-based ASSLMBs at 0.1C at 55 °C. (c) Charge-discharge curves of LiCoO₂-based ASSLMBs at the 2nd and 60th cycles. (d) Cycle performance of LiCoO₂-based ASSLMBs at 55 °C.

Coupled with the LiCoO₂ cathode, ASSLMBs were fabricated with the bare Li metal anode and 30alucone Li metal anode, respectively. First, ASSLMBs were cycled at room temperature with a current density of 0.01C (1C=140 mA/g). It is clearly shown that ASSLIBs with 30alucone Li shows smaller polarization and higher initial efficiency (98 %) compared to those with bare Li metal (92 %) (**Figure 8-5a**). This coincides with the EIS and Li symmetric cell results discussed above. Moreover, to increase the current density, ASSLMBs were further tested at 55 °C at 0.1C. ASSLMBs with 30alucone Li shows a specific capacity of 120 mAh.g⁻¹, which is higher than that of ASSLMBs with bare Li (107 mAh.g⁻¹) (**Figure 8-5b**). After 60 cycles, ASSLMBs with bare Li metal show almost no capacity and surprisingly large polarization (**Figure 8-5c**), which is believed to be caused by the large interfacial resistance at the anode interface. As a sharp

comparison, ASSLMs with 30 alucone Li shows smaller polarization at the 60th cycle and can be stably cycled over 150 cycles. The capacity still remains at 60 mAh.g^{-1} after 150 cycles (**Figure 8-5d**). Obviously, the improved cycle performance is resulted from the improved anode interface by MLD coating. Interestingly, the low initial efficiency jumped to 98% after several cycles, which means that a part of Li consumed to lithiate the alucone thin film during the initial charge process, forming an artificial SEI.

8.4 Conclusions

Li metal is regarded as the ultimate choice of ASSLMs because of the high capacity and lowest electrochemical potential of Li metal, which enable the solid-state lithium batteries with high energy density. However, the interfacial instability of LSPS and Li metal imposes a big barrier for its application in ASSLMs. In this work, we use MLD to develop an inorganic-organic interlayer (alucone) at the interface between Li and LSPS. With the help of the alucone coating layer, the interfacial reactions between Li metal and LSPS are greatly suppressed. In addition, lithium dendrite formation is also inhibited. By XPS analysis, the reduction of Sn^{4+} in LSPS was restrained with the MLD coating layer. Compared with bare Li, LiCoO_2 -based ASSLMs with 30aluocne Li exhibit smaller polarization, higher Coulombic efficiency, higher capacity, and longer cycle life. This demonstration clearly suggests that Li metal with MLD coating can be successfully applied to ASSLMs without compromising the output voltage and energy density of ASSLMs.

8.5 Acknowledgments

This work was supported by Natural Sciences and Engineering Research Council of Canada (NSERC), Canada Research Chair Program (CRC), China Automotive Battery Research Institute, Canada Foundation for Innovation (CFI), the Canada Light Source at

University of Saskatchewan (CLS) and University of Western Ontario.

8.6 Author Contribution

C. W., Y. Z., and Q. S. conceived the idea and designed the experiments. X. S. directed the project. R. L helps with purchasing chemicals and characterizations. Y. L., J. L., X. L., and X. L help in data analysis. C. W. wrote the manuscript. All authors discussed the results and commented on the manuscript.

8.7 References

- [1] S. Xin, Y. You, S. Wang, H.-C. Gao, Y.-X. Yin, Y.-G. Guo, *ACS Energy Lett.*, 2 (2017) 1385-1394.
- [2] C. Sun, J. Liu, Y. Gong, D.P. Wilkinson, J. Zhang, *Nano Energy*, 33 (2017) 363-386.
- [3] X. Yu, A. Manthiram, *Acc. Chem. Res.*, 50 (2017) 2653-2600.
- [4] A. Manthiram, X. Yu, S. Wang, *Nat. Rev. Mater.*, 2 (2017) 16103.
- [5] Y. Kato, S. Hori, T. Saito, K. Suzuki, M. Hirayama, A. Mitsui, M. Yonemura, H. Iba, R. Kanno, *Nat. Energy*, 1 (2016) 16030.
- [6] K. Xu, *Chem. Rev.*, 104 (2004) 4303-4418.
- [7] D. Lin, Y. Liu, Y. Cui, *Nat Nano*, 12 (2017) 194-206.
- [8] N.-W. Li, Y.-X. Yin, C.-P. Yang, Y.-G. Guo, *Adv. Mater.*, 28 (2016) 1853-1858.
- [9] N. Ohta, K. Takada, L. Zhang, R. Ma, M. Osada, T. Sasaki, *Adv. Mater.*, 18 (2006) 2226-2229.
- [10] T. Kobayashi, A. Yamada, R. Kanno, *Electrochim. Acta*, 53 (2008) 5045-5050.

- [11] X. Yao, N. Huang, F. Han, Q. Zhang, H. Wan, J.P. Mwizerwa, C. Wang, X. Xu, *Adv. Energy Mater.*, 7 (2017) 1602923.
- [12] Z. Zhang, Y. Zhao, S. Chen, D. Xie, X. Yao, P. Cui, X. Xu, *J. Mater. Chem. A*, 5 (2017) 16984.
- [13] W. Luo, Y. Gong, Y. Zhu, Y. Li, Y. Yao, Y. Zhang, K. Fu, G. Pastel, C.-F. Lin, Y. Mo, E.D. Wachsman, L. Hu, *Adv. Mater.*, 29 (2017) 1606042.
- [14] K. Fu, Y. Gong, B. Liu, Y. Zhu, S. Xu, Y. Yao, W. Luo, C. Wang, S.D. Lacey, J. Dai, Y. Chen, Y. Mo, E. Wachsman, L. Hu, *Sci. Adv.*, 3 (2017) e1601659.
- [15] A.C. Kozen, C.-F. Lin, A.J. Pearse, M.A. Schroeder, X. Han, L. Hu, S.-B. Lee, G.W. Rubloff, M. Noked, *ACS Nano*, 9 (2015) 5884-5892.
- [16] Z. Zhang, S. Chen, J. Yang, J. Wang, L. Yao, X. Yao, P. Cui, X. Xu, *ACS Appl. Mater. Interfaces*, 10 (2017) 2556-2565.
- [17] X. Han, Y. Gong, K. Fu, X. He, G.T. Hitz, J. Dai, A. Pearse, B. Liu, H. Wang, G. Rubloff, Y. Mo, V. Thangadurai, E.D. Wachsman, L. Hu, *Nat Mater*, 16 (2017) 572-579.
- [18] Y. Zhu, X. He, Y. Mo, *Adv. Sci.*, 4 (2017) 1600517.
- [19] X. Li, A. Lushington, Q. Sun, W. Xiao, J. Liu, B. Wang, Y. Ye, K. Nie, Y. Hu, Q. Xiao, R. Li, J. Guo, T.-K. Sham, X. Sun, *Nano Lett.*, 16 (2016) 3545-3549.
- [20] Y. Zhao, L.V. Goncharova, Q. Zhang, P. Kaghazchi, Q. Sun, A. Lushington, B. Wang, R. Li, X. Sun, *Nano Lett.*, 17 (2017) 5653-5659.
- [21] Z. Yang, G.L. V., S. Qian, L. Xia, L. Andrew, W. Biqiong, L. Ruying, D. Fang, C. Mei, S. Xueliang, *Small Methods*, 0 (2018) 1700417.

- [22] L. Yue, J. Ma, J. Zhang, J. Zhao, S. Dong, Z. Liu, G. Cui, L. Chen, *Energy Storage Materials*, 5 (2016) 139-164.
- [23] X.B. Cheng, R. Zhang, C.Z. Zhao, F. Wei, J.G. Zhang, Q. Zhang, *Adv. Sci.*, 3 (2015) 1500213.
- [24] B.H. Lee, B. Yoon, V.R. Anderson, S.M. George, *J. Phys. Chem. C*, 116 (2012) 3250-3257.
- [25] S.P. Ong, Y. Mo, W.D. Richards, L. Miara, H.S. Lee, G. Ceder, *Energy Environ. Sci.*, 6 (2013) 148-156.
- [26] P. Bron, S. Johansson, K. Zick, J. Schmedt auf der Günne, S. Dehnen, B. Roling, *J. Am. Ceram. Soc.*, 135 (2013) 15694-15697.
- [27] C. Vinado, S. Wang, Y. He, X. Xiao, Y. Li, C. Wang, J. Yang, *J. Power Sources*, (2018) doi:<https://doi.org/10.1016/j.jpowsour.2018.1006.1038>.
- [28] Y. Wang, W.D. Richards, S.P. Ong, L.J. Miara, J.C. Kim, Y. Mo, G. Ceder, *Nat Mater*, 14 (2015) 1026-1031.
- [29] J.C. Bachman, S. Muy, A. Grimaud, H.-H. Chang, N. Pour, S.F. Lux, O. Paschos, F. Maglia, S. Lupart, P. Lamp, L. Giordano, Y. Shao-Horn, *Chem. Rev.*, 116 (2016) 140-162.
- [30] P. Bron, B. Roling, S. Dehnen, *J. Power Sources*, 352 (2017) 127-134.
- [31] J. Jamnik, J. Maier, S. Pejovnik, *Electrochimica Acta*, 44 (1999) 4139-4145.
- [32] X.-B. Cheng, R. Zhang, C.-Z. Zhao, Q. Zhang, *Chem. Rev.*, 117 (2017) 10403-10473.
- [33] Y. Sohn, *J. Am. Ceram. Soc.*, 97 (2014) 1303-1310.

[34] S.C. Jung, H.-J. Kim, J.W. Choi, Y.-K. Han, *Nano Lett.*, 14 (2014) 6559-6563.

[35] Y. Zhao, L.V. Goncharova, A. Lushington, Q. Sun, H. Yadegari, B. Wang, W. Xiao, R. Li, X. Sun, *Adv. Mater.*, 29 (2017) 1606663.



8.8 Supporting Information

Table 8-S1. The thickness of alucone with different coating cycles on the Li foils.

Sample name	MLD cycles	Thickness (nm)
10alucone Li	10	3~5
30alucone Li	30	9~15
50alucone Li	50	15~25

Based on our previous study, the growth rate of polymeric alucone on Li metal foils is 0.3~0.5 nm per cycle.[1, 2]

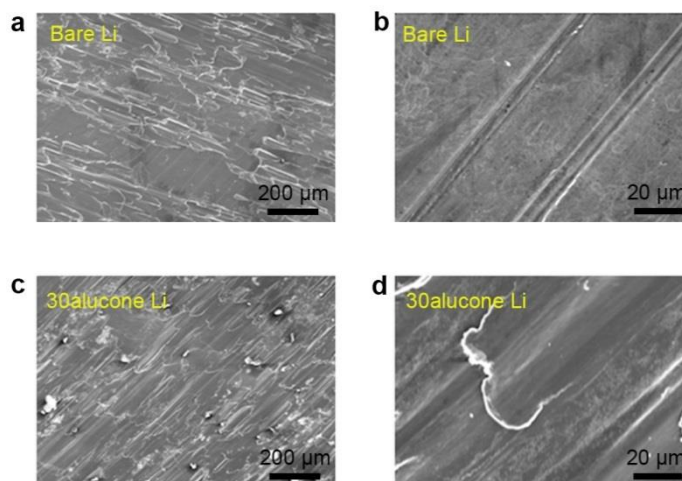


Figure 8-S1. SEM images of bare Li foils (a,b) and 30alucone Li foils (c,d). After 30 cycles MLD coating, there is no obvious change on the Li foil surface.

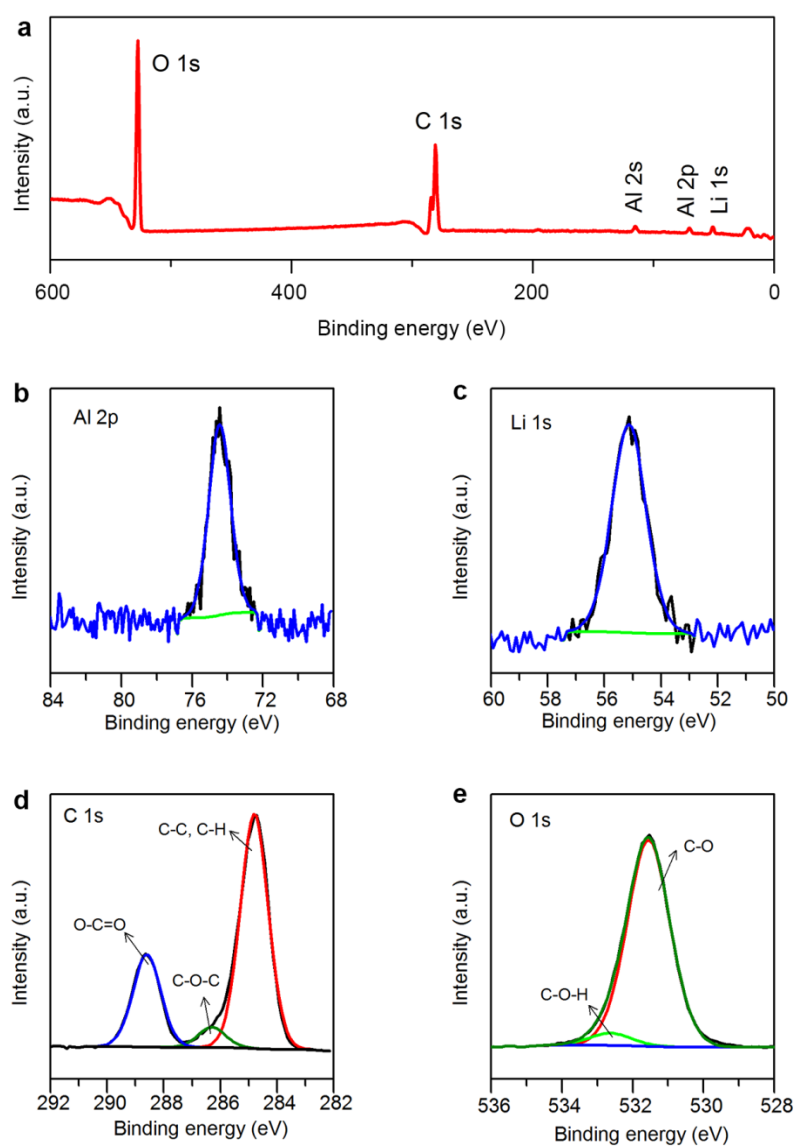


Figure 8-S2. XPS spectra of 30alucone Li. (a) full survey, (b) Al 2p spectrum, (c) Li 1s spectrum, (d) C 1s spectra, and (e) O 1s spectra.

The Al spectrum can be detected on the Li foil surface, which is resulted from the alucone coating layer. Besides, the C, O spectra are attributed to the organic links between Al^{3+} ions.

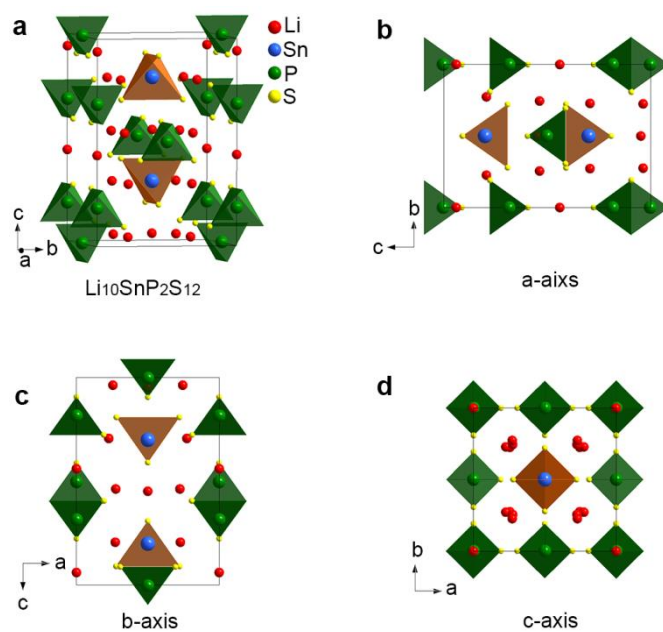


Figure 8-S3. (a) crystal structure framework of LSPS along a-axis (b), b-axis (c), and c-axis (d).

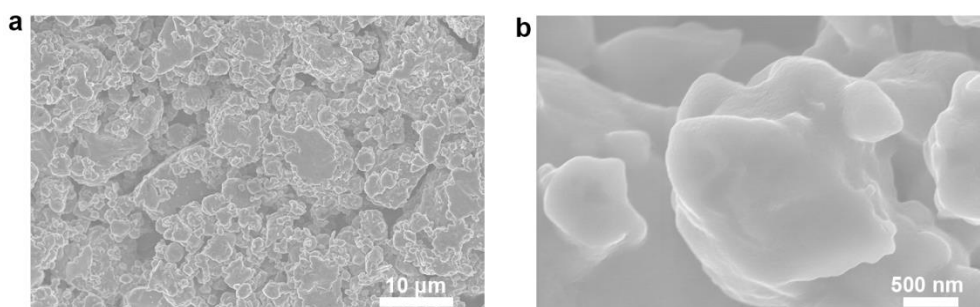


Figure 8-S4. (a,b) SEM image of LSPS at different magnifications.

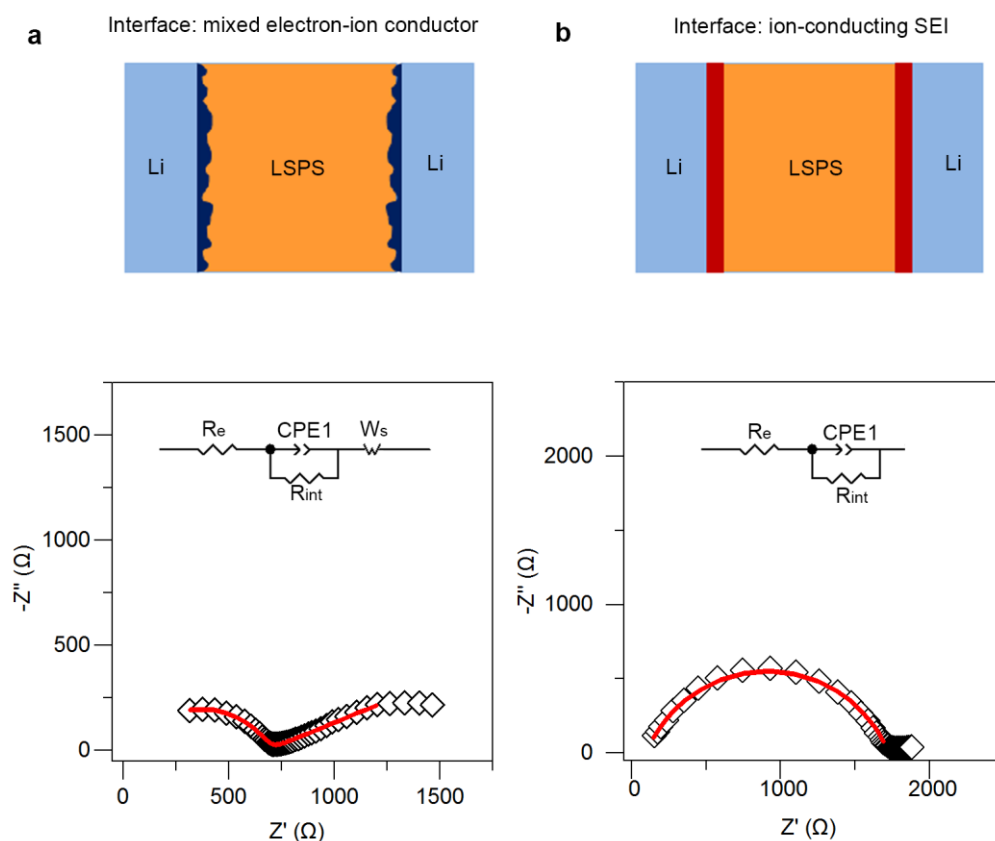


Figure 8-S5. Two typical EIS spectra of Li symmetric cells, in which mixed electron-ion conductor interface (a) dominates the interfacial resistance or ion-conducting SEI interface (b) determines the interfacial resistance. SEI is an acronym for solid electrolyte interphase.

In the case of Li/LSPS/Li cells, the Nyquist plot is characterized by a high-frequency semicircle and a finite-length Warburg impedance at low frequencies. These characteristics are typical for mixed ion-electron conductor (MCI, an acronym for mixed conductor interphases), which is usually described by an equivalent circuit as an inset in Figure S4(a). The $R_{int}||CPE1$ element describes the high-frequency semicircle and represents the parallel migration of ions and electrons in the MCI layer and dielectric capacitance of the MCI layer. The finite-length Warburg impedance W_s (Warburg short) describes the formation of Li^+ and e^- diffusion layer in the MCI layer due to the blocking of electrons by the bulk phase of SE.[3, 4]

In contrast, the representative Nyquist plot of Li/alucone/LSPS/alucone/Li is dominated by a single large semicircle, which is typical for a formation of ion-conducting SEI (SEI, an acronym for solid electrolyte interphase) at the interface between LSPS and Li. The corresponding equivalent circuits are shown in Figure S4(b), in which $R_{int}||CPE1$ element represents the ion migration in the SEI layer and dielectric capacitance of the SEI layer.[3, 4]

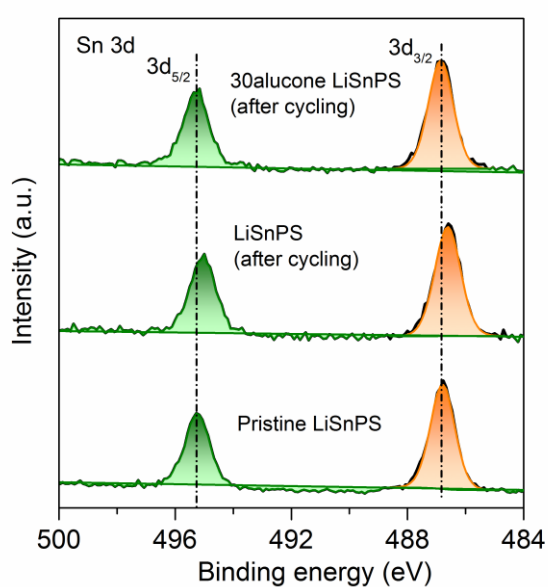


Figure 8-S6. XPS spectra of Sn 3d for LSPS pellets after 25 cycles. The Sn 3d spectra exhibited spin-orbit doublet peaks at 486.76 eV ($\text{Sn}^{4+}3d_{5/2}$) and 495.22 eV ($\text{Sn}^{4+} 3d_{3/2}$).

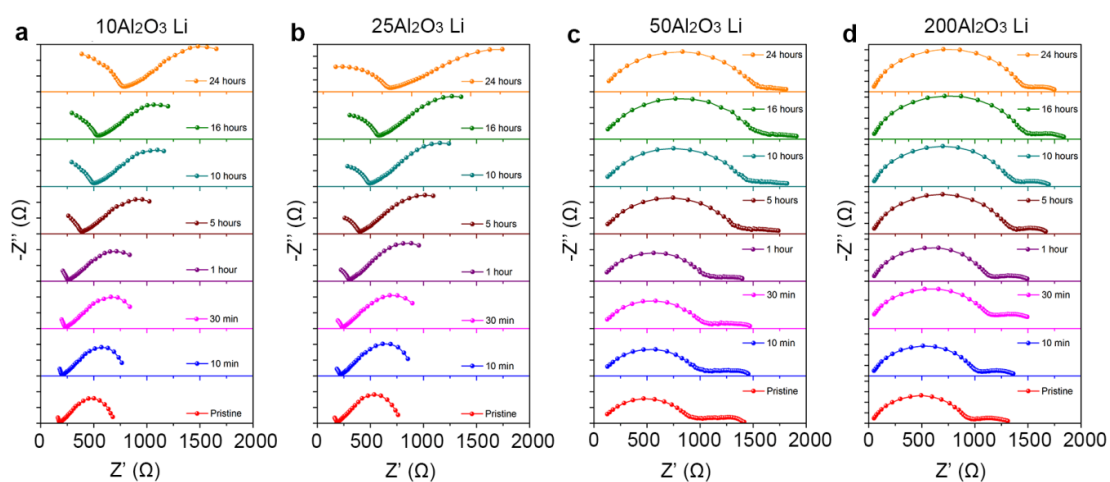


Figure 8-S7. Electrochemical impedance spectra of Li symmetric cells. (A) Time-dependent EIS spectra of bare $10\text{Al}_2\text{O}_3$ Li-LSPS-Li. (B) Time-dependent EIS spectra of $25\text{Al}_2\text{O}_3\text{Li}$ -LSPS-Li. (C) Time-dependent EIS spectra of $25\text{Al}_2\text{O}_3$ Li-LSPS-Li. (D) Time-dependent EIS spectra of $200\text{Al}_2\text{O}_3$ Li-LSPS-Li.

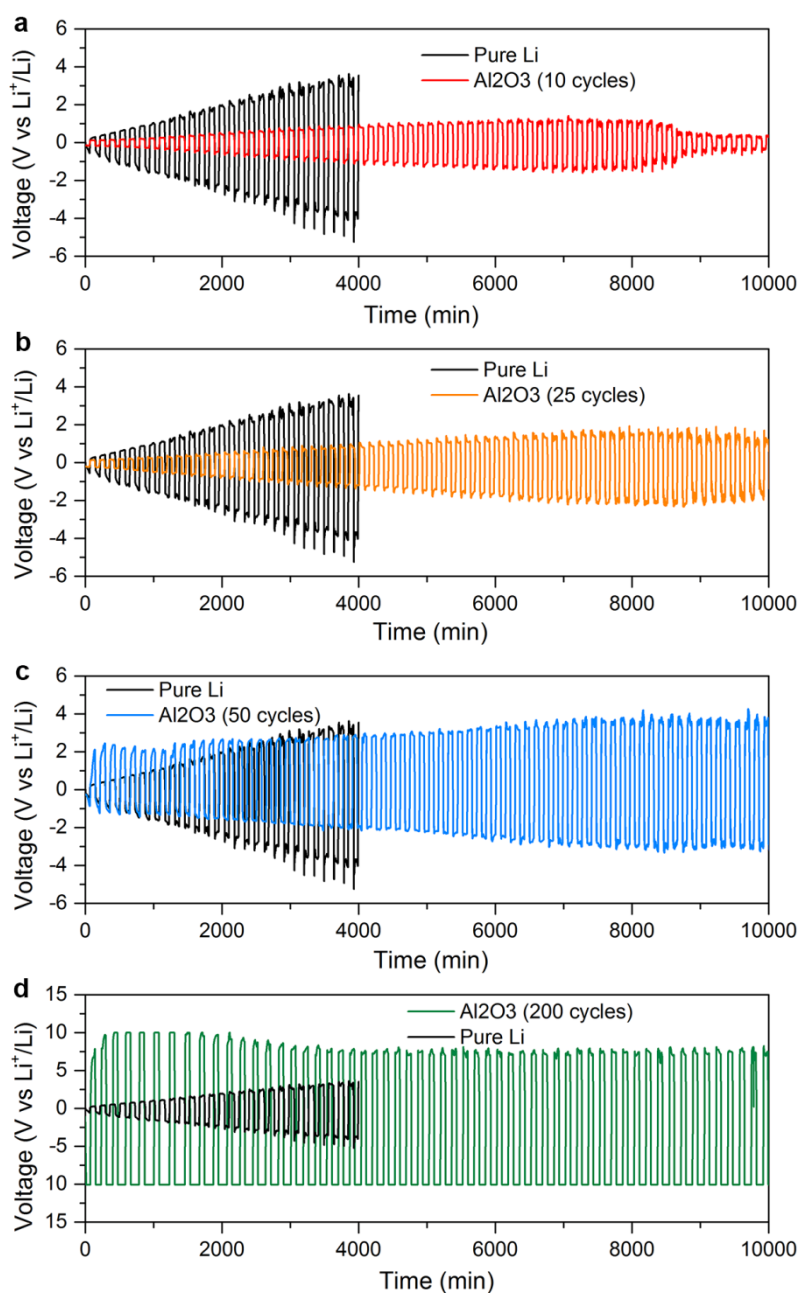


Figure 8-S8. Electrochemical performance of Li symmetric cells. (a) Comparison of the cycling stability between the Li with 10Al₂O₃ (10Al₂O₃ Li) and the bare Li foil at a current density of 0.1 mA cm⁻². (b) Comparison of the cycling stability between the Li with 25Al₂O₃ (25Al₂O₃ Li) and the bare Li foil at a current density of 0.1 mA cm⁻². (c) Comparison of the cycling stability between the Li with 50Al₂O₃ (50Al₂O₃ Li) and the bare Li foil at a current density of 0.1 mA cm⁻². (d) Comparison of the cycling stability

between the Li with 200Al₂O₃ (200Al₂O₃ Li) and the bare Li foil at a current density of 0.1 mA cm⁻². The total areal capacity corresponding to the plating/stripping of Li is 0.1 mAh cm⁻².

References

- [1] Z. Yang, G.L. V., S. Qian, L. Xia, L. Andrew, W. Biqiong, L. Ruying, D. Fang, C. Mei, S. Xueliang, *Small Methods*, 0 (2018) 1700417.
- [2] Y. Zhao, L.V. Goncharova, Q. Zhang, P. Kaghazchi, Q. Sun, A. Lushington, B. Wang, R. Li, X. Sun, *Nano Lett.*, 17 (2017) 5653-5659.
- [3] J. Jamnik, J. Maier, S. Pejovnik, *Electrochimica Acta*, 44 (1999) 4139-4145.
- [4] P. Bron, B. Roling, S. Dehnen, *J. Power Sources*, 352 (2017) 127-134.

Chapter 9

9. Solid-State Plastic Crystal Electrolytes: Effective Protection Interlayers for Sulfide-based All-Solid-State Lithium Metal Batteries*

Following the success of the inorganic-organic hybrid coating layer at the anode interface. In this work, a solid-state plastic crystal electrolyte (PCE) was engineered as an interlayer in SE-based ASSLMBs. It is demonstrated that the PCE interlayer can prevent interfacial reactions and lithium dendrite formation between SEs and Li metal. As a result, ASSLMBs with LiFePO_4 exhibit a high initial capacity of 148 mAh.g^{-1} at 0.1 C and 131 mAh.g^{-1} at 0.5 C ($1\text{C}=170 \text{ mA.g}^{-1}$), which remains at 122 mAh.g^{-1} after 120 cycles at 0.5C . All-solid-state Li-S batteries based on the polyacrylonitrile-sulfur composite are also demonstrated, showing an initial capacity of 1682 mAh.g^{-1} . The second discharge capacity of 890 mAh.g^{-1} keeps at 775 mAh.g^{-1} after 100 cycles. This work provides a new avenue to address the interfacial challenges between Li metal and SEs, enabling the successful adoption of Li metal in sulfide-based all-solid-state lithium metal batteries with high energy density.

***Note:** This work has been published in **Advanced Functional Materials**

Changhong Wang, Keegan R Adair, Jianwen Liang, Xiaona Li, Yipeng Sun, Xia Li, Jiwei Wang, Qian Sun, Feipeng Zhao, Xiaoting Lin, Ruying Li, Huan Huang, Li Zhang, Rong Yang, Shigang Lu, Xueliang Sun, Solid - State Plastic Crystal Electrolytes: Effective Protection Interlayers for Sulfide - Based All - Solid - State Lithium Metal Batteries, **Advanced Functional Materials**. 2019, 29, 1900392

9.1 Introduction

With the rapid development of electric vehicles and large-scale energy storage systems, batteries with improved safety and high energy density are in great demand. In terms of the conventional lithium-ion battery (LIB), it falls short of the requirements of safety and high energy density due to the combustible nature and limited electrochemical window of organic electrolytes.^[1] Under these circumstances, all-solid-state lithium batteries based on a solid electrolyte have been proposed.^[1a, 2] Taking into account the intrinsic properties of inorganic solid-state electrolytes, such as the inflammability and wide electrochemical windows (0~5V),^[3] all-solid-state lithium batteries are believed to be an excellent candidate for the future energy storage system that requires the high energy density and high safety.^[2b] Over the past decades, significant achievements have been made in solid-state electrolytes with high ionic conductivity, such as sulfide electrolytes (SEs),^[4] oxide electrolytes,^[5] polymer electrolytes,^[6] and hybrid electrolytes.^[7] So far, the ionic conductivity of solid-state electrolytes can reach up to $10^{-3} \sim 10^{-2}$ S/cm. In particular, the ionic conductivity of SEs represented by $\text{Li}_{9.54}\text{Si}_{1.74}\text{P}_{1.44}\text{S}_{11.7}\text{Cl}_{0.3}$ (2.5×10^{-2} S.cm⁻¹),^[4] $\text{Li}_{10}\text{GeP}_2\text{S}_{12}$ (1.2×10^{-2} S.cm⁻¹),^[3] and $\text{Li}_{10.35}[\text{Sn}_{0.27}\text{Si}_{1.08}]\text{P}_{1.65}\text{S}_{12}$ (1.1×10^{-2} S.cm⁻¹)^[8] can rival that of commercial liquid electrolytes (1.02×10^{-2} S.cm⁻¹).^[9] However, the huge interfacial resistance, originating from the inferior solid-solid contact and significant interfacial reactions at both cathode and anode interfaces, restricts the electrochemical performance of all-solid-state lithium batteries.^[10] To address the cathode interface issues, various strategies have been proposed over the past years, for example, using soluble SEs to coat on active materials to increase the electrode-electrolyte contact area,^[11] adding some ionic liquids to enhance the ionic contact,^[12] and using a buffer layer to suppress the interfacial reactions, such as $\text{Li}_4\text{Ti}_5\text{O}_{12}$ ^[13] and LiNbO_3 .^[14] In a sharp contrast to the great progress on the cathode interface, little progress has been made on the anode interface, especially using lithium

(Li) metal as the anode, because the challenges at the interface between Li metal and SEs are very difficult to address, such as the remarkable interfacial reactions, Li dendrite formation, and volume change. Until now, only a few all-solid-state lithium batteries based on the Li metal anode (namely, all-solid-state lithium metal batteries, ASSLMBs) has been demonstrated.^[15] In view of the high theoretical specific capacity (3860 mAh.g⁻¹) and low reduction potential (-3.040 V) of Li metal,^[2b] enabling Li metal as the anode in all-solid-state lithium batteries is a must, especially for achieving high energy density over 400 Wh. Kg⁻¹^[16]

Solid-state plastic crystal electrolytes (PCE) have long been known for their high room-temperature ionic conductivity.^[17] It has also been demonstrated that succinonitrile (SN)-based on PCE possess good thermal stability and nonflammability, which shows a great promise as a safe electrolyte.^[18] In addition, using the SN as an additive in conventional carbonate electrolytes can improve the thermal stability of LIBs.^[19] Inspired by these good properties, the SN-based PCE was engineered as an interlayer to resolve the instability of SEs against Li metal, enabling the successful adoption of Li metal anodes in all-solid-state lithium batteries. Besides, the chemical compatibility between SEs and PCE guarantees the long-term cycling stability of ASSLMBs. As a proof of concept, ASSLMBs based on LiFePO₄ exhibit a high initial capacity of 148 mAh.g⁻¹ at 0.1 C and 131 mAh.g⁻¹ at 0.5 C (1C=170 mA.g⁻¹), which remains 122 mAh.g⁻¹ after 120 cycles at 0.5C. Furthermore, all-solid-state lithium-sulfur (Li-S) batteries based on Li metal and polyacrylonitrile-sulfur composites present an initial capacity of 1682 mAh.g⁻¹, a second discharge capacity of 890 mAh.g⁻¹ and capacity retention of 775 mAh.g⁻¹ after 100 cycles. The decay rate of the specific capacity is as low as 0.14%. This demonstration provides a new avenue to address the interfacial challenges between Li metal and SEs, enabling the successful adoption of Li metal anodes in SE-based ASSLMBs.

9.2 Experimental Section

9.2.1 Preparation of Plastic Crystal Electrolytes

Plastic crystal electrolytes (PCE) were made with 5 mol% LiTFSI (lithium bis(trifluoromethanesulfonyl)imide, Sigma Aldrich, 99.95%) in succinonitrile (Alfa Aesar, 98%) at 60°C. In addition, 2 wt% additives LiNO₃ was added to stabilize the Li metal interface. Then the mixture was cooled down to room temperature. To get a PCE pellet, glass fiber was used as host and emerged into PCE at 60°C, and then cooling down to room temperature to get a solid-state PCE pellet. The thickness of the PCE pellets is 300 μm (Figure S15). The ionic conductivity of PCE was measured with stainless steel as a current collector. Li₁₀GeP₂S₁₂ was purchased from MSE supplies. To evaluate the ionic conductivity of LGPS, 100 mg LGPS was pelletized under 350 MPa. The thickness of the LGPS pellets is 500 μm (Figure S13). Indium foils were used as current collectors.

9.2.2 Electrochemical Measurements

Electrochemical impedance analysis was performed on a biologic electrochemical station with a frequency range from 7MHz to 0.1 Hz with an amplitude of 20 mV. To fabricate solid-state lithium-ion batteries, LiFePO₄ and Li₁₀GeP₂S₁₂ and acetylene black were thoroughly mixed in an agate mortar with a weight ratio of 60:34:6. 80 mg Li₁₀GeP₂S₁₂ was pelletized under 150 MPa with a home-made mold cell. Then 10 mg cathode composites were spread on one side of the Li₁₀GeP₂S₁₂ pellet and pressed under 350 MPa for 2 min. A piece of Li foil was polished and put on another side of the Li₁₀GeP₂S₁₂ pellet and pressed under 50MPa. To make solid-state lithium-sulfur batteries, polyacrylonitrile-sulfur (PAN-S) composites were synthesized following the same method in our previous reports.[24] Then PAN-S composites were mixed with

LGPS in an agate mortar with a weight ratio of 50:50, then using the same method as making solid-state lithium-ion batteries to make all-solid-state Li-S batteries. For comparison, a PCE pellet was added at the interface between LGPS and Li metal. To improve the ionic contact between LGPS and active materials, 50~100 μL PCE was added into the cathode composites. ASSLMBs were tested by a LAND system from 2.5 V to 4.1 V at room temperature. All-solid-state Li-S batteries were tested by the LAND system from 1.0 V to 3.0V at room temperature.

9.2.3 Characterizations

XRD patterns were recorded using a Bruker D8 diffractometer, using Cu $K\alpha$ radiation. XPS was recorded using Thermo Scientific ESCALAB 250Xi with Al $K\alpha$ -radiation. The pressure in the analysis chamber was typically 2×10^{-9} torr during acquisition. For probing the LGPS change on the LGPS-Li interface after cycling, we scratched LGPS powder from Li metal after cycling. For probing the LGPS change on the LGPS-PCE-Li after cycling, the LGPS pellets were taken out from the cell after cycling. Raman spectra were collected using a laser with a wavelength of 532 nm. Morphology was examined by Scanning electron microscopy (SEM) using a Hitachi S-4800 operated at 5 kV accelerating voltage. X-ray absorption spectroscopy was done in Canadian Light Source with an energy range of 1.7 ~ 10 keV.

9.3 Results and Discussion

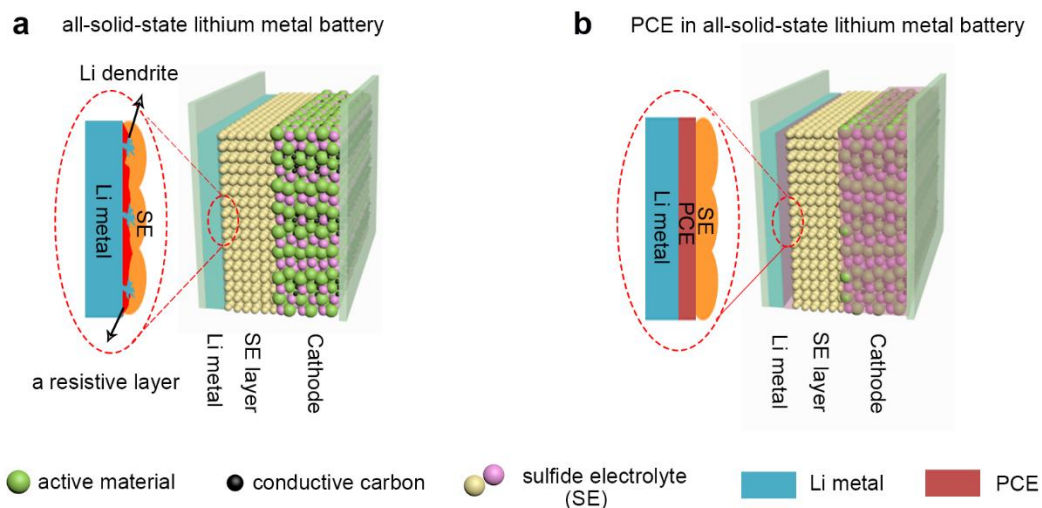


Figure 9-1 (a) Schematic diagram of ASLMBs. (b) Schematic diagram of ASLMBs with the PCE interlayer.

Figure 9-1a shows the schematic diagram of SE-based ASLMBs. If Li metal directly contacts SEs, thermodynamically, SEs are easily reduced by Li metal, forming highly resistive interphase, which blocks the Li^+ transport across the interface,^[20] as circled in Figure 1a. Using the PCE as an interlayer, the interfacial reactions between SEs and Li metal can be avoided by preventing the direct contact between SEs and Li metal. As long as the PCE is stable against SEs and Li metal, ASLMBs can be successfully achieved (Figure 1b). At the cathode side, point-to-point contact can be also improved by submerging the cathode in a PCE matrix, thus forming a continuous three-dimensional Li^+ conduction pathway.

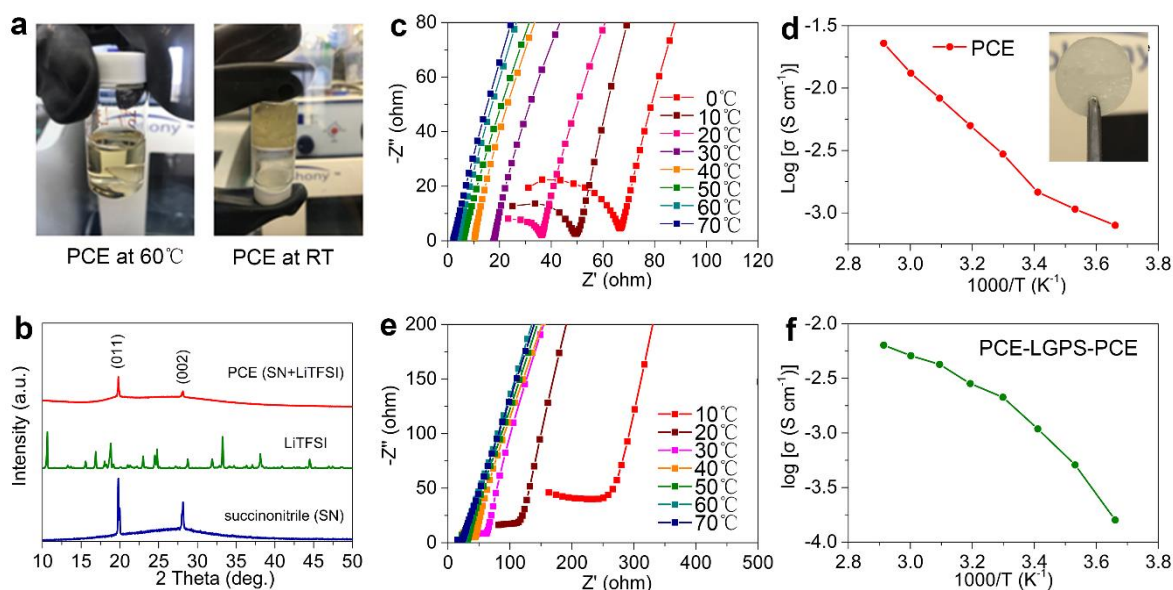


Figure 9-2 (a) Photographs of PCE (5 mol% LiTFSI in SN) at 60 °C (left) and room temperature (right), (b) XRD patterns of SN, LiTFSI, and PCE. (c) EIS spectra of PCE. (d) Arrhenius plot of PCE. The insert is the photo of the laminated PCE. (e) EIS spectra of PCE-LGPS-PCE composite electrolytes. (f) Arrhenius plot of PCE-LGPS-PCE composite electrolytes.

To make the solid-state PCE, 5 mol% lithium bis(trifluoromethanesulfonyl)imide (LiTFSI) was added into SN. Based on the differential scanning calorimetry (DSC) curves of pristine SN (Figure S1), the melting point of SN is 55°C. The SN become a liquid-like solution when heating to 60 °C and the LiTFSI salt was completely dissolved (**Figure 9-2a**). When cooling down to room temperature, SN-based PCE becomes a solid electrolyte as the melting point of as-prepared PCE is 36 °C (**Figure 9-S1**). The X-ray diffraction (XRD) peaks of LiTFSI are not shown in the XRD pattern of PCE, suggesting the LiTFSI was completely dissolved into the SN matrix (**Figure 9-2b**). The two sharp XRD peaks of PCE are originated from the long-range ordered structure of SN molecules.^[21] **Figure 9-2c** shows the electrochemical impedance spectra (EIS) of PCEs at various temperatures. It can be seen that the impedance decreases as the temperature increases, as shown by the Arrhenius plot of PCEs in Figure 2d. The ionic conductivity

of PCEs reaches $1.47 \times 10^{-3} \text{ S.cm}^{-1}$ at $20 \text{ }^\circ\text{C}$. $\text{Li}_{10}\text{GeP}_2\text{S}_{12}$ (LGPS) was chosen as a typical representative of sulfide electrolytes in this study. The ionic conductivity of LGPS at room temperature is $2.76 \times 10^{-3} \text{ S.cm}^{-1}$ (**Figure 9-S2**) and the particle size of LGPS is around several micrometers (**Figure 9-S3**). The room temperature ionic conductivity of the PCE-LGPS-PCE composite electrolyte is $2.12 \times 10^{-3} \text{ S.cm}^{-1}$ (**Figure 9-2e, 9-2f**), showing the negligible decrease in conductivity of the overall solid-state electrolytes.

The chemical compatibility between LGPS and PCE was further investigated. As detected by Raman spectroscopy (**Figure 9-S4a**), the characteristic peaks of LGPS were unchanged after submerging LGPS in SN for 24 hours, indicating that the LGPS is chemically stable against SN. Furthermore, XRD was performed to evaluate the phase stability of LGPS in SN (**Figure 9-S4b**). No new peaks are present in the XRD patterns of LGPS after emerging the LGPS pellet in PCE for 24 hours. In addition, there is no significant change in the ionic conductivity within 24 hours, which is confirmed by the time-dependent EIS measurement (**Figure 9-S5**).

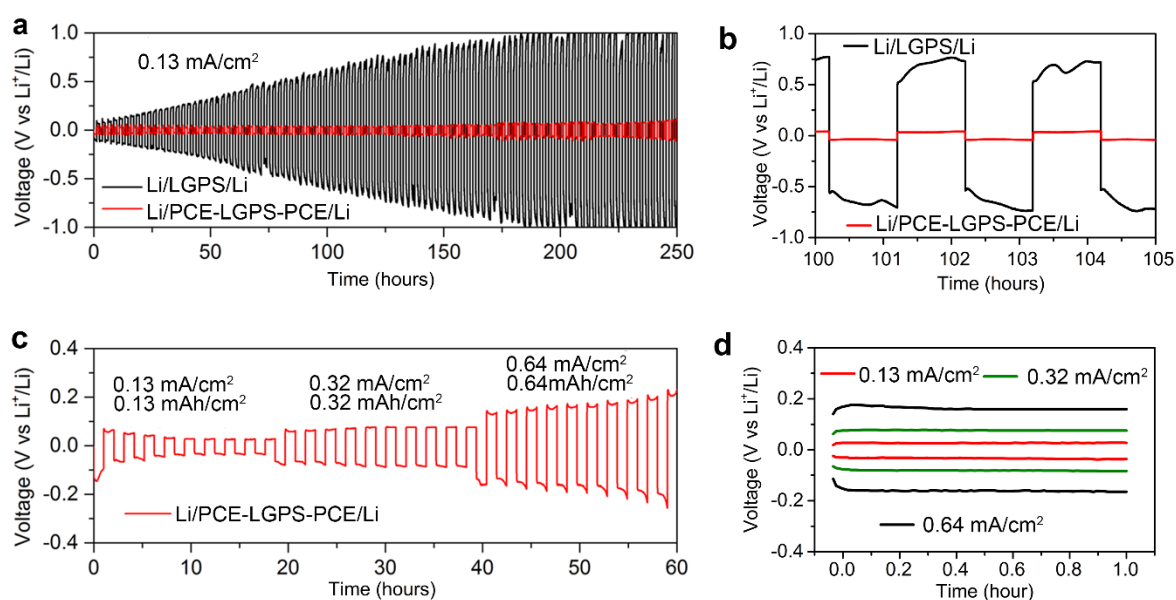


Figure 9-3 Overpotential of the Li⁺ plating/stripping of Li symmetric cells. (a) Li/LGPS/Li and Li/PCE-LGPS-PCE/Li at 0.13 mA.cm⁻². (b) Voltage profile comparison from 100 to 105 hours. (c) rate-performance of Li/PCE-LGPS-PCE/Li at various current densities from 0.13 to 0.64 mA.cm⁻². (d) Typical voltage profiles at different current density.

The interfacial stability of LGPS against Li metal was evaluated by symmetric cells. **Figure 9-3a** compares the Li⁺ plating/stripping behaviors of Li/LGPS/Li and Li/PCE-LGPS-PCE/Li symmetric cells within 250 hours at 0.13 mA.cm⁻². After 50 cycles, the over-potential of Li/LGPS/Li is 750 mV, while the overpotential of Li/PCE-LGPS-PCE/Li remains at 40 mV (**Figure 9-3b**). The results confirm that using the PCE as the interlayer between Li metal and LGPS can suppress significant interfacial reactions between LGPS and Li metal. Furthermore, the Li⁺ plating/stripping behavior of Li/PCE-LGPS-PCE/Li at various current density with the corresponding areal capacity is shown in **Figure 9-3c**. It can be seen that Li/PCE-LGPS-PCE/Li shows stable cycling performance even at 0.64 mA.cm⁻² with an areal capacity of 0.64 mAh.cm⁻². **Figure 9-3d** displays the Li⁺ stripping and plating curves at different current densities. The over-potentials of Li/PCE-LGPS-PCE/Li cells are 85 mV and 160 mV under the current densities of 0.32 mA.cm⁻² and 0.64 mA.cm⁻², respectively. It should be mentioned that the rate performance of the symmetrical Li/PCE-LGPS-PCE/Li cells outperforms the most results from previous studies,^[15b, 15d, 15e, 22] as listed in the **Table 9-S1**. In addition, the PCE interlayer can also suppress the Li dendrite formation in the glass-ceramic Li₂S-P₂S₅ solid electrolytes (**Figure 9-S6**). In addition, the interfacial compatibility between PCE and Li metal was improved by the introduction of additives LiNO₃, which was confirmed by SEM, FT-IR, EIS, and XPS characterizations (**Figure 9-S7,9- S8, 9-S9, and 9-S10**).

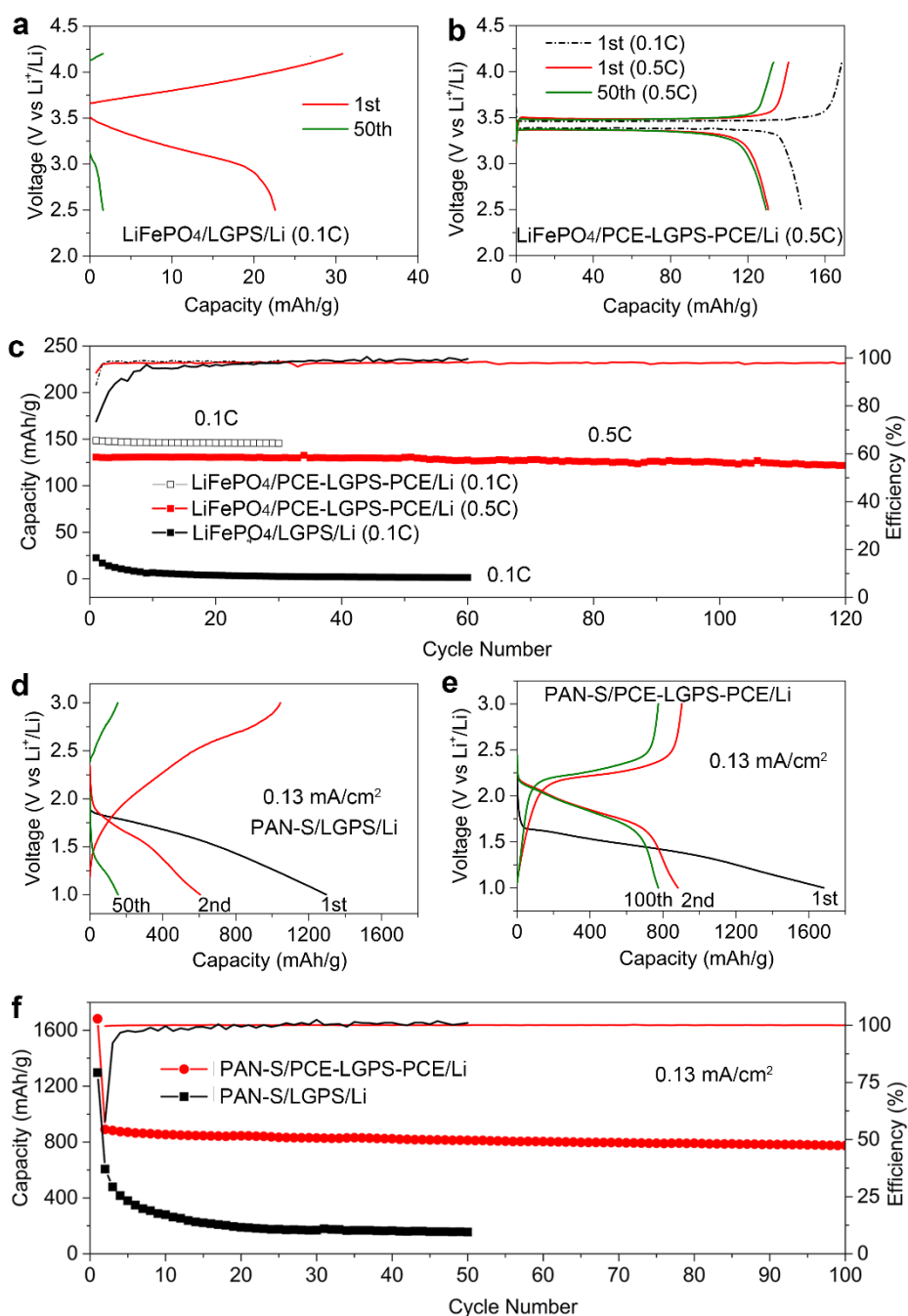


Figure 9-4 Electrochemical performances of ASSLMBs. (a) Charge-discharge curves of $\text{LiFePO}_4/\text{LGPS}/\text{Li}$ at 0.1C. (b) Charge-discharge curves of $\text{LiFePO}_4/\text{PCE-LGPS-PCE}/\text{Li}$ at 0.1C and 0.5C. (c) Cycle stabilities of $\text{LiFePO}_4/\text{LGPS}/\text{Li}$ at 0.1C and $\text{LiFePO}_4/\text{PCE-LGPS-PCE}/\text{Li}$ at 0.5C. (d) Charge-discharge curves of $\text{PAN-S}/\text{LGPS}/\text{Li}$ at $0.13 \text{ mA}/\text{cm}^2$. (e) Charge-discharge curves of $\text{PAN-S}/\text{PCE-LGPS-PCE}/\text{Li}$ at $0.13 \text{ mA}/\text{cm}^2$. (f) Cycle stabilities of $\text{PAN-S}/\text{PCE-LGPS-PCE}/\text{Li}$ and $\text{PAN-S}/\text{LGPS}/\text{Li}$ at $0.13 \text{ mA}/\text{cm}^2$.

curves of PAN-S/PCE-LGPS-PCE/Li at 0.13 mA.cm⁻². (f) Cycle stabilities of PAN-S/LGPS/Li and PAN-S/PCE-LGPS-PCE/Li at 0.13 mA.cm⁻².

To demonstrate the adoption of Li metal in SE-based all-solid-state lithium batteries, LiFePO₄ was chosen as the cathode material for this study. The cathode was fabricated by mixing LiFePO₄, LGPS, and carbon additives with a weight ratio of 60:34:6. Further details can be found in the Experimental Section. Without the PCE interlayer, the LiFePO₄ electrode exhibits a very low capacity of 22 mAh.g⁻¹ and large polarization even at a small C-rate of 0.1C (1C=170 mA.g⁻¹) (**Figure 9-4a**). Besides, the capacity drops very fast in the initial 10 cycles. The reason is believed to be the serious interfacial reactions between LGPS and Li metal and inferior solid-solid contact between SEs and LiFePO₄.^[11a, 20c] To eliminate the interference of solid-solid contact in the cathode composites, we also added some PCE in cathode composites to ensure good ionic contacts between LiFePO₄ and SEs.^[23] With the PCE interlayer, the LiFePO₄ electrode shows the typical charge-discharge curves of LiFePO₄ at 0.1C and 0.5C with negligible polarization. The high initial capacity is as high as 148 mAh.g⁻¹ at 0.1C and 131 mAh.g⁻¹ at 0.5 C (**Figure 9-4b**), indicating that LiFePO₄ electrodes are well infiltrated with PCE, thus forming a continuous Li⁺ conduction pathway. Figure 9-4c exhibits the comparison of the cycling performance of ASSLMB with and without PCE. With the PCE interlayer, the capacity of LiFePO₄ is 120 mAh.g⁻¹ after 120 cycles, suggesting that interfacial reactions between LGPS and Li metal are completely suppressed. In addition, the good chemical compatibility between PCE and LGPS also guarantees long-term cycling stability.

The Li metal anode is also an essential component in high-energy-density Li-S batteries. Here we also demonstrated the all-solid-state Li-S batteries with polyacrylonitrile-sulfur (PAN-S) composites. The reason for choosing PAN-S as the cathode materials is that PAN-S does not show the notorious shuttle effect of polysulfides upon cycling,^[24] thus

eliminate the effect of lithium polysulfides. The particle size of PAN-S is around 300 nm (**Figure 9-S11**). The cycling stability of PAN-S was first evaluated with liquid carbonate electrolytes,^[24] presenting excellent stability at 0.25C ($1C=1672 \text{ mA.g}^{-1}$) (**Figure 9-S12**). **Figure 9-4d** shows the typical charge-discharge curves of PAN-S composites at a current density of 0.13 mA.cm^{-2} . Obviously, the polarization between charge-discharge curves is phenomenal and the capacity decays very fast, which is likely due to the inferior contact between PAN-S and LGPS.^[25] In addition, PAN-S particles have a severe aggregation phenomenon (**Figure 9-S11**), which is not beneficial for dry mixing with LGPS particles when making a cathode composite. As a comparison, using PCE to fill the porous structure of the cathode, the polarization of the charge-discharge plateau become much smaller (**Figure 9-4e**). In addition, the initial discharge capacity is 1682 mAh.g^{-1} , indicating all the PAN-S particles are surrounded with PCE electrolytes. The discharge capacity from the second cycle is 890 mAh.g^{-1} and remains at 775 mAh.g^{-1} after 100 cycles (**Figure 9-4f**). The cycling stability is much more stable than PAN-S/LGPS/Li.

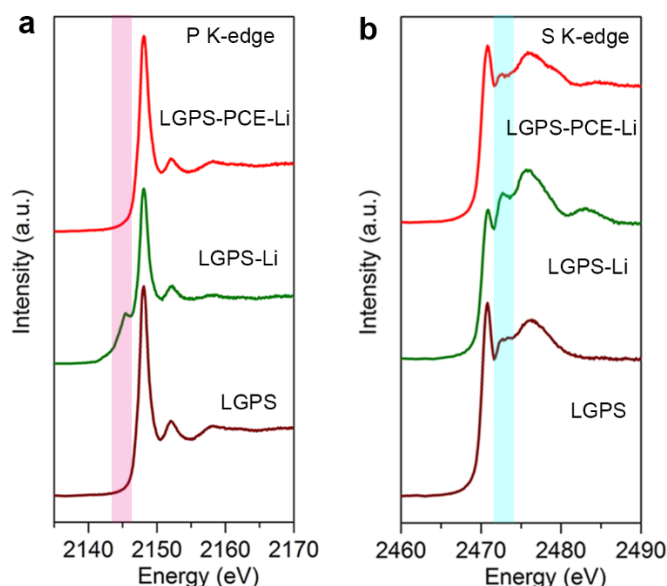


Figure 9-5 X-ray absorption spectra of LGPS, LGPS on the Li surface after cycling, and LGPS with the PCE interlayer after cycling, respectively. (a) P K-edge spectra. (b) S K-edge spectra.

To analyze the interface between LGPS and Li metal, the ASSLMs were disassembled after cycling. LGPS was analyzed by synchrotron-based X-ray absorption spectroscopy (XAS). Both P K-edge and S K-edge are analyzed. Interestingly, the P K-edge of LGPS-Li interface exhibits a small peak at 2140 eV, which is ascribed to the reduction of phosphorus by Li metal (**Figure 9-5a**).^[20b] In the S K-edge of LGPS-Li (**Figure 9-5b**), the characteristic peaks Li_2S were enhanced after cycling, comparing to the standard Li_2S (**Figure 9-S13**). By contrast, with PCE as an interlayer, the P K-edge and S K-edge show no change after cycling, which suggests that the reduction of LGPS by Li metal could be prevented by using PCE as an interlayer. In addition, there are no addition peaks detected, again showing that LGPS should be stable against PCE, which is consistent with the Raman and XRD results discussed above.

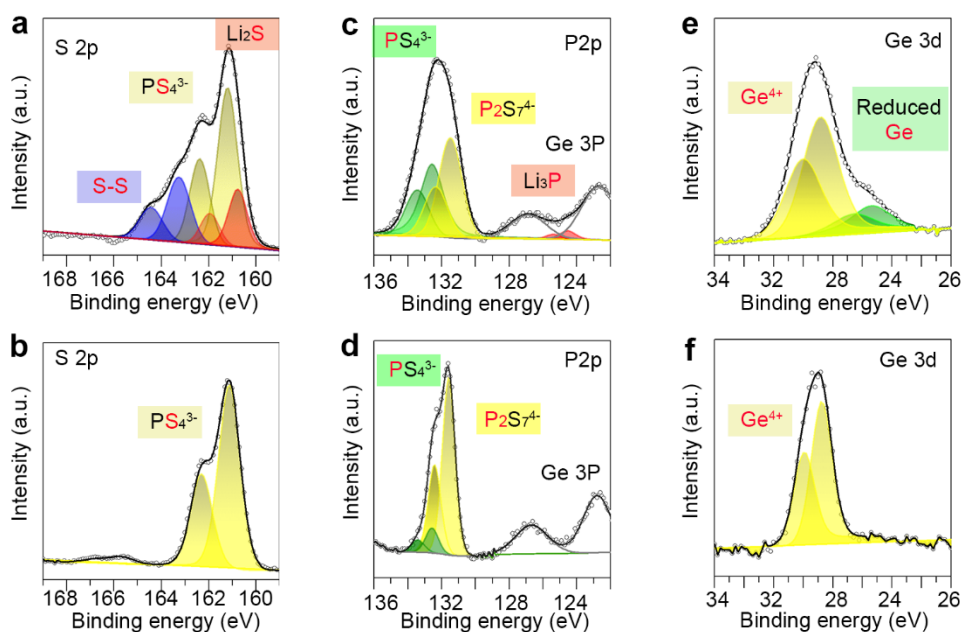


Figure 9-6 X-ray photoelectron spectroscopy of the LGPS on the Li surface after cycling (a, c, e) and the LGPS with the PCE interface after cycling (b, d, f), respectively. (a, b) S 2p spectra. (c,d) P 2p spectra. (e,f) Ge 3d spectra.

Furthermore, XPS was performed to inspect the interfacial reactions between LGPS and Li metal. **Figure 9-6a** exhibits the S 2p spectra of the LGPS-Li interface after cycling, where the peak at 160.8 eV can be assigned to Li_2S .^[20b, 26], indicating that the sulfur of LGPS is reduced by Li metal. In addition, a pair of peaks at 163.2 eV was detected, which is resulted from the structural evolution of LGPS during cycling.^[27] In comparison, LGPS-PCE-Li only presents a PS_4^{3-} peaks at 161.02eV (**Figure 9-6b**), which is exactly the same as the S 2p spectra of pristine LGPS (Figure S14), indicating that LGPS does not undergo any structural and/or valency-state changes when using PCE as an interlayer. P 2p spectra were analyzed. It should be noted that the P 2p peaks of reduced phosphorus species (e.g. Li_3P) are overlapped with the peaks of Ge 3p, which may interfere with the identification of reduced phosphorus compounds (**Figure 9-6c**).^[20a, 20c, 28] XPS spectra of Ge 3d of LGPS-Li and LGPS-PCE-Li after cycling are also investigated (**Figure 9-6e** and **Figure 9-6f**). Ge at the LGPS-Li interface was reduced by Li metal after cycling, while Ge^{4+} was well kept in the LGPS-PCE-Li interface. These results prove that LGPS was decomposed into Li_2S , reduced P, and reduced Ge during the cycling if directly contacting with Li metal.^[20c] The decomposition or reduction of LGPS by Li metal can be prevented by adopting the PCE interlayer, enabling the successful adoption of Li metal in high-energy-density all-solid-state lithium batteries.

9.4 Conclusion

In summary, we report a PCE interlayer to address the interface challenge between sulfide electrolytes and Li metal, leading to significant progress towards achieving high-energy-density ASSLMs. Using the PCE as an interlayer at the interface between

Li metal and SEs, the significant interfacial reactions between SEs and Li metal are suppressed. As a result, ASSLMs based on Li metal and LiFePO_4 exhibit a high initial capacity of 148 mAh.g^{-1} at 0.1 C and 131 mAh.g^{-1} at 0.5 C ($1\text{C}=170 \text{ mA.g}^{-1}$), which remains 122 mAh.g^{-1} after 120 cycles at 0.5C. In addition, all-solid-state Li-S batteries based on polyacrylonitrile-sulfur composites are also demonstrated, showing an initial capacity of 1682 mAh.g^{-1} . The second discharge capacity of 890 mAh.g^{-1} , which keeps at 775 mAh.g^{-1} after 100 cycles. The decay rate of the specific capacity is as low as 0.14%. This work provides a new strategy to address interfacial challenges between Li metal and sulfide electrolytes, enabling the successful adoption of Li metal anodes in all-solid-state lithium batteries toward next-generation safe and high-energy-density energy storage systems.

9.5 Acknowledgments

This work was supported by Natural Sciences and Engineering Research Council of Canada (NSERC), Canada Research Chair Program (CRC), China Automotive Battery Research Institute, Canada Foundation for Innovation (CFI), the Canada Light Source at University of Saskatchewan (CLS) and University of Western Ontario.

9.6 References

- [1] aJ. W. Choi, D. Aurbach, *Nat. Rev. Mater.* **2016**, *1*, 16013; bA. Manthiram, X. Yu, S. Wang, *Nat. Rev. Mater.* **2017**, *2*, 16103.
- [2] aG. Zhonghui, S. Huabin, F. Lin, Y. Fangliang, Z. Yi, L. Wei, H. Yunhui, *Adv. Mater.* **2018**, *30*, 1705702; bD. Lin, Y. Liu, Y. Cui, *Nat Nano* **2017**, *12*, 194-206; cJ. Janek, W. G. Zeier, *Nature Energy* **2016**, *1*, 16141.
- [3] N. Kamaya, K. Homma, Y. Yamakawa, M. Hirayama, R. Kanno, M. Yonemura, T. Kamiyama, Y. Kato, S. Hama, K. Kawamoto, A. Mitsui, *Nat. Mater.* **2011**, *10*, 682-686.
- [4] Y. Kato, S. Hori, T. Saito, K. Suzuki, M. Hirayama, A. Mitsui, M. Yonemura, H. Iba, R. Kanno, *Nat. Energy* **2016**, *1*, 16030.
- [5] F. Han, J. Yue, C. Chen, N. Zhao, X. Fan, Z. Ma, T. Gao, F. Wang, X. Guo, C. Wang, *Joule* **2018**, *2*, 497-508.
- [6] L. Yue, J. Ma, J. Zhang, J. Zhao, S. Dong, Z. Liu, G. Cui, L. Chen, *Energy Storage Mater.* **2016**, *5*, 139-164.
- [7] W. Liu, S. W. Lee, D. Lin, F. Shi, S. Wang, A. D. Sendek, Y. Cui, *Nat. Energy* **2017**, *2*, 17035.
- [8] Y. Sun, K. Suzuki, S. Hori, M. Hirayama, R. Kanno, *Chem. Mater.* **2017**, *29*, 5858-5864.
- [9] K. Xu, *Chem. Rev.* **2004**, *104*, 4303-4418.
- [10] aP. K. Ho, B. Qiang, K. D. Hyeon, O. D. Yang, Z. Yizhou, M. Yifei, J. Y. Seok, *Adv. Energy Mater.* **2018**, *0*, 1800035; bC. Wang, Q. Sun, Y. Liu, Y. Zhao, X. Li, X. Lin, M. N. Banis, M. Li, W. Li, K. R. Adair, D. Wang, J. Liang, R. Li, L. Zhang, R. Yang, S. Lu,

X. Sun, *Nano Energy* **2018**, *48*, 35-43; cR. C. Xu, X. H. Xia, S. Z. Zhang, D. Xie, X. L. Wang, J. P. Tu, *Electrochimica Acta* **2018**, *284*, 177-187; dJ. Liang, X. Li, Y. Zhao, L. V. Goncharova, G. Wang, K. R. Adair, C. Wang, R. Li, Y. Zhu, Y. Qian, L. Zhang, R. Yang, S. Lu, X. Sun, *Adv. Mater.* **2018**, *30*, 1804684; eL. Fan, S. Wei, S. Li, Q. Li, Y. Lu, *Adv. Energy Mater.* **2018**, *8*, 1702657.

[11]aK. H. Park, D. Y. Oh, Y. E. Choi, Y. J. Nam, L. Han, J.-Y. Kim, H. Xin, F. Lin, S. M. Oh, Y. S. Jung, *Adv. Mater.* **2016**, *28*, 1874-1883; bD. H. Kim, D. Y. Oh, K. H. Park, Y. E. Choi, Y. J. Nam, H. A. Lee, S.-M. Lee, Y. S. Jung, *Nano Lett.* **2017**, *17*, 3013-3020; cY. E. Choi, K. H. Park, D. H. Kim, D. Y. Oh, H. R. Kwak, Y.-G. Lee, Y. S. Jung, *ChemSusChem* **2017**, *10*, 2605-2611.

[12]D. Y. Oh, Y. J. Nam, K. H. Park, S. H. Jung, S.-J. Cho, Y. K. Kim, Y.-G. Lee, S.-Y. Lee, Y. S. Jung, *Adv. Energy Mater.* **2015**, *5*, 1500865.

[13]Y. Seino, T. Ota, K. Takada, *J. Power Sources* **2011**, *196*, 6488-6492.

[14]aN. Ohta, K. Takada, L. Zhang, R. Ma, M. Osada, T. Sasaki, *Adv. Mater.* **2006**, *18*, 2226-2229; bN. Ohta, K. Takada, I. Sakaguchi, L. Zhang, R. Ma, K. Fukuda, M. Osada, T. Sasaki, *Electrochem Commun.* **2007**, *9*, 1486-1490.

[15]aG. Liu, D. Xie, X. Wang, X. Yao, S. Chen, R. Xiao, H. Li, X. Xu, *Energy Storage Mater.* **2018**; bC. Wang, Y. Zhao, Q. Sun, X. Li, Y. Liu, J. Liang, X. Li, X. Lin, R. Li, K. R. Adair, L. Zhang, R. Yang, S. Lu, X. Sun, *Nano Energy* **2018**, *53*, 168-174; cX. Li, J. Liang, X. Li, C. Wang, J. Luo, R. Li, X. Sun, *Energy Environ. Sci.* **2018**; dZ. Zhang, S. Chen, J. Yang, J. Wang, L. Yao, X. Yao, P. Cui, X. Xu, *ACS Appl. Mater. Interfaces* **2017**, *10*, 2556-2565; eY. Gao, D. Wang, Y. C. Li, Z. Yu, T. E. Mallouk, D. Wang, *Angew. Chem. Int. Ed.* **2018**, *57*, 13608-13612.

- [16] J. Betz, G. Bieker, P. Meister, T. Placke, M. Winter, R. Schmuch, *Adv. Energy Mater.* **2018**, *0*, 1803170.
- [17] aM. D. R., F. M., *Adv. Mater.* **2001**, *13*, 957-966; bP.-J. Alarco, Y. Abu-Lebdeh, A. Abouimrane, M. Armand, *Nat. Mater.* **2004**, *3*, 476-481; cL. Z. Fan, Y. S. Hu, A. J. Bhattacharyya, J. Maier, *Adv. Funct. Mater.* **2007**, *17*, 2800-2807.
- [18] aH.-J. Ha, E.-H. Kil, Y. H. Kwon, J. Y. Kim, C. K. Lee, S.-Y. Lee, *Energy Environ. Sci.* **2012**, *5*, 6491-6499; bK. H. Choi, S. J. Cho, S. H. Kim, Y. H. Kwon, J. Y. Kim, S. Y. Lee, *Adv. Funct. Mater.* **2014**, *24*, 44-52; cL. Jin, P. C. Howlett, J. M. Pringle, J. Janikowski, M. Armand, D. R. MacFarlane, M. Forsyth, *Energy Environ. Sci.* **2014**, *7*, 3352-3361.
- [19] Y.-S. Kim, T.-H. Kim, H. Lee, H.-K. Song, *Energy Environ. Sci.* **2011**, *4*, 4038-4045.
- [20] aK. N. Wood, K. X. Steirer, S. E. Hafner, C. Ban, S. Santhanagopalan, S.-H. Lee, G. Teeter, *Nat. Commun.* **2018**, *9*, 2490; bS. Wenzel, S. J. Sedlmaier, C. Dietrich, W. G. Zeier, J. Janek, *Solid State Ion.* **2018**, *318*, 102-112; cS. Wenzel, S. Randau, T. Leichtweiß, D. A. Weber, J. Sann, W. G. Zeier, J. Janek, *Chem. Mater.* **2016**, *28*, 2400-2407.
- [21] Q. Wang, H. Fan, L.-Z. Fan, Q. Shi, *Electrochimica Acta* **2013**, *114*, 720-725.
- [22] Z. Zhang, Y. Zhao, S. Chen, D. Xie, X. Yao, P. Cui, X. Xu, *J. Mater. Chem. A* **2017**, *5*, 16984.
- [23] aX. Han, Y. Gong, K. Fu, X. He, G. T. Hitz, J. Dai, A. Pearse, B. Liu, H. Wang, G. Rubloff, Y. Mo, V. Thangadurai, E. D. Wachsman, L. Hu, *Nat. Mater.* **2017**, *16*, 572-579; bK. Fu, Y. Gong, B. Liu, Y. Zhu, S. Xu, Y. Yao, W. Luo, C. Wang, S. D. Lacey, J. Dai, Y. Chen, Y. Mo, E. Wachsman, L. Hu, *Sci. Adv.* **2017**, *3*, e1601659.

- [24]H. Chen, C. Wang, C. Hu, J. Zhang, S. Gao, W. Lu, L. Chen, *J. Mater. Chem. A* **2015**, *3*, 1392-1395.
- [25]Y. Ito, S. Yamakawa, A. Hayashi, M. Tatsumisago, *J. Mater. Chem. A* **2017**, *5*, 10658-10668.
- [26]H. Chen, C. Wang, W. Dong, W. Lu, Z. Du, L. Chen, *Nano Lett.* **2015**, *15*, 798-802.
- [27]aJ. Auvergniot, A. Cassel, J.-B. Ledeuil, V. Viallet, V. Seznec, R. Dedryvère, *Chem. Mater.* **2017**, *29*, 3883-3890; bT. Hakari, M. Deguchi, K. Mitsuhara, T. Ohta, K. Saito, Y. Orikasa, Y. Uchimoto, Y. Kowada, A. Hayashi, M. Tatsumisago, *Chem. Mater.* **2017**, *29*, 4768-4774.
- [28]S. Wenzel, D. A. Weber, T. Leichtweiss, M. R. Busche, J. Sann, J. Janek, *Solid State Ion.* **2016**, *286*, 24-33.

9.7 Supporting Information

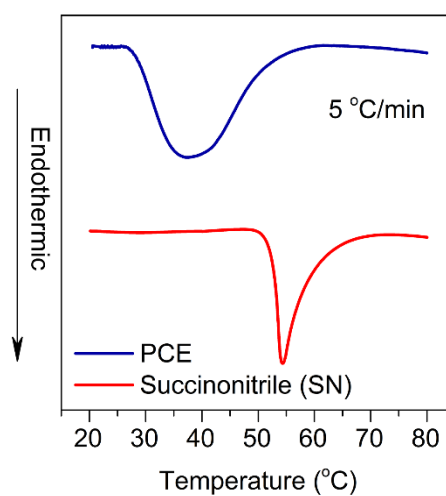


Figure 9-S1. DSC curves of succinonitrile (SN) and as-prepared PCE. The melting point of succinonitrile (SN) is 55°C, while that of as-prepared PCE is 36°C, which is still higher than ambient temperature (20~25°C).

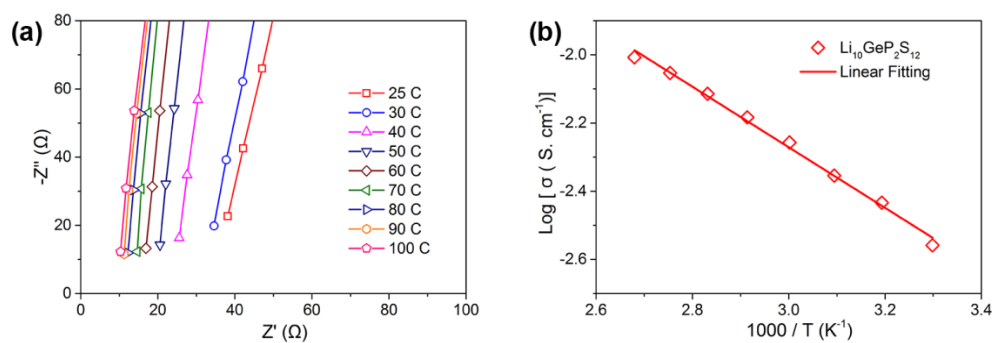


Figure 9-S2. (a) EIS Spectra of LGPS pellets with a thickness of 1 μm at various temperatures. (b) The Arrhenius plot of LGPS pellets. The room temperature ionic conductivity of LGPS is $2.76 \times 10^{-3} \text{ S}\cdot\text{cm}^{-1}$.

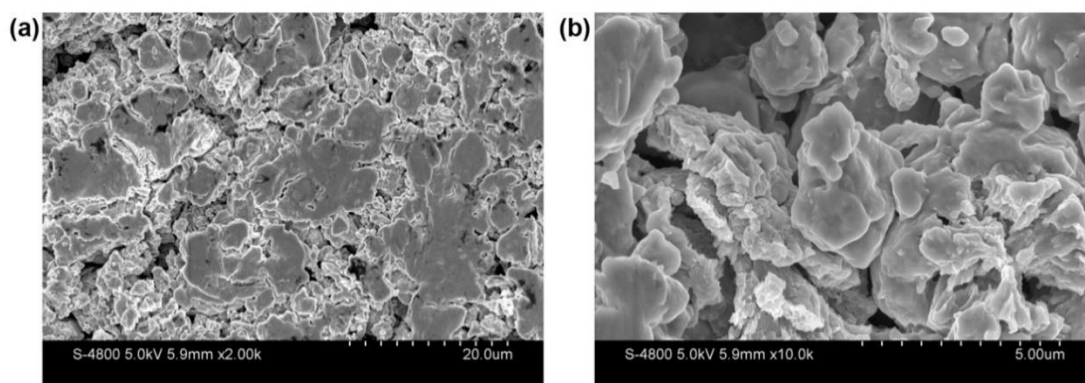


Figure 9-S3. (a,b) SEM image of LGPS at different magnifications.

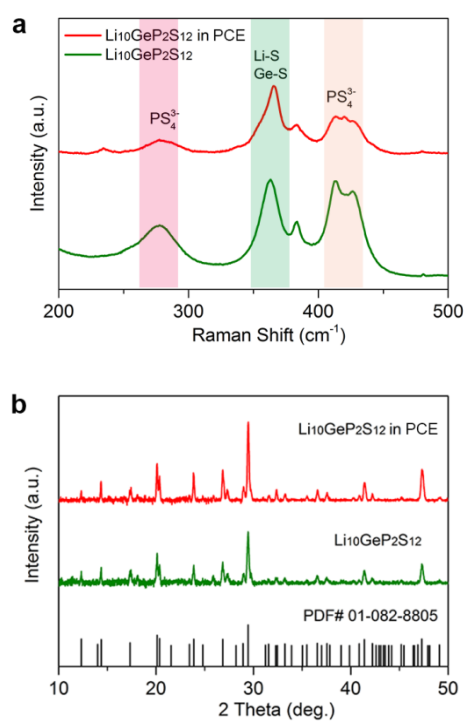


Figure 9-S4. (a) Raman spectra of LGPS and LGPS in PCE after 24 hours. (b) XRD pattern of LGPS and LGPS in PCE after 24 hours.

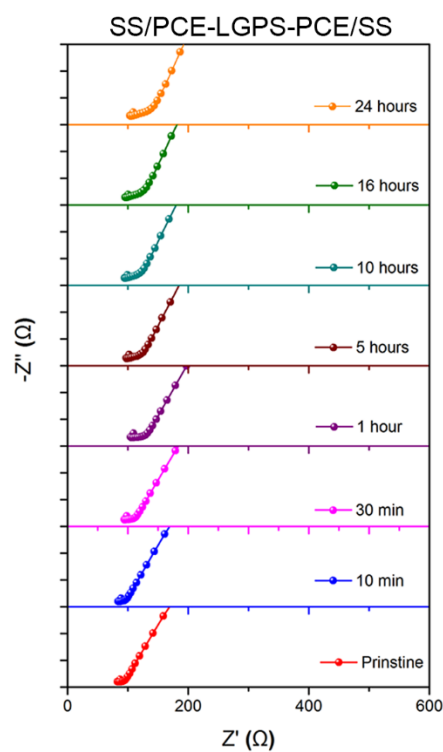


Figure 9-S5. The time-dependent EIS spectra of SS/PCE-LGPS-PCE/SS within 24 hours. SS stands for the stainless-steel current collector.

Table 9-S1. The comparison of the electrochemical performance of symmetric cells.

Current density (mA.cm ⁻²)	Cycling Capacity (mAh.cm ⁻²)	Polarization voltage (mV)	Solid Electrolyte	Reference
0.1	0.1	~500 mV	<i>Li₁₀SnP₂S₁₂</i>	<i>Nano Energy</i> , 2018 , 53, 168-174. ^[1]
0.1	0.05	50 mV	<i>Li₁₀GeP₂S₁₂</i>	<i>ACS Appl. Mater. Interfaces</i> 2017 , 10, 2556-2565. ^[2]
0.1	0.2	57 mV	<i>Li₁₀GeP₂S₁₂</i>	<i>Angew. Chem. Int. Ed.</i> 2018,

				57, 13608-13612. ^[3]
0.1	0.1	50 mV	$Li_{10}GeP_2S_{12}$ (at 60 °C)	J. Mater. Chem. A 2017, 5, 16984. ^[4]
0.13	0.13	50~60 mV	$Li_{10}GeP_2S_{12}$	This work
0.64	0.64	100 ~ 150 mV		

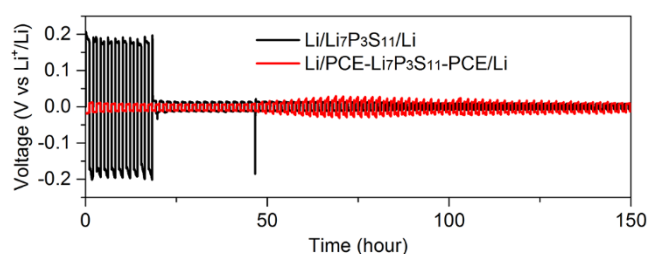


Figure 9-S6 Li^+ plating/stripping behavior of $Li/Li_7P_3S_{11}/Li$ and $Li/PCE-Li_7P_3S_{11}-PCE/Li$ symmetric cells at a current density of $0.13 \text{ mA}\cdot\text{cm}^{-2}$ with an areal capacity of $0.13 \text{ mAh}\cdot\text{cm}^{-2}$.

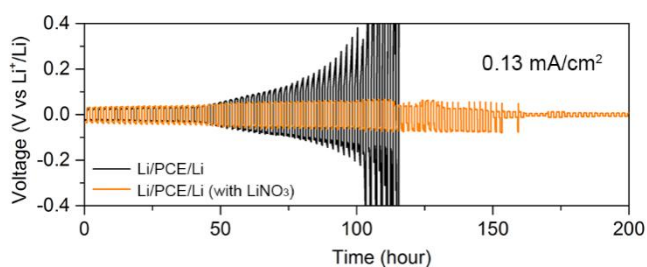


Figure 9-S7 Li^+ plating/stripping behavior of $Li/PCE/Li$ and Li/PCE (with $LiNO_3$)/ Li symmetric cells at a current density of $0.13 \text{ mA}\cdot\text{cm}^{-2}$ with an areal capacity of $0.13 \text{ mAh}\cdot\text{cm}^{-2}$.

The over-potential of Li/PCE/Li symmetrical cells increases after 45 hours, which hints that there are interfacial reactions between SN and Li metal, forming a resistive layer at the Li metal interface.^[5] Interestingly, when a trace amount of LiNO₃ was introduced into the PCE, the over-potential for Li⁺ plating/stripping remains stable upon cycling, indicating that LiNO₃ additives can stabilize the interface between SN and Li metal.

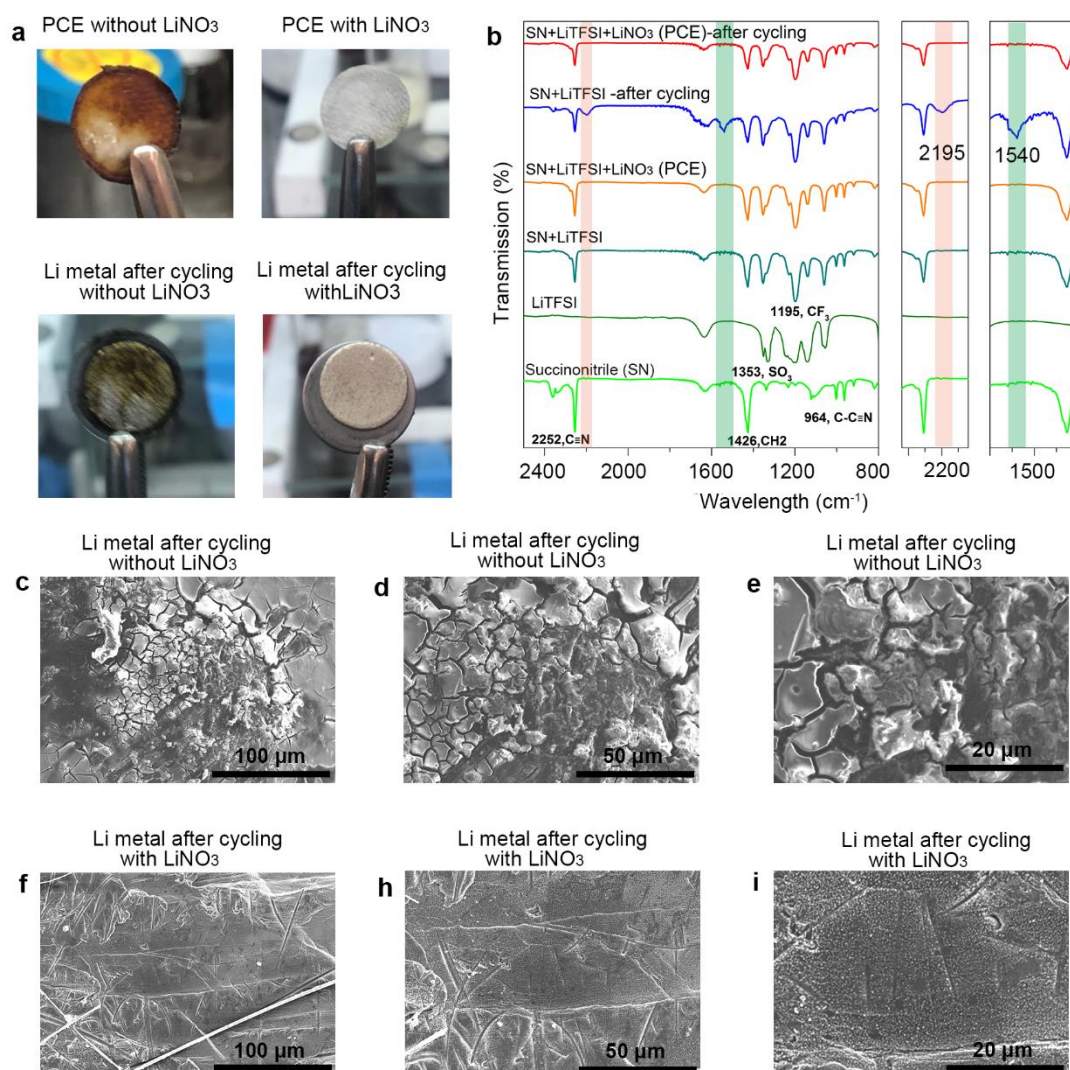


Figure 9-S8. (a) The photo of PCE and Li metal after 20 cycles. (b) FT-IR spectra of pristine SN, LiTFSI, SN+LiTFSI, SN+LiTFSI+LiNO₃ (PCE), SN+LiTFSI layer after 20 cycles, and SN+LiTFSI+LiNO₃ (PCE) layer after 20 cycles. (c, d, e) SEM images of Li metal surface without LiNO₃ additives after 20 cycles. (f, h, i) SEM images of Li metal

surface with LiNO₃ additives after 20 cycles.

To understand the interfacial stability between PCE and Li metal, the post-cycling analysis was conducted. As detected by EIS (Figure S9a, S9b), the interfacial resistance of Li/SN+LiTFSI/Li after cycling increases to over 10000 ohms. By contrast, the interfacial resistance of Li/SN+LiTFSI+LiNO₃/Li is around 420 ohms (Figure S9c,d), suggesting that SN+LiTFSI with LiNO₃ is compatible with Li metal. What is more, the color of the PCE layer without LiNO₃ and Li metal surface was changed significantly after cycling (**Figure 9-S8a**), which is due to the corrosion reactions or the polymerization of nitriles catalyzed by Li metal.^[5-6] Amazingly, the color of the PCE layer with LiNO₃ and Li metal surface after cycling were remained, suggesting that the LiNO₃ can stabilize the interface between Li metal and PCE. Considering that the SN is an organic molecule (N≡C-CH₂-CH₂-C≡N), Fourier-transform infrared spectroscopy (FT-IR) is a good technique to characterize the interface change. As revealed in **Figure 9-S8b**, 963 cm⁻¹ (C-CN, gauche), 1004 cm⁻¹ (CH₂, gauche), 1426 cm⁻¹ (CH₂, stretching, *trans*), and 2254 cm⁻¹ (C≡N stretching, gauche and *trans*) are observed, which is from the SN molecules and well in accordance with previously reported results.^[7] For the pure LiTFSI, the typical peaks of SO₃ and CF₃ are shown at 1356 cm⁻¹ and 1195 cm⁻¹, respectively.^[8] PCE spectrum is combined with that of pristine SN and LiTFSI, and no additional peaks are detected, suggesting that there are no chemical reactions between SN, LiTFSI, and LiNO₃. However, there are two new peaks (2195 cm⁻¹ and 1540 cm⁻¹) observed in the PCE layer without LiNO₃ after cycling, which are associated with the corrosion reactions or the polymerization of nitriles at the interface. Interestingly, these two peaks do not show up in PCE layers after cycling when adding LiNO₃ additives, confirming that the interfacial reactions between Li metal and SN can be suppressed by the addition of LiNO₃. Furthermore, SEM was performed to check the morphology of the Li metal surface after cycling. Without the LiNO₃ additives, the Li metal surface shows a lot of cracks and mossy Li dendrites after cycling, as shown in **Figure 9-S8(c, d)**,

e), Interestingly, Li metal surface is very smooth and covered by a lot of small particles when adding LiNO_3 into PCE **Figure 9-S8(f, h, i)**, which is associated with the uniform deposition of Li.^[9] Furthermore, X-ray photoelectron spectroscopy (XPS) results that solid electrolyte interphase was formed on the Li metal surface after cycling, which is consisted of organic compounds and lithium salts (**Figure 9-S10**). These results undoubtedly demonstrated that the interfacial reactions between SN and Li metal can be suppressed by the formation of a passivation layer on the Li metal surface.

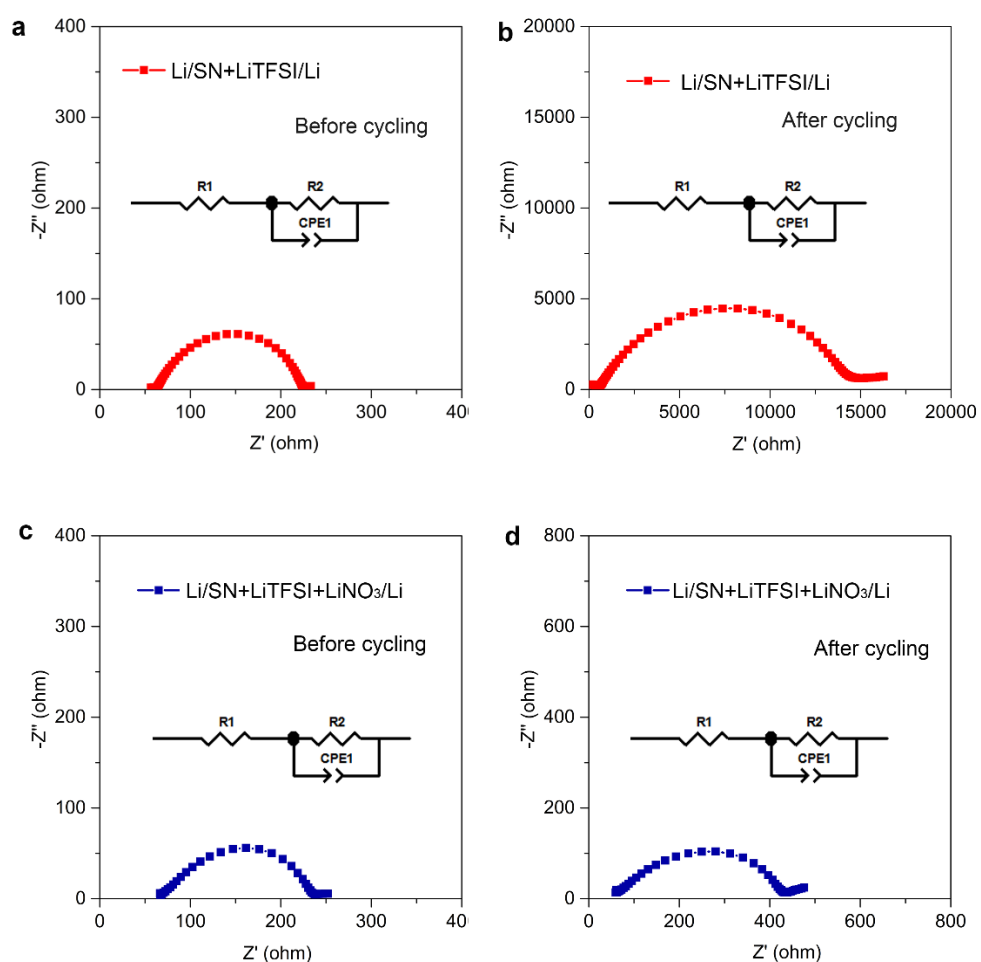


Figure 9-S9 EIS spectra of Li/SN+LiTFSI/Li symmetric cells without LiNO₃ additives before cycling (a) and after cycling 100 hours (b). EIS spectra of Li/PCE/Li symmetric cells with LiNO₃ additives before cycling (c) and after 100 hours (d).

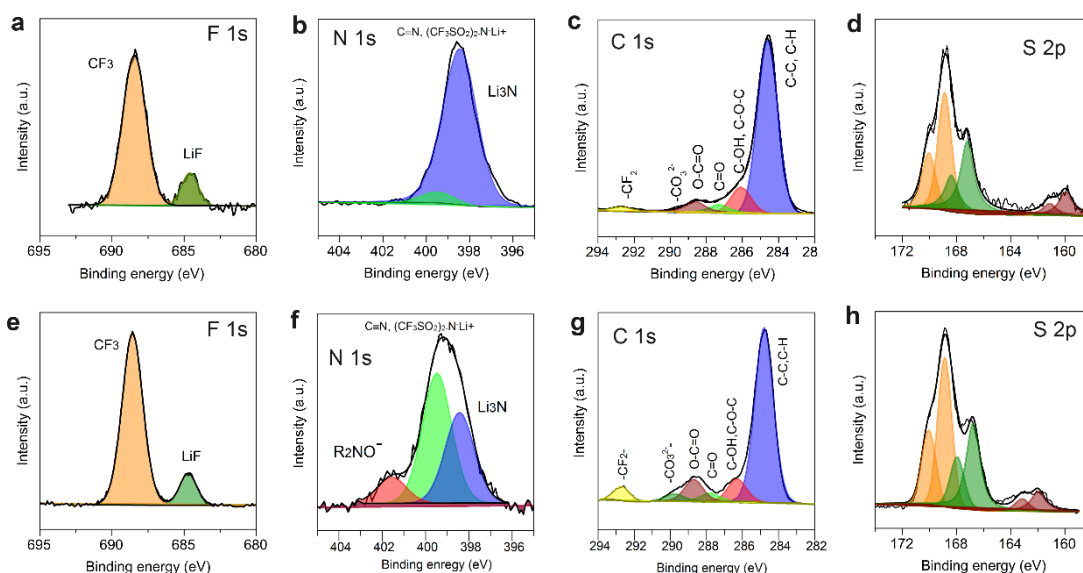
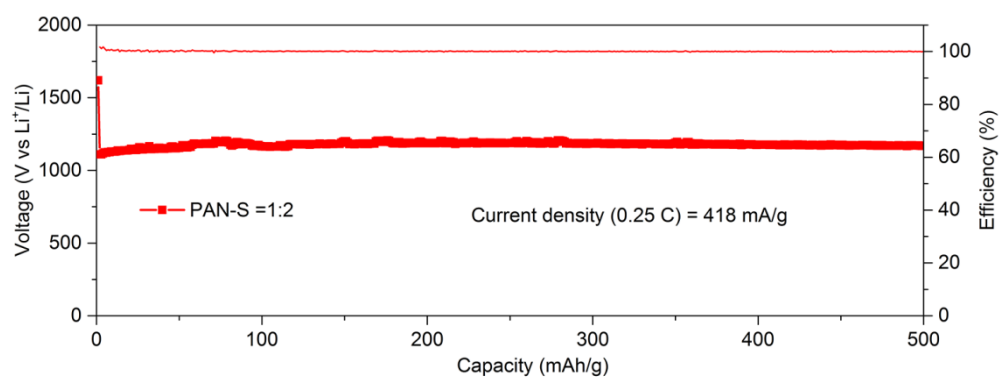
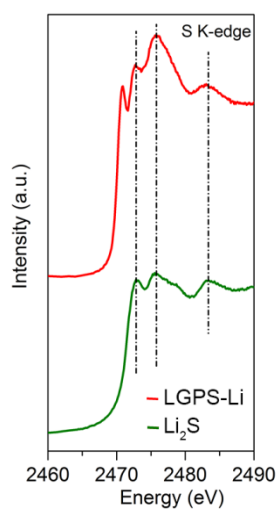


Figure 9-S10 XPS spectra of F 1s, N 1s (b), C 1s (c), and S 2p. (a-d) Li metal against the PCE without LiNO₃ after cycling. (e-h) Li metal against the PCE with LiNO₃ additives after cycling. Obviously, the SEI layer consists of inorganic lithium salts and organic compounds. Comparing the N 1s spectra, R₂NO⁻ compounds are formed on the Li metal surface when adding LiNO₃, which is due to the reactions between Li metal and LiNO₃^[10].



Figure 9-S11 SEM image of PAN-S composites.**Figure 9-S12** Cyclability of PAN-S(1:2) at the current density of 418 mA.g⁻¹ (0.25C).**Figure 9-S13** XAS spectra of commercial Li₂S powder and Li-LGPS-Li interface after cycling.

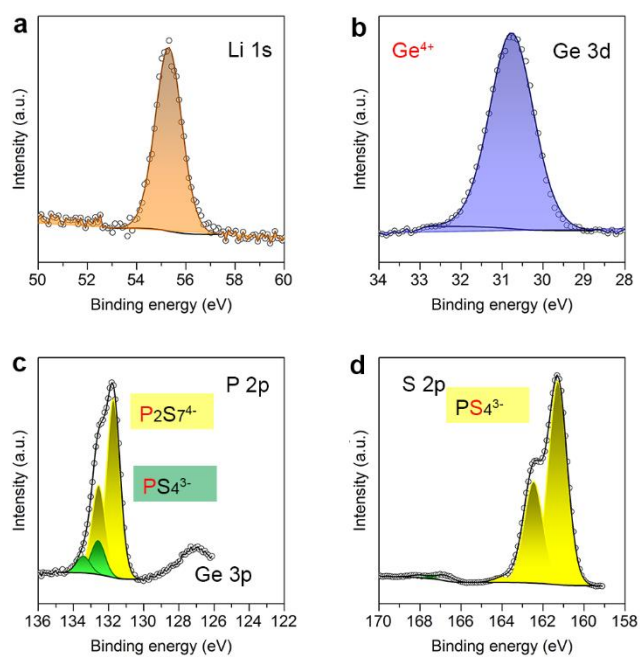


Figure 9-S14 The XPS spectra of pristine $\text{Li}_{10}\text{GeP}_2\text{S}_{12}$. (a) Li 1s. (b) Ge 3d. (c) P 2p. (d) S 2p.

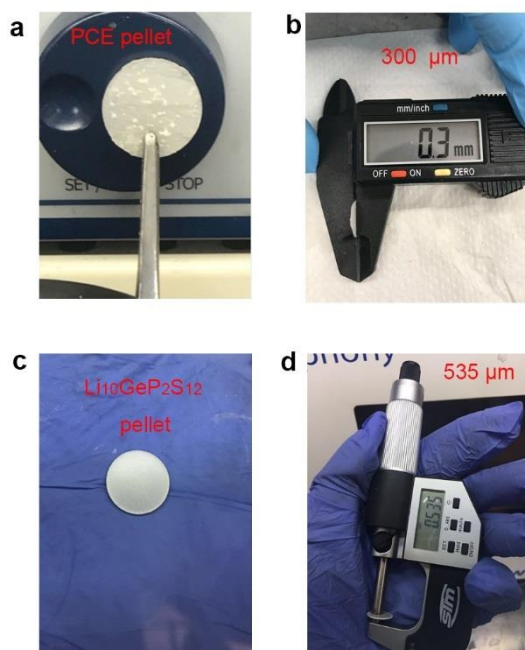


Figure 9-S15. (a) Image of PCE pellets. (b) The thickness measurement of the PCE layer.

(c) the image of $\text{Li}_{10}\text{GeP}_2\text{S}_{12}$ pellets. (d) the thickness measurement of $\text{Li}_{10}\text{GeP}_2\text{S}_{12}$ pellets.

References

- [1] C. Wang, Y. Zhao, Q. Sun, X. Li, Y. Liu, J. Liang, X. Li, X. Lin, R. Li, K. R. Adair, L. Zhang, R. Yang, S. Lu, X. Sun, *Nano Energy* **2018**, *53*, 168-174.
- [2] Z. Zhang, S. Chen, J. Yang, J. Wang, L. Yao, X. Yao, P. Cui, X. Xu, *ACS Appl. Mater. Interfaces* **2017**, *10*, 2556-2565.
- [3] Y. Gao, D. Wang, Y. C. Li, Z. Yu, T. E. Mallouk, D. Wang, *Angew. Chem. Int. Ed.* **2018**, *57*, 13608-13612.
- [4] Z. Zhang, Y. Zhao, S. Chen, D. Xie, X. Yao, P. Cui, X. Xu, *J. Mater. Chem. A* **2017**, *5*, 16984.
- [5] Q. Zhang, K. Liu, F. Ding, W. Li, X. Liu, J. Zhang, *ACS Appl. Mater. Interfaces* **2017**, *9*, 29820-29828.
- [6] aA. Abouimrane, I. Davidson, *J. Electrochem. Soc.* **2007**, *154*, A1031-A1034; bP.-J. Alarco, Y. Abu-Lebdeh, A. Abouimrane, M. Armand, *Nat. Mater.* **2004**, *3*, 476-481.
- [7] Q. Wang, H. Fan, L.-Z. Fan, Q. Shi, *Electrochimica Acta* **2013**, *114*, 720-725.
- [8] R. K. Gupta, H.-M. Kim, H.-W. Rhee, *J Journal of Physics D: Applied Physics*, **2011**, *44*, 205106.

[9] aW. Yang, W. Yang, B. Sun, S. Di, K. Yan, G. Wang, G. Shao, *ACS Applied Materials & Interfaces* **2018**, *10*, 39695-39704; bY. Zhang, J. Qian, W. Xu, S. M. Russell, X. Chen, E. Nasybulin, P. Bhattacharya, M. H. Engelhard, D. Mei, R. Cao, F. Ding, A. V. Cresce, K. Xu, J.-G. Zhang, *Nano Letters* **2014**, *14*, 6889-6896.

[10]aG. G. Eshetu, X. Judez, C. Li, A. Bondarchuk, L. M. Rodriguez-Martinez, H. Zhang, M. Armand, *Angewandte Chemie International Edition* **2017**, *129*, 15570–15574; bL. Zhang, M. Ling, J. Feng, L. Mai, G. Liu, J. Guo, *Energy Storage Mater.* **2018**, *11*, 24-29; cZ. Lu, J. Yu, J. Wu, M. B. Effat, S. C. T. Kwok, Y. Lyu, M. M. F. Yuen, F. Ciucci, *Energy Storage Mater.* **2019**, *18*, 311-319.

Chapter 10

10. Boosting the Performance of Lithium Batteries with Solid-Liquid Hybrid Electrolytes: Interfacial Properties and Effects of Liquid Electrolytes*

Solid-state lithium batteries have attracted significant attention recently due to their superior safety and energy density. Nevertheless, the large interfacial resistance has limited the development of SSLBs. To tackle this problem, a general strategy is to add liquid electrolytes (LE) at the interface to form a solid-liquid hybrid electrolyte. However, the effects and interfacial properties of LE in the solid-liquid hybrid electrolyte have not been well-understood. In this work, we quantitatively add LE at the interface to eliminate the large interfacial resistance and study its interfacial properties. As little as 2 μl of LE at the interface enables a hybrid $\text{LiFePO}_4/\text{LTP}/\text{Li}$ battery to deliver a specific capacity of 125 mAh g^{-1} at 1C and 98 mAh g^{-1} at 4C. Excess LE has no further contribution to the electrochemical performance. Furthermore, the rigid SSE could suppress the formation of lithium dendrites, especially in the case with a high cathode loading (9.1 mg/cm^2), suggesting the feasibility of high energy density SSLBs using Li metal anodes. The interfacial analysis reveals that an interfacial solid-liquid electrolyte interphase (SLEI) was formed at the interface, preventing the reduction of LTP by Li metal, thus ensuring the long-term durability of LTP in LE.

***Note:** This work has been published in **Nano Energy**.

Changhong Wang, Qian Sun, Yulong Liu, Yang Zhao, Xia Li, Xiaoting Lin, Mohammad Norouzi Banis, Minsi Li, Weihan Li, Keegan R Adair, Dawei Wang, Jianneng Liang, Ruying Li, Li Zhang, Rong Yang, Shigang Lu, Xueliang Sun. Boosting the performance of lithium batteries with solid-liquid hybrid electrolytes: Interfacial properties and effects of liquid electrolytes, **Nano Energy**, 2018, 48, 35-43.

10.1 Introduction

Solid-state lithium batteries (SSLBs) have attracted great interest recently due to their advantageous energy density and intrinsic safety, which can be realized through the use of lithium metal anodes and solid-state electrolytes (SSEs).[1, 2] To achieve an SSLB, the flammable liquid electrolyte (LE) and separator are replaced by SSEs. Currently, there are three categories of SSEs under development: oxide electrolytes, sulfide electrolytes, and polymer electrolytes.[1, 3-5] Compared with sulfide and polymer electrolytes, oxide electrolytes show great potential due to their unique characteristics, such as satisfactory ionic conductivity (nearly 10^{-3} S/cm), good air stability, low toxicity, and low cost.[5-7] However, there are three key challenges impeding the development of oxide electrolyte-based SSLBs. The first challenge is the large interfacial resistance originating from the poor contact between solid-state electrolytes and electrodes. The second challenge is the limited lithium-ion (Li^+) flux inside the electrodes, which arises from the poor contact between particles. The third issue is the chemical instability exhibited by the reduction and oxidation of oxide electrolytes by Li metal and high-voltage cathodes, respectively.[8-10]

Over the past decades, several attempts have been made to address the challenges faced by SSLBs, including (i) co-sintering of active materials with solid-state oxide electrolytes, where some additives, which generally have a low melting point, are employed as a sintering aid to form good contact between electrodes and electrolytes;[11, 12] (ii) the development of oxide-polymer (or plastic crystal) hybrid electrolytes, in which improved physical contact between electrodes and electrolytes can be achieved. However, they normally operate at an elevated temperature;[13-16] (iii) solid-liquid hybrid electrolytes, which utilize the wettability of liquid electrolytes to minimize the large contact resistance at the interfaces. Among these options, the use of solid-liquid hybrid electrolytes is one of the most feasible approaches for the development of lithium batteries. For instance,

by employing solid-liquid hybrid electrolytes, the plugging shuttling effect of soluble intermediates in Li-S and Li-Se batteries can be eliminated.[17, 18] Furthermore, solid-liquid hybrid electrolytes have been demonstrated to suppress the parasitic side reactions in Li-O₂ batteries.[19] However, the effects and interfacial properties of LE in solid-liquid hybrid electrolyte systems have not been well-understood.

In this work, a quantitative investigation on the volume of LE in solid-liquid hybrid electrolytes was performed and the interfacial properties of LE in the lithium batteries were performed. A hybrid lithium battery consists of LiFePO₄ as the cathode, a glass-ceramic Li_{1.4}Al_{0.4}Ti_{1.6}(PO₄)₃ (GC-LATP)/liquid electrolyte (LiPF₆ in EC/DMC/DEC) as the hybrid electrolyte and Li metal as the anode. As a result, the hybrid lithium battery can deliver impressive electrochemical performances, which are even comparable with those of their LE-based counterparts. It was found that the formation of an interfacial solid-liquid electrolyte interphase (SLEI) on the surface of GC-LATP prevents the reduction of GC-LATP by Li metal and enables the long-term electrochemical durability of GC-LATP in the LE. In addition, the robust SE could suppress the growth of lithium dendrites upon cycling, especially in the case with a high cathode loading (9.1 mg.cm⁻²), which suggests the feasibility of Li metal in SSLBs with improved safety and high energy density. This investigation can provide great insights into the solid-liquid hybrid electrolytes for lithium-ion batteries with improved safety and energy density.

10.2. Experimental Section

10.2.1 Synthesis of LATP and Glass-ceramic LATP

Analytical reagent-grade chemicals of Li₂CO₃, Al₂O₃, TiO₂, and (NH₄)₂HPO₄ were used as starting materials. Stoichiometric quantities of starting materials were weighed and placed in agate jars. To compensate for the volatility of lithium during the

high-temperature annealing process, an excess amount of Li_2CO_3 was added. Ball milling was conducted with ZrO_2 balls and a mass ratio of starting materials: balls of 1:10. Anhydrous ethanol was used as a solvent for wet ball milling. The powders were mixed by planetary ball milling for 2 hours at 300 rpm followed by collecting the mixture in a beaker. After drying in a vacuum oven, the powder was transfer to an alumina crucible and heated at 700°C for 2h in the air. Then the LATP precursor was obtained by grinding the products with a pestle and mortar. To obtain crystalline LATP, the LATP precursor was compressed into a pellet with a diameter of 1/2 inch. Then the pellet was post-annealed at 960°C for 6 hours in the air. The annealed pellets were denoted as LATP for this study. To obtain the glass-ceramic LATP (GC-LATP), the LATP precursor was first mechanically milled at 500 rpm for 80 hours. The mass ratio of the LATP powder and balls was 1:20. After the mechanical ball milling, the LATP powder was amorphized and pressed into a pellet. Finally, the pellet was sintered at 960°C for 6 hours in the air. The pellet was named as GC-LATP for this study.

10.2.2 Materials Characterizations

XRD patterns were recorded using a Bruker D8 diffractometer, using $\text{Cu K}\alpha$ radiation. XPS was recorded using Thermo Scientific ESCALAB 250Xi with $\text{Al K}\alpha$ -radiation. The pressure in the analysis chamber was typically 2×10^{-9} torr during acquisition. Raman spectra were collected using the laser with a wavelength of 532 nm. To measure the ionic conductivity of LATP pellets and GC-LATP pellets, gold electrodes were coated on the pellets by sputtering.

10.2.3 Electrochemical Measurements

LiFePO_4 was mixed with acetylene black, and PVDF with a mass ratio of 80:10:10 with N-Methyl pyrrolidone (NMP) as a solvent. The paste was coated with an aluminum foil

and dried at 110 °C overnight. Then the LiFePO_4 was cut into a disc with a diameter of 10 mm and as the cathode. The regular mass loading of LiFePO_4 is 1.5~2 mg/cm^2 . The LiCoO_2 cathode was also prepared with the same procedure. The electrochemical performances of the LiFePO_4 were tested in a coin cell (type CR-2032) assembled in an argon-filled glove box with both moisture and oxygen contents below 1 ppm. Glass ceramic LATP pellets with a thickness of (150~250 μm) were put between the LiFePO_4 cathode and the lithium metal anode. Different volumes of the liquid electrolyte (1M LiPF_6 in ethylene carbonate (EC)/dimethyl carbonate (DMC)/diethyl carbonate (DEC) with a volume ratio of 1:1:1), was added at the interfaces between electrodes and the LATP pellet, such as 5 μl , 2 μl , and 1 μl at each interface. A pipette with a metrological range from 0.5 μl to 10 μl was used to quantify the volume of the LE. For comparison, a cell with a LiFePO_4 cathode was also assembled with 300 μL liquid electrolyte. The cut-off voltages were set from 2.5 V to 4.1 V. Electrochemical impedance analysis was performed on a biologic electrochemical station with a frequency range from 500 kHz to 100 MHz with an amplitude of 10 mV. All the batteries were tested on the LAND system at room temperature.

10.3 Results and Discussion

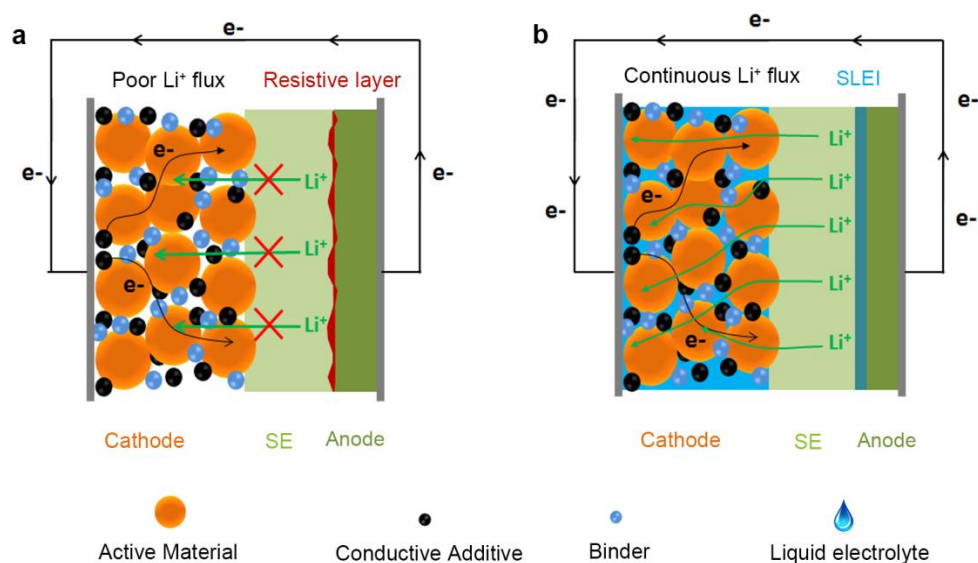


Figure 10-1 Schematic diagram of 3D continuous Li^+ ion flux. (a) Illustration of lithium-ion and electron fluxes inside the conventional cathode. (b) A trace amount of LE was added to both sides of the SE, filling the pores within the cathode as well as wetting the Li metal surface.

Figure 10-1 shows a schematic diagram of the strategy used to attenuate the interfacial resistance of SSLBs. The conventional cathode, which consists of active materials, conductive agents, and polymeric binder, is directly coupled with a solid-state electrolyte (SSE) and metallic Li anode, as shown in **Figure 10-1(a)**. Due to the poor contact between the SSE and electrode surfaces, the Li^+ flux becomes inhibited and limits the electrochemical performance. However, using a trace amount of LE to wet the interface can minimize the interfacial resistance between the electrodes and SSE. Meanwhile, the LE can infiltrate the pores of the cathode, enabling a three-dimensional (3D) continuous Li^+ flux with additional solid-liquid contact, as shown in **Figure 10-1(b)**. In addition, the addition of LE can induce the formation of an interfacial solid-liquid electrolyte interface (SLEI) on the surface of the solid electrolyte, which can serve as a buffer layer

to prevent the reduction of solid electrolytes by Li metal, ensuring the long-term durability of the SSE in LE.[8]

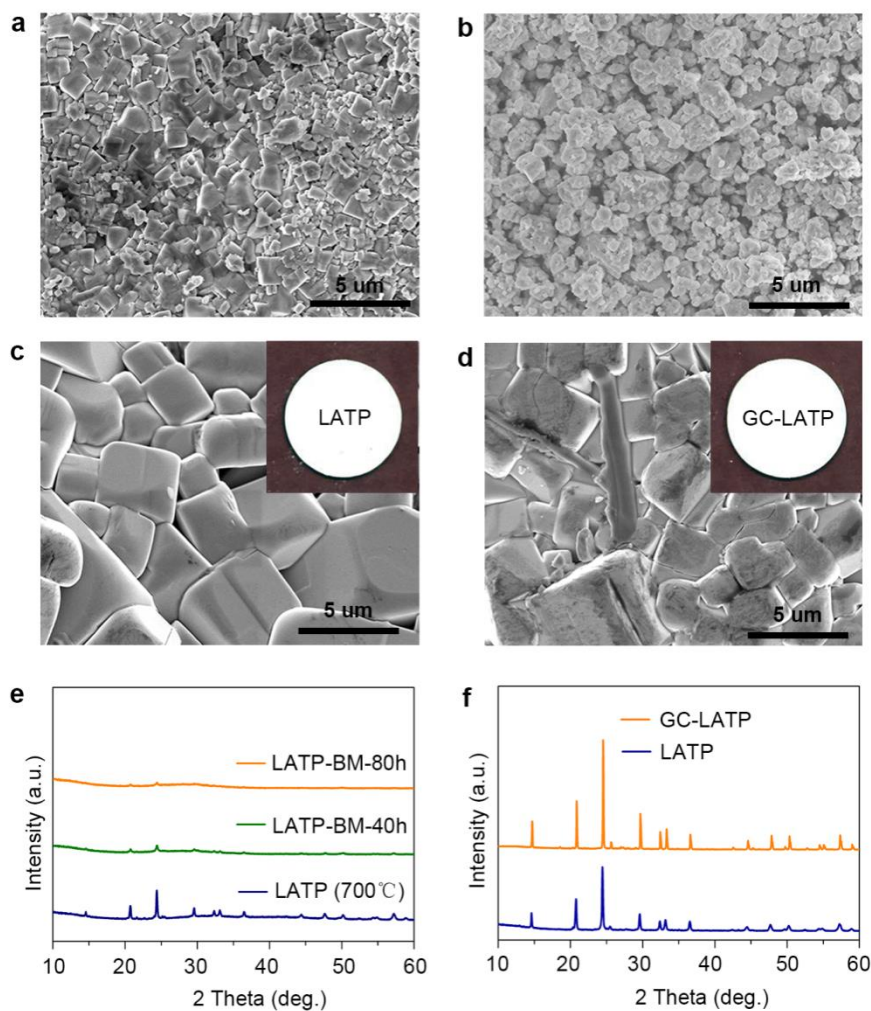


Figure 10-2 Comparison between LATP and GC-LATP. (a) the SEM image of the LATP precursor after annealing (700 °C, 2 hours). (b) the SEM image of the GC-LATP precursor after mechanical milling for 80 hours. (c) the SEM image of the LATP pellet after post-annealing (960 °C, 6 hours). (d) the SEM image of the GC-LATP pellet after post-annealing (960 °C, 6 hours). (e) XRD spectra of LATP precursors with different ball-milling time. (f) XRD spectra of LATP and GC-LATP pellets after post-annealing (960 °C, 6 hours).

To examine the effects of LE in solid-liquid hybrid electrolytes, the oxide electrolyte $\text{Li}_{1.4}\text{Al}_{0.4}\text{Ti}_{1.6}(\text{PO}_4)_3$ with a NASICON (acronym for sodium (Na) Super Ionic CONductors) structure was picked due its high ionic conductivity, wide electrochemical window, moderate sintering temperature, and good air stability.[20-22] As reported by Fu et al., LATP shows a bulk conductivity of $1.3 \times 10^{-3} \text{ S.cm}^{-1}$ at room temperature.[21] However, it is widely acknowledged that the large grain boundary resistance of LATP limits its overall ionic conductivity. To resolve this issue, glass-ceramic LATP was synthesized by mechanical milling to minimize the grain boundary resistance.[23] The synthesis procedure is described in the experimental section. Briefly, upon thermal annealing at 700°C , the LATP precursors can be seen to yield large particles in the micrometer size domain, as presented in **Figure 10-2(a)**. With mechanical milling, which is known as a vitrification process, the particle size could be reduced, as shown in **Figure 10-2(b)**. This sample is denoted as GC-LATP in the following discussion. After pelletizing the precursors followed by post-annealing at 960°C for 6 hours, LATP pellets show a significant amount of pores on the surface, as displayed in **Figure 10-2(c)** and **Figure 10-S1**. In contrast, the GC-LATP pellets have a densely-packed structure without pores on the surface, as demonstrated in **Figure 10-2(d)** and **Figure 10-S1**. The densified structure of GC-LATP is due to the amorphization of the precursors during the vitrification process, as evidenced by the XRD patterns in **Figure 10-2(e)**. After post-annealing, both LATP and glass-ceramic LATP show the high-purity $\text{LiTi}_2(\text{PO}_4)_3$ phase, as exhibited in **Figure 10-2(f)**. It should be noted that a 10% excess of Li_2CO_3 was added to complement the volatile loss of the lithium sources during the post-annealing process. Otherwise, some impurities, such as AlPO_4 ,[23] $\text{Li}_4\text{P}_2\text{O}_7$,[24] will form in LATP, as depicted in the XRD patterns in **Figure S2**. It should be highlighted that the LATP precursors still show pure phases even with the scale-up process, as demonstrated in **Figure S3**, indicating the feasibility of the mass production of LATP precursors.

To evaluate the ionic conductivity of the as-synthesized LATP, gold electrodes were coated on both sides of the LATP pellets by magnetron sputtering. GC-LATP shows an ionic conductivity of $4.1 \times 10^{-4} \text{ S cm}^{-1}$ at room temperature, which is almost one order of magnitude higher than that of LATP ($6.1 \times 10^{-5} \text{ S cm}^{-1}$), as exhibited in **Figure 10-S4(a)**. To obtain their activation energies, the temperature-dependent impedance analysis of LATP pellets was examined by varying the temperature from 20°C to 100°C (**Figure 10-S4(c)** and **Figure 10-S4(d)**). According to the Arrhenius equation, $\sigma(T) = \sigma_0 \cdot \exp(-E_a/k_B T)$, where E_a is the activation energy, T is the temperature, k_B is the Boltzmann constant, the activation energies of LATP and GC-LATP are 27.88 kJ.mol⁻¹ and 27.27 kJ.mol⁻¹, respectively, as shown in **Figure 10-S4(b)**, which are in a good agreement with the results reported in the references.[23, 25] For the following study, GC-LATP was selected due to its higher ionic conductivity and lower activation energy as well as increased density, in comparison with those of LATP.

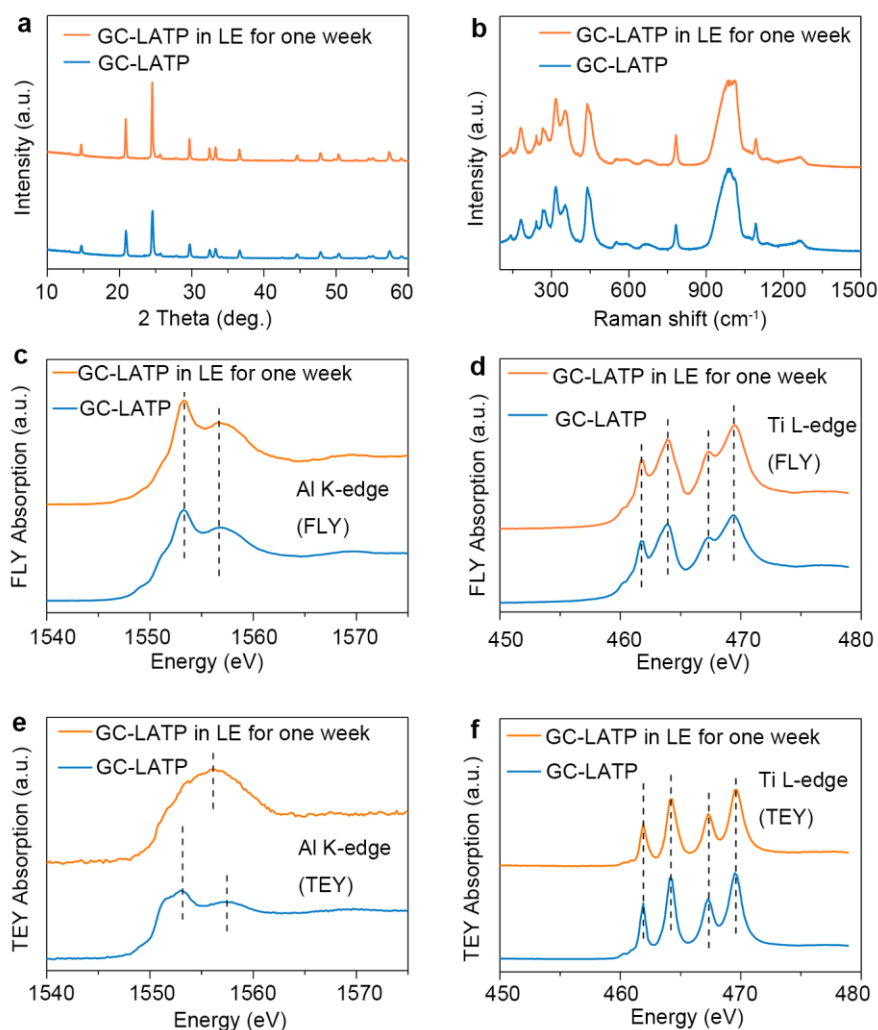


Figure 10-3 Chemical compatibility of GC-LATP in carbonate liquid electrolytes. (a) Comparison of XRD patterns of GC-LATP pellets before and after being soaking in LE for one week. (b) Comparison of Raman spectra of GC-LATP pellets before and after being soaking in LE for one week. (c) Al K-edge and (d) Ti L-edge XANES spectra recorded in the FLY mode and (e) Al K-edge & (f) Ti L-edge XANES spectra recorded in the TEY mode of GC-LATP pellets before and after being soaking in LE for one week.

In addition to the high ionic conductivity of the SSEs, the chemical stability of the SE in LE is another important factor for solid-liquid hybrid electrolytes.[9, 26] To reveal the

chemical stability of GC-LATP in LE, the GC-LATP was soaked in the conventional liquid electrolyte of 1M LiPF_6 in ethylene carbonate (EC)/dimethyl carbonate (DMC)/diethyl carbonate (DEC) with a volume ratio of 1:1:1. After one week, there is no visible change in color of the LE, as shown in **Figure S5**. From the XRD patterns of GC-LATP presented in **Figure 10-3(a)**, the $\text{LiTi}_2(\text{PO}_4)_3$ phase was well maintained, indicating that GC-LATP is structurally stable in the LE. **Figure 10-3(b)** exhibits the Raman spectra of the GC-LATP and shows several strong Raman bands appearing in the ranges of 150–500 and 900–1300 cm^{-1} . The bands in the range of 150–500 cm^{-1} should be assigned to symmetrical bending vibrations of PO_4 groups, while those in 900–1100 and 1100–1300 cm^{-1} should be ascribed to the stretching vibrations of PO_3 and PO_2 units, respectively.[27] Again, no new peaks were detected by Raman spectroscopy after soaking off the GC-LATP in the LE for one week, which suggests that the GC-LATP is chemically stable towards common carbonate electrolytes.

To further explore the chemical states of GC-LATP, the normalized Al K-edge and Ti L-edge X-ray absorption near-edge structure (XANES) spectra were examined before and after soaking in LE for one week. **Figure 10-3(c-d)** and **Figure 10-3(e-f)** show the XANES spectra recorded in the fluorescence yield (FLY) and total electron yield (TEY) modes, respectively. Based on the different probe depths in measurement modes (~ 100 nm in the FLY mode and ~ 10 nm in the TEY mode), the chemical states of the bulk and surface regions of GC-LATP can be obtained in FLY and TEY, respectively.[28] No peak shift and shape variation of the Al K-edge was found in the spectra measured in FLY mode, as displayed in **Figure 10-3(c)**, further verifying that the bulk of GC-LATP is chemically stable in the LE. In comparison, the XANES spectra of the Al K-edge measured in TEY mode showed obvious changes in peak shape (**Figure 10-3(e)**), indicating that AlF_3 is probably formed on the GC-LATP surface.[29, 30] This conclusion was further confirmed by the F K-edge XANES spectra in Figure 10-S6, which also suggests the formation of AlF_3 on the surface. Interestingly, no change was

observed in the Ti L-edge spectra measured in both TEY and FLY modes, as shown in **Figure 10-3(d)** and **Figure10-3(f)**. By combining the bulk and interfacial data observed by the XANES spectra, it can be concluded that GC-LATP is stable in carbonate-based liquid electrolytes, which is likely caused by the formation of a passivating AlF_3 layer on the surface. It has been previously reported that the electrochemical performance of hybrid-SSLBs is highly dependent on good chemical compatibility between the SSE and LE.[9, 26, 31] Furthermore, the long-term durability of GC-LATP in LE is a prerequisite to enable the commercialization of SSLBs with satisfactory electrochemical performance.

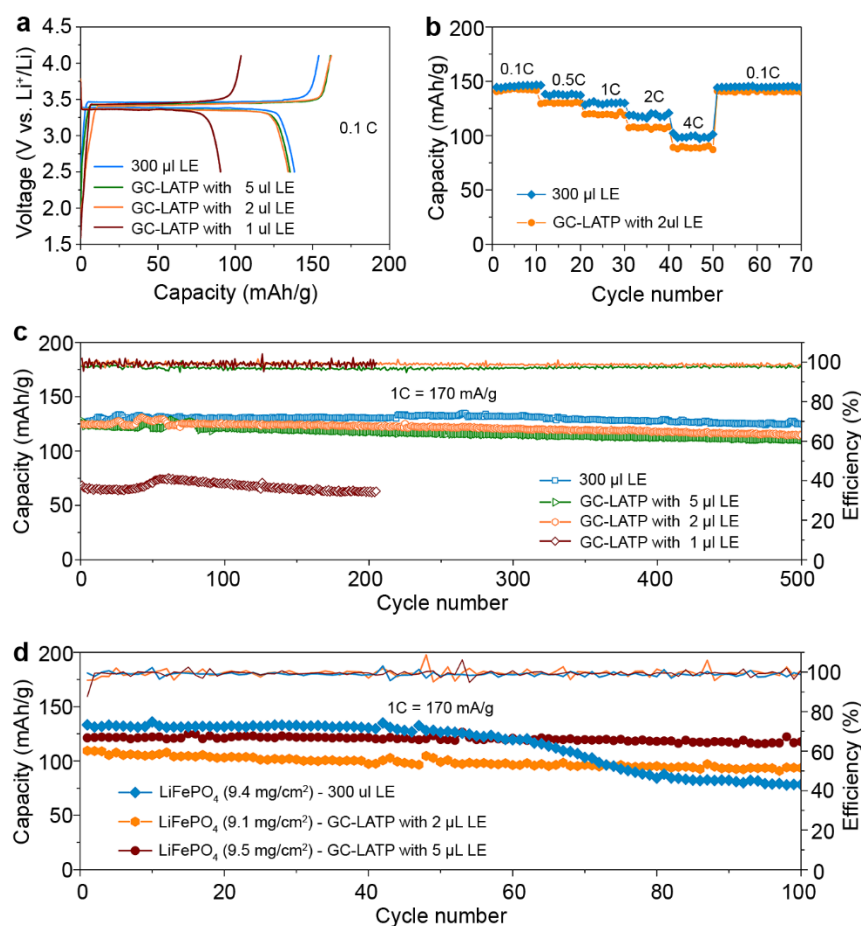


Figure 10-4 Electrochemical performances of LiFePO_4 -based quasi-solid-state lithium-ion batteries employing GC-LATP\LE hybrid electrolytes. (a)

Charge-discharge curves of LiFePO₄ at 0.1 C, (1 C = 170 mA.g⁻¹). (b) Rate performance of LiFePO₄ at various current densities ranging from 0.1 C to 4 C. (c) Long-term cycling performance of LiFePO₄ with quantified volume of LE at a current density of 1C. (d) The cycling performance of high areal loading LiFePO₄ cathodes in conventional LE and GC-LATP\LE hybrid electrolytes.

Employing a GC-LATP\LE hybrid electrolyte, LiFePO₄-based lithium batteries were fabricated and tested electrochemically. For the first time, how the volume of LE used to wet the SE/electrode surface affects the electrochemical performance of quasi-SSLBs and the formation of the SLEI was investigated. **Figure 10-4(a)** shows the initial charge-discharge curves of the lithium batteries employing GC-LATP\LE hybrid electrolytes with different volumes of LE, which is cycled at 0.1C (1C=170 mA g⁻¹). In the case of 1 μL of LE, the LiFePO₄ only delivers a specific capacity of 91 mAh g⁻¹, which suggests that 1 μL of LE is incapable of completely wetting the cathode. From the EIS results shown in Figure 10-S7, the interfacial resistance of the cell containing 1 μL LE is almost 1000 Ω. By increasing the volume of LE to 2 μl, the interfacial resistance decreases to 275 Ω. The LiFePO₄ shows a specific capacity of 134 mAh g⁻¹ at 0.1C and an initial Coulombic efficiency of 82.8%, which is only slightly lower than that of their LE-based counterparts (138 mAh g⁻¹, 89.6% Coulombic efficiency). This may be caused by the formation of a solid-liquid electrolyte interphase (SLEI) on the surface of GC-LATP.[8, 32] In our case, 2 μL of LE is the minimum volume required to enable fully functional lithium batteries with solid-liquid hybrid electrolytes. **Figure 10-4(b)** shows the rate performance of LiFePO₄ employing the GC-LATP\LE hybrid electrolyte (2 μl) and conventional LE at different current densities varying from 0.1C to 4C. Furthermore, their corresponding charge-discharge curves are presented in **Figures 10-S8(a)** and **Figure 10-S8(b)**. It is surprising that the LiFePO₄ delivers a specific

capacity of 98 mAh g^{-1} even at the rate of 4 C, which is comparable to the performance of the LE-based counterparts. The decrease in specific capacity at high rates is caused by the larger internal resistance of the lithium batteries with solid-liquid hybrid electrolytes. This observation is supported by **Figure 10-S7(a)**, where the overall resistance of LiFePO_4 in the LE is seen to be 169Ω , which is lower than that of the GC-LATP\LE hybrid electrolyte (275Ω). Moreover, **Figure 10-4(c)** displays the extended cycling of LiFePO_4 with the GC-LATP\LE ($2 \mu\text{L}$) hybrid electrolyte and yields a specific capacity of 125 mAh g^{-1} at 1C, which remains as high as 115 mAh g^{-1} after 500 cycles. The hybrid-SSLBs with as little as $2 \mu\text{l}$ LE show extremely stable cycling performance with a low capacity decay rate of 0.0167% per cycle. Comparatively, the LiFePO_4 in conventional LE delivers a specific capacity of 127 mAh g^{-1} at 1C and maintains a capacity of 125 mAh g^{-1} after 500 cycles with a capacity decay rate of 0.0032%. Compared to $2 \mu\text{L}$ of LE, $5 \mu\text{L}$ of LE shows no further contribution to the overall specific capacity but decreases the energy density of hybrid-SSLBs in practice. However, in the case of the hybrid cells with $1 \mu\text{L}$ LE, the specific capacity is only 68 mAh g^{-1} , which confirms the incomplete wetting of the cathode again.

To obtain high energy density hybrid-SSLBs, cathodes with a high active material loading are required. As demonstrated in **Figure 10-4(d)**, the specific capacity of LiFePO_4 with high active material loadings (over 9 mg cm^{-2}) in the conventional LE decreases gradually after 50 cycles. The reason for the capacity fade is believed to be the formation of mossy lithium and/or dendrites due to a large amount of deposited Li metal associated with high loading cathodes.[33] Employing the GC-LATP\LE hybrid electrolytes ($2 \mu\text{L}$), high-loading LiFePO_4 (9.1 mg.cm^{-2}) delivers a stable specific capacity of 100 mAh g^{-1} over 100 cycles at 1C ($1\text{C}=170 \text{ mA.g}^{-1}$). Similarly, using GC-LATP\LE hybrid electrolytes ($5 \mu\text{L}$), high-loading LiFePO_4 (9.5 mg.cm^{-2}) delivers a stable specific capacity of 120 mAh g^{-1} over 100 cycles at 1C. Both cases suggest that the lithium dendrites could be suppressed by the rigid GC-LATP, improving the safety of SSLBs.

To show the universal application of the GC-LATP\LE hybrid electrolyte, the hybrid system was also applied to LiCoO₂ cathodes, which exhibits an ultra-long cycle stability over 700 cycles as displayed in **Figure 10-S9**. To the best of our knowledge, the electrochemical performance of the hybrid-SSLBs in this study is superior to the previously reported literature, [2, 6, 9, 13, 31], especially in terms of cyclability and rate performance.

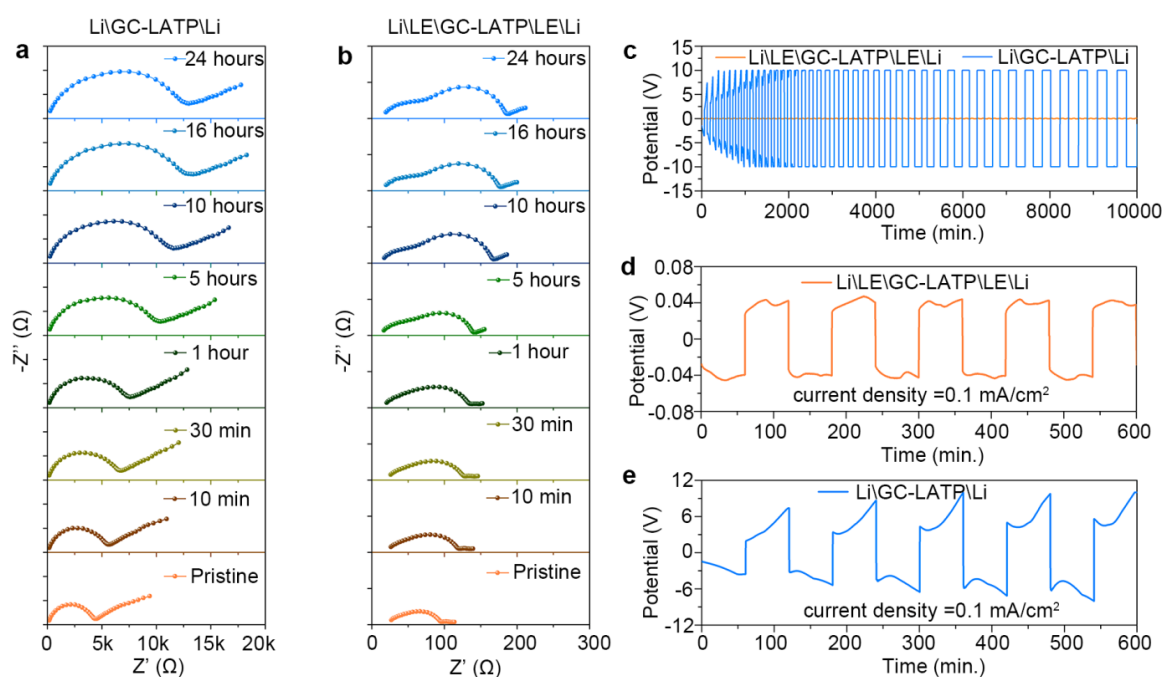


Figure 10-5 Evaluation of the GC-LATP and Li metal interface stability. (a) Electrochemical impedance spectra of the symmetric cell with a structure of Li\GC-LATP\Li. (b) Electrochemical impedance spectra of the symmetric cell with a structure of Li\LE\GC-LATP\LE\Li. The volume of LE is 2 μ L. (c) Comparison of the plating/stripping profiles between Li\GC-LATP\Li and Li\LE\GC-LATP\LE\Li symmetric cells. (d) The voltage profile of Li\LE\GC-LATP\LE\Li symmetric cells. (e) The voltage profile of Li\GC-LATP\Li symmetric cells.

To reveal the underlying mechanism for improved performance and cycling stability, a qualitative analysis was further conducted. Firstly, symmetric cells with a structure of Li\GC-LATP\Li were constructed to investigate the interfacial stability between glass-ceramic LATP and Li metal. The typical Nyquist plot of Li\GC-LATP\Li is characterized by a high-frequency semicircle and a finite-length Warburg impedance at low frequencies, as exhibited in **Figure 10-5(a)**, which indicates the formation of a mixed ion-electron conductor at the interface.[34] The equivalent circuit is shown in **Figure 10-S10(a)**. The Nyquist plot as a function of time reveals the interfacial resistance between GC-LATP and Li metal continuously grows from 4470 Ω to 12983 Ω over a period of 24 h, indicating significant interfacial reactions. The increasing interfacial resistance originates from the reduction of GC-LATP, forming new phases, such as Ti_3P , TiAl , Li_3P , and Li_2O , which are supported by first-principles studies.[10, 35] In the case of Li\LE\GC-LATP\LE\Li, the Nyquist plot is dominated by two semicircles, which is typical for a formation of ion-conducting SLEI (SEI, acronym for solid-liquid electrolyte interphase) at the interface between LATP and Li.[34] The corresponding equivalent circuits are shown in **Figure 10-S10(b)**, in which the first semicircle at high frequency represents the resistance of LATP grain (R_g). The $R_{int}||CPE2$ element represents the ion migration in the SLEI layer and dielectric capacitance of the SEI layer.

Comparatively, the large interfacial resistance is dramatically minimized through the use of trace amounts of LE to wet the interface between glass-ceramic LATP and Li metal. As displayed in **Figure 5(b)**, the interfacial resistance decreases to 90 Ω after wetting with 2 μL of LE, which is almost 50 times lower than the original resistance (4470 Ω). **Figure 10-5(c)** presents the plating/stripping profiles of lithium of Li\GC-LATP\Li and Li\LE\GC-LATP\LE\Li symmetric cells, showing that the large overpotential (~ 10 V) of Li\GC-LATP\Li cells could be decreased significantly to 40 mV by adding as little as 2 μL LE on the surface between GC-LATP and Li metal. **Figure 10-5(d)** and **Figure 10-5(e)** shows the galvanostatic cycling of Li\LE\GC-LATP\LE\Li and Li\GC-LATP\Li

cells, respectively. After adding 2 μL LE at the interface, the overpotential of Li nucleation is completely eliminated.[36] The separated cycling initial voltage profiles of $\text{Li}\backslash\text{LE}\backslash\text{GC-LATP}\backslash\text{LE}\backslash\text{Li}$ and $\text{Li}\backslash\text{GC-LATP}\backslash\text{Li}$ cells are presented in **Figure 10-S11**. The symmetric cell illustrates that the Li plating/stripping profiles of $\text{Li}\backslash\text{LE}\backslash\text{GC-LATP}\backslash\text{LE}\backslash\text{Li}$ and $\text{Li}\backslash\text{GC-LATP}\backslash\text{Li}$ cells are completely different, indicating that the underlying mechanism of Li plating/stripping based on SE is different from that in conventional LE.[36-38] Further studies are required to fully understand this phenomenon.

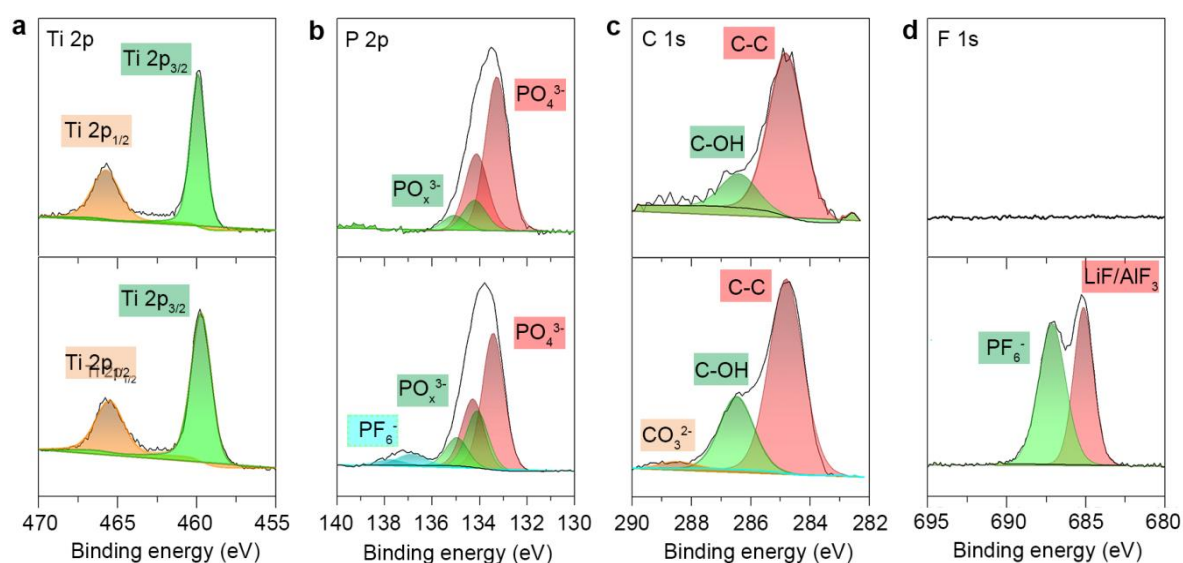


Figure 10-6 X-ray photoelectron spectra of GC-LATP pellets before and after electrochemical cycling. (a) Ti 2p. (b) P 2p. (c) C 1s. (d) F 1s. Top: before cycling, Bottom: after cycling.

Furthermore, the post-cycling analysis was performed to investigate the solid-liquid electrolyte interphase (SLEI) on the GC-LATP surface. As shown in Figure 10-S12(b), the clear LATP surface was covered by a thin film layer after 100 cycles, which is believed to be the SLEI layer. SEM coupled with energy-dispersive X-ray spectroscopy (EDX) was performed to investigate the composition of the interface. As shown in **Figure 10-S13(a-f)**, elements such as C, P, F, Ti, and Al, are evenly distributed on the surface. The chemical information on the SLEI was further analyzed by X-ray

photoelectron spectroscopy (XPS). The full survey XPS spectra of GC-LATP pellets before and after cycling is included in **Figure S14**, and the high-resolution spectra of Ti, P, C, and F are displayed in **Figure 6**. In comparison with the Ti spectra **Figure 10-6(a)**, there is no change after cycling, indicating that the reduction of Ti in GC-LATP by Li metal is prevented by the formation of the SLEI layer.[39, 40] **Figure 10-6(b)** shows the high-resolution P spectra before and after cycling, which clearly shows new peaks at around 137 eV, which is resulted from PF_6^- . **Figure 10-6(c)** exhibits the high-resolution spectra of C 1s. After cycling the CO_3^{2-} peak was detected, suggesting Li_2CO_3 forms on the surface of GC-LATP after cycling.[8] As a sharp comparison, the high-resolution F 1s spectra were shown in **Figure 10-6(d)**, suggesting that PF_6^- and LiF (or AlF_3) are formed on the surface of GC-LATP after cycling, which did not show up before cycling. To supplement these results, high-resolution O 1s spectra are also presented in **Figure S15**. These results strongly suggest that an SLEI layer is formed on the surface of the GC-LATP pellets after electrochemical cycling, and consists of both lithium salts and organic compounds.[8]

10.4 Conclusion

A lithium battery with a configuration of $\text{LiFePO}_4/\text{GC-LATP}/\text{Li}$ was successfully realized, yielding a specific capacity of 125 mAh g^{-1} when cycled at 1C and 98 mAh g^{-1} at 4C. To the best of our knowledge, the electrochemical performances are superior to all previously reported results. The superior electrochemical performance is attributed to the long-term durability of GC-LATP in LE and the formation of the SLEI on the GC-LATP surface, which prevents the reduction of GC-LATP by Li metal and enables a stable cycling performance. Moreover, the robust SE could suppress the growth of lithium dendrites upon cycling, improving the safety and energy density of lithium batteries. Furthermore, we have exemplified the importance of quantitatively controlling the volume of LE to enable high-performance quasi-SSLB systems. This demonstration can

help guide future research in solid-liquid hybrid electrolyte systems for SSLBs with improved safety and energy density.

10.5 Acknowledgements

This work was supported by Natural Sciences and Engineering Research Council of Canada (NSERC), Canada Research Chair Program (CRC), China Automotive Battery Research Institute, Canada Foundation for Innovation (CFI), the Canada Light Source at University of Saskatchewan (CLS) and University of Western Ontario.

10.6 References

- [1] A. Manthiram, X. Yu, S. Wang, *Nat. Rev. Mater.*, 2 (2017) 16103.
- [2] K. Fu, Y. Gong, B. Liu, Y. Zhu, S. Xu, Y. Yao, W. Luo, C. Wang, S.D. Lacey, J. Dai, Y. Chen, Y. Mo, E. Wachsman, L. Hu, *Sci. Adv.*, 3 (2017).
- [3] C. Sun, J. Liu, Y. Gong, D.P. Wilkinson, J. Zhang, *Nano Energy*, 33 (2017) 363-386.
- [4] J.C. Bachman, S. Muy, A. Grimaud, H.-H. Chang, N. Pour, S.F. Lux, O. Paschos, F. Maglia, S. Lupart, P. Lamp, L. Giordano, Y. Shao-Horn, *Chem. Rev.*, 116 (2016) 140-162.
- [5] V. Thangadurai, S. Narayanan, D. Pinzaru, *Chem. Soc. Rev.*, 43 (2014) 4714-4727.
- [6] X. Han, Y. Gong, K. Fu, X. He, G.T. Hitz, J. Dai, A. Pearse, B. Liu, H. Wang, G. Rubloff, Y. Mo, V. Thangadurai, E.D. Wachsman, L. Hu, *Nat Mater*, 16 (2017) 572-579.
- [7] E. Quartarone, P. Mustarelli, *Chem. Soc. Rev.*, 40 (2011) 2525-2540.
- [8] M.R. Busche, T. Drossel, T. Leichtweiss, D.A. Weber, M. Falk, M. Schneider, M.-L. Reich, H. Sommer, P. Adelhelm, J. Janek, *Nat Chem*, 8 (2016) 426-434.

- [9] B. Xu, H. Duan, H. Liu, C.A. Wang, S. Zhong, *ACS Appl. Mater. Interfaces*, 9 (2017) 21077-21082.
- [10] Y. Zhu, X. He, Y. Mo, *ACS Appl. Mater. Interfaces*, 7 (2015) 23685-23693.
- [11] P. Birke, F. Salam, S. Döring, W. Weppner, *Solid State Ion.*, 118 (1999) 149-157.
- [12] S. Ohta, J. Seki, Y. Yagi, Y. Kihira, T. Tani, T. Asaoka, *J. Power Sources*, 265 (2014) 40-44.
- [13] W. Zhou, S. Wang, Y. Li, S. Xin, A. Manthiram, J.B. Goodenough, *J. Amer. Chem. Soc.*, 138 (2016) 9385-9388.
- [14] Z. Zhang, Y. Zhao, S. Chen, D. Xie, X. Yao, P. Cui, X. Xu, *J. Mater. Chem. A*, (2017).
- [15] H. Gao, L. Xue, S. Xin, K. Park, J.B. Goodenough, *Angew. Chem. Int. Ed.*, 56 (2017) 5541-5545.
- [16] P.-J. Alarco, Y. Abu-Lebdeh, A. Abouimrane, M. Armand, *Nat Mater*, 3 (2004) 476-481.
- [17] L. Wang, Y. Wang, Y. Xia, *Energy Environ. Sci.*, 8 (2015) 1551-1558.
- [18] Y. Zhou, Z. Li, Y.-C. Lu, *Nano Energy*, 39 (2017) 554-561.
- [19] L. Li, S.-H. Chai, S. Dai, A. Manthiram, *Energy Environ. Sci.*, 7 (2014) 2630-2636.
- [20] R.J. Chen, W.J. Qu, X. Guo, L. Li, F. Wu, *Mater. Horizons*, 3 (2016) 487-516.
- [21] J. Fu, *Solid State Ion.*, 96 (1997) 195-200.
- [22] K. Arbi, S. Mandal, J.M. Rojo, J. Sanz, *Chem. Mater.*, 14 (2002) 1091-1097.

- [23] X. Xu, Z. Wen, J. Wu, X. Yang, *Solid State Ion.*, 178 (2007) 29-34.
- [24] X. Liu, J. Tan, J. Fu, R. Yuan, H. Wen, C. Zhang, *ACS Appl. Mater. Interfaces*, 9 (2017) 11696-11703.
- [25] X. Xu, Z. Wen, X. Yang, J. Zhang, Z. Gu, *Solid State Ion.*, 177 (2006) 2611-2615.
- [26] S. Wang, Y. Ding, G. Zhou, G. Yu, A. Manthiram, *ACS Energy Lett.*, 1 (2016) 1080-1085.
- [27] R. Pikel, D. de Waal, A. Aatiq, A. El Jazouli, *Mater. Res. Bull.*, 33 (1998) 955-961.
- [28] W. Huang, A. Marcelli, D. Xia, *Adv. Energy Mater.*, 7 (2017) 1700460-n/a.
- [29] S.L.M. Schroeder, N. Weiher, *Phys. Chem. Chem. Phys.*, 8 (2006) 1807-1811.
- [30] I. Grohmann, A. Hess, E. Kemnitz, W. Fentrup, W. E. S. Unger, J. Wong, M. Rowen, T. Tanaka, M. Froba, *J. Mater. Chem.*, 8 (1998) 1453-1457.
- [31] T. Liu, Y. Ren, Y. Shen, S.-X. Zhao, Y. Lin, C.-W. Nan, *J. Power Sources*, 324 (2016) 349-357.
- [32] Y. Kato, S. Hori, T. Saito, K. Suzuki, M. Hirayama, A. Mitsui, M. Yonemura, H. Iba, R. Kanno, *Nat. Energy*, 1 (2016) 16030.
- [33] X.-B. Cheng, R. Zhang, C.-Z. Zhao, Q. Zhang, *Chem. Rev.*, 117 (2017) 10403-10473.
- [34] P. Bron, B. Roling, S. Dehnen, *J. Power Sources*, 352 (2017) 127-134.
- [35] Y. Zhu, X. He, Y. Mo, *J. Mater. Chem. A*, 4 (2016) 3253-3266.
- [36] K. Yan, Z. Lu, H.-W. Lee, F. Xiong, P.-C. Hsu, Y. Li, J. Zhao, S. Chu, Y. Cui, *Nat. Energy*, 1 (2016) 16010.

[37] K.-H. Chen, K.N. Wood, E. Kazyak, W.S. LePage, A.L. Davis, A.J. Sanchez, N.P. Dasgupta, *J. Mater. Chem. A*, 5 (2017) 11671-11681.

[38] K.N. Wood, E. Kazyak, A.F. Chadwick, K.-H. Chen, J.-G. Zhang, K. Thornton, N.P. Dasgupta, *ACS Cent. Sci.*, 2 (2016) 790-801.

[39] C. Ye, L. Zhang, C. Guo, D. Li, A. Vasileff, H. Wang, S.-Z. Qiao, *Adv. Funct. Mater.*, 27 (2017) 1702524.

[40] F. Xie, L. Zhang, D. Su, M. Jaroniec, S.-Z. Qiao, *Adv. Mater.*, 29 (2017) 1700989.

10.7 Supporting Information

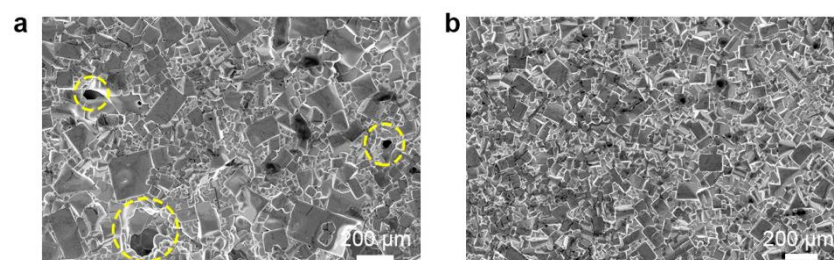


Figure 10-S1. SEM images of LAMP (a) and GC-LAMP (b). Comparing GC-LAMP with LAMP, it is clearly seen that the particle size of GC-LAMP is more uniform. In addition, the GC-LAMP pellet is more densely packed, and there are no large holes present on the pellet surface, while the LAMP pellets have some holes as highlighted by yellow circles.

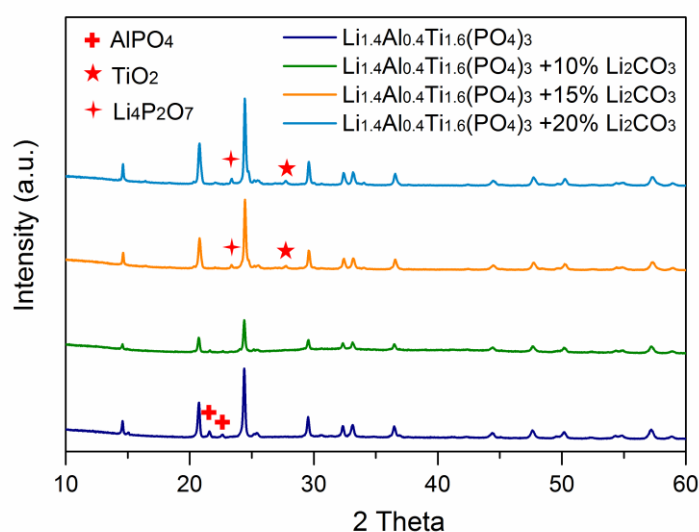


Figure 10-S2. XRD spectra of LAMP with excess amounts of Li_2CO_3 . Without the addition of excess Li_2CO_3 , there will be some impurity phases, such as AlPO_4 , in the LAMP.[23] The formation of AlPO_4 impurities is related to the volatilization of lithium precursors. In view of this, introducing an excess amount of Li_2CO_3 could suppress the impurity formation. Thus, when 10% of excess Li_2CO_3 was introduced into the

stoichiometric LATP precursors, AlPO_4 impurities in the XRD spectrum of LATP (green line) can be inhibited. However, if 15% and 20% excess amount of Li_2CO_3 was introduced, other new impurities, such as TiO_2 and $\text{Li}_4\text{P}_2\text{O}_7$, [40] were formed in LATP.

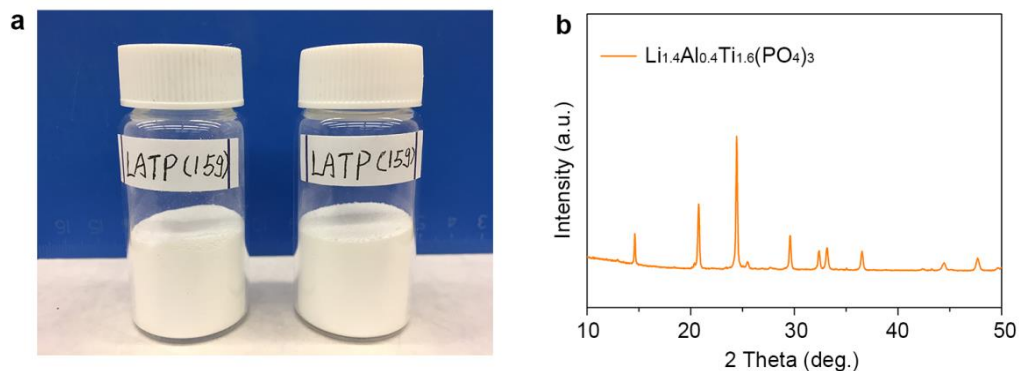


Figure 10-S3. LATP powder synthesized by the scale-up process. (a) Photo of the LATP powder. (b) XRD pattern of the LATP powder.

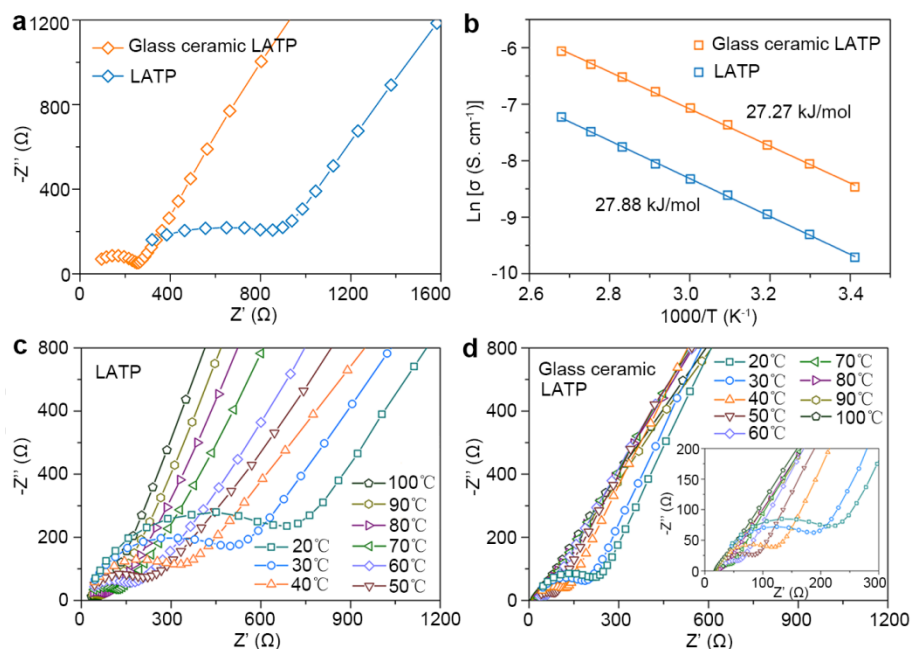


Figure 10-S4. Ionic conductivity of LATP and GC-LATP. (a) Electrochemical impedance spectra of LATP and GC-LATP. (b) Activation energy of electrochemical

impedance spectroscopy of LATP and GC-LATP. (c) Electrochemical impedance spectra of LATP at various temperatures. (d) Electrochemical impedance spectroscopy of GC-LATP at various temperatures.

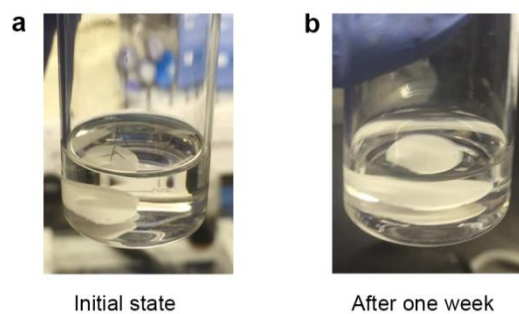


Figure 10-S5. Photos of LATP in liquid carbonate electrolytes at the initial state (a) and after one week(b). After one week, there is no visible color change.

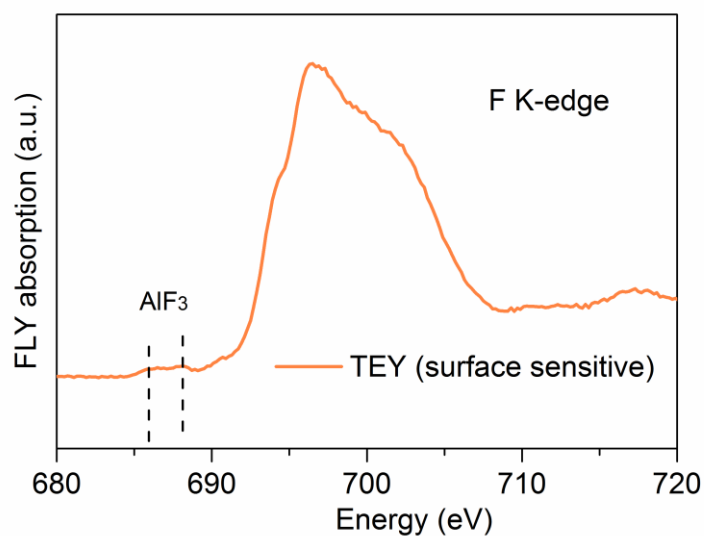


Figure 10-S6. F K-edge spectra of GC-LATP pellets after being soaked in LE for one week. It shows the AlF_3 signal on the pellet surface.

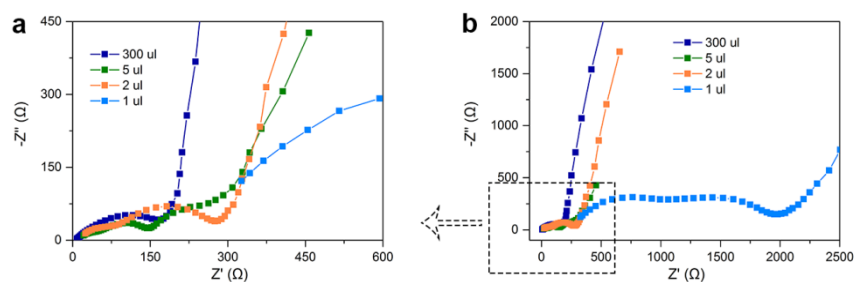


Figure 10-S7. Electrochemical impedance spectra of LiFePO₄ cathode quasi-SSLBs employing the GC-LATP\LE hybrid electrolytes with different volumes of LE. The overall resistance of LiFePO₄ in the LE is 169 Ω, which is lower than that in the LATP-LE hybrid electrolyte (275 Ω).

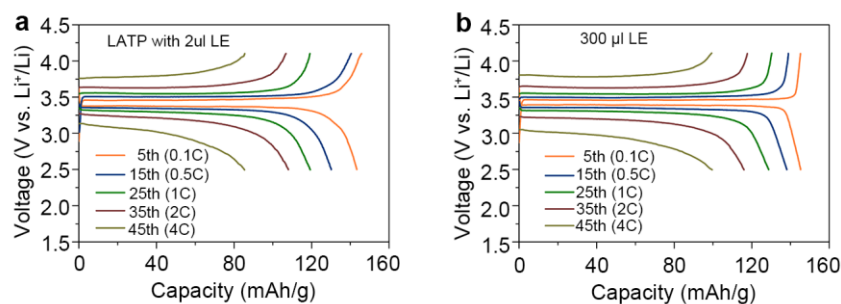


Figure 10-S8. Charge-discharge curves of LiFePO₄ employing the GC-LATP\LE hybrid electrolyte compared to conventional LE. (a) The charge-discharge curves of LiFePO₄ employing the LATP-LE hybrid electrolyte at different current densities varying from 0.1C to 4C. (b) The charge-discharge curves of LiFePO₄ employing only convention LE at different current densities varying from 0.1C to 4C. The over-potential between the charge and discharge plateau of LiFePO₄ in the hybrid electrolytes is comparable with that of the LE-based counterparts.

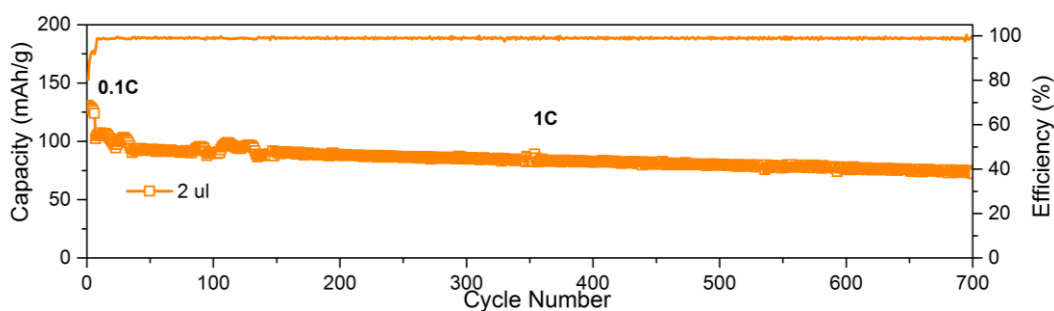


Figure 10-S9. The long-term cycling performance of LiCoO_2 in the GC-LATP/LE hybrid electrolyte. The volume of LE used is $2 \mu\text{L}$. The initial discharge capacity of LiCoO_2 is 131 mAh/g at 1C and 102 mAh/g at 1C . Furthermore, the capacity remains at 72 mAh/g after 700 cycles.

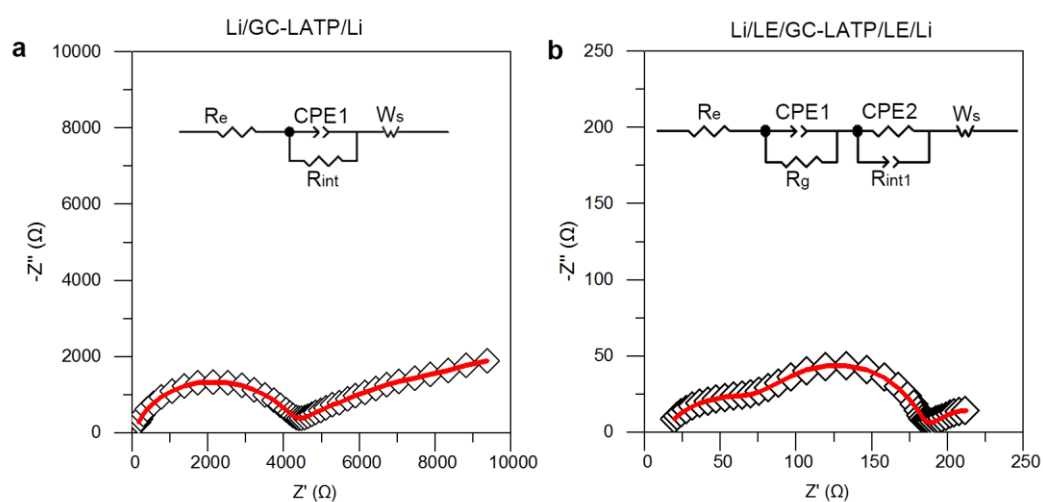


Figure 10-S10. Two typical EIS spectra of Li symmetric cells, in which mixed electron-ion conductor interface (a) dominates the interfacial resistance or ion-conducting SLEI interface (b) determines the interfacial resistance. SLEI is an acronym of solid-liquid electrolyte interphase.

In the case of Li/GC-LATP/Li cells, the Nyquist plot is characterized by a high-frequency semicircle and a finite-length Warburg impedance at low frequencies. These characteristics are typical for mixed ion-electron conductor (MCI, the acronym for mixed conductor interphases)[1], which is usually described by an equivalent circuit as an inset

in Figure S4(a). The $R_{int}||CPE1$ element describes the high-frequency semicircle and represents the parallel migration of ions and electrons in the MCI layer and dielectric capacitance of the MCI layer. The finite-length Warburg impedance W_s (Warburg short) describes the formation of Li^+ and e^- diffusion layer in the MCI layer due to the blocking of electrons by the bulk phase of SE.[1]

Comparatively, the representative Nyquist plot of Li/LE/GC-LATP/LE/Li is dominated by two semicircles, which is typical for a formation of ion-conducting SLEI (SEI, acronym for solid-liquid electrolyte interphase) at the interface between LATP and Li. The corresponding equivalent circuits are shown in Figure S4(b), in which the first semicircle at high frequency represents the resistance of LATP grain (R_g). The $R_{int}||CPE1$ element represents the ion migration in the SLEI layer and dielectric capacitance of the SEI layer.[1, 2]

Hence, the interface between LATP and Li is a mixed ion-electron conductor, which cannot suppress the interfacial reactions between Li and LATP. By adding some LE at the interface, and ion-conducting SLEI layer will form at the interface, which could prevent the reduction of LATP from Li metal, thus guaranteeing the long-term stability of LATP in lithium metal batteries.

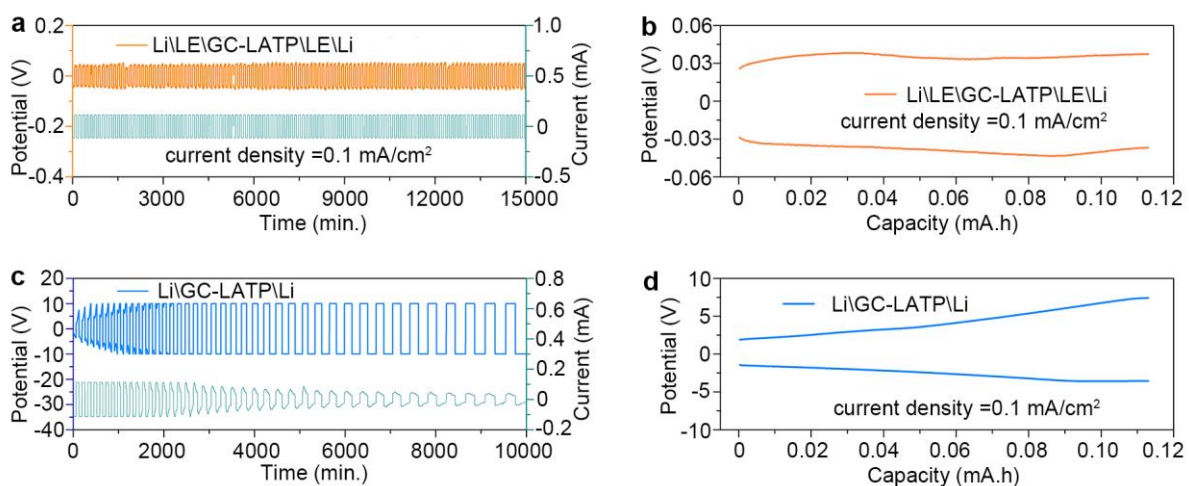


Figure 10-S11. Evaluation of the anode interface stability between GC-LATP and Li metal. (a) The voltage profile of Li\LE\GC-LATP\LE\Li symmetric cells. (b) The initial voltage-capacity profiles of Li\LE\GC-LATP\LE\Li symmetric cells. (c) The voltage profile of Li\GC-LATP\Li symmetric cells. (d) The initial voltage-capacity profiles of Li\GC-LATP\Li symmetric cells. Compared to the Li plating/stripping overpotential of Li\GC-LATP\Li cells upon cycling (which varies from 6 V to over 10 V), Li\LE\GC-LATP\LE\Li shows a stable overpotential of 45 mV upon cycling, suggesting that the large resistance between GC-LATP and metal Li is minimized by adding a small amount of LE.

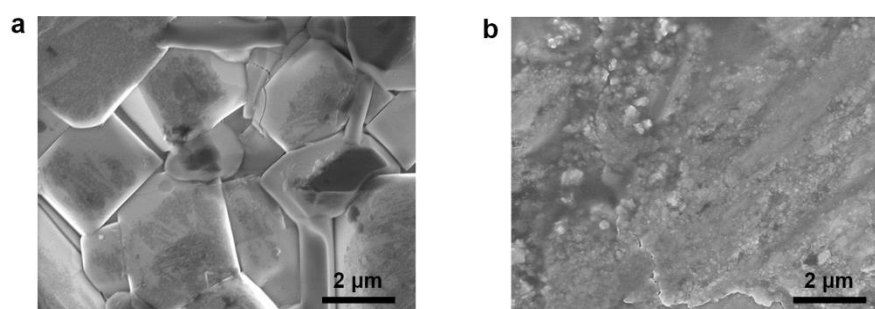


Figure 10-S12. Post-cycling analysis on the solid-liquid electrolyte interphase. (a) An SEM image of GC-LATP pellets before battery cycling. (b) An SEM image of glass-ceramic LATP pellets after 100 cycles.

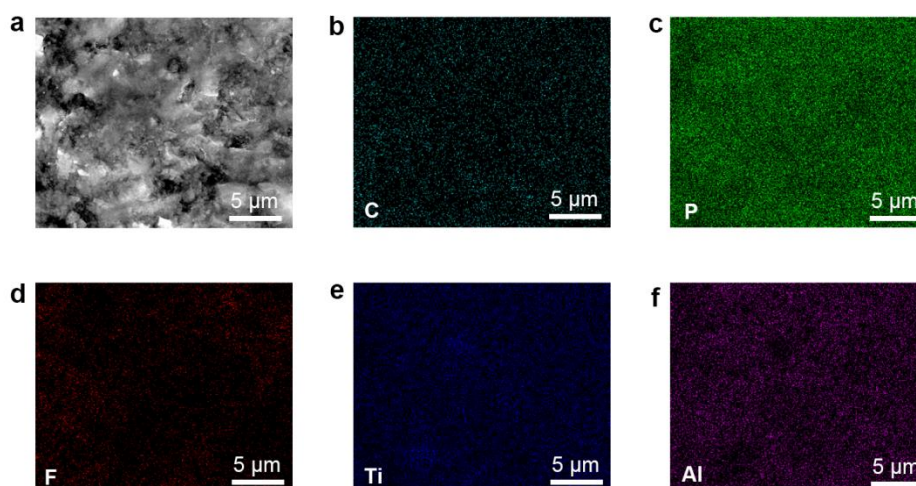


Figure 10-S13. Post-cycling analysis on the SLEI layer. (a) An SEM image of GC-LATP pellets after 100 cycles. (b-f) Elemental mapping of C, P, F, Ti, and Al, respectively.

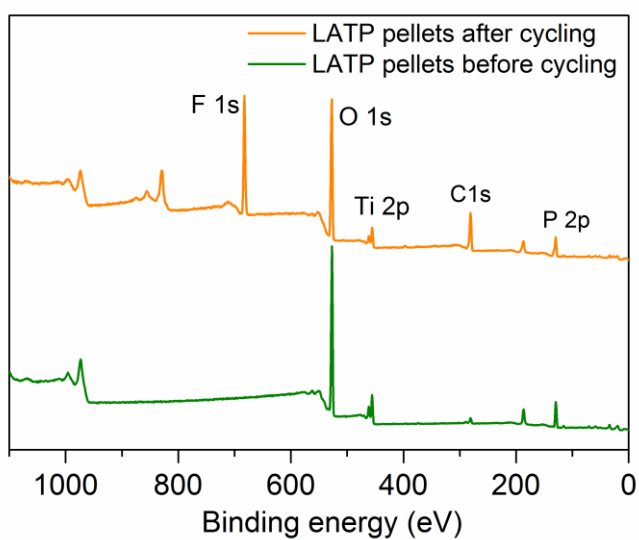


Figure 10-S14. The full survey XPS spectra of GC-LATP pellets before and after cycling.

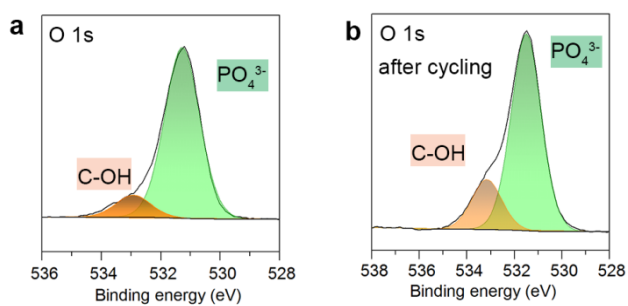


Figure 10-S15. X-ray photoelectron spectroscopy of GC-LATP pellets before and after electrochemical cycling. (a) high-resolution O 1s spectra obtained from the GC-LATP pellets before cycling. (b) high-resolution O 1s spectra obtained from the GC-LATP pellets after cycling.

Chapter 11

11. Conclusions and Perspectives

This chapter summarizes the results and contributions of this thesis and proposes suggestions on the interface design of all-solid-state lithium-ion batteries.

11.1 Conclusions

SE-based all-solid-state lithium-ion batteries (ASSLIBs) have received tremendous attention in recent years owing to their improved safety and energy density over conventional liquid electrolyte-based lithium-ion batteries. However, there are three main challenges impeding the development of SE-based ASSLIBs, including (1) insufficient ionic conductivity and bad air-stability of solid-state sulfide electrolytes, (2) large interfacial resistance originating from the detrimental interfacial reaction and poor solid-solid contact between electrode materials and solid-state electrolytes, and (3) lithium dendrite growth when using Li metal as the anode of SE-based ASSLIBs (**Figure 11-1**).

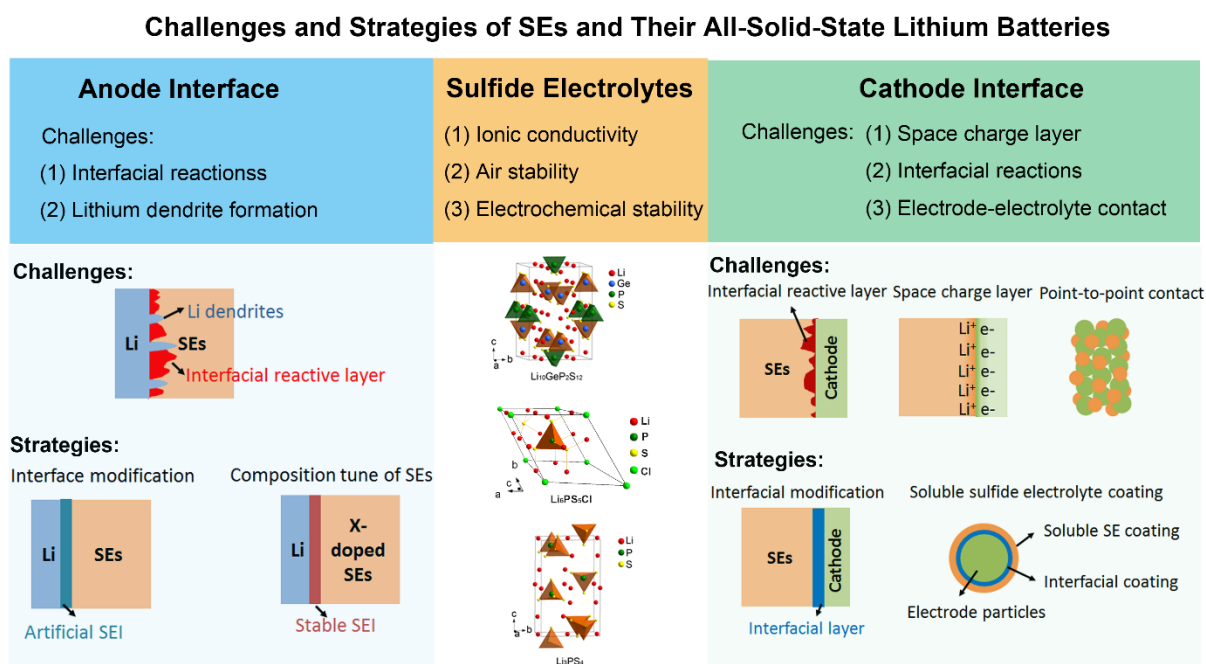


Figure 11-1 Summary of challenges and proposed strategies of SEs and their ASSLIBs.

With the tremendous efforts made over past years, corresponding strategies have been proposed. For example, (1) increasing Li^+ vacancies to improve the ionic conductivity

and doping with aliovalent elements (such as Sb) to improve the air stability of SEs. (2) developing soluble SEs to coat on cathode materials, thus significantly improving the solid-solid ionic contact. (3) engineering different interfacial coating layers (i.e. LiNbO_3 , LiTaO_3 , Li_3PO_4) to suppress the interfacial reactions. (4) introduction of lithium halides into SEs or modification of Li metal surface to suppress lithium dendrite formation in ASSLIBs.

The main objective of this thesis is to engineer the cathode/anode interface, aiming at suppressing interfacial resistance and improving the electrochemical performance of ASSLIBs. Meanwhile, advanced characterization techniques are used to reveal the interfacial reaction mechanisms, such as HRTEM and synchrotron radiation. All the research can be summarized in the following two parts:

Part 1: Different strategies to stabilize the cathode interface

Firstly, we rationally designed a dual shell interfacial nanostructure to enable high-performance ASSLIBs, in which the inner shell LiNbO_3 suppresses the interfacial reactions while the outer shell $\text{Li}_{10}\text{GeP}_2\text{S}_{12}$ enables intimate electrode-electrolyte contact. As a result, the dual shell structured $\text{Li}_{10}\text{GeP}_2\text{S}_{12}@\text{LiNbO}_3@\text{LiCoO}_2$ exhibits a high initial specific capacity of 125.8 mAh.g^{-1} (1.35 mAh.cm^{-2}) with an initial Coulombic efficiency of 90.4 % at 0.1 C and 87.7 mAh.g^{-1} at 1C. More importantly, in-situ X-ray absorption near-edge spectroscopy (XANES) was performed for the first time to reveal the interfacial reactions between $\text{Li}_{10}\text{GeP}_2\text{S}_{12}$ and LiCoO_2 .

Secondly, we use SC-NMC532 as the cathode material in SE-based ASSLIBs for the first time. By electrochemical analysis, the SC-NMC532 exhibits a Li^+ diffusion coefficient of 6~14 times higher than PC-NMC532. Therefore SC-NMC532 exhibits an initial specific capacity of 151.2 mAh.g^{-1} and retains a specific capacity of 88.9 mAh.g^{-1} after 150 cycles. More importantly, SC-NMC532 exhibits a specific capacity of 82 mAh.g^{-1}

under a high current density of $1.3 \text{ mA}\cdot\text{cm}^{-2}$ while PC-NMC532 only shows $2.1 \text{ mAh}\cdot\text{g}^{-1}$. This work demonstrates that single-crystal NMC cathodes could simultaneously enable the high energy density and high-power density of ASSLIBs at room temperature.

Furthermore, the root cause of the large interfacial resistance of ASSLIBs is well-analyzed by TEM, XAS, and XPS. It is found that the oxygen loss from single-crystal $\text{LiNi}_{0.5}\text{Mn}_{0.3}\text{Co}_{0.2}\text{O}_2$ (SC-NMC532) contributes to significant oxidation of the sulfide electrolyte $\text{Li}_{10}\text{GeP}_2\text{S}_{12}$ upon cycling. In addition, the structural degradation from a layered structure to a rock-salt structure further impedes interfacial Li^+ transport in ASSLIBs. Fortunately, the interfacial coating is demonstrated to be effective in preventing oxygen release and interfacial structure change, successfully mitigating the large interfacial resistance of ASSLIBs. As a result, $\text{LiNb}_{0.5}\text{Ta}_{0.5}\text{O}_3$ -coated SC-MC532 exhibits an initial specific capacity of $161.4 \text{ mAh}\cdot\text{g}^{-1}$, which remains at $92.1 \text{ mAh}\cdot\text{g}^{-1}$ after 300 cycles. These results provide new insights into the large interfacial resistance of ASSLIBs and presents new opportunities to design high-performance ASSLIBs.

In the fourth part, the interfacial coating layer was engineered with different ionic conductivity. By manipulating the interfacial Li^+ transport conductivity, it is found that the interfacial Li^+ transport is the most crucial step for high-performance ASSLIBs and improving the interfacial Li^+ conductivity of coating layer can significantly improve the electrochemical performance of ASSLIBs.

In order to realize the intimate solid-solid contact between electrode materials and solid-state electrolyte, a solid-state halide electrolyte (Li_3InCl_6) was in-situ grown on the electrode surface. Owing to strong interfacial interaction and excellent interfacial compatibility, the interfacial resistance is as low as $0.13 \text{ }\Omega\cdot\text{cm}^{-2}$. Consequently, LCO with 15wt% LIC exhibits a high initial capacity of $131.7 \text{ mAh}\cdot\text{g}^{-1}$ at 0.1C ($1\text{C}=1.3 \text{ mA}\cdot\text{cm}^{-2}$) and can be cycled up to 4C at room temperature. The discharge capacity retains $90.3 \text{ mAh}\cdot\text{g}^{-1}$ after 200 cycles. More importantly, a high areal capacity of 6

mAh.cm⁻² is realized with a high LCO loading of 48.7 mg.cm⁻². This work offers a new route toward the development of high-energy-density and high-power-density AISSBs without interfacial obstacles.

Part 2: Different Strategies to Stabilize the Cathode Interface

In the sixth part, Li metal anode was successfully enabled in solid-state batteries by an inorganic/organic hybrid interfacial layer, which was realized by an advanced molecular layer deposition technique. With the help of the alucone coating layer, the interfacial reactions between Li metal and LSPS are greatly suppressed. In addition, lithium dendrite formation is also inhibited. By XPS analysis, the reduction of Sn⁴⁺ in LSPS was restrained with the MLD coating layer. Compared with bare Li, LiCoO₂-based ASSLMBs with 30aluocne Li exhibit smaller polarization, higher Coulombic efficiency, higher capacity, and longer cycle life. This demonstration clearly suggests that Li metal with MLD coating can be successfully applied to ASSLMBs without compromising the output voltage and energy density of ASSLMBs.

In the seventh part, a novel plastic crystal electrolyte (PCE) was developed to improve the solid-solid contact as well as suppress the interfacial reactions. Due to the excellent compatibility between PCE and sulfide electrolytes, ASSLMBs based on Li metal and LiFePO₄ exhibit a high initial capacity of 148 mAh.g⁻¹ at 0.1 C and 131 mAh.g⁻¹ at 0.5 C (1C=170 mA.g⁻¹), which remains 122 mAh.g⁻¹ after 120 cycles at 0.5C. In addition, all-solid-state Li-S batteries based on polyacrylonitrile-sulfur composites are also demonstrated, showing an initial capacity of 1682 mAh g⁻¹. The second discharge capacity of 890 mAh.g⁻¹, which keeps at 775 mAh.g⁻¹ after 100 cycles. The decay rate of the specific capacity is as low as 0.14%. This work provides a new strategy to address interfacial challenges between Li metal and sulfide electrolytes, enabling the successful adoption of Li metal anodes in all-solid-state lithium batteries toward next-generation safe and high-energy-density energy storage systems.

Last but not least, the effects and interfacial properties of LE in the solid-liquid hybrid electrolyte have been investigated. We quantitatively add LE at the interface to eliminate the large interfacial resistance and study its interfacial properties. As little as 2 μl of LE at the interface enables a hybrid $\text{LiFePO}_4/\text{LATP}/\text{Li}$ battery to deliver a specific capacity of 125 mAh g^{-1} at 1C and 98 mAh g^{-1} at 4C. Excess LE has no further contribution to the electrochemical performance. Furthermore, the rigid SSE could suppress the formation of lithium dendrites, especially in the case with a high cathode loading (9.1 mg/cm^2), suggesting the feasibility of high energy density SSLBs using Li metal anodes. The interfacial analysis reveals that an interfacial solid-liquid electrolyte interphase (SLEI) was formed at the interface, preventing the reduction of LATP by Li metal, thus ensuring the long-term durability of LATP in LE.

11.2 Perspectives

Although a lot of remarkable achievements have been made, there are still a lot of remaining challenges to be addressed. Herein, we provided the potential directions and our perspectives in this field.

(1) Improvements of Solid-State Sulfide Electrolytes:

(I) Improving the Ionic Conductivity of SEs: Although some of SEs exhibit comparable ionic conductivity with those of liquid electrolytes. Improving the ionic conductivity of solid-state sulfide electrolytes is still necessary for fast-charging solid-state batteries. In the future, SEs with not only high ionic conductivity but also good air stability, wide electrochemical windows, and low cost should be developed to meet the requirements of large-scale applications.

(II) Air Stability: SEs generally suffer from the hydrolysis in air, which releases harmful H_2S and devalues the ionic conductivity of SEs. Improving the air stability of SEs now

is an urgent task for the commercialization of SE-based ASSLIBs. Current strategies, such as the introduction of metal oxides and composition tuning can improve the air stability of SEs but generally sacrifice their high ionic conductivity. New strategies, such as nano-thin film coating on SE particles, or nanostructured SE particles with a stable shell could give some contribution, as long as the out shell does not block the Li^+ transport.

(III) Electrochemical Stability: The intrinsic stable electrochemical window is generally from 2.1 V to 2.7V. which is unstable against Li metal and high-voltage cathodes. Tuning the chemical composition of SEs can alter the electrochemical stability. In addition, a dielectric buffer layer may also block the electron transfer at the electrode-electrolyte interface, thus successfully enabling the application of SEs in ASSLIBs.

(IV) Low-cost Synthesis Route: New synthesis route beyond ball milling and high-temperature glass-tube sealed post-annealing should be developed for large scale production with a low cost and environmental friendliness, such as the economic and eco-friendly liquid method, which also enable the size and morphology controllability.

(V) Alternative Ionic Conductors: Discovering new solid electrolytes with high ionic conductivity, good chemical and electrochemical stability, and low cost is also recommended, such as recently-found Li_3YCl_3 , Li_3InCl_6 .

(2) Understanding and Overcoming Interfacial Challenges of All-Solid-State Lithium Batteries:

At the Cathode Interface:

(I) Interfacial coating is required to suppress the interfacial reactions and space charge layer at the cathode interface and lithium dendrite growth at the anode interface.

However, the stability of interfacial coating during the cycling needs to be investigated. In addition, the multilayer interfacial layers with different electrochemical windows or different mechanical stability should be developed to suppress the reduction/oxidation reactions by electrodes and accommodate the volume change of electrode upon cycling.

(II) The interfacial layer is generally developed by the sol-gel method or fluidized bed coating, which is very difficult to control the thickness and uniformity. The interfacial coating materials developed by ALD by our group can exactly control the thickness and uniformity to design the interfacial layer. In addition, the complexed interfacial coating layer, such as inorganic-organic hybrid coatings, can also be developed by combining ALD and molecular layer deposition (MLD) techniques, which can act as an artificial cathode electrolyte interphases (CEI).

(III) The electronic and ionic conductivity of the interfacial coating layer should be investigated to figure out the basic requirement of interfacial layers.

(III) Interfacial ionic contact between the electrode and SEs can be improved by soluble SE coating. However, improving the ionic conductivity of soluble SEs is very urgent for high-power solid-state batteries.

(IV) To ensure the high energy density of ASSLIBs, the SE content in the cathode composites should be minimized.

At the Anode Interface:

(I) the interfacial reactions and lithium dendrite formation between Li metal and SEs should be avoided. So far, these challenges can be overcome by either internal composition tuning of SEs or external surface modification. However, the capacity of Li⁺ plating/stripping is too low for real applications. The large cycling capacity of Li metal (> 3mAh.cm⁻²) need to be achieved.

(II) In addition, the Coulombic efficiency of Li metal in solid-state batteries should be investigated to guarantee the long lifespan of ASSLIBs.

(III) Importantly, advanced characterization techniques, particularly in-situ techniques, are required to retrieve more in-depth interfacial information in ASSLIBs.

(3) Mass Production of SE-based ASSLIBs

(I) Although the manufacturing protocols have been proposed and some prototypes of SE-based ASSLIBs have been demonstrated, the remained engineering challenges, such as the solvent and binder selection criteria, quality control, and compatible battery manage the system, manufacturing cost should be addressed in the near future.

Foreseeably, with tremendous endeavors to overcome the challenges, safe and high-energy-density SEs-based ASSLIBs could be realized for the applications in electric vehicles, smart grids, consumer electronics, and even flexible electronics.

11.3 Main Contribution of This Thesis

Because of the great safety feature and potential to achieve high energy density, all-solid-state lithium batteries have gained substantial attentions in recent years, however, large interfacial resistance, which originates from poor solid-solid contact and detrimental interfacial reactions between electrodes and SEs, significantly suppressed the electrochemical performance of ASSLBs. Therefore, high-performance ASSLBs would not be achieved without addressing the interfacial challenges. My research activity is dedicated to addressing the interfacial challenges in SE-based ASSLBs. For example, at the cathode interface, I came up with 5 strategies in total, which successfully suppressed the large interfacial resistance at the cathode interface. I also demonstrated that the high

ionic conductivity of interfacial coating is highly recommended for realizing high-power ASSLBs. Furthermore, using advanced characterization tools including synchrotron radiation and high-resolution TEM, I also identified that the oxygen loss from the cathode materials may be another under-emphasized factor for significant interfacial reactions after long-term cycling. I believe these research findings would provide an in-depth understanding about the interface of SE-based ASSLBs.

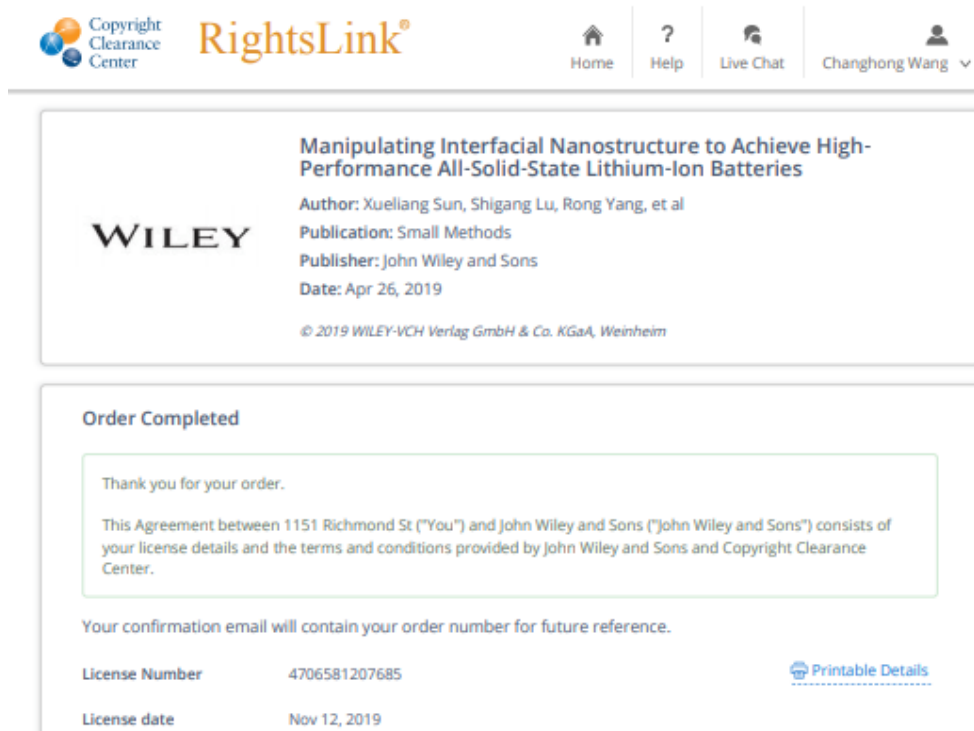
At the anode interface, an inorganic-organic hybrid coating layer between the SE and Li metal was realized by molecular layer deposition for the first time, which successfully suppressed anode interfacial reactions and lithium dendrite growth. More importantly, the plastic crystal electrolyte (PCE) was first studied as a buffer layer in SE-based ASSLBs. I believe these findings would serve as a useful guidance for developing high-performance all-solid-state lithium metal batteries.

Appendices

Appendix A: Permission John Wiley and Sons for Published Article on Small Methods

Published Article:

Changhong Wang, Xia Li, Yang Zhao, Mohammad N Banis, Jianwen Liang, Xiaona Li, Yipeng Sun, Keegan R Adair, Qian Sun, Yulong Liu, Feipeng Zhao, Sixu Deng, Xiaoting Lin, Ruying Li, Yongfeng Hu, Tsun - Kong Sham, Huan Huang, Li Zhang, Rong Yang, Shigang Lu, Xueliang Sun. Manipulating Interfacial Nanostructure to Achieve High-Performance All-Solid-State Lithium-Ion Batteries. **Small Methods**. 2019, 1900261. Doi: <https://doi.org/10.1002/smt.201900261>



Copyright Clearance Center **RightsLink**[®] Home ? Help Live Chat Changhong Wang ▾

WILEY

Manipulating Interfacial Nanostructure to Achieve High-Performance All-Solid-State Lithium-Ion Batteries
 Author: Xueliang Sun, Shigang Lu, Rong Yang, et al
 Publication: Small Methods
 Publisher: John Wiley and Sons
 Date: Apr 26, 2019
 © 2019 WILEY-VCH Verlag GmbH & Co. KGaA, Weinheim

Order Completed

Thank you for your order.

This Agreement between 1151 Richmond St ("You") and John Wiley and Sons ("John Wiley and Sons") consists of your license details and the terms and conditions provided by John Wiley and Sons and Copyright Clearance Center.

Your confirmation email will contain your order number for future reference.

License Number 4706581207685 [Printable Details](#)
 License date Nov 12, 2019

Appendix B: Permission from Elsevier for Published Article on *Nano Energy***Published Article:**

Changhong Wang, Yang Zhao, Qian Sun, Xia Li, Yulong Liu, Jianwen Liang, Xiaona Li, Xiaoting Lin, Ruying Li, Keegan R Adair, Li Zhang, Rong Yang, Shigang Lu, Xueliang Sun, Stabilizing interface between $\text{Li}_{10}\text{SnP}_2\text{S}_{12}$ and Li metal by molecular layer deposition, **Nano Energy**, 2018,53,168-174.



The screenshot displays the Elsevier RightsLink interface. At the top left, there is a logo for the Copyright Clearance Center and the RightsLink® logo. To the right, there are navigation icons for Home, Help, Live Chat, and a user profile for Changhong Wang. The main content area features the Elsevier tree logo and the article title: "Stabilizing interface between $\text{Li}_{10}\text{SnP}_2\text{S}_{12}$ and Li metal by molecular layer deposition". Below the title, the author list is provided: Changhong Wang, Yang Zhao, Qian Sun, Xia Li, Yulong Liu, Jianwen Liang, Xiaona Li, Xiaoting Lin, Ruying Li, Keegan R. Adair, Li Zhang, Rong Yang, Shigang Lu, Xueliang Sun. The publication is identified as Nano Energy, published by Elsevier in November 2018. A copyright notice states "© 2018 Published by Elsevier Ltd.". A text box at the bottom contains a permission notice: "Please note that, as the author of this Elsevier article, you retain the right to include it in a thesis or dissertation, provided it is not published commercially. Permission is not required, but please ensure that you reference the journal as the original source. For more information on this and on your other retained rights, please visit: <https://www.elsevier.com/about/our-business/policies/copyright#Author-rights>". At the bottom of this box are "BACK" and "CLOSE WINDOW" buttons.

Appendix C: Permission John Wiley and Sons for Published Article on Advanced Functional Materials.

Published Article:

Changhong Wang, Keegan R Adair, Jianwen Liang, Xiaona Li, Yipeng Sun, Xia Li, Jiwei Wang, Qian Sun, Feipeng Zhao, Xiaoting Lin, Ruying Li, Huan Huang, Li Zhang, Rong Yang, Shigang Lu, Xueliang Sun. Solid - State Plastic Crystal Electrolytes: Effective Protection Interlayers for Sulfide - Based All - Solid - State Lithium Metal Batteries.

Advanced Functional Materials. 2019, 1900392. DOI: <https://doi.org/10.1002/adfm.201900392>

Dear Mr. Changhong Wang,

Thank you for placing your order through Copyright Clearance Center's RightsLink® service.

Order Summary

Licensee: 1151 Richmond St
Order Date: Nov 12, 2019
Order Number: 4706571280947
Publication: Advanced Functional Materials
Solid-State Plastic Crystal Electrolytes: Effective Protection
Title: Interlayers for Sulfide-Based All-Solid-State Lithium Metal Batteries
Type of Use: Dissertation/Thesis
Order Total: 0.00 USD

View or print complete [details](#) of your order and the publisher's terms and conditions.

Sincerely,

Copyright Clearance Center

Appendix D: Permission from Elsevier for Published Article on *Nano Energy***Published Article:**

Changhong Wang, Qian Sun, Yulong Liu, Yang Zhao, Xia Li, Xiaoting Lin, Mohammad Norouzi Banis, Minsi Li, Weihan Li, Keegan R Adair, Dawei Wang, Jianneng Liang, Ruying Li, Li Zhang, Rong Yang, Shigang Lu, Xueliang Sun. Boosting the performance of lithium batteries with solid-liquid hybrid electrolytes: Interfacial properties and effects of liquid electrolytes, **Nano Energy**, 2018,48,35-43.



The screenshot shows a web interface for Elsevier's RightsLink service. At the top left, there is a logo for the Copyright Clearance Center and the RightsLink® logo. On the top right, there are navigation links for Home, Help, Live Chat, and a user profile for Changhong Wang. The main content area displays the title of the article: "Boosting the performance of lithium batteries with solid-liquid hybrid electrolytes: Interfacial properties and effects of liquid electrolytes". Below the title is the Elsevier logo and the author list: Changhong Wang, Qian Sun, Yulong Liu, Yang Zhao, Xia Li, Xiaoting Lin, Mohammad Norouzi Banis, Minsi Li, Weihan Li, Keegan R. Adair, Dawei Wang, Jianneng Liang, Ruying Li, Li Zhang, Rong Yang, Shigang Lu, Xueliang Sun. The publication is identified as Nano Energy, published by Elsevier in June 2018. A copyright notice states "© 2018 Elsevier Ltd. All rights reserved." Below this, a disclaimer notes that the author retains the right to include the article in a thesis or dissertation, provided it is not published commercially. A link is provided for more information: <https://www.elsevier.com/about/our-business/policies/copyright#Author-rights>. At the bottom of the window, there are buttons for "BACK" and "CLOSE WINDOW".

Curriculum Vitae

Name: Changhong Wang

Post-secondary Education and Degrees: University of Science and Technology of Anhui
Bengbu, Anhui, China
2007-2011 B.A.

University of Science and Technology of China
Hefei, Anhui, China
2011-2014 Master

The University of Western Ontario
London, Ontario, Canada
2016-2019 Ph.D.

Honors and Awards: Western Engineering Full Scholarship
2016-2020
MITACS Accelerate Fellowships
2019-2020

Related Work Experience: Teaching Assistant
The University of Western Ontario
2016-2019

Publications:

(A) Peer-Reviewed Journal Papers as the First Author

- Changhong Wang**, Keegan R Adair, Jianwen Liang, Xiaona Li, Yipeng Sun, Xia Li, Jiwei Wang, Qian Sun, Feipeng Zhao, Xiaoting Lin, Ruying Li, Huan Huang, Li Zhang, Rong Yang, Shigang Lu, Xueliang Sun, Solid-State Plastic Crystal Electrolytes: Effective Protection Interlayers for Sulfide-Based All-Solid-State Lithium Metal

- Batteries, **Advanced Functional Materials**. 2019, 29, 1900392.
- 2. Changhong Wang**, Xia Li, Yang Zhao, Mohammad N Banis, Jianwen Liang, Xiaona Li, Yipeng Sun, Keegan R Adair, Qian Sun, Yulong Liu, Feipeng Zhao, Sixu Deng, Xiaoting Lin, Ruying Li, Yongfeng Hu, Tsun-Kong Sham, Huan Huang, Li Zhang, Rong Yang, Shigang Lu, Xueliang Sun, Manipulating Interfacial Nanostructure to Achieve High-Performance All-Solid-State Lithium-Ion Batteries, **Small Methods**. 2019, 1900261.
 - 3. Changhong Wang**, Yang Zhao, Qian Sun, Xia Li, Yulong Liu, Jianwen Liang, Xiaona Li, Xiaoting Lin, Ruying Li, Keegan R Adair, Li Zhang, Rong Yang, Shigang Lu, Xueliang Sun, Stabilizing interface between $\text{Li}_{10}\text{SnP}_2\text{S}_{12}$ and Li metal by molecular layer deposition. **Nano Energy**, 2018, 53, 168-174.
 - 4. Changhong Wang**, Qian Sun, Yulong Liu, Yang Zhao, Xia Li, Xiaoting Lin, Mohammad Norouzi Banis, Minsi Li, Weihan Li, Keegan R Adair, Dawei Wang, Jianneng Liang, Ruying Li, Li Zhang, Rong Yang, Shigang Lu, Xueliang Sun. Boosting the performance of lithium batteries with solid-liquid hybrid electrolytes: Interfacial properties and effects of liquid electrolytes, **Nano Energy**, 2018, 48, 35-43.
 - 5. Changhong Wang**, Sooyeon Hwang, Jianwen Liang, Xiaona Li, Changtai Zhao, Yipeng Sun, Jiwei Wang, Nathaniel Holmes, Ruying Li, Huan Huang, Shangqian Zhao, Li Zhang, Shigang Lu, Dong Su, and Xueliang Sun, Single Crystal Cathodes Enabling High-Energy and High-Power All-Solid-State Lithium-Ion Batteries. **To be submitted**.
 - 6. Changhong Wang**, Jianwen Liang, Ming Jiang, Xiaona Li, Sankha, Mukherjee, Keegan Adair, Matthew Zheng, Yang Zhao, Feipeng, Zhao, Shuming Zhang, Ruying Li, Huan Huang, Shangqian Zhao, Li Zhang, Shigang Lu, Chandra Veer Singh, and Xueliang Sun. Eliminating Interfacial Resistance in All-Inorganic Solid-State Batteries by In-situ Interfacial Growth of Halide Electrolytes. **Advanced Energy Materials**. Submitted.

7. **Changhong Wang**, Jianwen Liang, Yang Zhao, Xiaona Li, Sooyeon Hwang, Keegan Adair, Yulong Liu, Xia Li, Sixu Deng, Xiaofei Yang, Ruying Li, Huan Huang, Li, Zhang, Shigang Lu, Dong Su, and Xueliang Sun, “Revealing Interfacial Ion Transport Kinetics in All-Solid-State Lithium-Ion Batteries. **Submitted to Nano Energy**
8. **Changhong Wang**, Sooyeon Hwang, Jianwen Liang, Xiaona Li, Yipeng Sun, Sankha Mukherjee, Nathaniel Holme, Mohammad Norouzi Banis, Changtai Zhao, Ruying Li, Huan Huang, Shangqian Zhao, Li, Zhang, Shigang Lu, Chandra Veer Singh, Dong Su, and Xueliang Sun. Understanding Oxygen Release from Layered Oxide Cathodes in Sulfide-based All-Solid-State Batteries. **Ready for submission**
9. **Changhong Wang**, Yang Zhao, Jianwen Liang, Xiaona Li, Solid-State Sulfide Electrolytes and Their All-Solid-State Lithium Batteries: From Fundamental Research to Real Application. **To be submitted**
10. **Changhong Wang**, Xueliang Sun, Ammonia-coordinated synthesis of Li_3YCl_6 for High-Performance All-Solid-State Lithium-Ion Batteries. **In Preparation**
11. **Changhong Wang**, Xueliang Sun, Unravelling Interfacial Reactions of Single-crystal NMC622-based ASSLIBs. **In preparation**

Publications: (B) Peer-reviewed Journal Papers as a Co-author

12. Xiaona Li, Jianwen Liang, Jing Luo, **Changhong Wang**, Xia Li, Qian Sun, Ruying Li, Li Zhang, Rong Yang, Shigang Lu, Huan Huang, Xueliang Sun. High-Performance Li–SeS_x All-Solid-State Lithium Batteries. **Advanced Materials**. 2019, 31, 1808100. <https://doi.org/10.1002/adma.201808100>.
13. Yipeng Sun, Yang Zhao, Jiwei Wang, Jianneng Liang, **Changhong Wang**, Qian Sun, Xiaoting Lin, Keegan R Adair, Jing Luo, Dawei Wang, Ruying Li, Mei Cai, Tsun-Kong Sham, Xueliang Sun. A Novel Organic “Polyurea” Thin Film for Ultralong-Life Lithium-Metal Anodes via Molecular-Layer Deposition. **Advanced Materials**. 2019, 31, 1806541. <https://doi.org/10.1002/adma.201806541>.

14. Xia Li, Zhouhong Ren, Mohammad Norouzi Banis, Sixu Deng, Yang Zhao, Qian Sun, **Changhong Wang**, Xiaofei Yang, Weihan Li, Jianwen Liang, Xiaona Li, Yipeng Sun, Keegan Adair, Ruying Li, Yongfeng Hu, Tsun-Kong Sham, Huan Huang, Li Zhang, Shigang Lu, Jun Luo, Xueliang Sun, Unravelling the Chemistry and Microstructure Evolution of Cathodic Interface in Sulfide-Based All-Solid-State Li-Ion Batteries, **ACS Energy Letters**. 2019, 4, 10, 2480-2488.
15. Xiaoting Lin, Fei Sun, Qian Sun, Sizhe Wang, Jing Luo, Changtai Zhao, Xiaofei Yang, Yang Zhao, **Changhong Wang**, Ruying Li, Xueliang Sun. An O₂/O₂-Crossover-and Dendrite-Free Hybrid Solid-State Na-O₂ Battery. **Chemistry of Materials**. 2019. Doi: <https://doi.org/10.1021/acs.chemmater.9b03266>
16. Yang Zhao, Jianwen Liang, Qian Sun, Lyudmila V Goncharova, Jiwei Wang, **Changhong Wang**, Keegan R Adair, Xiaona Li, Feipeng Zhao, Yipeng Sun, Ruying Li, Xueliang Sun. In situ formation of highly controllable and stable Na₃PS₄ as a protective layer for Na metal anode, **J. Mater. Chem. A**, 2019,7, 4119-4125.
17. Xiaona Li, Jianwen Liang, Xia Li, **Changhong Wang**, Jing Luo, Ruying Li, Xueliang Sun. High-performance all-solid-state Li-Se batteries induced by sulfide electrolytes, **Energy & Environmental Science**. 2018,11, 2828-2832. Doi: 10.1039/C8EE01621F
18. Keegan R Adair, Muhammad Iqbal, **Changhong Wang**, Yang Zhao, Mohammad Norouzi Banis, Ruying Li, Li Zhang, Rong Yang, Shigang Lu, Xueliang Sun. Towards high-performance Li metal batteries: Nanoscale surface modification of 3D metal hosts for pre-stored Li metal anodes. **Nano Energy**. 2018, 54, 375-382. Doi: <https://doi.org/10.1016/j.nanoen.2018.10.002>.
19. Jianwen Liang, Xiaona Li, Yang Zhao, Lyudmila V Goncharova, Gongming Wang, Keegan R Adair, **Changhong Wang**, Ruying Li, Yongchun Zhu, Yitai Qian, Li Zhang, Rong Yang, Shigang Lu, Xueliang Sun. In Situ Li₃PS₄ Solid-State Electrolyte Protection Layers for Superior Long-Life and High-Rate Lithium-Metal Anodes. **Advanced Materials**. 2018, 30, 1804684. <https://doi.org/10.1002/adma.201804684>.

20. Xia Li, Mohammad Banis, Andrew Lushington, Xiaofei Yang, Qian Sun, Yang Zhao, Changqi Liu, Qizheng Li, Biqiong Wang, Wei Xiao, **Changhong Wang**, Minsi Li, Jianwen Liang, Ruying Li, Yongfeng Hu, Lyudmila Goncharova, Huamin Zhang, Tsun-Kong Sham, Xueliang Sun. A high-energy sulfur cathode in carbonate electrolyte by eliminating polysulfides via solid-phase lithium-sulfur transformation, **Nature Communications**. 2018, 9, 4509. Doi: <https://doi.org/10.1038/s41467-018-06877-9>.
21. Yang Zhao, Xiaofei Yang, Qian Sun, Xuejie Gao, Xiaoting Lin, **Changhong Wang**, Feipeng Zhao, Yipeng Sun, Keegan R Adair, Ruying Li, Mei Cai, Xueliang Sun. Dendrite-free and minimum volume change Li metal anode achieved by three-dimensional artificial interlayers. **Energy Storage Materials**, 2018. 15, 415-421.
22. Yang Zhao, Qian Sun, Xia Li, **Changhong Wang**, Yipeng Sun, Keegan R Adair, Ruying Li, Xueliang Sun. Carbon paper interlayers: a universal and effective approach for highly stable Li metal anodes. **Nano Energy**, 2018, 43, 268-375. Doi: <https://doi.org/10.1016/j.nanoen.2017.11.032>.
23. Jiwei Wang, Qian Sun, Xuejie Gao, **Changhong Wang**, Weihan Li, Frederick Benjamin Holness, Matthew Zheng, Ruying Li, Aaron David Price, Xuhui Sun, Tsun-Kong Sham, Xueliang Sun. Toward High Areal Energy and Power Density Electrode for Li-Ion Batteries via Optimized 3D Printing Approach. **ACS Applied Materials & Interfaces**. 2018, 10, 46, 39794-39801. Doi: <https://doi.org/10.1021/acsami.8b14797>.
24. Changtai Zhao, Chang Yu, Shaofeng Li, Wei Guo, Yang Zhao, Qiang Dong, Xiaoting Lin, Zhongxin Song, Xinyi Tan, **Changhong Wang**, Matthew Zheng, Xueliang Sun, Jieshan Qiu. Ultrahigh-Capacity and Long-Life Lithium–Metal Batteries Enabled by Engineering Carbon Nanofiber–Stabilized Graphene Aerogel Film Host. **Small**. 2018, 14, 1803310. Doi: <https://doi.org/10.1002/sml.201803310>.
25. Xiaoting Lin, Qian Sun, Hossein Yadegari, Xiaofei Yang, Yang Zhao, Changhong Wang, Jianneng Liang, Alicia Koo, Ruying Li, Xueliang Sun. On the Cycling

Performance of Na-O₂ Cells: Revealing the Impact of the Superoxide Crossover toward the Metallic Na Electrode. **Advanced Functional Materials**. 2018. 28 (35), 1801904. Doi: <https://doi.org/10.1002/adfm.201801904>.

26. Jianneng Liang, Qian Sun, Yang Zhao, Yipeng Sun, **Changhong Wang**, Weihan Li, Minsi Li, Dawei Wang, Xia Li, Yulong Liu, Keegan Adair, Ruying Li, Li Zhang, Rong Yang, Shigang Lu, Huan Huang, Xueliang Sun. Stabilization of all-solid-state Li–S batteries with a polymer–ceramic sandwich electrolyte by atomic layer deposition. **Journal of Materials Chemistry A**. 2018,6, 23712-23719. Doi: 10.1039/C8TA09069F.
27. Xiaofei Yang, Ying Yu, Xiaoting Lin, Jianneng Liang, Keegan Adair, Yang Zhao, **Changhong Wang**, Xia Li, Qian Sun, Hongzhang Zhang, Xianfeng Li, Ruying Li, Huamin Zhang, Xueliang Sun. Multi-functional nanowall arrays with unrestricted Li⁺ transport channels and an integrated conductive network for high-areal-capacity Li–S batteries. **Journal of Materials Chemistry A**. 2018,6, 22958-22965. Doi: 10.1039/C8TA08188C.

Patents:

28. **Changhong Wang**, Jianwen Liang, Xiaona Li, Shigang Lu, Li Zhang, Shangqian Zhao, Xueliang Sun, An electrode, solid-state electrolyte thin layer, and their preparation method and applications. (application number: 201910843405.4)
29. Jianwen Liang, Xiaona Li, **Changhong Wang**, Shigang Lu, Li Zhang, Shangqian Zhao, Xueliang Sun, a new solid-state electrolyte for secondary lithium batteries, preparation method, and its application. (application number: 201910381153.8)
30. Keegan Adair, **Changhong Wang**, Yang Zhao, Shigang Lu, Li Zhang, Shangqian Zhao, Xueliang Sun, A three-dimensional Li-Cu host for Li Metal Anode. (application number: 201910386661 .5)

Conferences:

- 31. Poster: Changhong Wang, Xueliang Sun, Protected Lithium Metal Enabling All-Solid-State Lithium-Ion Batteries with High Energy Density. 2017 MRS Fall Meeting.** Boston, USA. Nov. 26th -Dec. 1st. 2017.
- 32. Oral Presentation:** Changhong Wang, Xueliang Sun, A dual-core-shell structured cathode for sulfide-based all-solid-state lithium-ion batteries. **2018 ECS symposium.** London, Ontario, Canada. Dec. 12th, 2018.
- 33. Oral Presentation:** Changhong Wang, Xueliang Sun, Interface Engineering of Sulfide Electrolyte-based All-Solid-State Lithium Batteries. **CSME-CFDSC Congress 2019,** June 2-5. London, Ontario. Canada.
- 34. Oral Presentation:** Changhong Wang, Xueliang Sun, Interface Engineering of Sulfide Electrolyte-based All-Solid-State Lithium Batteries. **2019 CCEM Symposium.** May 30, 2019, Mcmaster, Ontario, Canada
- 35. Poster:** Changhong Wang, Feipeng Zhao, Weihan Li, Xueliang Sun. Surface Engineering of Sulfide-based All-Solid-State Lithium Batteries: Challenges and Strategies. **2019 CAMBR Symposium.** April 17, 2019, Western University, London, On. Canada.
- 36. Oral Presentation:** Changhong Wang, Xueliang Sun, Interface Engineering of Solid-State Lithium Battery: Revealing the Effect of Interfacial Li⁺ Conductivity. **2019 ECS symposium.** London, Ontario, Canada. Dec. 9th, 2019.
- 37. Oral Presentation:** Changhong Wang, Huan Huang, Xueliang Sun, Interface Engineering of Sulfide-based All-Solid-State Lithium Batteries. **237th ECS Meeting, Montreal, Canada,** May 10-14, 2020